수의학박사 학위논문

고농도 포도당에 의한 엔도리소좀 기능장애가 신경세포의 아밀로이드 베타 축적에 미치는 영향

The effect of high glucose-induced endolysosomal dysfunction on neuronal Amyloid β accumulation

2023년 2월

서울대학교 대학원

수의학과 수의생명과학 전공

(수의생리학)

채 창 우

고농도 포도당에 의한 엔도리소좀 기능장애가 신경세포의 아밀로이드 베타 축적에 미치는 영향

The effect of high glucose-induced endolysosomal dysfunction on neuronal Amyloid β accumulation

지도 교수 한 호 재

이 논문을 수의학 박사 학위논문으로 제출함

2022년 11월

서울대학교 대학원

수의학과 수의생명과학 전공

(수의생리학)

채 창 우

채창우의 수의학 박사 학위논문을 인준함

2022년 12월

위 원 장 _____ 이 장 헌 (인)

부위원장 _____ 한 호 재 (인)

위 원 _____ 이 민 영 (인)

위 원 _____ 이 세 중 (인)

위 원 _____ 이 현 직 (인)

Doctoral Thesis

The effect of high glucose-induced endolysosomal dysfunction on neuronal Amyloid β accumulation

Chang Woo Chae

Advisor: Ho Jae Han, D.V.M. Ph.D.

Major in Veterinary Biomedical Sciences

(Veterinary Physiology)

Department of Veterinary Medicine

The Graduate School Seoul National University

February 2023

ABSTRACT

The effect of high glucose-induced endolysosomal dysfunction on neuronal Amyloid β accumulation

Chang Woo Chae
Major in Veterinary Biomedical Sciences
(Veterinary Physiology)
Department of Veterinary Medicine
The Graduate School Seoul National University

Although diabetes mellitus (DM) is considered as a risk factor for Alzheimer' s disease (AD), the detailed mechanism by which DM regulates amyloid beta (Aβ) accumulation is still unclear. Endolysosomal dysfunction is a pathological link that may explain the causal relationship between the two diseases; however, there is little information on the regulation of neuronal endolysosomal function by hyperglycemia. Therefore, this study aims to investigate 1) the effects of high glucose on amyloid precursor protein (APP)-processing endosomes and its related signaling pathways, 2) the effects of high glucose on the retromer and defined the dysregulation of mechanisms of APP processing and tau phosphorylation, and 3) the effect and related mechanisms of action of high glucose on lysophagy impairment and subsequent Aβ accumulation.

Results were as followings:

1) The hippocampus of diabetic animals presented endosomal abnormalities and Aβ up-regulation. High glucose increased Aβ production through early endosomal enlargement achieved by increased lipid raft-mediated APP endocytosis. High glucose induced ROS-stimulated Sp1 activation, up-regulating phosphatidylinositol binding clathrin assembly protein (PICALM), clathrin heavy chain, and adaptor-related protein complex 2 alpha 1. PICALM facilitated clathrin-mediated APP endocytosis resulting in early endosomal enlargement. Meanwhile, AMPK/mTORC1-mediated autophagy defect and ROS- and mTORC1-mediated

lysosomal dysfunction aggravated early endosomal enlargement under high glucose. Moreover, the increased Aβ production and cognitive deficits in diabetic mice were reversed by inhibition of early endosomal enlargement [*Br J Pharmacol*. 2020;177: 3828–3847].

2) Vacuolar protein sorting–associated protein 26a (VPS26a) was decreased in the hippocampus of diabetic mice and high glucose–treated human neuronal cells. High glucose down–regulated VPS26a through ROS/NF–κB/DNA methyltransferase1–mediated promoter hypermethylation. VPS26a recovery blocked retention of APP and cation–independent mannose–6–phosphate receptor in endosomes and promoted transport to the trans–Golgi, which decreased Aβ levels, and improved cathepsin D activity, reducing p–Tau levels, respectively. Retromer enhancement ameliorated synaptic deficits, astrocyte overactivation, and cognitive impairment in diabetic mice [*Br J Pharmacol*. 2022;179: 3934–3950].

3) High glucose induced neuronal lysosomal dysfunction through reactive oxygen species–mediated lysosomal membrane permeabilization and lysophagy impairment. Among lysophagy–related factors, the expression of tripartite motif containing 16 (TRIM16) was reduced in high glucose–treated neuronal cells and the diabetic hippocampus through mTORC1–mediated inhibition of transcription factor EB (TFEB) activity. TRIM16 overexpression recovered lysophagy and lysosomal biogenesis through the

recruitment of microtubule-associated protein 1A/1B-light chain 3 (LC3), p62, and ubiquitin to damaged lysosomes, which inhibited the high-glucose-induced accumulation of Aβ and p-Tau. In the diabetic mice model, TFEB enhancer recovered lysophagy in the hippocampus, resulting in the amelioration of cognitive impairment.

In conclusion, present study demonstrated that high glucose induced 1) early endosomal abnormalities through PICALM-induced APP endocytosis and mTORC1-inhibited endosomal clearance, 2) retromer dysfunction through NF-κB/DNA methyltransferase1-mediated VPS26a downregulation, and 3) neuronal lysophagy impairment through mTORC1/TFEB-mediated TRIM16 downregulation, which induced Aβ accumulation. Thus, endolysosomal dysfunction is a promising candidate for the inhibition of diabetes-associated Alzheimer's disease pathogenesis.

Keyword : Alzheimer's disease, Autophagy, Diabetes mellitus, Endosome, Lysosome, Vesicle trafficking

Student Number : 2016-27822

CONTENTS

LIST OF FIGURES

LIST OF TABLES

ABBREVIATIONS

Aβ	Amyloid beta
AD	Alzheimer’s disease
AMPK	5’adenosine monophosphate-activated protein kinase
AP2A1	Adaptor-related protein complex 2 alpha 1
APP	Amyloid precursor protein
BACE1	Beta-Site APP Cleaving Enzyme
CAV1	Caveolin-1
CHC	Clathrin heavy chain
CI-MPR	Cation-independent mannose-6-phosphate receptor
CME	Clathrin-mediated endocytosis
CRC	Cargo recognition core
CTSB	Cathepsin B
CTSD	Cathepsin D
Diabetes mellitus	DM
ELN	Endolysosomal network
ESCRT	Endosomal sorting complex required for transport
FBXO27	F-box protein 27
FLOT1	Flotillin-1
iPSC-NDs	Induced-pluripotent stem cell-derived neuronal differentiated cells
LAMP1	Lysosomal-associated membrane protein 1
LC3	Microtubule-associated protein 1A/1B-light chain 3

LLOMe	H−Leu−Leu−OMe · HBr
LMP	Lysosomal membrane permeabilization
LRSAM1	Leucine−rich repeat and sterile alpha motif containing 1
MβCD	Methyl−β−cyclodextrin
mTORC1	Mammalian target of rapamycin complex 1
NAC	N−acetylcysteine
NFT	Neurofibrillary tangles
PICALM	Phosphatidylinositol binding clathrin assembly protein
p−Tau	phosphorylated tau
ROS	Reactive oxygen species
SORCS1	Sortilin related VPS10 domain containing receptor 1
SORL1	Sortilin related receptor 1
SNX	Sorting nexin
STZ	Streptozotocin
TFE3	Transcription factor E3
TFEB	Transcription factor EB
TRIM16	Tripartite motif containing 16
UBE2QL1	Ubiquitin−conjugating enzyme e2q family like 1
VCP	Valosin−containing protein
VPS	Vacuolar protein sorting−associated protein
ZDF	Zucker diabetic fatty
ZLC	Zucker lean control
5−mC	5−methylcytosine

BACKGROUND

A substantial body of epidemiological and clinical research indicates that hyperglycemia in diabetic and prediabetic conditions is a risk factor for Alzheimer's disease (AD). Hyperglycemia induce pathophysiological dysfunction which is commonly observed in both diseases. This includes excessive generation of reactive oxygen species (ROS), accumulation of oxidative stress, unregulated intracellular calcium homeostasis, and mitochondrial dysfunction. However, the causal relationship between diabetes mellitus (DM) and amyloid beta (Aβ) accumulation remains unclear.

Dysfunction of endolysosomal network (ELN) is a pathophysiological link that may explain the above problems, but little information is available on how high glucose affects and modulates neuronal ELN. Before describing my findings and suggestions for the pathogenesis of diabetes-related AD, I would like to outline the prevalence of AD, risk factors, pathophysiological mechanisms, current treatments, and associations with diabetes. Moreover, the definition of ELN, its role in AD pathogenesis, and potential triggers such as PICALM, mTOR, retromer, and lysophagy will also be briefly described.

1. Alzheimer’s disease

A. Prevalence and risk factors

With between 60% and 80% of all dementia cases in the elderly population, AD is the most common serious neurocognitive disorder (Boccardi *et al.,* 2019). Given this, society currently faces a significant health burden, and as the population ages, AD prevalence will increase. Clinical symptoms of AD typically involve progressive memory loss, behavioral abnormalities, and gradual impairment of cognitive abilities. The aberrant buildup of amyloid plaques in the brain brought on by the aggregation of Aβ peptides, neurofibrillary tangles (NFT), made of hyperphosphorylated tau protein, and substantial neuronal loss in the brain tissue are the pathological features of AD that are most generally observed (Meng *et al.,* 2020).

Risk factors for early-onset AD accounted for 1% of all AD cases are mutations in the three genes: *APP, PSEN1*, and *PSEN2*. On the other hand, risk factors for late-onset AD include single nucleotide polymorphisms of numerous genes such as *APOE, CLU, SORL1, PICALM, SORL1, CD33*, and *BIN1*, heavy alcohol consumption, smoking, hypertension, obesity, dyslipidemia, diabetes mellitus, and depression (Kivipelto *et al.,* 2018; Hampel *et al.,* 2021). Moreover, studies conducted *in vitro*, *in vivo*, and after death on human brain samples showed that oxidative stress, mitochondrial stress, a decline

in proteostasis, inflammation, and senescence are linked to cellular damages in the etiology of AD (Saez-Atienzar *et al.,* 2020), (Figure 1A).

B. Mechanism of Aβ and p-Tau production

There are two distinct pathways involved in the Aβ generation: (1) In the non-amyloidogenic pathway α-secretase cleaves APP, releasing extracellularly released soluble APPα and the membrane-tethered C83 fragment (Figure 1). (2) In the amyloidogenic pathway, β-secretase initially cleaves APP. The γ-secretase, which is made up of Presenilin 1 or 2, Nicastrin, PEN2 and APH-1, then cleaves the CTF-fragment (also known as C99) (Figure 1C), (Hampel *et al.,* 2021). Tau protein has numerous phosphorylation sites. Glycogen synthase kinase 3 beta (GSK-3β), cyclin dependent kinase 5 (CDK5), tau-tubulin kinases (TTBK), microtubule affinity regulated kinases (MARK), Fyn, and Abl kinases are the main groups of kinases which can phosphorylate tau protein. Phosphatases carry out dephosphorylation, or the elimination of a phosphate group. Approximately 70% of the total tau dephosphorylation activity is accounted for by the protein phosphatase 2A (PP2A) enzyme, with PP1, PP5, and PP2B also contributing (Xia *et al.,* 2021).

C. Current treatment

Despite the fact that AD was initially identified more than a century ago, the only short-term symptomatic effects of the medications used to

treat AD are those that are labeled for the disease's clinical dementia stage and target the neurochemical systems that underlie cognitive impairment and behavioral symptoms. A few anti-Aβ therapy pipelines have lately been developed to AD preclinical phases, but there are currently no effective disease-modifying medicines with fewer side effects for AD (Swanson *et al.,* 2021; Sevigny *et al.,* 2016). Given that Aβ peptides and hyperphosphorylated tau protein are already saturated in the brain before AD onset (Masters *et al.,* 2015; Hampel *et al.,* 2021), focusing on early stage of disease pathogenesis is a promising therapeutic strategy for AD.

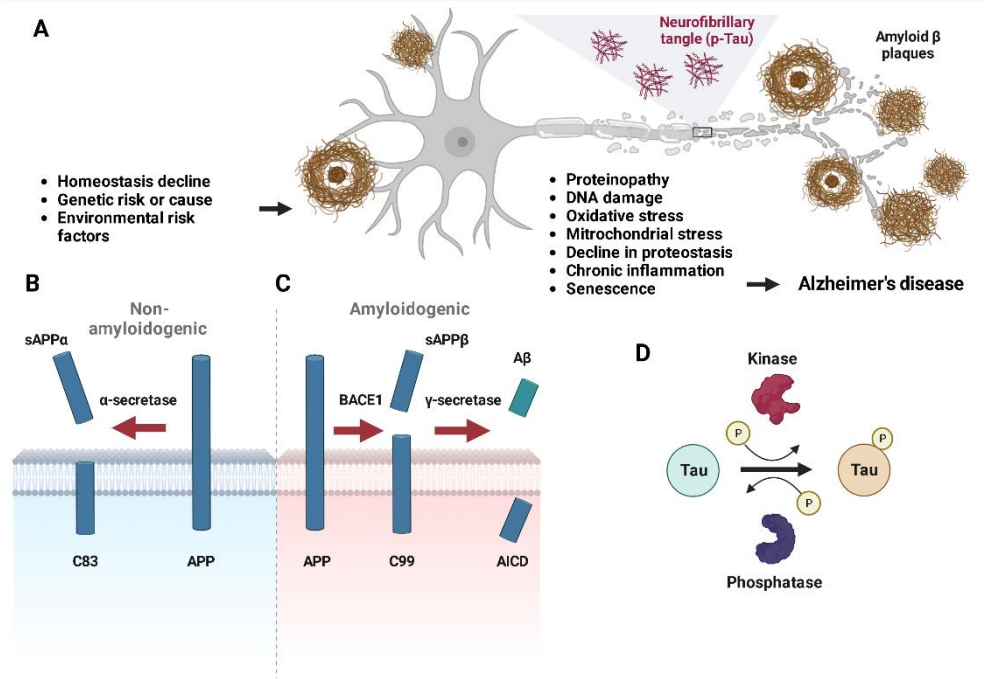

Figure 1. The pathophysiology of AD.

A Genetic mutation associated with the disease and environmental risk factors induce additional internal stressors associated with Alzheimer's disease such as DNA damage, oxidative stress, mitochondrial stress, inflammation, senescence, and proteinopathy. B For the nonamyloidogenic pathway, α-secretase cleaves APP to produce the extracellularly released soluble APP alpha (sAPP) and the membrane-tethered C83 fragment. C β-secretase cleaves APP first in the amyloidogenic process. After that, γ-secretase cleaves the C99 resulting in Aβ generation.

D. Diabetes as a risk factor for AD

i. Prevalence and characteristics of type 1 and type 2 diabetes

DM is a common metabolic disease that can result in long-term consequences include peripheral neuropathy, cardiovascular disease, nephropathy, and retinopathy. The damage of insulin-producing pancreatic β-cell that is immune-associated is generally regarded to be the cause of type 1 diabetes. 5-10% of diabetes cases are type 1 diabetes, which typically appears in young adults. Insulin resistance, which frequently results from obesity and also includes increasing β-cell dysfunction, is the underlying cause of type 2 diabetes. Type 2 diabetes is primarily a disease of older age. Although their pathogenesis, related comorbidities, and epidemiology are distinct, hyperglycemia is a feature of both type 1 and type 2 diabetes (Koekkoek *et al.,* 2015).

ii. Pros and cons of diabetes-mediated AD

According to a significant body of epidemiological and pathological research, diabetic and prediabetic states of hyperglycemia or insulin resistance are risk factors for AD (Ohara *et al.,* 2011; McIntosh *et al.,* 2019; Willette *et al.,* 2015; Wang *et al.*, 2021). Numerous researches using diabetic animal models have supported up the idea that DM increases the growth and accumulation of AD pathologies. Indeed, when diabetes is genetically or pharmacologically induced in mice without

pre-existing AD pathology, there is an increase in Aβ production and hyperphosphorylation of tau. Similarly, cerebrovascular abnormalities and increased cerebral Aβ were seen in diabetic Alzheimer disease animals (Biessels *et al.,* 2018). However, others have not discovered any connections between longitudinal glucose tolerance measurements and amyloid PET or post-mortem AD pathology findings (Arnold *et al.,* 2018; Abner *et al.,* 2016). Since the majority of the negative research were cross-sectional and carried out after the development of clinical AD symptoms, they mainly fall short of taking the AD disease's time course into account. Thus, additional longitudinal studies focusing on people who are asymptomatic are enable to examine the diabetes-mediated possibilities that can affect the course of AD.

iii. Therapeutic potential of antidiabetic drugs in AD

Furthermore, there has been a great deal of interest in the possibility of diabetic medications for the treatment of AD, with encouraging results (Meng *et al.,* 2020). A lot of studies show that hypoglycemic agents such as insulin and glinides, and anti-hyperglycemic agents such as metformin, thiazolidinediones, glucagon-like peptide-1 analogue, amylin analogue, and sodium glucose co-transporters 2 inhibitor ameliorate protein aggregation and neuroinflammation, and improve synapse plasticity and cognition in DM or AD mice models (Boccardi*et al.*, 2019). Although there is no anti-diabetic drug pipeline developed in the preclinical stage of AD, accumulated results indirectly indicate that DM is related with AD pathogenesis.

iv. The suggested mechanisms of diabetes-associated AD

Diabetes-related hyperglycemia and altered insulin signaling may be pathophysiologic causes of Alzheimer disease. Insulin and Aβ compete for the insulin-degrading enzyme during hyperinsulinemia, which causes Aβ buildup. Tau is hyperphosphorylated when insulin receptor signaling is reduced because this causes Akt to be inhibited and GSK-3β to be activated (Figure 2A). Increased intracellular glucose flux results in an overproduction of ROS in the mitochondria, which can then be amplified by activating NADPH oxidases and decoupling endothelial nitric oxide synthase (eNOS). A feed-forward cycle of continuous mitochondrial damage brought on by oxidative stress and an increase in intracellular calcium can result in neuronal death and, as a result, contribute to the pathophysiology of AD (Sims-Robinson *et al.,* 2010), (Figure 2B). Taken together, Hyperglycemia or insulin resistance may have an impact on the synthesis and clearance of substances associated to AD pathogenesis during the preclinical stage.

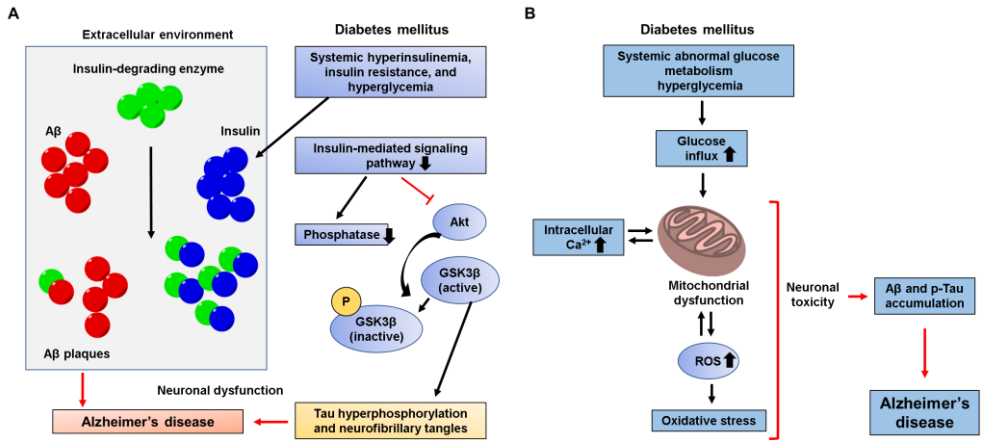

Figure 2. The potential mechanisms of DM-associated AD.

A Insulin and Aβ compete for the insulin-degrading enzyme during hyperinsulinemia, which causes Aβ buildup and plaque development. Tau is hyperphosphorylated when insulin receptor signaling is reduced because this causes Akt to be inhibited and GSK-3β to be activated. B Hyperglycemia is linked to mitochondrial dysfunction, oxidative stress, and dysregulated calcium homeostasis, which may all play a role in the development of AD. A feed-forward cycle of ongoing mitochondrial damage brought on by oxidative stress and an increase in intracellular calcium can result in neuronal death and, as a result, contribute to the pathophysiology of AD.

2. Endolysosomal network

A. Definition

The ELN is a system of vesicles that communicate dynamically and sort and transport absorbed extracellular substances to different locations within the cell. Endocytosis comprises the internalization of extracellular substance and plasma membrane, as well as the delivery of additional cargoes from the Golgi-apparatus to an early endosome with both cargo-sorting and signaling capabilities. Proteins and lipids are also recycled to the plasma membrane as part of the cargo sorting process. Additional trafficking signals direct other early endosome cargoes to retrograde transport or breakdown, or downstream sorting via retromer, lysosomes, and late endosomes (LEs). In neurons, LEs more frequently merge with autophagosomes to generate amphisomes before fusing with lysosomes to form autolysosomes (Nixon 2017).

B. ELN dysfunction as a contributing factor in the early stages of AD

Since larger endosomes are typical observations in neurons or organoids obtained from autosomal-dominant AD cases as well as induced pluripotent stem cell-derived neurons generated from late-onset sporadic AD patients, enlarged endosomes are recognized as an AD cytopathological characteristic (Raja *et al.,* 2016; Israel *et al.,*

2012). The endosomopathy of AD are primarily caused by the pathological overactivation of the rab5 small GTPase, increased endocytic gene expression, accelerated endocytosis, and failure in degradation of enlarged endosomes (Small *et al.,* 2017). In addition, endosomal abnormalities can conceivably begin as a fundamental event in AD, prior to the accumulation of intracellular APP fragments, according to the finding of the vesicular trafficking class of genes as being significantly associated to AD. The *SORL1, BIN1, PICALM*, and *CD2AP* genes that stand out as the most representative of this class affect endosomal abnormalities through regulation endocytosis or recycling to plasma membrane, or retrograde transport to the TGN. Furthermore, lysosomes progressively malfunction as they accumulate autophagic and endocytic substrates, which is reflected in their expansion. The majority of enlarged lysosomes are actually autolysosomes and amphisomes, which develop into lipofuscin granules as hydrolysis decreases further (Nixon 2017).

C. The pathophysiological mechanism of ELN dysfunction in Aβ accumulation

The pathophysiological mechanism of ELN dysfunction in the pathogenesis of AD is to produce or degrade Aβ (Figure 3). Indeed, BACE1, the rate-limiting enzyme of Aβ production, is distributed in acidic cellular organelles of the secretory pathway, notably the endosomes and Golgi apparatus, where its activity is most optimal at a pH of 4.5 (Cole *et al.,* 2007). Furthermore, there is a general agreement

that BACE1 is present in the endosomal membrane of neurons, where it is also most likely to cleave APP and induce Aβ production. The proof of lysosomal dysfunction in the AD brain and AD model systems comes from reduced specific activity of cathepsin B and a few other hydrolases, which impairs Aβ degradation (Mueller-Steiner *et al.,* 2006) and deficiencies of autophagy leading to Aβ production in the autophagic vesicles (Fleming *et al.,* 2022). In addition, accumulated C99 and Aβ also exacerbate endolysosomal abnormalities, and these positive feedback between Aβ and endolysosomal abnormalities accelerate AD progression (Hung *et al.,* 2021). Combined with aforementioned contents and the fact that the earliest neuropathology associated specifically with AD has thus far been recognized as endosome structural abnormalities, the functional recovery of ELN is a promising approach for the early diagnosis and prevention of AD.

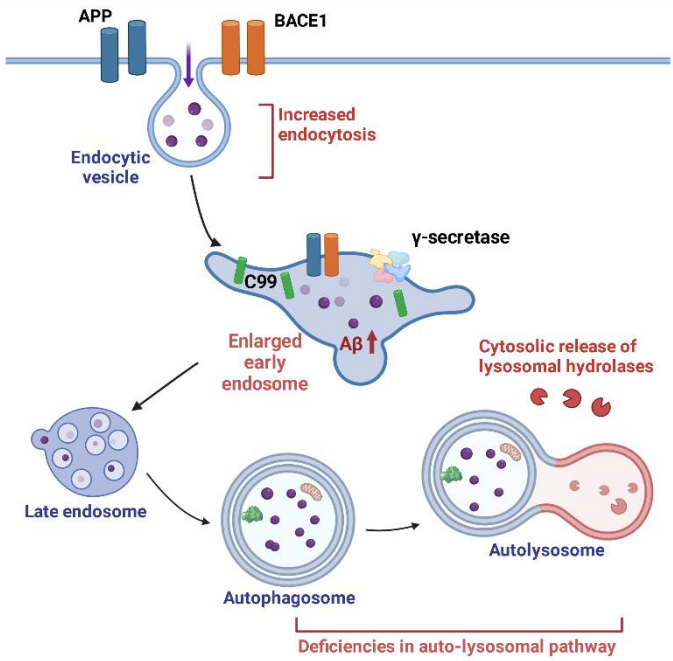

Figure 3. The potential mechanism of ELN dysfunction in A β accumulation.

Enlarged early endosomes are caused through increased endocytosis and deficiencies in auto-lysosomal pathway. A β is overproduced in early endosomes and autophagosome.

D. Potential factors of ELN dysfunction

i. PICALM

PICALM, a 112 kb gene that codes for a protein also known as clathrin assembly lymphoid myeloid leukemia protein, is found on chromosome 11q14. Numerous vertebrate species, organs, and cells have been found to express PICALM universally. Neurons, astrocytes, and oligodendrocytes in the central nervous system have all been found to have PICALM. PICALM play a significant function in clathrin-mediated endocytosis (CME) in addition to putative involvement in growth, hematopoiesis, and iron metabolism (Xu *et al.,* 2015). Clathrin and adaptor protein 2 (AP-2) assemble to attach to the C-terminal region of PICALM on the cytoplasmic side of the membrane after receiving the signal produced by attachment of the target ligand to a particular receptor on the cell membrane. On the other hand, the N-terminal region of PICALM links to the plasma membrane compound phosphatidylinositol-4,5-bisphosphate (PIP2), causing the creation of a clathrin coating made up of polyhedral clathrin network lattices and subsequently the deformation of the membrane (Figure 4).

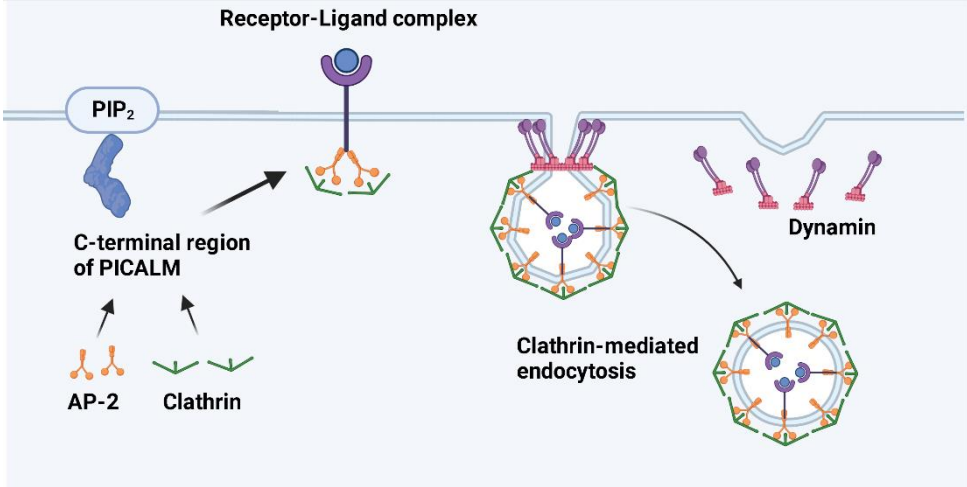

Figure 4. The role of PICALM in clathrin-mediated endocytosis.

When the target ligand binds to a specific cell membrane receptor, a signal is produced, and clathrin and adaptor protein 2 (AP-2) combine to attach to the C-terminal portion of PICALM on the cytoplasmic side of the membrane. The N-terminal region of PICALM, on the other hand, forms a connection with the plasma membrane molecule phosphatidylinositol-4,5-bisphosphate (PIP2), which results in the production of a clathrin coating made up of polyhedral clathrin network lattices and, as a result, the deformation of the membrane.

ii. mTOR

A member of the PI3K-related protein kinases (PIKK) family, mTOR is a 289-kDa serine/threonine protein kinase. It is the catalytic subunit of the mTOR complex 1 (mTORC1) and mTORC2 in mammals, which are two separate complexes. These complexes can be identified by their specific substrates and activities, auxiliary proteins, and varying rapamycin sensitivity (Figure 5). A downstream anabolic pathway that increases the synthesis of proteins, lipids, nucleotides, and other macromolecules is started when the mTORC1 is activated, whereas catabolic processes like autophagy and lysosome biogenesis are inhibited (Liu and Sabatini 2020), (Figure 5B). Furthermore, mTORC1 regulates the expression of genes that stimulate organelle formation or modulate metabolic flow through biochemical processes by controlling the expression or nuclear localization of transcription factors.

Because mTORC1 begins an anabolic program that consumes a lot of resources, it should only be activated when energy and macromolecular building blocks are all in ample supply. By attaching to the Rag GTPases in the presence of abundant nutrition, mTORC1 translocate to the lysosome. The small GTPase Rheb can then activate mTORC1 once it has been localized to the lysosomal surface and is in its GTP-bound state.

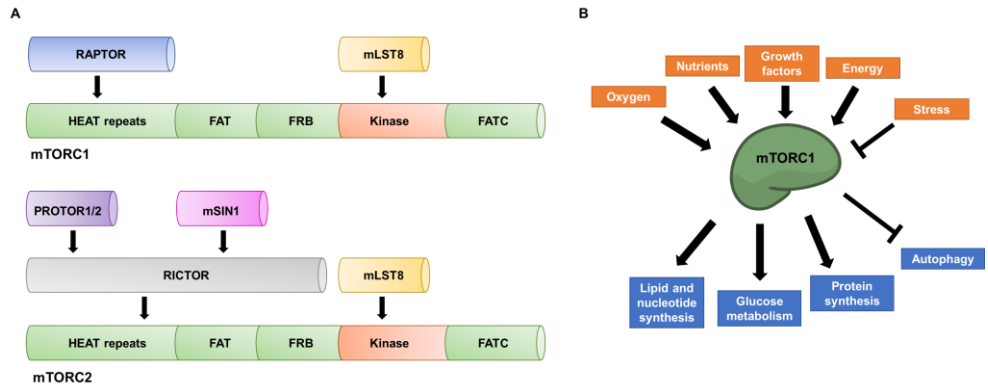

Figure 5. Structure and function of mTOR.

A In mTORC1, Clusters of huntingtin, elongation factor 3, a protein phosphatase 2A subunit, and TOR1 (HEAT) repeats are found at the N-terminus of mTOR. These are followed by the FRAP, ATM, and TRRAP (FAT) domains, the FKBP12-rapamycin binding (FRB) domain, the catalytic kinase domain, and the C-terminal FATC domain. With the support of SEC13 protein 8 (mLST8), a crucial part of the complex, mTOR binds to mammalian lethal. The defining subunit of mTORC1, regulatory-associated protein of mTOR (Raptor), binds mTOR with its own HEAT repeats and is necessary for the complex's lysosomal location. mTORC2 include the defining element of mTORC2, RICTOR, and mLST8. PROTOR1/2 and MAPK-interacting protein are both recruited to the complex by RICTOR, which functions as a scaffolding protein (mSIN1). B To adjust the balance of anabolism and catabolism in the cell, mTORC1 combines information regarding dietary abundance and environmental conditions.

iii. Retromer

The hetero-pentameric protein complex known as Retromer is so named because it transports protein cargo from the endosome to the TGN in a retrograde direction. Through the retromer, cargo is sorted in two different ways: (1) Retrieving cargo from endosomes and delivering it retrogradely to the trans-Golgi network are both done by the retromer (TGN). It is crucial for the proper hydrolase and protease delivery to the endosomal-lysosomal pathway. (2) The recycling pathway entails moving cargo from the endosome to the plasma membrane, which is crucial for neurons because, effective delivery of glutamatergic and other receptors to the plasma membrane is necessary for synaptic plasticity and remodeling (Vagnozzi *et al.*, 2019) (Figure 6A).

The retromer assembly consists of four components that are considered as essential. First of all, the "cargo recognition core", which is made up of the trimeric proteins VPS35/VPS26/VPS29, attaches to transmembrane endosomal proteins to be transported; VPS35 acts as the structural basis for VPS26 and VPS29. Second, the "tubulation" module, a collection of proteins that collaborate to create tubules that protrude from endosomes and direct the movement of cargo to its destination. The sorting nexin (SNX) family subgroup characterized by the presence of a BIN-amphiphysin-RVS (BAR) domain at the

carboxy terminus, includes the proteins in this module, which directly bind the cargo-recognition core. These subgroups are SNX1, SNX2, SNX5, and SNX6. Third, the "recruitment and stabilization" module, brings the cargo-recognition core to the membranes of endosomes and maintains the core once it is there. These modules include SNX3, the RAS-related protein RAB7A, and TBC1 domain family member 5 (TBC1D5), a protein that belongs to the family of RAB GTPase activating proteins (GAPs). Fourth, the "actin-remodeling" module, also known as WASH complex, works by rapidly polymerizing actin to form patches of actin filaments on endosomal membranes and then directing cargo away from the degradation pathway and toward retromer transport pathways. The WAS protein family homologue 1 (WASH1), strumpellin KIAA1033, FAM21, and coiled-coil domain-containing protein 53 (CCDC53) make up this module (Small *et al.,* 2015), (Figure 6B).

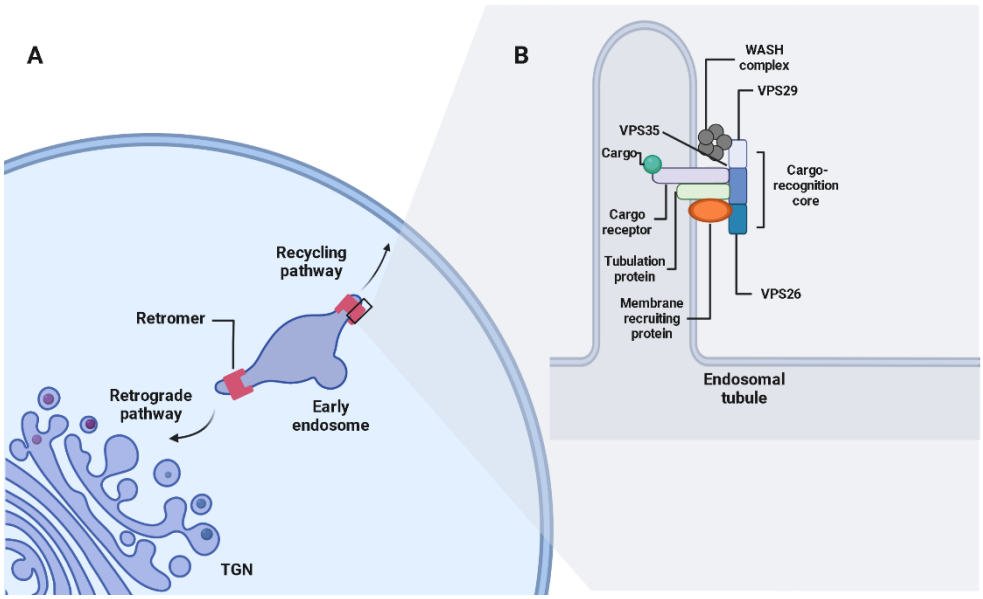

Figure 6. Retromer-mediated endosomal transport and its structure.

A Through tubules that protrude from endosomal membranes, retromer mediates two transport pathways out of endosomes. The first is the retrograde pathway, which transports cargo to the TGN after being retrieved from the endosome. The second is the recycling pathway, which transports cargo back to the cell surface from the endosome. B The retromer assembly proteins can be divided into four functional modules, all of which cooperate to fulfill the transport function of the retromer: 'Cargo-recognition core', 'tubulation', 'membrane-recruiting', and 'actin remodeling' modules.

iv. Lysophagy

When the lysosomal membrane is damaged, lysosomal function is lost, which induces ELN dysfunction and abnormal accumulation of wastes. Additionally, the release of lysosomal contents to cytosol leads to cell death. Lysophagy is the process by which autophagosomes engulf damaged lysosomes in an attempt to prevent the spread of damage. The ubiquitination of injured lysosomes triggers the autophagy machinery to be recruited in response to lysosomal injury (Yim *et al.,* 2020).

To date, there are four representative lyosphagy-related proteins: TRIM16, FBXO27, LRSAM1, and UBE2QL1 (Figure 7). Indeed, damage to the lysosomal membrane makes the normally buried β-galactosides exposed, drawing galectins. One of these, Galectin-3, recruits the E3 ligase TRIM16 to the lumen of lysosomes that have been damaged. The injured lysosomes are then ubiquitinated by TRIM16, and ULK1, Beclin1, and ATG16L are recruited as upstream autophagic factors. On the other hand, Galectin-8 can bind to the autophagy receptor NDP52 directly and draw in autophagic membranes, at least for endomembrane damage brought on by bacteria. The SKP1-CUL1-F-box protein 27 (SCF^{FBXO27}) ubiquitin ligase complex, which can directly connect to the revealed glycocalyx and interact with the damaged membrane via myristoylated FBXO27, has been identified as another E3 ligase involved in lysophagy. The E3 ligase LRSAM1 was

demonstrated to be involved in lysosome damage caused by bacteria (Papadopoulos *et al.,* 2017). Although which E3 ligase that functions downstream of UBE2QL1 has not been elucidated, the E2 ubiquitin conjugating enzyme UBE2QL1 controls K48-linked ubiquitination of lysosomal membrane proteins, the recruitment of p62, the interaction of the LC3-decorated phagophore, and the ATPase VCP/p97 for lysophagy. Proteins with the K48-linked ubiquitination may be extracted by VCP, which could prevent or slow down the efficient engulfment of lysosomes (Papadopoulos *et al.,* 2020).

Based on research background, the purpose of this study is to investigate at how ELN dysfunction brought on by high glucose affects the buildup of Aβ in neurons. The present research elucidated the effects of high glucose on 1) endosomal abnormalities in APP processing, 2) retromer dysfunction in APP processing and tau phosphorylation, and 3) lysophagy impairment in Aβ accumulation.

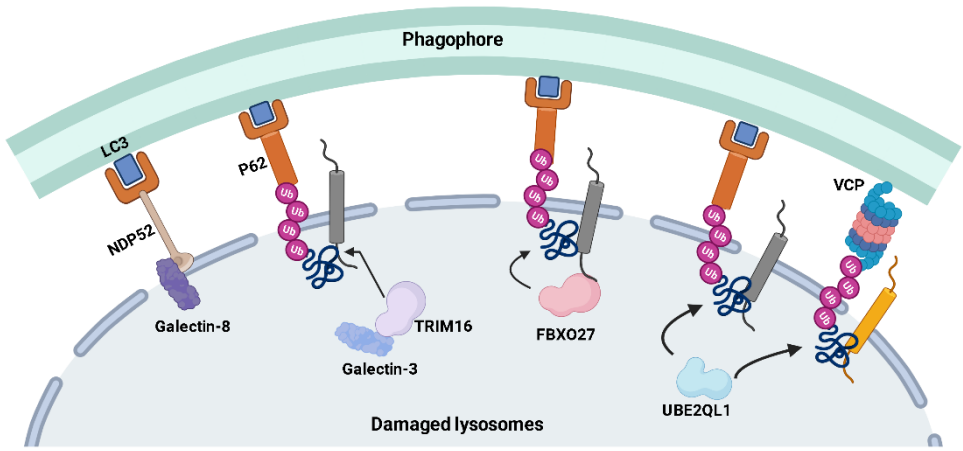

Figure 7. Molecular mechanism of lysophagy.

Galectin-8 attaches to exposed glycans and directly engages the autophagy receptor NDP52, binding it to LC3 on the phagophore. Galectin-3 brings TRIM16 to the lumen of injured lysosomes. TRIM16 then ubiquitinates the membrane proteins of damaged lysosomes. The FBXO27 can directly connect to the revealed glycocalyx and ubiquitinate membrane protein of damaged lysosome. UBE2QL1 participates in membrane ubiquitination and is recruited by an unidentified mechanism. Targeting proteins modified with lysine-48 (K48) ubiquitin chains, VCP/p97 is primarily recruited through UBE2QL1-mediated ubiquitination. It removes ubiquitinated proteins from the lysosomal membrane that are still unidentified.

CHAPTER I

The effect of endosomal abnormalities induced by high glucose-mediated PICALM and mTORC1 on the modulation of amyloid precursor protein processing

Manuscript is published in *Br J Pharmacol.* 2020;177(16): 3828-3847

INTRODUCTION

Epidemiological and neuropathological studies have suggested that DM can contribute substantially to the onset or progression of AD (Biessels *et al.*, 2018; Lacy *et al.,* 2018). Although there are many potential causal factors (Moreno-Gonzalez *et al.,* 2017), the precise molecular mechanisms by which DM contributes to the development of AD are still unknown. Regarding the dysregulation of endosomal trafficking, a focus has been placed on Aβ generation (Small *et al.,* 2017). In particular, the enlargement of early endosomes with Aβ immunoreactivity is the earliest pathological change in both diagnosed and undiagnosed AD patients (Cataldo *et al.,* 2004). Furthermore, AD models using human induced pluripotent stem cell-derived neurons commonly have endosomal abnormalities (Kwart *et al.,* 2019). Early diagnosis of disease is important because Aβ is already saturated before the onset of symptoms (Masters *et al.,* 2015). Therefore, investigating what causes endosomal disorders may present a high potential for disease prevention. A previous report showed that DM up-regulates Aβ production by aggravating endosomal dysfunction (Okabayashi *et al.,* 2015). Although the precise role and regulation of endosomes in Aβ generation have not yet been clarified, the above investigations suggest the possibility that the abnormalities of early endosomes could be a risk factor for DM-induced AD pathology at an early stage.

Abnormalities in the early endosome can be the result of numerous factors, including the up-regulation of endocytic genes, increased endocytosis, and the overactivation of Rab5, which is a small GTPase that is a marker of the early endosome (Nixon 2017). According to a genome-wide association study, endocytic genes are risk factors for AD via mechanisms related to the impairment of trafficking (Guimas Almeida *et al.,* 2018). The allelic variants of those factors aggravate the effects of DM on cognitive decline (McFall *et al.,* 2015). Among them, *PICALM* encoding PICALM, which plays an important role in CME (Xu, Tan, and Yu 2015), is associated with an increased risk of both AD and gestational diabetes (Vacinova *et al.,* 2017). Given that endocytic disturbance is an important pathological cause in diabetes (Teng *et al.,* 2016), PICALM has a high probability of inducing endosomal abnormalities in the diabetes. However, the mechanism of PICALM regulation by diabetes is poorly understood. Thus, investigating PICALM and related signaling pathways in DM may provide clues to alleviate endosomal dysfunction. On the one hand, as endosomes are degraded through the autophagy pathway or direct fusion with intact lysosomes (Colacurcio *et al.,* 2018), impairments of those pathways contribute to the dysregulation of early endosomes. Previous studies indicated that endocytic materials such as APP substrates and secretases are enriched at AD-induced dysfunctional autophagic vacuoles (Yu *et al.,* 2005), which up-regulates Aβ generation. Furthermore, such impairments functionally retard the

turnover rates of endosomal trafficking, resulting in defective endosomal clearance (Lee *et al.,* 2015). Although it is controversial whether DM-mediated oxidative stress or intracellular signaling induce the impairment of intracellular clearance systems (Gonzalez *et al.,* 2014) or their overactivation (Moruno *et al.,* 2012), an altered clearance system may influence early endosomal degradation.

In the present study, I used a STZ-induced mouse model (Furman, 2015) and a ZDF rat (Srinivasan *et al.,* 2007) for type 1 and type 2 DM, respectively, to determine whether early endosomal enlargement is a common risk factor for AD in different types of diabetes. To investigate the precise molecular mechanisms involved, I used a human neuroblastoma cell line, SK-N-MC, and applied high glucose treatment to create hyperglycemic condition which is the main pathophysiological feature of both DM. Using these experimental models, I hypothesized that DM is a metabolic risk factor for AD through inducing early endosomal abnormalities leading to the up-regulation of Aβ production. To address this hypothesis, I investigated the role of enlarged early endosomes in APP processing and assessed the associated regulatory mechanisms. I also measured the effects of regulating early endosomes as a potential strategy for treating diabetes-associated AD.

MATERIALS & METHODS

Animals

Handling and care of animal were conducted in compliance with the guidelines established by the international laws and policies (NIH Guide for the Care and Use of Laboratory Animals, NIH Publication No. 85-23, 1985, revised 2011). The experimental protocols were approved by the Institutional Animal Care and Use Committee of Seoul National University (Approvals No.: SNU-140219-1 and No. SNU-190122-1). Animal studies are reported in compliance with the ARRIVE guidelines (Kilkenny *et al.,* 2010) and with the recommendations made by the British Journal of Pharmacology. Male and female heterozygous types ($Lepr^{fa/+}$) of ZDF rats were obtained from Genetic Models Co. (Indianapolis, USA) and were mated with each other. Based on PCR genotyping, homozygous ZDF ($Lepr^{fa/fa}$, leptin receptor deficiency) and Zucker lean control (ZLC) ($Lepr^{+/+}$) rats were used for Type 2 DM and its control group, respectively. The rats were housed in a standard environmental state which sets adequate temperature (20-25℃) and humidity (under 60%) with a 12-h light/12-h dark cycle. They were allowed ad libitum access to proper diet (Purina 5008, Purina Korea, Korea; recommended by Genetic Models Co.) and tap water. Male ICR mice (9 weeks of age) were purchased from Han Lim Experimental Animal (Suwon, Korea) and housed in a conventional environmental condition (20-25℃, 60% humidity, and 12-h light/12-h dark cycle).

The mice were allowed free access to chow and drinking solution.

Experimental designs of animal study

Although sex is an important consideration for animal experiments (Curtis *et al.,* 2018), I determined that using male animals in these experiments was reasonable, as the aim of my study is to determine how DM modulates the processing of APP, which induces the up-regulation of Aβ and cognitive impairment. A total of 16 rats and 60 mice were used in these experiments. Experiments were designed to generate groups of equal size using randomization and blinded analysis. Group size estimation was conducted in compliance with guidelines established by the Institutional Animal Care and Use Committee of Seoul National University (expected effect size: 12% and 15%, SD: 6%, number of groups: 2 and 4, power $(1-\beta)$: 0.8, α: 0.05 for both rats and mice). The number of animals used was increased to account for potential decreases in animal numbers due to death during the experiments. Randomization was also applied to the drug treatments. In order to investigate the effects of type 2 DM on early endosomal disturbance, male rats were divided into two groups: ZLC and ZDF groups (n = 6 per each group). For chronic type 2 DM, I kept rats for 33 weeks of age. Blood glucose and body weight were determined with a portable glucose monitor (ACCU-CHEK® GO; Roche, Mannheim, Germany) and a scale, respectively at 6 and 33 weeks of age (Table

1). Rats were euthanized at 33 weeks of age. To investigate the effects of type 1 DM on endosomal dysregulation, STZ-induced DM mice were made in accordance with previous reports (Furman 2015). Briefly, mice were randomly chosen for intraperitoneal injection (IP) of STZ (180 mg/kg) in 200 μL of sodium citrate buffer (0.1 M, pH 4.5, Vehicle) and 200 μL of vehicle for Type 1 DM and its control group, respectively. Blood glucose levels were measured with a portable glucose monitor (ACCU-CHEK® GO; Roche, Mannheim, Germany) every two days starting 72 h after injection of STZ. The mouse with blood glucose levels exceeding 300 mg/dL was considered severe diabetes (Furman 2015). 7 days after injection of STZ, enough number of diabetic mice were obtained. Animal experiments consist of two parts. In experiment 1, mice were randomly divided into four groups (n = 6 per each group). Vehicle; STZ; STZ with Dynasore; and Dyansore. Dyansore (80 μM) (Hansen *et al.,* 2011) in 4 μL of DMSO (1:1,000 with PBS, Vehicle) and 4 μL of vehicle were applied with intracerebroventricular injection (ICV) (Kim *et al.,* 2016) to mice. Drugs were injected twice at 5 and 21 days after DM induction. In experiment 2, mice were randomly divided into four groups (n = 6 per each group). Vehicle; STZ; STZ with Rapamycin; and Rapamycin. Rapamycin (8.5 mg/kg) (Zhou *et al.,* 2009) in 200 μL of the solution (containing 99% corn oil and 1% DMSO, vehicle) and 200ul of vehicle were applied with IP injection to mice. Drugs were injected once a day for 5 consecutive days from 5 days after DM induction. Blood glucose levels and body weight were

measured at 9 and 18 weeks of age (Table 2). Mice were subjected to behavior test at 18 weeks of age and euthanized for further biochemical experiments.

Table 1. Body weight and blood glucose in ZLC and ZDF rats.

	ZLC	ZDF
Body weight (g), 6 weeks	119 ± 1.82	144.4 ± 5.22
Body weight (g), 33 weeks	394.2 ± 9.05	355.2 ± 6.77
Blood glucose (mg/dl), 6 weeks	102.8 ± 5.38	153.3 ± 15.85
Blood glucose (mg/dl), 33 weeks	124.5 ± 5.05	575.9 ± 25.53

(mean ± S.E.M).

Table 2. Body weight and blood glucose in experimental mice.

	Vehicle	Dynasore	STZ	STZ + Dynasore
Body weight (g), 9 weeks	38.5 ± 0.42	37.17 ± 0.7	37.5 ± 1.58	39 ± 0.63
Body weight (g), 18 weeks	42.33 ± 1.45	44.83 ± 0.87	34.83 ± 1.62	42.6 ± 1.2
Blood glucose (mg/dl), 9 weeks	116.3 ± 4.64	137.7 ± 7.08	120.3 ± 15.02	135.7 ± 7.24
Blood glucose (mg/dl), 18 weeks	126.7 ± 6.29	131.8 ± 4.64	497.7 ± 20.49	439.6 ± 35.15

	Vehicle	Rapamycin	STZ	STZ + Rapamycin
Body weight (g), 9 weeks	37.33 ± 0.33	36.33 ± 10.8	37 ± 1.09	37.67 ± 0.55
Body weight (g), 18 weeks	44.83 ± 1.24	43.5 ± 0.92	40.67 ± 1.47	46.67 ± 1.145
Blood glucose (mg/dl), 9 weeks	126.7 ± 7.37	116.5 ± 7.85	118.2 ± 9.26	118.5 ± 5.38
Blood glucose (mg/dl), 18 weeks	127.3 ± 8.78	120.8 ± 6.39	484.7 ± 5.94	503.7 ± 10.56

(mean ± S.E.M).

Cell cultivation

The SK-N-MCs were cultured with low glucose Dulbecco's essential medium (DMEM; Hyclone, #SH30021FS), 10% FBS and 1% antibiotic-antimycotic solution at 37° C with 5% CO_2. After cells grown to 70% confluency, the medium was replaced with DMEM with 2% Knockout™ serum replacement (SR; Gibco, #10828028) and 1% antibiotic-antimycotic mixture for 12 h prior to experiments. In order to create hyperglycemic condition, the cells were treated with 25 mM D-glucose (Haythorne *et al.,* 2019).

Y-maze spontaneous alternation test

Y-maze behavior test is used for assessing the cognitive dysfunction which is dependent on the hippocampus. Rodents instinctively prefer to challenge a new arm of the Y-maze. Before the test, the animals were placed at the testing room for 2 h to minimize the effects of stress on behavior. The mice were placed in the randomly selected arm of Y-shaped maze acquired from Sam-Jung Company (Seoul, Korea). Each mouse was allowed to explore freely through the open field for 8 min. The total number of arm entries and sequence were recorded. Only an entry when all four limbs were placed in the arm was considered to be completed. Percentage alteration is the number of triads which was divided by the maximum alterations (total entries-2) × 100. When the animals show lower alteration percentage, the animals show impaired memory function.

Immunohistochemistry (IHC)

Mice and rats were fully anesthetized and were perfused transcardially with PBS followed by 4% PFA in 0.1 M phosphate buffer (pH 7.4). The brains were removed and underwent post-fixation with 4% PFA. Then, brains were placed in 30% sucrose in PBS for 1-2 d. Coronal sections (40 μm-thick) were obtained by cutting serially using a cryostat (Leica Biosystems, Nussloch, Germany). Free-floating hippocampus sections were processed carefully. Sections were blocked with 5%

normal goat serum (NGS; Sigma-Aldrich, #566380) at room temperature for 1 h. Samples were incubated with primary antibody (1:1,000 dilution) for overnight at room temperature. Sections were washed three times with PBS and incubated with secondary antibody (1:200 dilution) for 2 h. Immunostained slides were visualized by Eclipse Ts2™ fluorescence microscopy (Nikon, Tokyo, Japan). All IHC images were analyzed with the Fiji software. Signal intensities were measured after applying the same threshold and normalized by each area.

siRNA transfections for gene silencing

When the SK-N-MCs grown to 60%, cells were incubated with low glucose DMEM containing 25 nM of the indicated siRNAs, transfection reagent TurboFect™ (Thermo Fisher, #R0531), and 2% SR for 12 h. The medium was replaced to the medium with 1% antibiotics prior to experiments. NT siRNA was used as the negative control. The efficacies of siRNAs were confirmed.

Western blot analysis

Harvested cells or tissues were incubated with the proper lysis buffer and protease and phosphatase inhibitors cocktail (100X) (Thermo Fisher, #78440). Then, samples were homogenized by using sonicator

and vortexer for 30 min on ice. The lysates were cleared by centrifugation (13,000 × g, 4° C, 20 min). Protein concentration was determined by using the bichichoninic acid (BCA) quantification assay (Thermo Fisher, #23227). Equal amount of samples (5-10 μg) were loaded into 8-12% SDS-polyacrylamide gel (SDS-PAGE) and transferred to a polyvinylindene fluoride (PVDF) membrane. Tris-buffered saline containing 0.2% Tween-20 [TBST; 150 mM NaCl, 10 mM Tris-HCl (pH 7.6)] was used for washing and incubating membrane. The membrane was blocked with 5% skim milk (Gibco, #232100) for 1 h. Blocked membrane was washed 3 times and incubated with a primary antibody (1:1,000 dilution) for overnight at 4° C. Then, the membrane was washed and incubated with horseradish peroxidase (HRP)-conjugated secondary antibody (1:10,000 dilution) at room temperature for 2 h. Blotting bands were detected by using chemiluminescence detection kit (Advansta Inc., #K-12045-D50). Protein bands quantification were carried out by using the Image J software (developed by Wayne Rasband, National Institutes of Health, Bethesda, MD, USA). Protein expression levels were normalized by β-actin expression levels. The EzSubcell™ subcellular fractionation kit (Atto, #WSE-7421) was applied to the preparation of the cytosolic and nuclear fractionized samples. Cytosolic and nuclear samples were acquired according to the manufacturer's instructions. Protein expression levels of cytosolic and nuclear samples were normalized by β-tubulin and lamin A/C expression levels, respectively.

Sucrose density gradient fractionation

The SK-N-MCs were washed with cold phosphate-buffered saline (PBS; Hyclone, #SH30256) and scraped into 1 mL of lysis buffer (10 mM EDTA, 500 mM Na_2CO_3, pH 11 in distilled water) with the proteinase and phosphatase inhibitor cocktail (100X). Lysates were homogenized by using sonicator (Branson Sonicator 250, Branson Ultrasonic Corp., Danbur, CT, USA) and incubated with vortexing for 30 min on ice. To form 5-45% discontinuous gradient, 4 mL of 45% sucrose and 4 mL of 5% sucrose dissolved in MES-buffered solution [MBS: 25 mM MES (pH6.5), 0.15 M NaCl] were sequentially placed in an ultracentrifuge tube (Beckman Coulter, Fullerton, CA, USA). Then, equal amount of protein was adjusted to form 4 mL of 5% sucrose and added to the ultracentrifuge tube. Sample tubes were centrifugated at 200,000 × g for 24 h in an SW41 rotor (Beckman Coulter). Fractionized samples were acquired and analyzed by western blotting.

Immunofluorescence analysis

The SK-N-MCs were washed twice with PBS and fixed with 4% paraformaldehyde (PFA; Lugen Sci, Seoul, Korea, #LGB-1175) for 10 min. So as to permeabilize the cell membrane, cells were incubated in 0.2% TBST or 0.1% Triton X-100 (Sigma, T8787) for 10 min. Cells were blocked with 5% NGS for 40 min and incubated with primary antibodies (1:100 dilution) for overnight in 4° C. Then, cells were

washed three times with PBS and incubated with Alexa Fluor™ 488 or 555-conjugated secondary antibodies (1:200 dilution) at room temperature for 2 h. Immunostained samples were visualized by a super-resolution radial fluctuations (SRRF) imaging system (Andor Technology, Belfast, UK) (Gustafsson *et al.,* 2016). Fiji software was used to quantified the fluorescent intensities. The area of $Rab5^+$ endosomes and acidic lysosomes were measured after applying the same threshold. The manders coefficients were used to analyze co-localization. The Pitstop 2 could detect transient cargo-adaptor interactions by binding to the terminal domain of clathrin heavy chain and perturbing clathrin-coated pit dynamics without affecting pit assembly nor the sequestration of the cargos (von Kleist *et al.,* 2011).

Measurements of intracellular pH and ROS.

The cell permeable pH-sensitive fluorescent probe BCECF-AM [2',7'-Bis-(2-carboxyethyl)-5-(and-6)-carboxyfluorescein, acetoxymethyl ester; Thermo Fisher, #B1150] and CM-H2DCFDA (Thermo Fisher, #C6821) were used for measuring the intracellular pH and ROS, respectively. After drug treatment, the cells were incubated with 2 μM BCECF-AM or 10 μM DCFDA in medium and kept at 37° C for 30 min. Then, cells were washed three times with PBS. The signals of BCECF-AM- and DCFDA-stained cells were measured via flow cytometry (Beckman Coulter, Atlanta, USA).

Staining intact lysosomes

Lysotracker deep red (Thermo Fisher, #L12492) was used for staining the intact lysosomes. After drug treatment, the cells were incubated with 2 μM Lysotracker red in medium and kept at 37° C for 30 min. Then, cells were washed three times with PBS. The signals of Lysotracker-stained cells were measured via flow cytometry (Beckman Coulter, Atlanta, USA) or cells were further experimented with ICC.

Quantitative real-time polymerase chain reaction (qPCR)

RNA samples were extracted by using RNA extraction kit (TaKaRa, #9767), according to the manufacturer's instructions. Then, the cDNA was made by using reverse transcription-PCR premix (iNtRON Biotechnology, #25081). Reverse transcription was performed for 1 h at 45° C followed by 5 min at 95° C. The cDNA samples were amplified with the mRNA primers listed in Table 3 and a TB™ Green Premix Ex Taq™ (TaKaRa, #RR420A) by using Rotor-Gene 6000 real-time thermal cycling system (Corbett Research, NSW, Australia). The qPCR was performed as follows: 15 min at 95° C for DNA polymerase activation and 60 cycles of 20 sec at 94° C, 20 sec at 55° C, and 30 sec at 72° C. The specificity and identity of the amplified product were validated by the analysis of melting curve. The quantification of mRNA expression levels of the target genes was

performed with double delta Ct analysis and the data were normalized with those of *ACTB* gene.

Table 3. Human gene primers for real-time qPCR.

Gene	Forward primer	Reverse primer
PICALM	TTCCTGTTGCCAAACTCCCA	TGGTTCCATTTCCGATGCCA
AP2A1	TCCTGCTTGGCCATGACATT	AGTTCGAGTTCACCAGCACA
RAB5A	CATTGGGGCTGCTTTTCTAA	GGACTTGCTTGCCTCTGAAG
EEA1	TGCATCTGAAACCTCACT GC	RCTAGTTGGCGCTCTGTCTCC
RABGEF1	AAGCCTCCGAAT CAACCGTT	TGCAGTGGTGGAGGAAGTTT
RABEP1	TCCAGATGCCAAGTGGGTTT	TGTTCTGGTGTCATCGCCTT
APPL1	AGCGTTTTCCATTGGGAGGT	AGCACTGCATGACAAGAGCT
ATG14	ACAACGGAGACACCAGCATT	ACCAGCTGAGTTGCATAGCA
SNAP29	ACCCAAAGAACCCACACCTT	TGTCAGCCGGTCAAGAATGT
VTI1B	TTTCGAGAAGCTGCACGAGA	TGCCAGCGTTTCATTTGCTT
STX17	AAATGCTGCAGAATCGTGGG	AAGTCAGTGACCAGTTGGCT
VAMP7	TGAACGTTCCCGAGCCTTTA	ATGGAAGTGCTGTCTGTGCT
ACTB	AACCGCGAGAAGATGACCCAGA TCATGTTT	AGCAGCCGTGGCCATCTCTTGCTCGAAGT C

Measurement of Aβ in *in vitro* and *in vivo* samples

In *in vitro*, the culture medium of SK-N-MCs was collected and stored -70° C with phosphatase inhibitors cocktail (100X). In *in vivo*, the equal amount of the hippocampus samples (200 μg) obtained from sacrificed animals were prepared with proper lysis buffer and BCA assay. According to the manufacturer's instructions, the optical density (OD) of Aβ (1- 42) in culture medium and animal samples were acquired by using human Aβ (1- 42) ELISA kit (Thermo Fisher, #KHB3544) and mouse & rat Aβ (1- 42) ELISA kit (Thermo Fisher, #KMB3441), respectively. The OD values were converted into the concentration by using the standard curve.

GTP-Rab5 activation assay

Measurement of Rab5 activation was performed by using Rab5 activation assay kit (Neweast Bioscience, #83701). All procedures were done in accordance with manufacturer's instructions. Briefly, cells were incubated with the provided lysis buffer containing anti-active Rab5 monoclonal antibody. Then, by using A/G agarose, pulled down the bound active Rab5 from lysates. The precipitated active Rab5 was detected by western blot using Rab5-specific polyclonal antibody. The ratio of expression levels of active Rab5 and total Rab5 were analyzed.

APP internalization assay

The SK-N-MCs were washed with cold PBS, and incubated with Aβ antibody (Xiao *et al.,* 2012) (1:100 dilution) at 4° C for 1 h to label surface APP. Cells were washed with cold PBS twice and incubated at 37° C for 0 and 15 min to permit internalization. Internalization was stopped by rapid cooling on ice. Cells were fixed with 4% PFA for 10 min at room temperature, permeabilized with 0.1% Triton X-100 for 10 min, and blocked with 5% NGS for 40 min. Cells were incubated with primary antibodies (1:100 dilution) for overnight in 4° C. Then, cells were washed three times with PBS and incubated with Alexa Fluor™ 488 or 555-conjugated secondary antibodies (1:200 dilution) at room temperature for 2 h. Immunostained samples were visualized by a super-resolution radial fluctuations (SRRF) imaging system (Andor Technology, Belfast, UK).

Cell surface biontinylation assay & internalization assay

In order to prevent proteins from shedding at the cell surface, GM6001(an MMP inhibitor; 20 μM) was pretreated for 30 min prior to drug treatments (Kanatsu *et al.,* 2014). Surface protein isolation was conducted by using Cell surface protein isolation kit (Biovision, #K295-10). All procedures were done in accordance with manufacturer's instructions. Briefly, cells were washed with cold PBS and labeled with Sulfo-NHS-SS-Biotin, a non-membrane-permeable,

thiol-cleavable, biotinylation reagent. For the internalization assay, biotinylated cells were incubated at 37° C for 0 and 15 min to permit internalization. Internalization was stopped by rapid cooling on ice. To remove remained biotin at the cell surface, cells were incubated with MesNA (50 mM 2-mercaptoethanesulfonic acid in 50 mM Tris-HCl, 100 mM NaCl, 2.5 mM $CaCl_2$, and pH 8.7) three times for 20 min at 4° C. After quenching the biotin reagent with 0.1 M glycine, cells were lysed and labeled surface proteins were isolated by using streptavidin beads. Then, cells were incubated with Dithiothreitol (DTT) solution to release attached beads. Biotin-labeled proteins were subjected to western blot.

Data and Statistical analysis

The data and statistical analysis comply with the recommendations on experimental design and analysis in pharmacology (Curtis *et al.,* 2018). The group size represents the number of independent values, and statistical analyses were performed using these independent values. Statistical analysis was performed only for studies where each group size was at least $n = 5$. The exploratory data with large effects and accuracy have a small sample size but may have significant implications. Outliers were assessed in compliance with the exclusion criteria beyond an outer fence (Q1-3 * IQ or Q3 + 3 * IQ) in a box plot construction, and we did not observe any outliers. All the data achieved

normality (using the Shapiro–Wilk test) and were analysed by parametric statistics. Imaging experiments and animal tests were conducted and assessed in a blinded fashion. The unpaired Student's t–test was used to compare the means of the treatment groups with that of the control group. One–way ANOVA (with Dunnett's multiple comparison test) or Two–way ANOVA (with Tukey's multiple comparison test) was used for analysing the differences among multiple groups. The homogeneity of sample variance was confirmed (with Levene's test), and logarithmic transformation was performed if the variance was not satisfied. The units of a variable were determined by percentage–matched control values following data transformation. Quantitative data are expressed as the mean ± SEM and analysed with the Prism 6 software (Graphpad, CA, USA, RRID:SCR_000306) and SigmaPlot 12.0 (Systat software Inc., CA, USA, RRID:SCR_003210). The level of probability (P) constitutes the threshold for statistical significance for determining whether groups differ and is not varied later in results. A p value <0.05 was considered statistically significant.

Materials

Cells from the human neuroblastoma cell line SK–N–MC were obtained by Korean Cell Line Bank (Seoul, South Korea). FBS and antibiotics were purchased from Hyclone (Logan, UT, USA) and Gibco (Grand

Island, NY, USA) respectively. The antibodies of β-actin (sc-47778), CAV1 (sc-53564), FLOT1 (sc-74566), CHC (sc-12734), PICALM (sc-271224), lamin A/C (sc-2068), LAMP1 (sc-20011), p-AMPKα (Thr 172) (sc-33524), BACE1 (sc-33711), and CSTB (sc-365558) were acquired from Santa Cruz Biotechnology (Santa Cruz, CA, USA). The antibodies of β-tubulin (CSB-PA03874A0Rb) and AP2A1 (610502) were purchased from Cusabio (Wuhan, Hubei, China) and BD biosciences (San Jose, CA, USA), respectively. The antibodies of Rab5 (NB120-13253), P62 (NBP1-48320), and LC3 (NB100-2220) were obtained from Novus Biologicals (Centennial, CO, USA). The antibodies of p-mTOR (Ser 2448) (2971S), mTOR (2983 S), AMPK (2532 S) were acquired from Cell Signaling Technology (Beverly, MA, USA). The antibodies of APP (ab32136), Sp1 (ab227383), Aβ (ab2539) were purchased from Abcam (Cambridge, England). The antibody of C99 (802801) was obtained from Biolegend (San Diego, CA, USA). MβCD, dynasore hydrate, rapamycin, NAC, DAPI, D-glucose, L-glucose, leupeptin, and STZ were purchased from Sigma Chemical Company (St. Louis, MO, USA). GM6001 and mithramycin A were acquired from Cayman Chemical (Ann Arbor, MI, USA) and Tocris Bioscience (Bristol, UK), respectively. mRNA primers for *PICALM, AP2A1, RAB5, EEA1, RABGEF1, RABEP1, APPL1, ATG14, SNAP29, VTI1B, STX17, VAMP7,* and *ACTB* were purchased from Cosmo Genetech (Seoul, Korea). Primer for *CHC* and siRNAs for *RAB5* and

PICALM were acquired from Bioneer (Daejeon, Korea). NT siRNA was purchased from Dharmacon (Lafayette, CO, USA).

RESULTS

High glucose up-regulates Aβ production through early endosomal abnormalities

To elucidate the effects of DM on APP-processing early endosomes, first, I measured hippocampal C99 and Rab5 located in early endosomes and used as an early endosomal marker by western blotting. Compared with the levels in ZLC rats, both proteins increased in ZDF rats (Figure 8A). In addition, ZDF rats had higher Aβ levels than ZLC rats (Figure 8B). Early endosomes had higher staining intensities (Law *et al.,* 2017) at the hippocampus of ZDF rats than those of ZLC rats (Figure 8C). Moreover, STZ-induced type 1 DM mice had increased C99 and Rab5 (Figure 9A) compared with vehicle-treated mice. Furthermore, hippocampal early endosomes of the STZ model had similar alterations to those of ZDF rats (Figure 9B). In *in vitro* experiments involving treatment of cells with either D- or L-glucose, only D-glucose increased C99 and Rab5 (Figure 10A). Similarly, the levels of Aβ in cell culture medium increased only for D-glucose-treated samples (Figure 10B), which means that the osmotic effect was not involved in amyloidogenesis. In addition to the increment of Rab5 protein expression, high glucose also increased early endosomal activation,

which was measured by determining the level of the GTP-Rab5 form (Figure 10C). To investigate that high glucose increased APP-processing in early endosomes, along with my previous report demonstrating upregulation of the protein expression levels and activity of not γ-secretase (presenilin 1) but BACE1 under high glucose(Lee *et al.,* 2016), I proved that high glucose induced early endosomal enlargement (Kwart *et al.,* 2019) and increased co-localization with APP (C-terminus) and BACE1, reflecting an increment of APP-processing in enlarged early endosomes (Figure 11A, B) Furthermore, high glucose-induced increment of C99 in cell lysate and Aβ in culture medium were reversed by *RAB5* knockdown (Figure 11C, D). These findings suggest that early endosomal abnormalities are critical feature for the increment of Aβ in DM conditions.

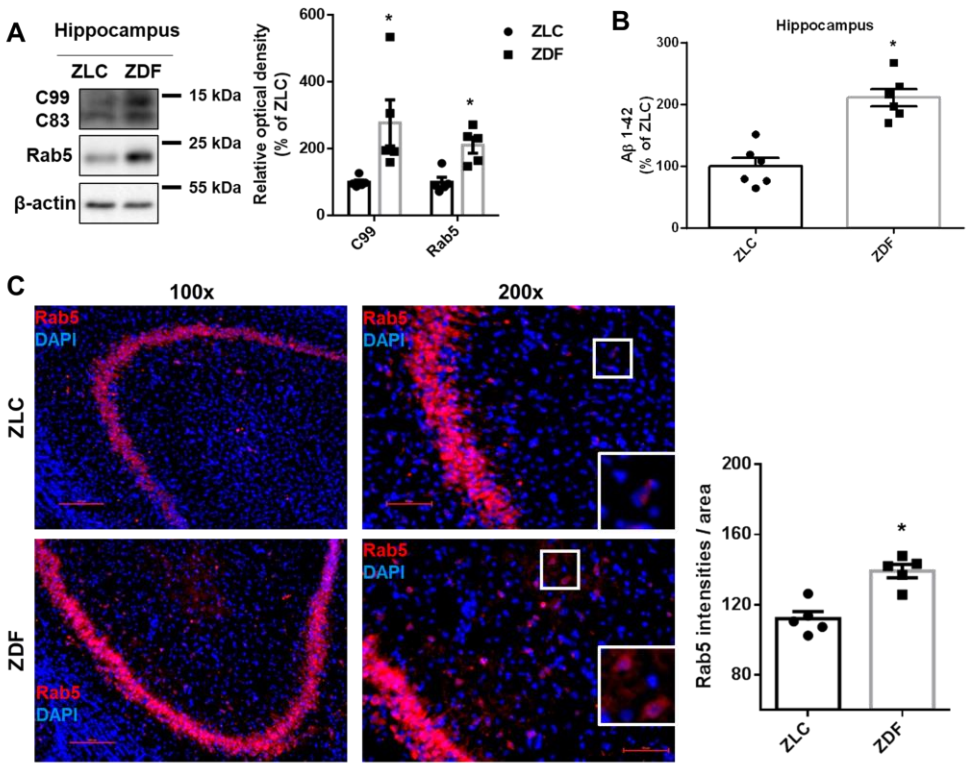

Figure 8. Early endosomal enlargement and amyloidogenesis are induced in the hippocampus of type 2 diabetic rodents.

A–C Samples were obtained from ZLC and ZDF rat hippocampus. **A** C99, Rab5, and β-actin were detected by western blot. $n = 5$. **B** Aβ 1–42 were measured. $n = 6$. **C** Tissue slides for IHC were immunostained with Rab5-specific antibody and counterstained with DAPI. Scale bars, 50 μm. $n = 5$. $^{*}p < 0.05$ vs. ZLC rats.

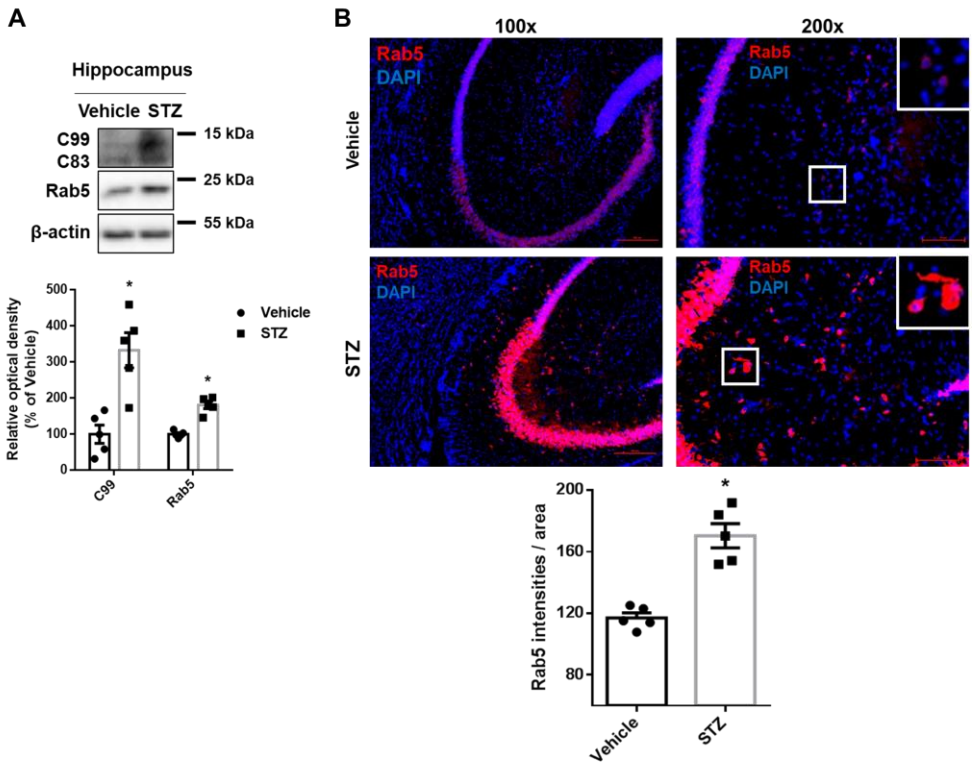

Figure 9. Early endosomal enlargement and amyloidogenesis are induced in the hippocampus of type 1 diabetic rodents.

A, B Samples were obtained from vehicle- and streptozotocin (STZ)-treated mice hippocampus. **A** C99, Rab5, and β-actin were detected by western blot. $n = 5$. **B** Tissue slides for IHC were immunostained with Rab5-specific antibody and counterstained with DAPI. Scale bars, 200 μm. $n = 5$. $^{*}p < 0.05$ vs. vehicle-treated mice.

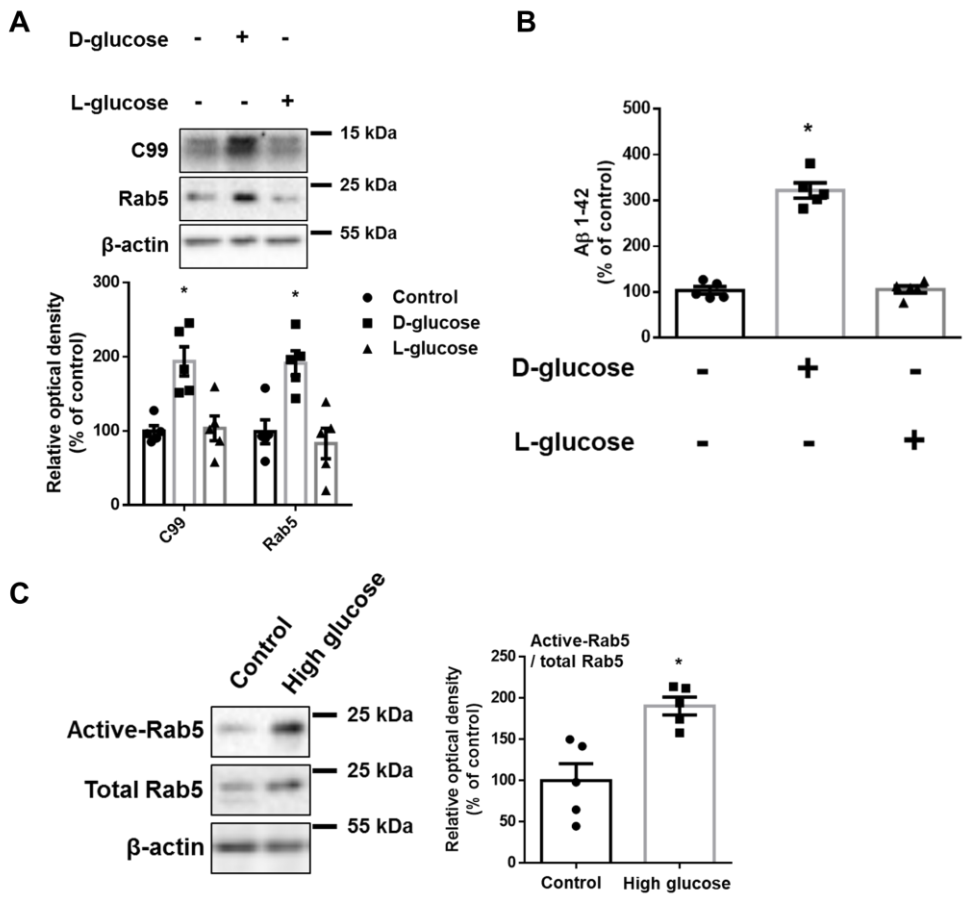

Figure 10. High glucose up-regulates Aβ and activates Rab5.

A, B The SK-N-MC cells were treated with D-glucose (25 mM) or L-glucose (25 mM) for 24 or 48 h respectively. Then, C99, Rab5, and β-actin were detected by western blot. n = 5. B Aβ 1-42 from cell culture medium were measured. n = 5. C The cells were treated with high glucose (25 mM) for 24 h. Active Rab5 (GTP-bound Rab5) was immunoprecipitated with Rab5-specific antibody (upper panels). Expression of Rab5 and β-actin in total lysate is shown in the middle and lower panels. n = 5. $^{*}p < 0.05$ vs. control.

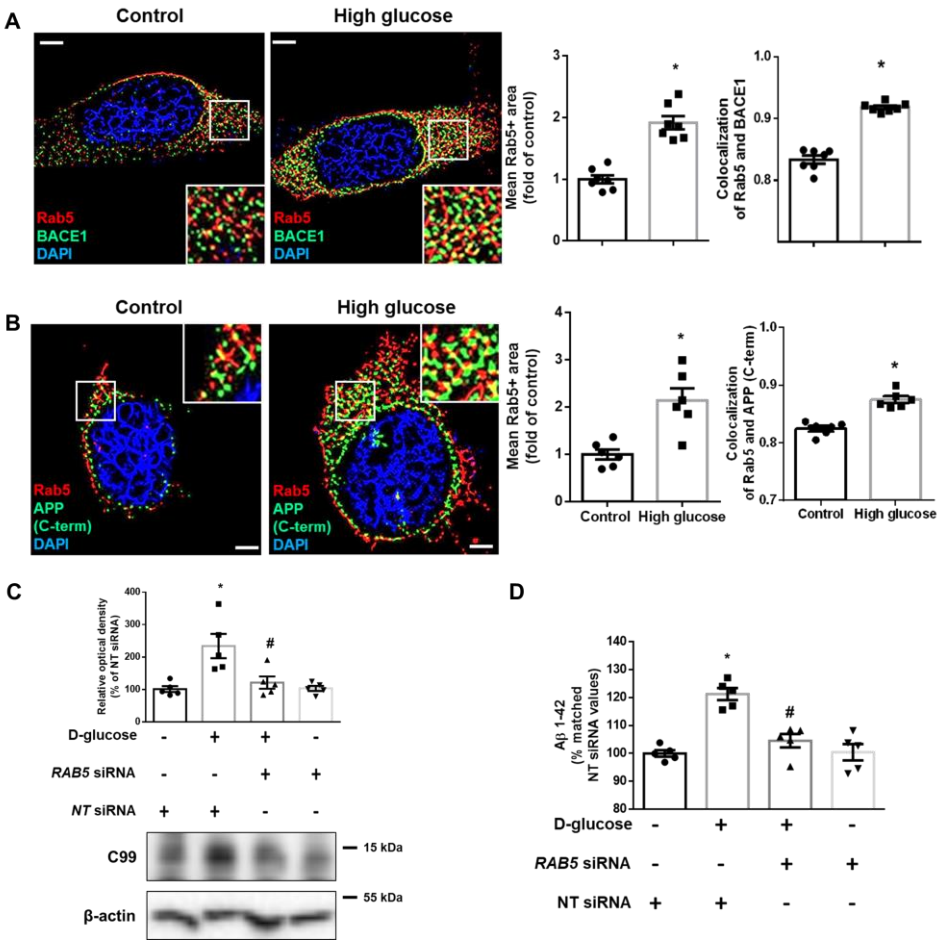

Figure 11. High glucose up-regulates Aβ through early endosomal enlargement.

A The cells were treated with high glucose (25 mM) for 24 h which were immunostained with Rab5 and BACE1-specific antibodies and counterstained with DAPI. Scale bars, 8 μm. $n = 7$. **B** Immunostaining of cells treated with high glucose (25 mM) for 24 h were visualized. Rab5 and C99-specific antibodies were used and counterstained with DAPI. Scale bars, 8 μm. $n = 6$. $^{*}p < 0.05$ vs. control. **C, D** The cells were transfected with NT siRNA or *RAB5* siRNA for 12 h prior to high glucose (25 mM) treatment for 24 h and 48 h, respectively. **C** C99 and β-actin were detected by western blot. $n = 5$. **D** Aβ 1-42 from cell culture medium were measured. $n = 5$. Logarithmic transformations were performed for homogeneity of the sample variance. $^{*}p < 0.05$ vs. NT siRNA transfection, $^{\#}p < 0.05$ vs. high glucose with NT siRNA transfection.

High glucose induces early endosomal enlargement by increasing APP endocytosis at lipid rafts

To explore how high glucose induces early endosomal overactivation along with the increment of Rab5 protein expression (Figure 10C), I measured mRNA expression levels of Rab5 and its effector proteins. However, I did not identify any significant changes (Figure 12A). Next, I hypothesized that high glucose increased APP endocytosis resulting in early endosomal enlargement. I confirmed that high glucose increased protein expression levels of APP (Figure 12B) and its endocytosis (Figure 12C). Given that high glucose facilitated lipid raft reorganization (Lee *et al.,* 2016), I found that high glucose markedly moved APP to the lipid raft part as indicated by CAV1 and FLOT1 (Figure 12D). The expression levels of surface APP in cells treated with high glucose and MβCD (lipid raft disruptor) were higher than those of cells treated with high glucose (Figure 13A). In addition, high glucose increased internalization of APP, which was reversed by MβCD (Figure 13B). Furthermore, pretreatment with MβCD decreased high glucose-induced early endosomal enlargement and increment of Aβ, which means that APP endocytosis at lipid rafts contributed to early endosomal enlargement (Figure 13C, D). These results suggest that early endosomal enlargement under high glucose conditions is mediated by APP endocytosis at lipid rafts.

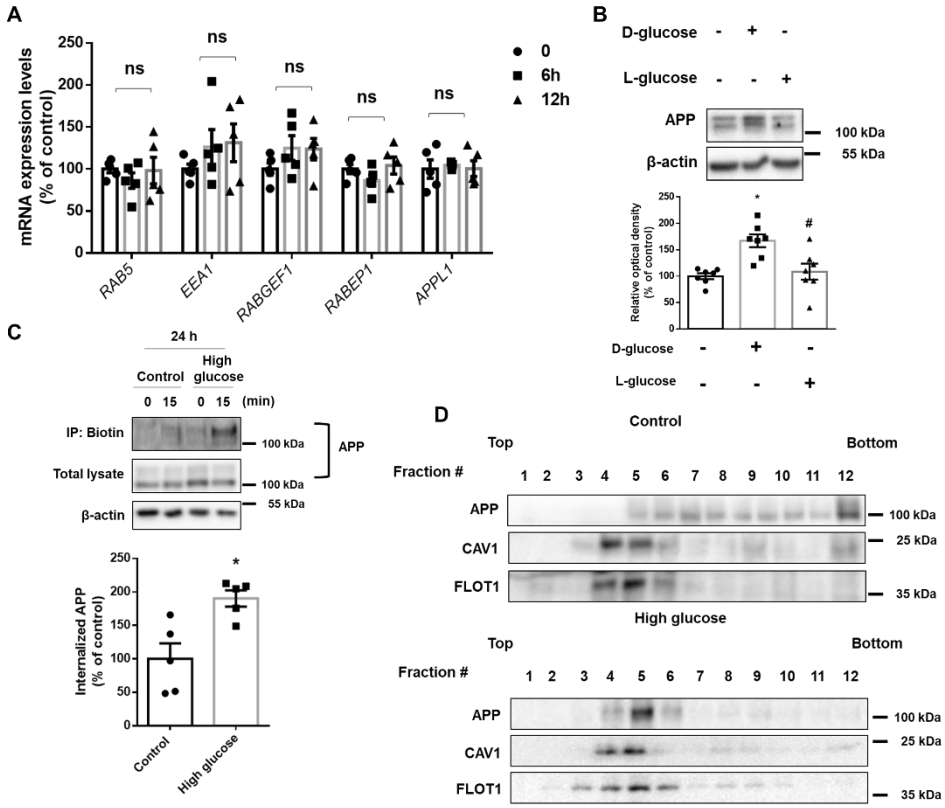

Figure 12. High glucose facilitates APP endocytosis.

A The SK−N−MCs were treated with high glucose (25 mM) in a time dependent manner. The mRNA expression levels of *RAB5, EEA1, RABGEF1, RABEP1, and APPL1* were analyzed by. $n = 5$. **B** The cells were treated with D−glucose (25 mM) or L−glucose (25 mM) for 24 h. Then, APP and β−actin were detected by western blot. $n = 7$. **C** Biotin surface labeling and internalization assay from the SK−N−MCs treated with high glucose (25 mM) for 24 h were done. 0 and 15 min indicate time points of internalization. In the bottom, total lysates were subjected to western blot. APP and β−actin were detected. Percent of internalized APP were measured by normalizing with total APP at time 15 in each condition. $n = 5$. **D** High glucose (25 mM) were treated for 24 h in the cells. Sucrose gradient−fractionized lysates were subjected to western blot. APP, CAV1, and FLOT1 were detected. $^{*}p < 0.05$ vs. control, $^{\#}p < 0.05$ vs. D−glucose.

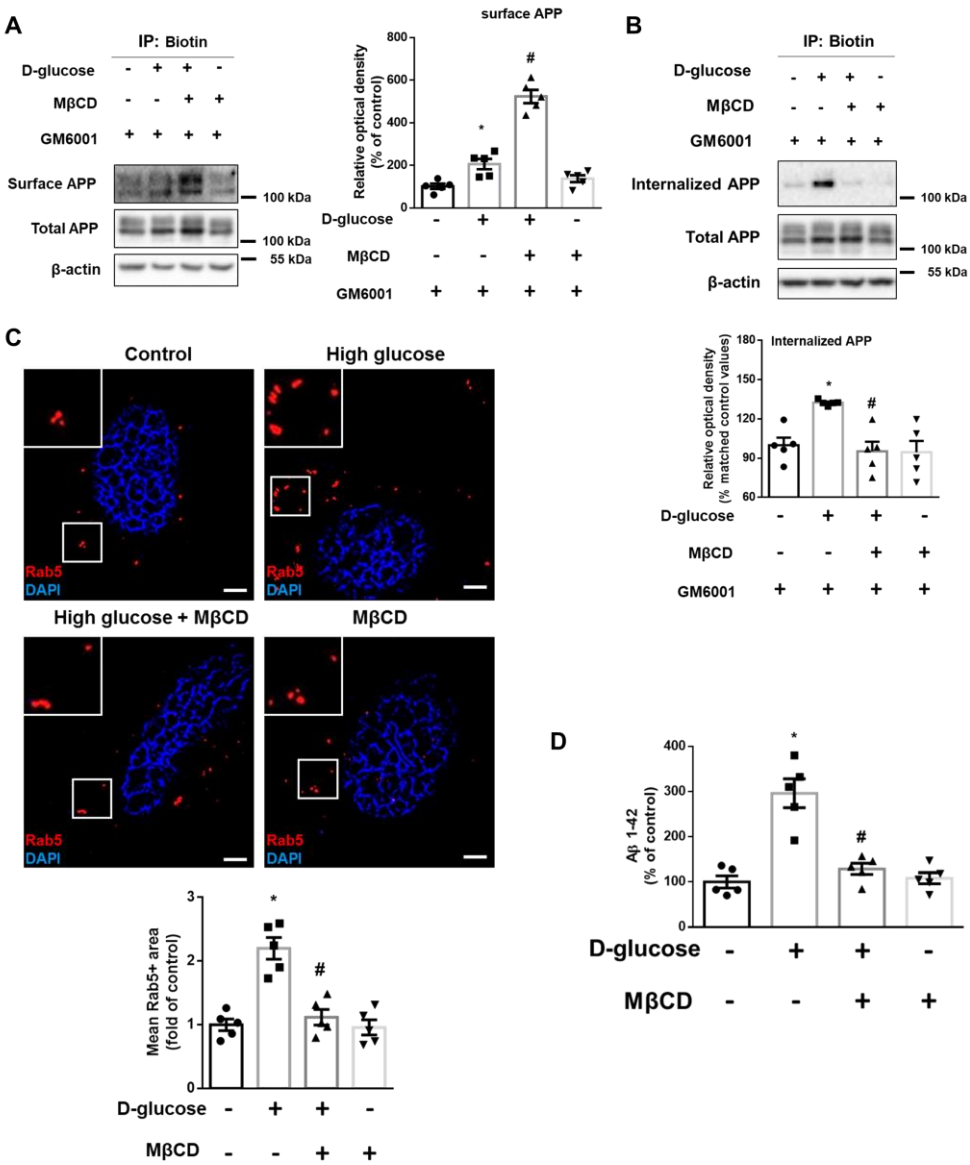

Figure 13. Lipid-raft mediated APP endocytosis induces early endosomal enlargement under high glucose conditions.

A, B The cells were treated with GM6001 (20 μM) for 30 min and then with MβCD (1 mM) for 30 min and high glucose (25 mM) for 24 h. **A** Cell surface were biotinylated and labelled proteins were pulled down by streptavidin beads. Surface APP, total APP, and β-actin were detected by western blot. n = 5. **B** Biotin surface labeling and internalization assay including 15 min for internalization were done. Internalized APP, total APP, and β-actin were detected by western blot. n = 5. Logarithmic transformations were performed for homogeneity of the sample variance. **C** The cells were incubated with MβCD (1 mM) for 30 min prior to high glucose treatment (25 mM) for 24 h. The cells were immunostained with Rab5-specific antibody and counterstained with DAPI. Scale bars, 8 μm. n = 5. **D** The cells were pretreated with MβCD (1 mM) for 30 min before high glucose treatment (25 mM) for 48 h. Aβ 1-42 from cell culture medium were measured. n = 5. $^{*}p < 0.05$ vs. control, $^{\#}p < 0.05$ vs. high glucose.

High glucose-induced ROS increase the expression of endocytic proteins by facilitating Sp1 nuclear translocation

Next, I investigated how high glucose facilitates APP endocytosis and hypothesized that it regulates endocytosis-related proteins. Given that the main cause of pathological situations under high glucose conditions is ROS, I found high glucose significantly increased the amount of ROS after 24 h (Figure 14A). However, there was no significant changes over time in the control conditions. Furthermore, among the kinases controlled by ROS, I found that Sp1 is related to endocytic protein expression (Bai *et al.,* 2017). Indeed, high glucose-stimulated Sp1 nuclear translocation were blocked by pretreatment of NAC (ROS scavenger) (Figure 14B, C). As shown in Figure 15A, B, mRNA and protein expression levels of PICALM, AP2A1, and CHC were increased by high glucose but inhibited by pretreatment with mithramycin A (Sp1 inhibitor). Moreover, compared with the levels in control animals, ZDF rats and STZ-treated mice had high expression levels of the hippocampal endocytic proteins PICALM, AP2A1, and CHC (Figure 15C, D). These findings suggest that high glucose up-regulates the expression of endocytic proteins by ROS-stimulated Sp1 activation.

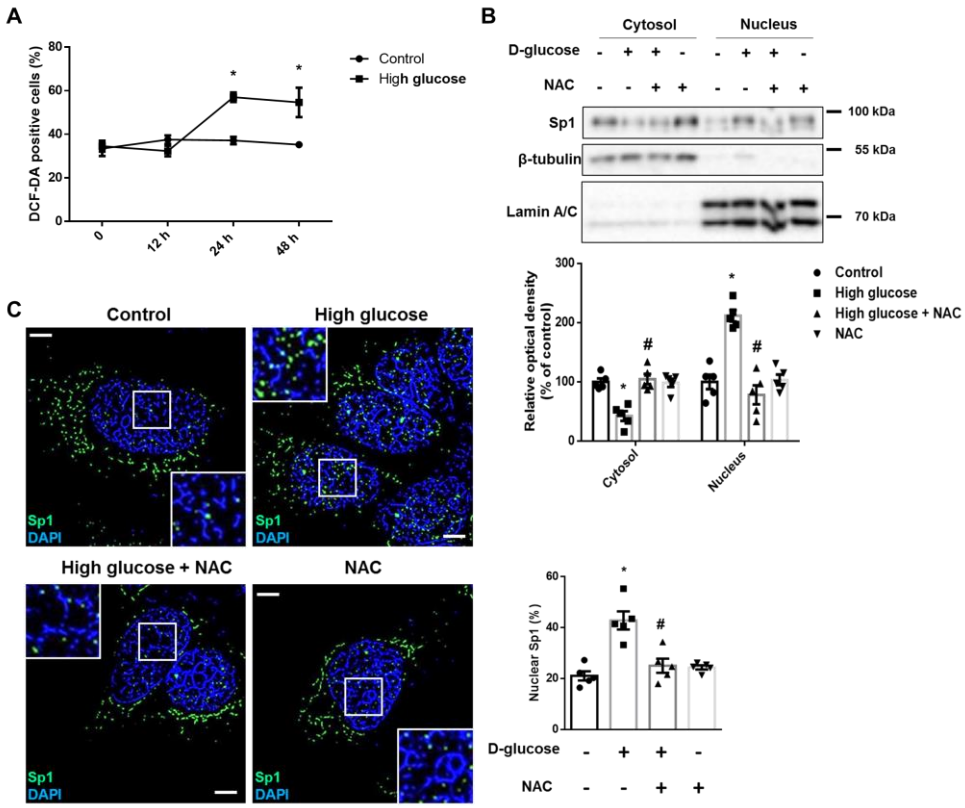

Figure 14. High glucose-induced ROS facilitates Sp1 nuclear translocation.

A The SK-N-MCs were treated with distilled water (DW) or 25 mM high glucose in a time response. Intracellular ROS was measured by DCF-DA staining and analyzed by flow cytometry. **B, C** The cells were incubated with NAC (4 mM) for 30 min prior to high glucose treatment (25 mM) for 6 h. **B** Sp1, β-tubulin, and Lamin A/C in cytosolic and nuclear fractionized samples were detected by western blot. **C** The cells were immunostained with Sp1-specific antibody and counterstained with DAPI. Scale bars, 8 μm. $n = 5$. $^{*}p < 0.05$ vs. control, $^{\#}p < 0.05$ vs. high glucose.

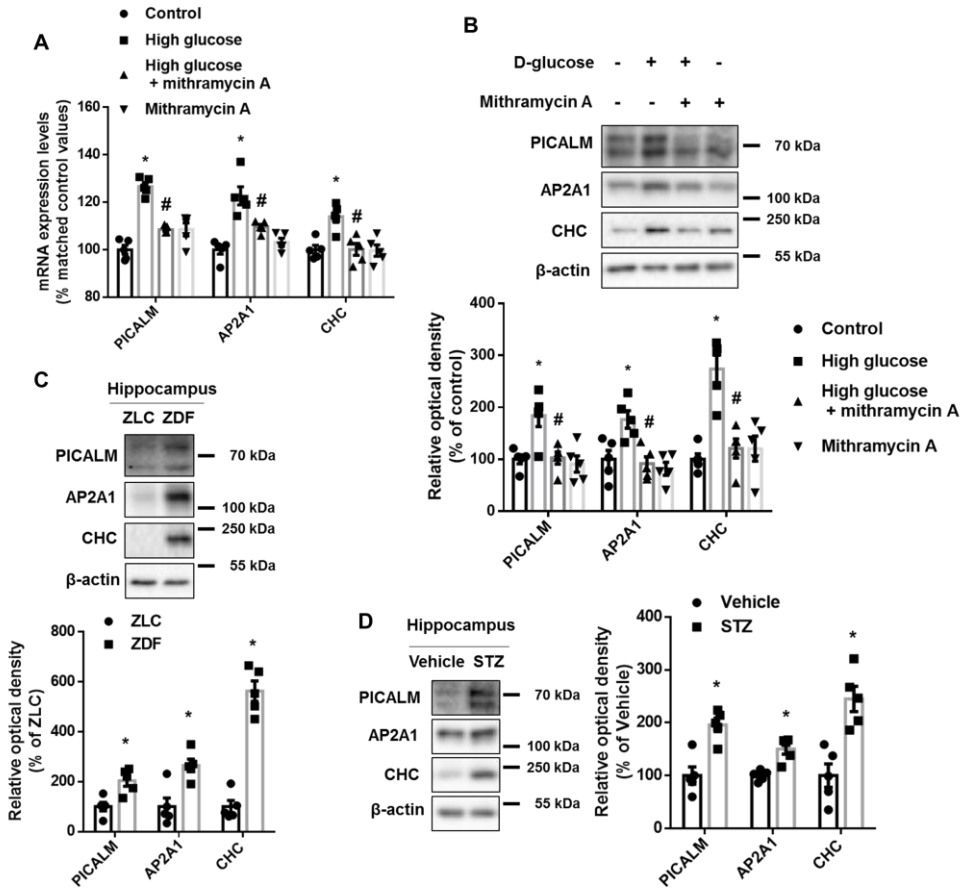

Figure 15. High glucose-stimulated Sp1 up-regulates the expression of endocytic proteins, and the levels of these proteins are increased in the hippocampus of diabetic rodents.

A, B The cells were pretreated with mithramycin A (25 nM) for 30 min before high glucose treatment (25 mM) for 12 h and 24 h, respectively. **A** mRNA expression levels of *PICALM*, *AP2A1*, and *CHC* were analyzed. Logarithmic transformations were performed for homogeneity of the sample variance. **B** PICALM, AP2A1, CHC, and β−actin were subjected to western blot. $n = 5$. $^{*}p < 0.05$ vs. control, $^{\#}p < 0.05$ vs. high glucose. **C, D** The hippocampal samples were obtained from ZLC and ZDF rats, and vehicle−and STZ−treated mice, respectively. PICALM, AP2A1, CHC, and β−actin were detected by western blot. $n = 5$. $^{*}p < 0.05$ vs. diabetic rodents.

PICALM regulates clathrin-dependent APP endocytosis, which up-regulates Aβ production

Given that PICALM is considered to be a common risk factor for both AD and DM (Vacinova *et al.,* 2017; McFall *et al.,* 2015) and recruits CHC and AP-2 complex (Xu, Tan, and Yu 2015), I studied the role of PICALM in the endocytosis under high glucose conditions and AD pathology. First, exploratory data showed that PICALM was located in lipid rafts under both normal and high glucose conditions. I further found that the levels of co-localization of APP with AP2A1 and CHC under high glucose in the cell transfected with a NT siRNA were higher than those of the *PICALM* siRNA transfected cell treated with high glucose (Figure 16A, B). Moreover, prior to endocytosis (0 min), surface-labelled APP and PICALM were observed exclusively on the cell surface. After endocytosis (15 min), surface-labelled APP and PICALM were observed in intracellular vesicles and were co-localized. This indicates that high glucose caused APP co-localization with PICALM during endocytosis (Figure 16C). Similarly, the expression levels of surface APP in cells transfected with *PICALM* siRNA under high glucose conditions were higher than those of NT siRNA-transfected cells treated with high glucose (Figure 17A). Additionally, high glucose increased the internalization of APP, which was reversed by *PICALM* RNAi (Figure 17B). As I aimed to measure APP

internalization and not the recruitment ability of PICALM, we used GM6001, which inhibited APP shedding in Figure 17A, B. Thus, compared with total and surface APP levels of Figure 16A, B, those of Figure 17A, B were not reduced by *PICALM* siRNA. High glucose-induced increases in Aβ were reversed by *PICALM* knockdown (Figure 17C). These results indicate that up-regulation of PICALM by high glucose induces clathrin-mediated APP endocytosis. To confirm the effects of CME on APP endocytosis, I used a Dynasore. The expression levels of surface APP in the samples treated with high glucose and dynasore were higher than those of samples treated with high glucose alone (Figure 18A). Furthermore, Dynasore reversed high glucose-induced early endosomal enlargement and increment of Aβ (Figure 18B, C). These results demonstrated that increased PICALM facilitated clathrin-dependent APP endocytosis, resulting in Aβ production.

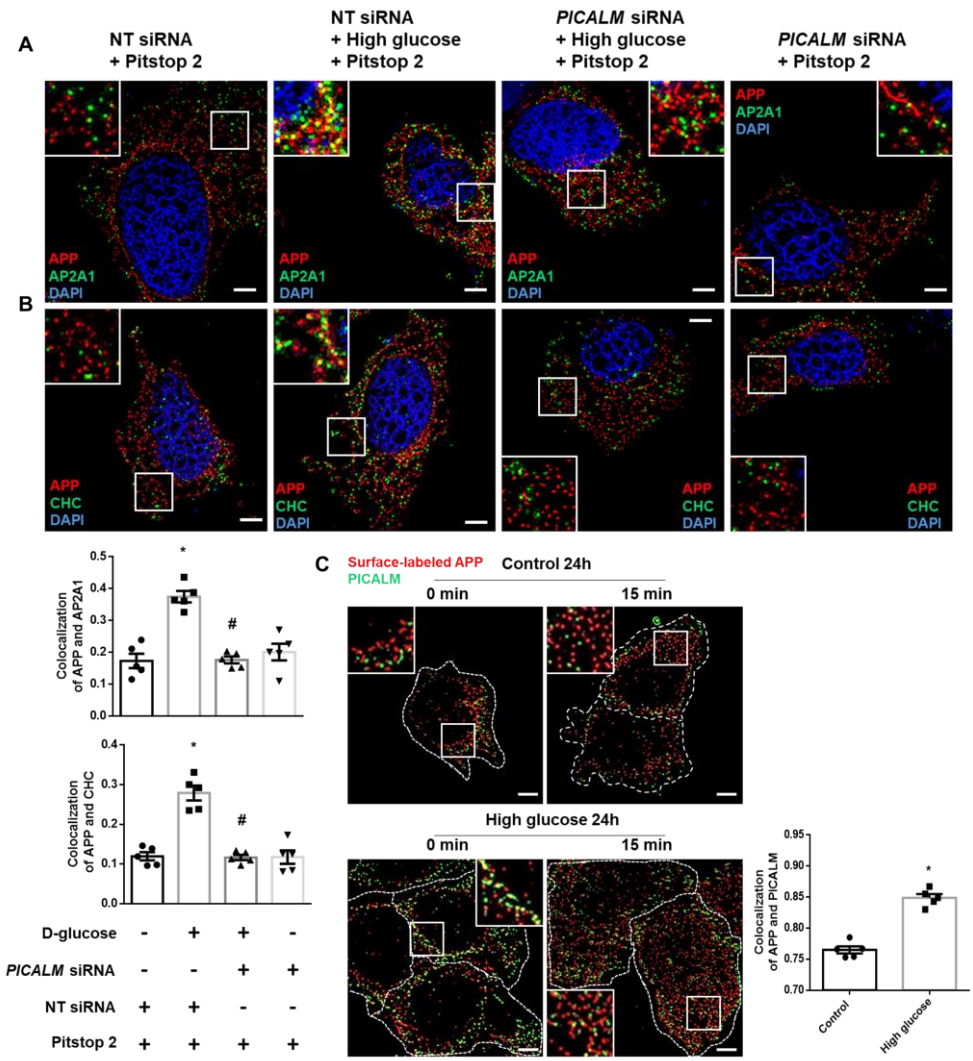

Figure 16. PICALM mediates recruitment of AP2A1 and CHC to APP and co-localizes with internalized APP.

A, B The SK-N-MCs were transfected with NT siRNA or *PICALM* siRNA for 12 h and then treated with Pitstop 2 (30 μM) for 30 min prior to high glucose treatment (25 mM) for 24 h. **A** The cells were immunostained with APP-and AP2A1-specific antibodies and counterstained with DAPI. Scale bars, 8 μm. **B** The cells were immunostained with APP-and CHC-specific antibodies. **C** Internalization assay from the cells treated with high glucose (25 mM) for 24 h were done by immunostaining with Aβ for surface-labeled APP and PICALM specific antibodies. 0 and 15 min indicate time points of internalization. Scale bars, 8 μm. $n = 5$. $^{*}p < 0.05$ vs. NT siRNA transfection, $^{\#}p < 0.05$ vs. NT siRNA transfection with high glucose.

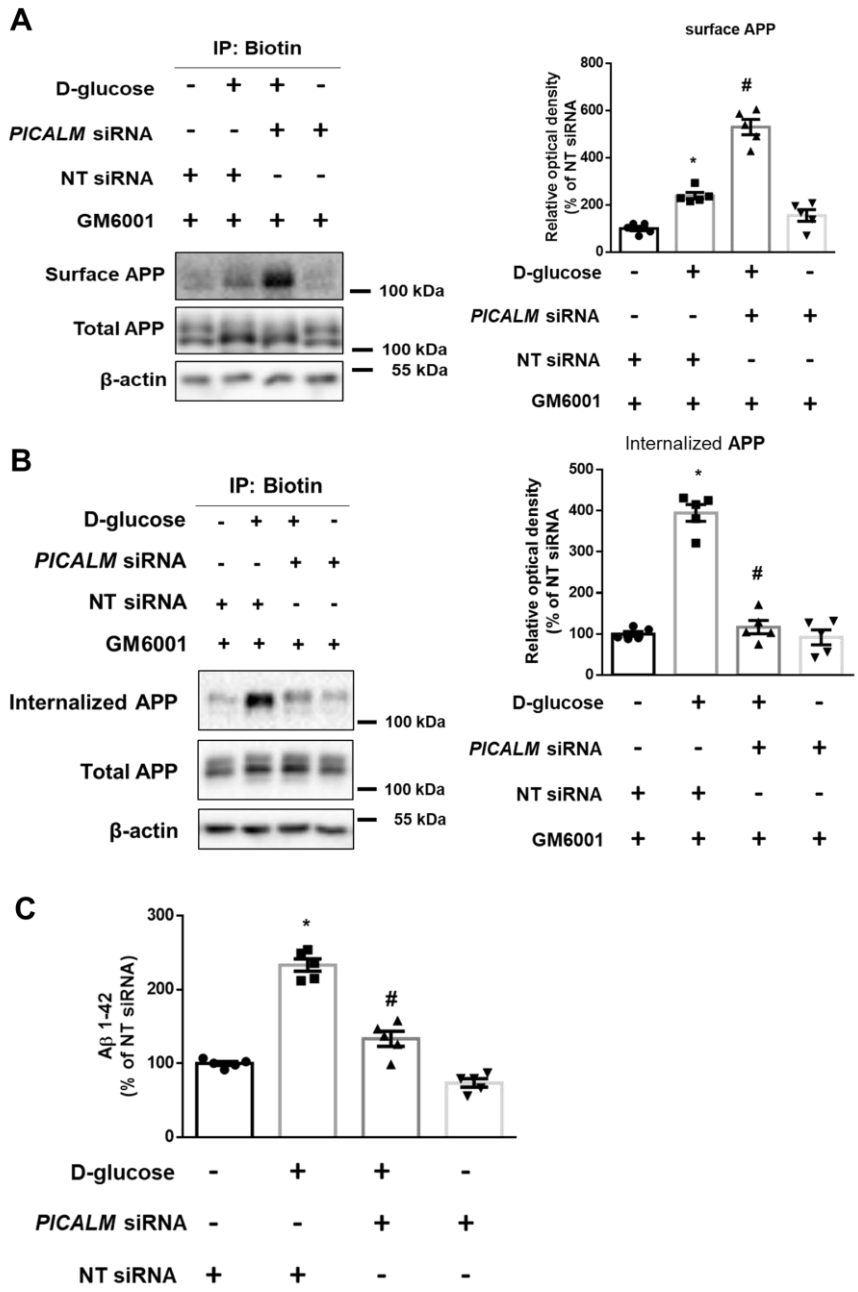

Figure 17. PICALM mediates APP endocytosis, which up-regulates A β production.

A, B The cells were transfected with NT siRNA or *PICALM* siRNA for 12 h and then treated with GM6001 (20 μM) for 30 min prior to high glucose treatment (25 mM) for 24 h. **A** Cell surface was biotinylated, and labelled proteins were pulled down by streptavidin beads. Surface APP, total APP, and β-actin were detected by western blot. **B** Biotin surface labelling and internalization assay including 15 min for internalization were done. Internalized APP, total APP, and β-actin were detected by western blot. **C** The cells were transfected with NT siRNA or *PICALM* siRNA for 12 h prior to high glucose treatment (25 mM) for 48 h. Aβ 1-42 from cell culture medium were measured. n = 5. $^{\#}p < 0.05$ vs. NT siRNA transfection with high glucose.

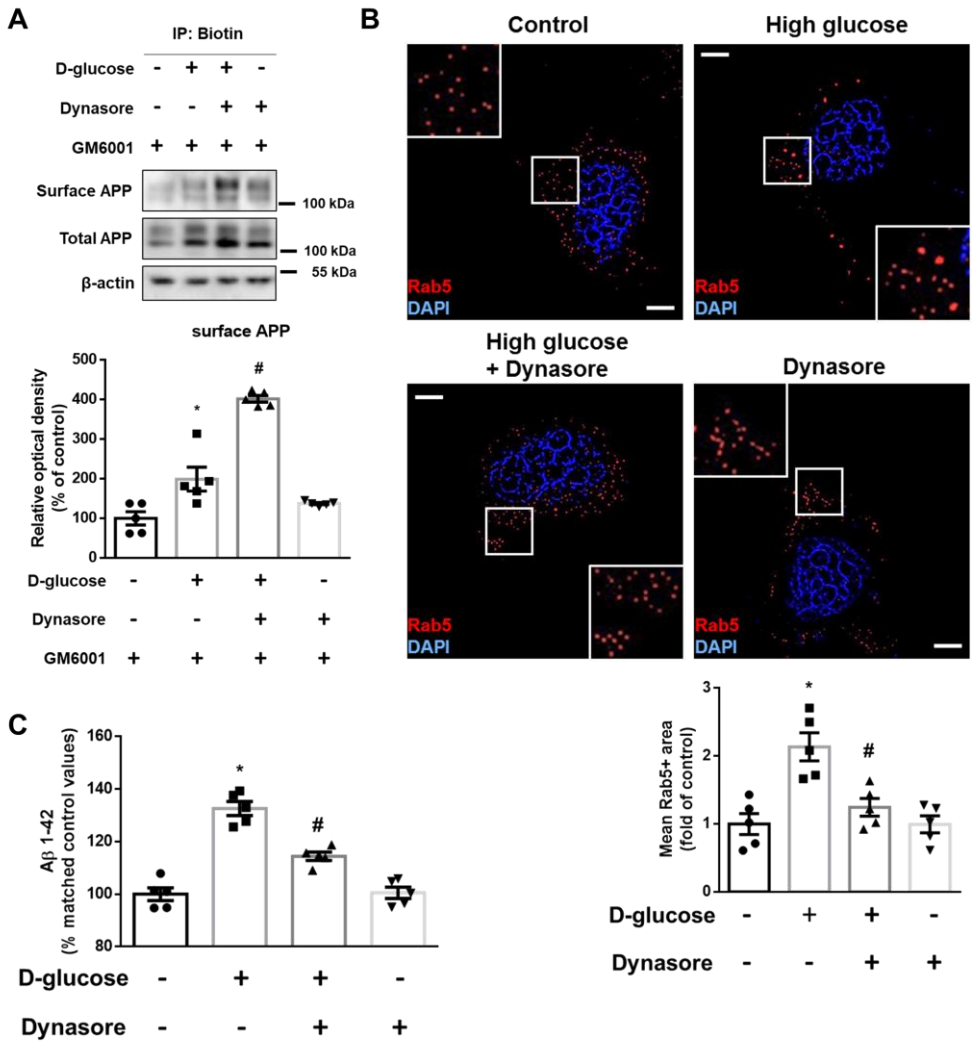

Figure 18. Clathrin-dependent APP endocytosis induces early endosomal enlargement, which up-regulates Aβ production.

A The cells were pretreated with GM6001 (20 μM) for 30 min and then treated with dynasore (25 μM) for 30 min before high glucose treatment (25 mM) for 24 h. Cell surface were biotinylated and labelled proteins were pulled down by streptavidin beads. Surface APP, total APP, and β-actin were detected by western blot. **B, C** The cells were pretreated with dynasore (25 μM) for 30 min prior to high glucose treatment (25 mM) for 24 h or 48 h, respectively. **B** The cells were immunostained with Rab5-specific antibody and counterstained with DAPI. Scale bars, 8 μm. **C** Aβ 1-42 from cell culture medium were measured. n = 5. Logarithmic transformations were performed for homogeneity of the sample variance. $^{*}p < 0.05$ vs. control, $^{\#}p < 0.05$ vs. high glucose.

Defects in AMPK/mTORC1-mediated autophagy impairs early endosomal clearance under high glucose conditions

I hypothesized that the block of the degradative trafficking pathway also causes early endosomal enlargement. Compared with the levels in control animals, ZDF rats and STZ-treated mice had increased hippocampal P62 and decreased LC3II/LC3I ratio (Figure 19A, B). In *in vitro* models, high glucose decreased the LC3II/LC3I ratio and increased P62 after 12h (Figure 19C). Compared with L-glucose, only D-glucose decreased the LC3II/LC3I ratio and increased P62 (Figure 19D). This suggests that autophagic dysfunction is induced under DM. As PICALM is known to induce autophagy, I further investigated whether PICALM regulates autophagy under high glucose conditions. The interaction between LC3 and PICALM (Figure 20A) (Tian *et al.,* 2013) and endocytosis of VAMP3 (Figure 20B) (Moreau *et al.,* 2014) were increased under high glucose conditions. *PICALM* siRNA transfection further reduced the LC3-II/LC3-I ratio compared to high glucose, with NT siRNA transfection (Figure 20C). These data suggest that increased PICALM under high glucose conditions facilitates autophagy but is insufficient to fully reverse the reduction in autophagy. Furthermore, ROS promote autophagy through increasing the expression of Beclin1 through MAPK signaling (Moruno *et al.,* 2012). However, I did not identify any significant changes (Figure 21A). The ROS/Beclin1-mediated pathway was not dominant in autophagy under my experimental conditions. Given that mTORC1 is a master regulator

of autophagy, I found that high glucose down-regulated AMPKα phosphorylation at Thr172 and upregulated mTORC1 phosphorylation at Ser2448 in a time-dependent manner (Figure 21B). The decrease in the LC3II/LC3I ratio, co-localization of lysosomes with LC3, and the increase in P62 that is induced by high glucose were reversed by pretreatment with Rapamycin (Figure 21C and Figure 22A). To investigate the relationship between mTORC1-mediated autophagic impairment with the increase in Rab5 protein levels, I used PF-4708671 and Rapamycin. Under high glucose conditions, Rab5 protein expression levels were decreased after pretreatment with Rapamycin, but not upon pretreatment with PF-4708671. This suggests that increased Rab5 is not due to increased protein synthesis by S6k1, but rather, due to a deficiency in autophagy (Figure 22B). Indeed, I confirmed that Rapamycin attenuated the high glucose-induced increment of $Rab5^+$ endosomal size and Aβ (Figure 22C, D). These results revealed that high glucose impairs early endosomal clearance through AMPK/mTORC1-mediated defect in autophagy.

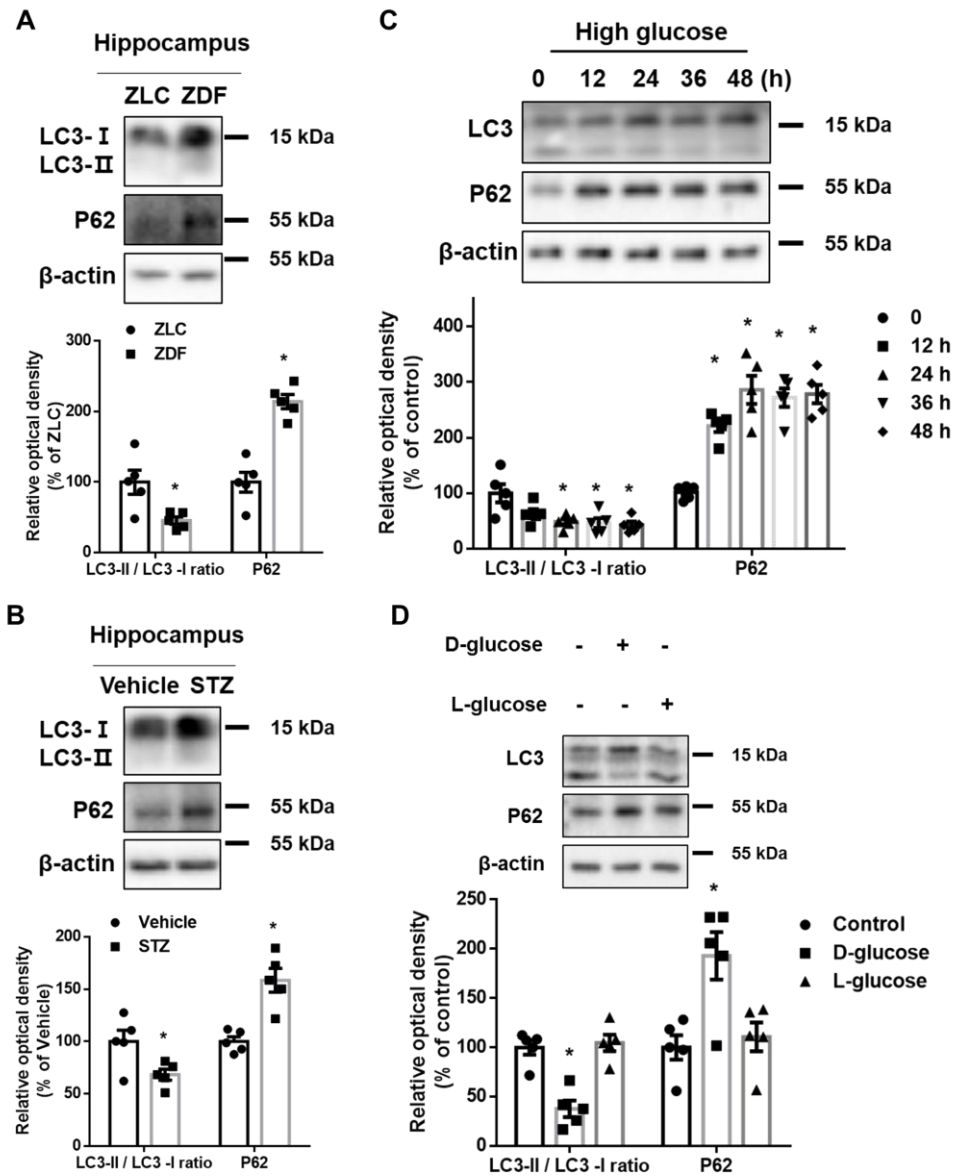

Figure 19. Autophagy is impaired in the hippocampus of diabetic rodents and SK-N-MCs exposed to high glucose.

A, B The hippocampal samples were obtained from ZLC and ZDF rats or vehicle-and STZ-treated mice, respectively. $n = 5$. $^{*}p < 0.05$ vs. vehicle-treated rodents. **C** The SK-N-MCs were treated with high glucose (25 mM) in a time dependent manner. LC3, P62, and β-actin were subjected to western blot. **D** The cells were treated with D-glucose (25 mM) or L-glucose (25 mM) for 24 h. Then, LC3, P62, and β-actin were detected by western blot. $n = 5$. $^{*}p < 0.05$ vs. control.

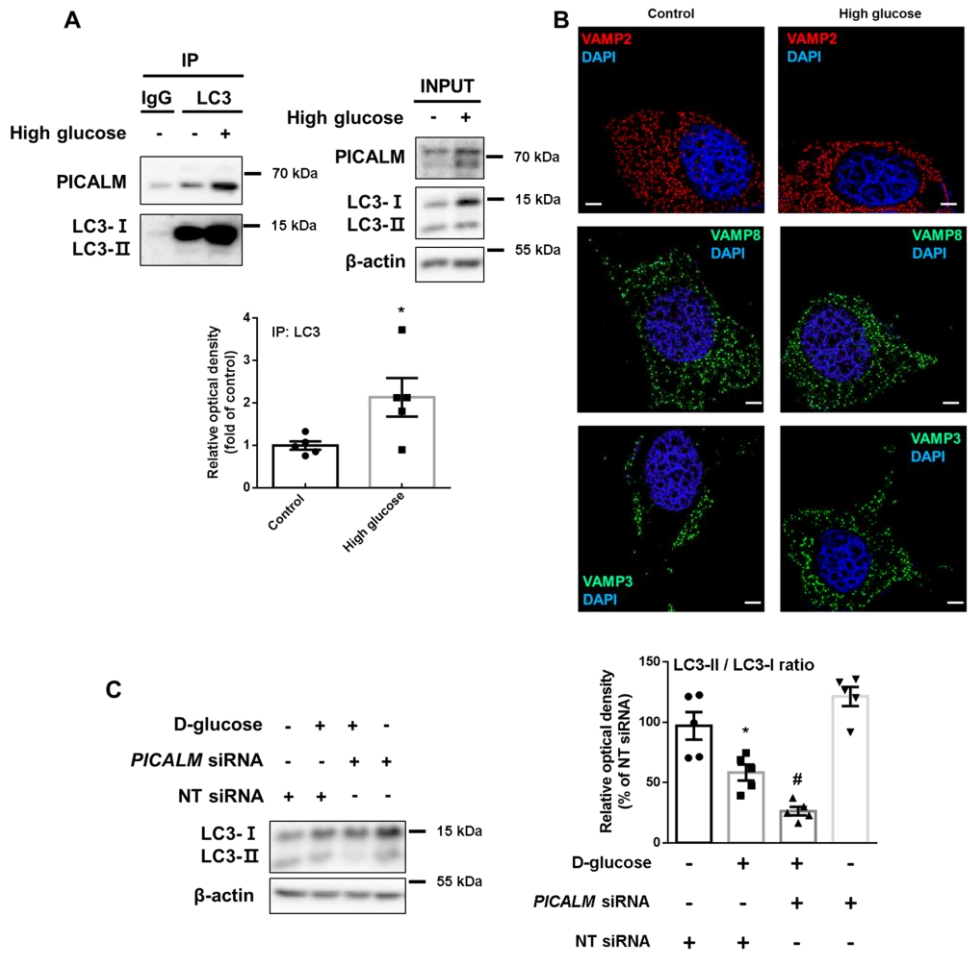

Figure 20. PICALM induces autophagy under high glucose conditions.

A, B The SK-N-MCs were treated with high glucose (25 mM) for 24 h. **A** Co-immunoprecipitation of PICALM with IgG and LC3 antibodies were shown in left panel. Total protein expressions in lysate were shown in right panel. $n = 5$. $^{*}p < 0.05$ vs. Control. **B** The cells were immunostained with VAMP2 or VAMP8 or VAMP3-specific antibodies and counterstained with DAPI. Scale bars, 8 μm. $n = 5$. **C** The cells were transfected with NT siRNA or *PICALM* siRNA for 12 h prior to high glucose (25 mM) treatment for 24 h. LC3 and β-actin were detected by western blot. $n = 5$. Logarithmic transformations were performed for homogeneity of the sample variance. $^{*}p < 0.05$ vs. NT siRNA transfection, $^{\#}p < 0.05$ vs. NT siRNA transfection with high glucose.

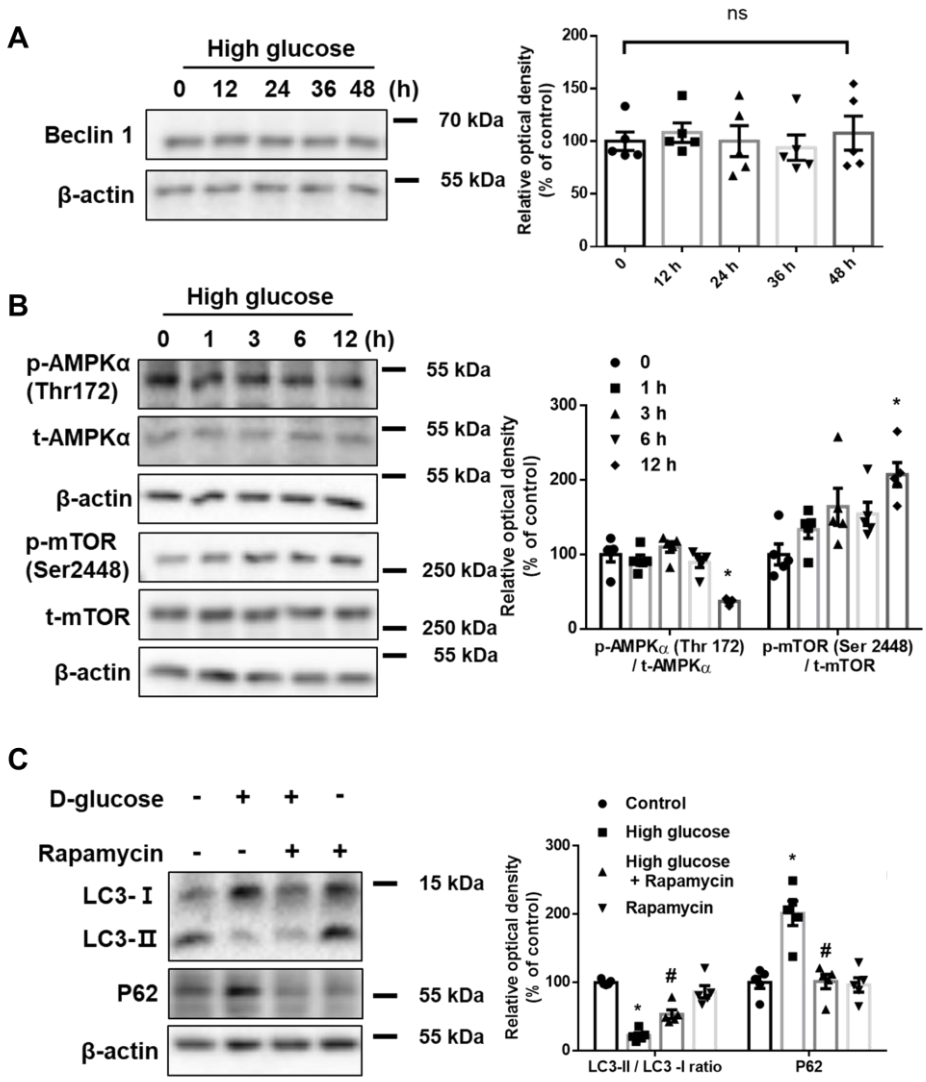

Figure 21. High glucose-mediated AMPK/mTORC1 signaling impairs autophagy.

A The SK-N-MCs were treated with high glucose (25 mM) in a time dependent manner. The Beclin1 were detected by western blot. B The SK-N-MCs were treated with high glucose (25 mM) in a time response. p-AMPKα (Thr 172), t-AMPKα, p-mTOR (Ser 2448), t-mTOR, and β-actin were detected by western blot. C The cells were incubated with rapamycin (200 nM) for 30 min before high glucose treatment (25 mM) for 24 h. LC3, P62, and β-actin were subjected to western blot. $n = 5$. $^{*}p < 0.05$ vs. control, $^{\#}p < 0.05$ vs. high glucose.

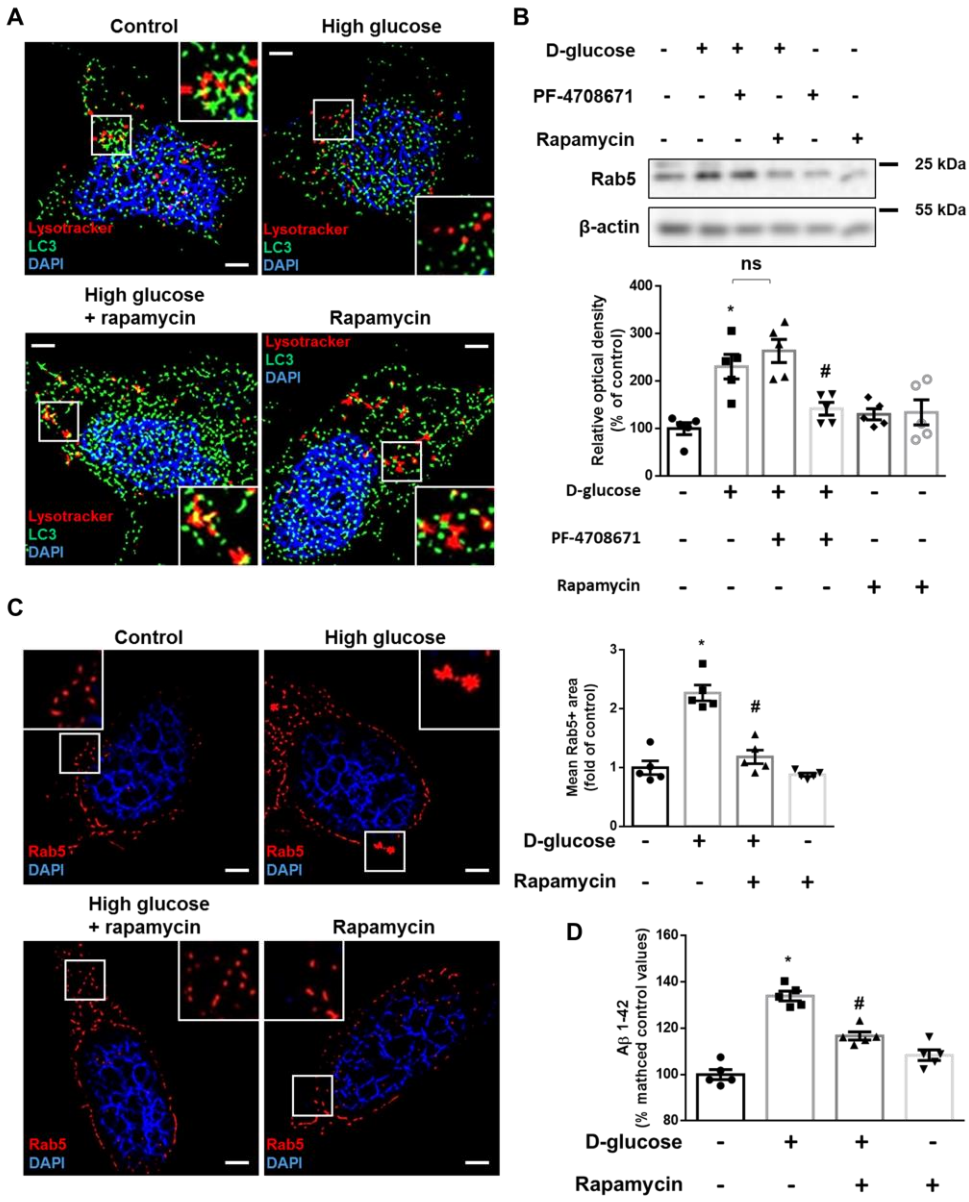

Figure 22. Defects in mTORC1-mediated autophagy impairs early endosomal clearance, which up-regulates Aβ.

A, C The cells were incubated with rapamycin (200 nM) for 30 min before high glucose treatment (25 mM) for 24 h. **A** The cells were immunostained with LC3-specific antibody and stained with Lysotracker red and DAPI. Scale bars, 8 μm. **B** The cells were pretreated with PF-4708671 (10 μM) or rapamycin (200 nM) for 30 min prior to high glucose treatment (25 mM) for 24 h. Rab5 and β-actin were detected by western blot. **C** The cells were immunostained with Rab5-specific antibody and counterstained with DAPI. Scale bars, 8 μm. **D** The cells were pretreated with rapamycin (200 nM) for 30 min before high glucose treatment (25 mM) for 48 h. Aβ 1-42 from cell culture medium were measured. n = 5. Logarithmic transformations were performed for homogeneity of the sample variance. $^{*}p < 0.05$ vs. control, $^{\#}p < 0.05$ vs. high glucose.

Lysosomal dysfunction induced by ROS and mTORC1 up-regulates Aβ production through impairment of endosomal clearance

To further investigate endosomal degradative trafficking, I tested the relationship between early endosomes with lysosomes. High glucose increased Rab5 co-localization with lysosomes (Figure 23A). As there were no significant alterations of mRNA expression levels of endolysosomal fusion-related genes (Figure 23B), I hypothesized that lysosomal dysfunction impairs the degradation of enlarged endosomes. Indeed, high glucose decreased the mean size of acidic lysosomes (Usenovic *et al.,* 2012) (Figure 23A) and the percentage of lysotracker-positive cells after 12h. However, there was no significant changes over time in the control conditions (Figure 23C), which meant that high glucose reduced the number of intact lysosomes. Hippocampal LAMP1 increased in ZDF rats and STZ-treated mice compared with that of control groups (Figure 24A, B). In *in vitro* models, LAMP1 also increased after 12h under high glucose conditions (Figure 24C). Given that lysosomal dysfunction is caused by ROS-mediated lysosomal membrane permeabilization (LMP) (Serrano-Puebla *et al.,* 2016) and impairment of lysosomal quality control (Papadopoulos *et al*., 2017), I demonstrated that pretreatment with NAC or rapamycin reversed the elevated LAMP1 expression levels induced by high glucose (Figure 25A, B). Furthermore, the attenuation of the signals of both lysotracker

and BCECF-AM, an intracellular pH indicator, by high glucose was recovered by pretreatment with NAC and rapamycin, respectively (Figure 25C, D). In addition to the impairment of early endosomal degradation, I found that co-localization of CTSB, an Aβ-degradative lysosomal enzyme (Mueller-Steiner *et al.,* 2006) was decreased by high glucose (Figure 26A). Moreover, the pretreatment of leupeptin (inhibitor of serine and thiol proteases) further increased the amount of Aβ up-regulated by high glucose (Figure 26B). These findings suggest that ROS- and mTORC1-mediated lysosomal dysfunction is critical for the blockage of endosomal clearance and increment of Aβ under high glucose conditions.

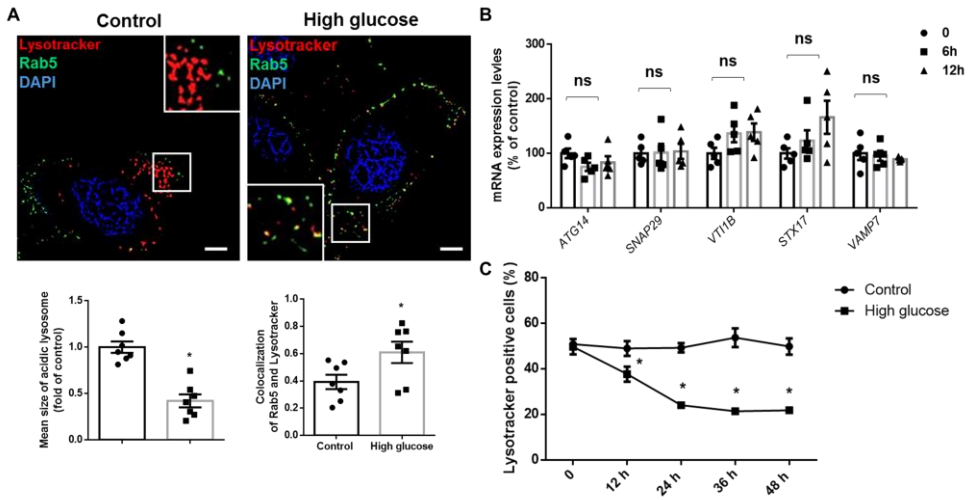

Figure 23. Lysosomal dysfunction leads to endosomal clearance failure under high glucose conditions.

A The SK-N-MCs were treated with high glucose (25 mM) for 24 h. The cells were immunostained with Rab5-specific antibody and stained with Lysotracker red and DAPI. Scale bars, 8 μm. n = 7. B, C The cells were treated with high glucose (25 mM) in a time dependent manner. B The mRNA expression levels of *ATG14*, *SNAP29*, *VTI1B*, *STX17*, and *VAMP7* were analyzed. C The cells were labeled with Lysotracker red and analyzed by flow cytometry. n = 5. $^{*}p < 0.05$ vs. control.

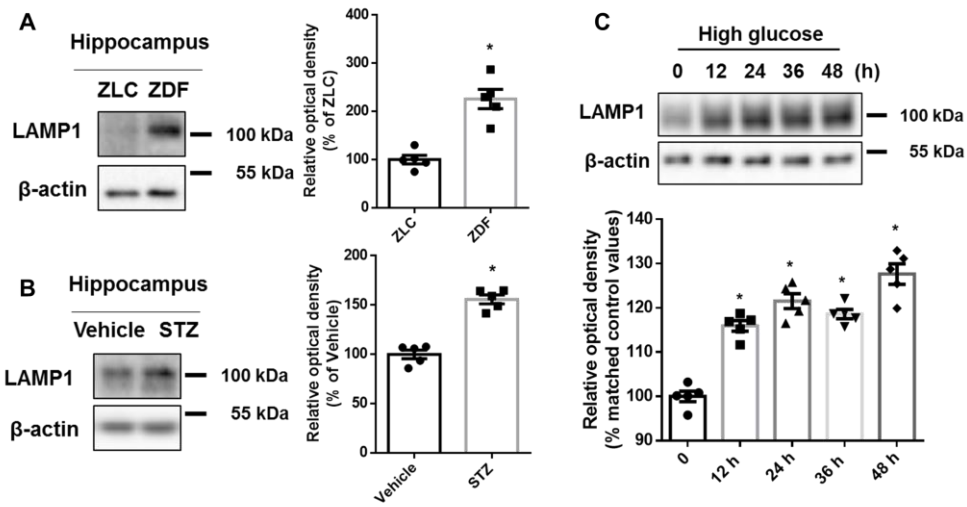

Figure 24. Protein levels of LAMP1 increases in the hippocampus of diabetic rodents and SK-N-MCs exposed to high glucose.

A, B The hippocampal samples were obtained from ZLC and ZDF rats or vehicle-and STZ-treated mice, respectively. LAMP1 and β-actin were detected by western blot. $n = 5$. $^{*}p < 0.05$ vs. vehicle-treated rodents. C The SK-N-MCs in a time response with 25 mM high glucose were subjected to western blot. LAMP1 and β-actin were detected. $n = 5$. Logarithmic transformations were performed for homogeneity of the sample variance. $^{*}p < 0.05$ vs. control.

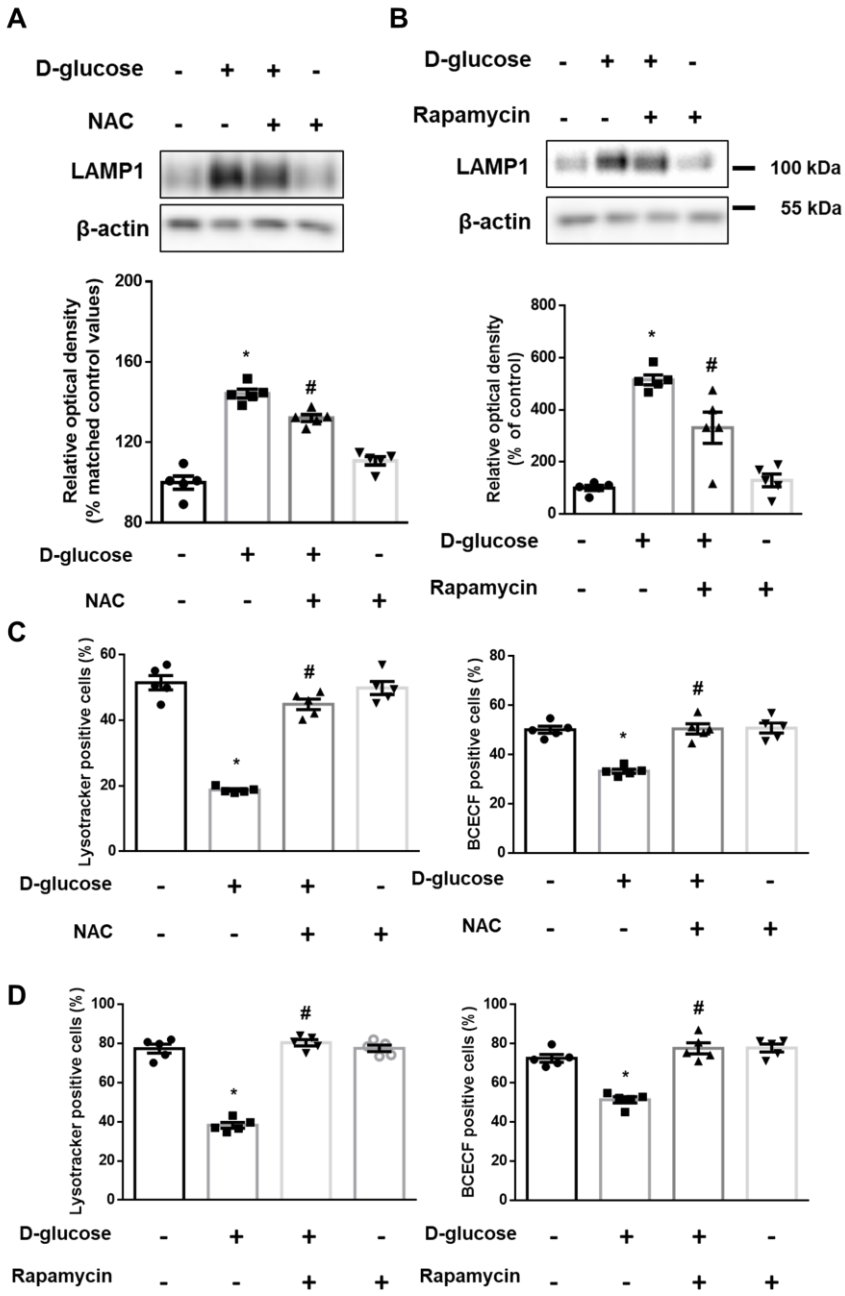
A
D-glucose - + + -
NAC - - + +
LAMP1
β-actin
Relative optical density (% matched control values)
200
160
120
80
*
#
D-glucose - + + -
NAC - - + +
B
D-glucose - + + -
Rapamycin - - + +
LAMP1
β-actin
100 kDa
55 kDa
Relative optical density (% of control)
800
600
400
200
0
*
#
D-glucose - + + -
Rapamycin - - + +
C
Lysotracker positive cells (%)
60
40
20
0
*
#
D-glucose - + + -
NAC - - + +
BCECF positive cells (%)
80
60
40
20
0
*
#
D-glucose - + + -
NAC - - + +
D
Lysotracker positive cells (%)
100
80
60
40
20
0
*
#
D-glucose - + + -
Rapamycin - - + +
BCECF positive cells (%)
100
80
60
40
20
0
*
#
D-glucose - + + -
Rapamycin - - + +

Figure 25. High glucose induced lysosomal dysfunction through ROS and mTORC1-mediated signaling.

A, C The cells were pretreated with NAC (4 mM) for 30 min before high glucose treatment (25 mM) for 24 h. A LAMP1 and β-actin were detected by western blot. Logarithmic transformations were performed for homogeneity of the sample variance. B, D The cells were incubated with rapamycin (200 nM) for 30 min prior to high glucose treatment (25 mM) for 24 h. B LAMP1 and β-actin were detected by western blot. n = 5 from independent experiments. C, D Intact lysosomes and intracellular pH were measured by Lysotracker red and BCECF-AM staining respectively. n = 5. $^{*}p < 0.05$ vs. control, $\#p < 0.05$ vs. high glucose.

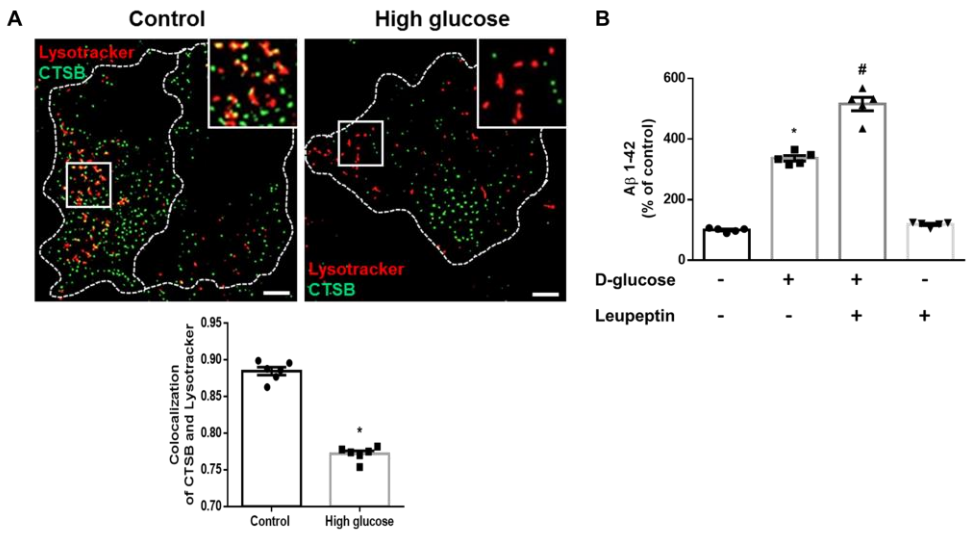

Figure 26. High glucose-mediated cytosolic release of CTSB leads to Aβ accumulation.

A The cells were immunostained with CTSB-specific antibody and stained with Lysotracker red. Scale bars, 8 μm. n = 6. B The cells were pretreated with leupeptin (100 nM) for 30 min before high glucose treatment (25 mM) for 48 h. Aβ 1-42 from cell culture medium were measured. n = 5. $^{*}p < 0.05$ vs. control, $^{\#}p < 0.05$ vs. high glucose.

Increased early endosomes, Aβ increment, and cognitive impairment are recovered by dynasore and rapamycin in STZ-induced DM mice model

To show clinical relevance, I tested alterations of signature proteins and the clinical symptoms in STZ-treated mice. As described in the method section, animal experiments consisted of two parts (Figure 27A). In the histological data, signal intensities of hippocampal early endosomes of STZ-treated mice were higher than both those of vehicle-treated mice and those of STZ with dynasore-treated mice (Figure 28A). With increased early endosomes, STZ up-regulated hippocampal Aβ levels, which were inhibited by dynasore treatment (Figure 28B). Furthermore, the Y-maze results showed that STZ-treated mice showed cognitive impairment, whereas STZ-treated mice with dynaosre treatment showed recovery of cognition (Figure 28C). Meanwhile, in STZ-treated mice, phosphorylation of mTORC1 at Ser2448 was increased, which was down-regulated by treatment with Rapamycin (Figure 29A). In the histological data, signal intensities of hippocampal early endosomes of STZ-treated mice were higher than both those of vehicle-treated mice and those of STZ with Rapamycin-treated mice (Figure 29B). Increased protein expression levels of hippocampal Rab5 in STZ-treated mice were reversed in STZ with Rapamycin-treated mice (Figure 29C). In addition, STZ increased hippocampal Aβ levels and induced cognitive impairment, which were recovered by Rapamycin treatment (Figure 29D, E). These results

demonstrate that DM induces cognitive impairment and Aβ increments through endocytosis- and autophagy-mediated early endosomal dysregulation.

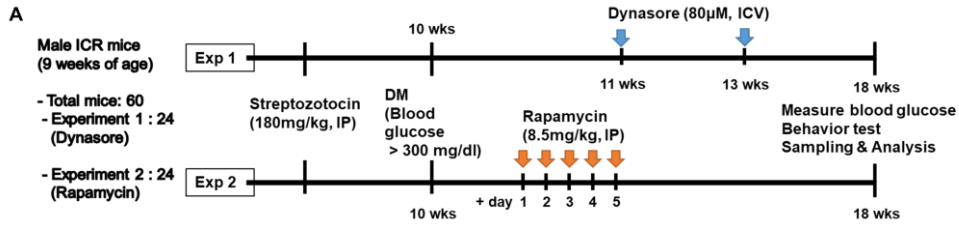

Figure 27. Scheme of an *in vivo* experimental protocol using Dyansore or Rapamycin injection.

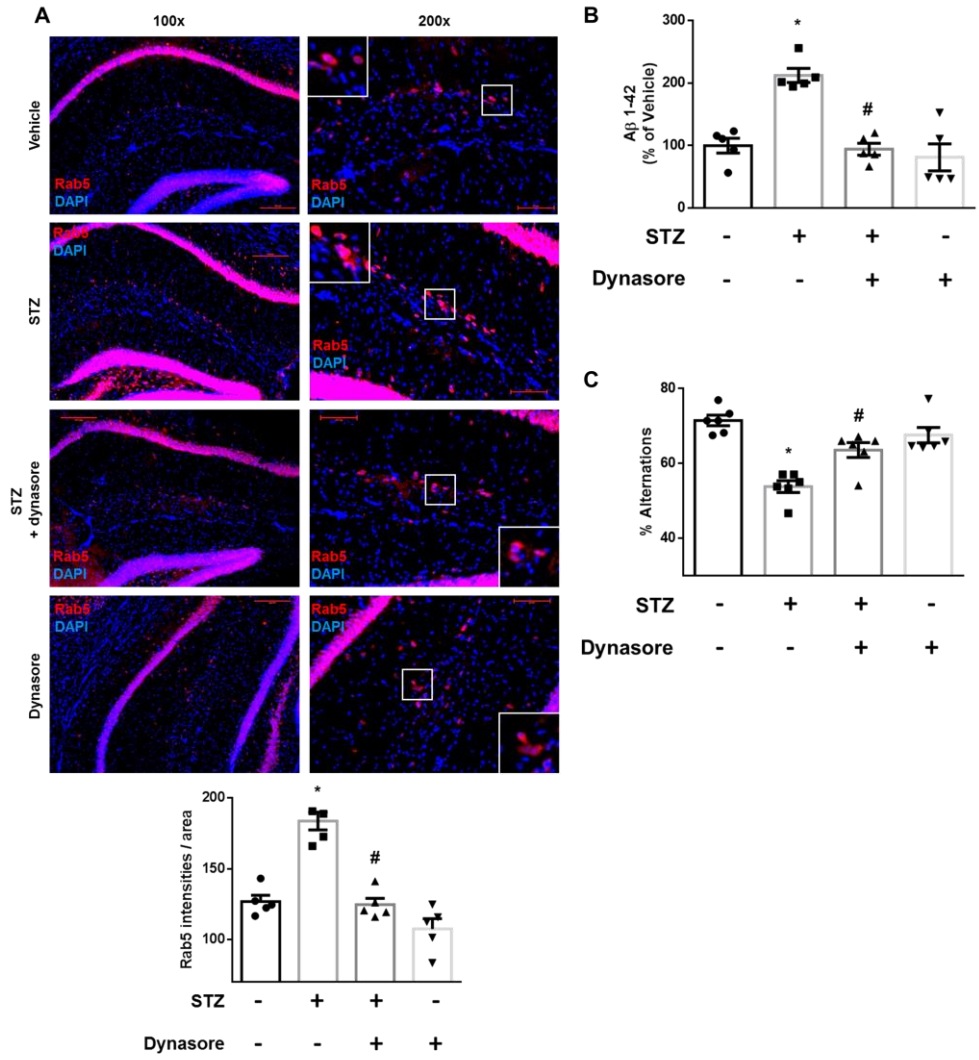

Figure 28. Increased early endosomes, Aβ increment, and cognitive impairment are recovered by pharmacological inhibition of clathrin-mediated endocytosis in STZ-induced diabetic mice.

A Hippocampal slide for IHC was immunostained with Rab5-specific antibody and counterstained with DAPI. Scale bars, 50 μm. **B** Hippocampal Aβ 1-42 were measured by rat and mouse Aβ 1-42 specific ELISA assay. **C** Mice were subjected to Y-maze test to evaluate cognitive function. $n = 5$. $^{*}p < 0.05$ vs. vehicle-treated mice, $^{\#}p < 0.05$ vs. STZ-treated mice.

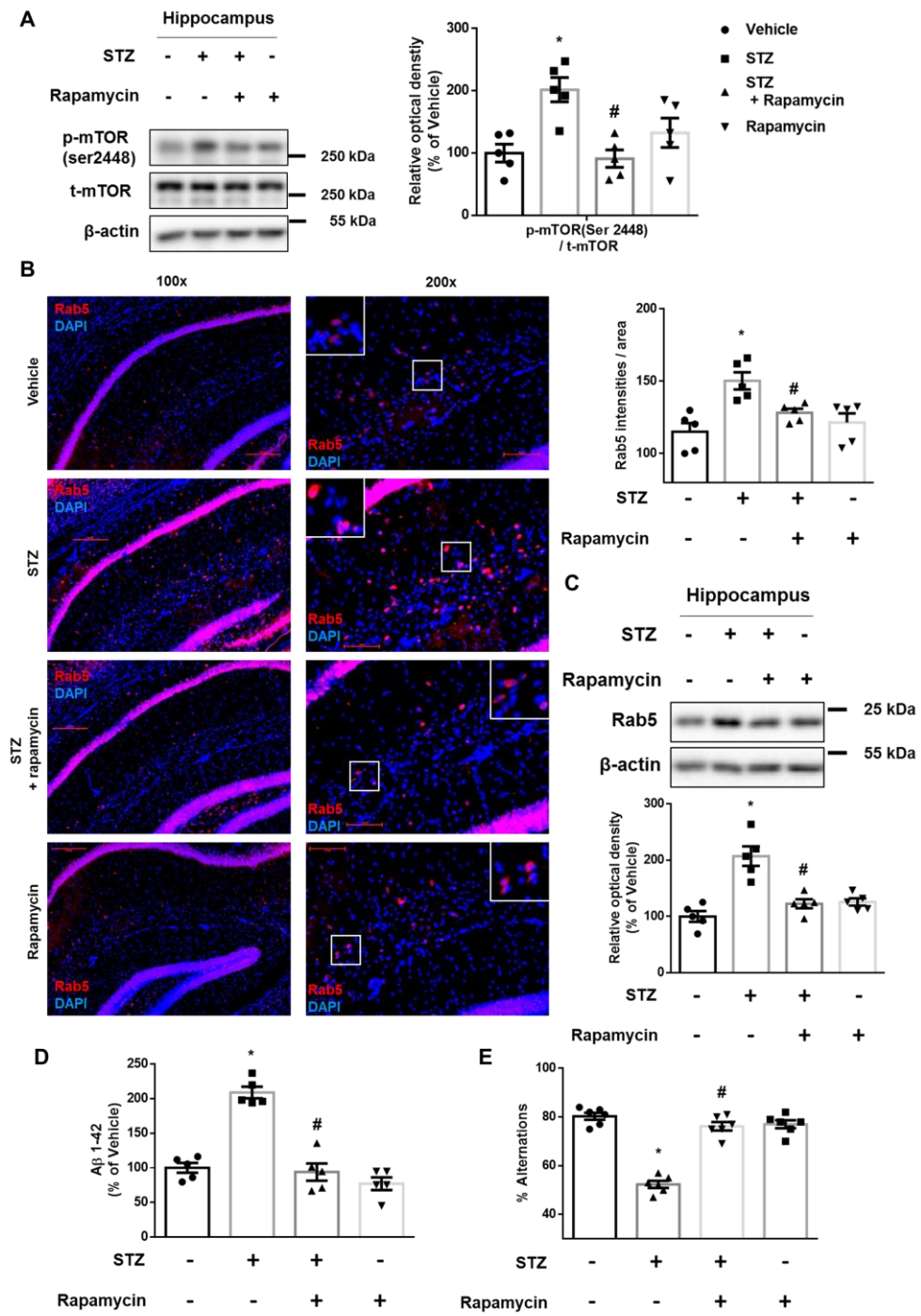
A
Hippocampus
STZ - + + -
Rapamycin - - + +
p-mTOR (ser2448)
t-mTOR
β-actin
250 kDa
250 kDa
55 kDa
Relative optical denstiy (% of Vehicle)
p-mTOR(Ser 2448) / t-mTOR
Vehicle
STZ
STZ + Rapamycin
Rapamycin
B
100x
200x
Rab5
DAPI
Vehicle
STZ
STZ + rapamycin
Rapamycin
Rab5 intensities / area
C
Hippocampus
Rab5
β-actin
25 kDa
55 kDa
Relative optical density (% of Vehicle)
D
Aβ 1-42 (% of Vehicle)
E
% Alternations

Figure 29. Increased early endosomes, Aβ increment, and cognitive impairment are recovered by pharmacological enhancement of autophagy in STZ-induced diabetic mice.

A Hippocampal p-mTOR (Ser 2448), t-mTOR, and β-actin were subjected to western blot. **B** Hippocampal slides for IHC were immunostained with Rab5-specific antibody and counterstained with DAPI. Scale bars, 50 μm. **C** Hippocampal Rab5 and β-actin were subjected to western blot. **D** Hippocampal Aβ 1-42 were measured. **E** Mice were subjected to Y-maze test to evaluate cognitive function. $n = 5$. $^{*}p < 0.05$ vs. vehicle-treated mice, $^{\#}p < 0.05$ vs. STZ-treated mice.

DISCUSSION

The present study has revealed that high glucose facilitates early endosomal abnormalities through increasing APP endocytosis and impairment of endosomal clearance, which leads to the up-regulation of Aβ production (Figure 30). A previous paper had demonstrated that membrane cholesterol and lipid rafts are important factors for amyloidogenic APP endocytosis (Cheng *et al.,* 2007). High glucose-induced lipid raft reorganization has also been shown to facilitate BACE1 localization on lipid rafts, leading to increased Aβ production (Lee *et al.,* 2016). Consistent with these findings, I found that lipid rafts mediate APP endocytosis under high glucose conditions. In addition to lipid rafts, proteins involved in endocytosis are associated with the pathogenesis of AD (Alsaqati *et al.,* 2018) and DM (Teng *et al.,* 2016). My data showed that high glucose contributed to increases in PICALM, CHC, and AP2A1, through ROS-stimulated Sp1 activation. Levels of the long-form of PICALM (upper band) appear to be decreased compared to the short form, in Mithramycin-treated groups, and these levels were lower than those of the control. As Sp1 is a transcription factor that regulates PICALM expression, it would not have a significant effect on PICALM isoforms made via alternative splicing. Thus, differences in mRNA stability between the isoforms may be the reason for these findings. As all the isoforms increased under high glucose conditions, the differences in the isoform expression should not significantly affect overall outcome. Therefore, I suggest that

excessive production of endocytic proteins due to ROS-activated Sp1 are crucial molecular factors for APP endocytosis under high glucose conditions, leading to functional abnormalities. PICALM mediated APP endocytosis and Aβ generation in neural cell and PICALM knockdown decreased plaque deposition in APP transgenic mice (Xiao *et al.,* 2012). PICALM up-regulated Aβ generation by regulating clathrin-mediated endocytosis of γ-secretase (Kanatsu *et al.,* 2014) and β-secretase (Thomas *et al.,* 2016) in neural cell and Aβ was reduced in the Picalm$^{+/-}$ mouse brain (Kanatsu *et al.,* 2016). In addition, my data showed that PICALM facilitated APP endocytosis through the recruitment of CHC and AP2A1 to APP. On the other hand, PICALM-induced transendocytosis of Aβ in endothelial cells, which plays a role in Aβ clearance (Zhao *et al.,* 2015). These distinct functions of PICALM are probably achieved by specific signalling in different cell types but require further study. However, considering my finding that high glucose increased both Aβ and PICALM and the knockdown of PICALM decreased Aβ production, I suggest that targeting PICALM is an efficient strategy for the down-regulation of Aβ production.

A previous study reported that overexpression of the dominant inhibitory form of Rab5 in human adipocytes could mitigate pathophysiological changes in diabetes (Tessneer *et al.,* 2014). On the other hand, a study showed that *RAB5* knockdown in murine fibroblasts aggravated DM (Su *et al.,* 2006). Even if the effects of early endosomes on DM are still debatable, I showed that abnormalities in early

endosomes were induced in high glucose conditions. Consistent with my results, early endosomal enlargement was reported in diabetic monkey brain, which upregulated Aβ production (Okabayashi *et al.,* 2015). These findings indicate that the overactivation of early endosomes induced by high glucose may have a detrimental effect in AD. Persistent activation of an adaptor protein localized at early endosomes induced the activation of Rab5(Kim, Sato, *et al.,* 2016) and the mRNA (Ginsberg, Alldred, *et al.,* 2010) and protein levels (Ginsberg, Mufson, *et al.,* 2010) of Rab5 were upregulated in AD patients. My finding that increased APP endocytosis is the cause of endosomal disorders differs from previous studies, and this finding may be specific to diabetes. Although further studies on the expression and activity of other secretases associated with Aβ production in diabetes and its association with endosomal disorders are needed, my data show that high glucose increased Rab5 co-localization with both BACE1 and APP-CTFβ, which produced excess Aβ. Similarly, a previous study described that the overexpression of Rab5 increased the coincidence of APP-CTFβ and early endosomal compartments and Aβ generation (Grbovic *et al.,* 2003). Taking these findings together, I demonstrate that high glucose upregulates Aβ production through inducing abnormalities in early endosomes.

Early endosomes are degraded by the auto-lysosomal pathway. However, there is controversy over the changes in this degradative pathway in diabetes. DM increased autophagy in a STZ-induced mouse

model and primary cultured mouse hippocampal neurons through promotion of the JNK pathway (Kong *et al.,* 2018) and in mouse osteoblasts through inhibition of the mTORC1 pathway (Wang *et al.,* 2016). On the other hand, autophagy was impaired in diabetic beta-cells (Bartolome *et al.,* 2014) and in high glucose-treated human glomerular endothelial cells (Lim *et al.,* 2018) through hyper-activation of mTORC1. My results demonstrate that the impairment of autophagy was induced by the AMPK/mTORC1 signalling pathway under high glucose conditions. These findings indicate the different regulation of autophagy may depend on the cell type and preferentially involved mechanisms. Indeed, a previous study suggested that decreased activity of AMPK is a common characteristic for both DM and AD (Steinberg *et al.,* 2009). In addition, activation of AMPK protected hippocampal neurons against Aβ toxicity (Culmsee *et al.,* 2001). The post mortem brains from adults with AD-like pathology have high levels of mTORC1 and low levels of DEPTOR, the inhibitory protein of mTOR (Crino 2016). I showed that the inhibition of mTORC1 down-regulated high glucose-induced Rab5 protein expression and Aβ production. These results suggest that dysfunction of the mTORC1-mediated autophagy is a critical cause of AD pathology by causing defects in the clearance of early endosomes, in high glucose conditions. Meanwhile, destabilization of lysosomes was demonstrated in the hippocampus of DM mice (Sims-Robinson *et al.,* 2016). In accordance with these results, my data also indicated that high glucose

facilitated lysosomal dysfunction. Previous reports demonstrated that high glucose facilitated ROS-mediated increase of LMP (Abuarab *et al.,* 2017). Furthermore, severe DM accompanying mTORC1-mediated impairment of autophagy induced the defective clearance of lysosomes, lysophagy, which aggravated lysosomal dysfunction (Takahashi *et al.,* 2017). Indeed, my data showed that lysosomal dysfunction was induced by both ROS and mTORC1. Although there is a need for more precise study of the molecular mechanisms behind lysosomal dysfunction, my findings reveal that ROS and mTORC1-mediated lysosomal dysfunction aggravate the impairment of early endosomal clearance and upregulate Aβ production. Overall, I suggest that targeting the auto-lysosomal pathway is a promising strategy for reducing the amount of Aβ by enhancing the clearance of APP-producing early endosomes. My data showed that DM animal models also presented increased levels of early endosomes, which induced increased Aβ production and cognitive impairment. Although previous studies reported that treatment with an endocytosis blocker (Wang *et al.,* 2018) and rapamycin (Zhou *et al.,* 2009) restored cognitive impairment, the mechanisms underlying these processes had not been previously identified. I tested the relevance of APP-producing endosomes by applying pharmacological treatments to the diabetic STZ-treated mice. As the drugs did not act as insulin, they may have little effect on controlling hyperglycaemia induced by STZ. Thus, reducing Aβ without decreasing blood glucose may be used in

combination with conventional anti-diabetic drugs, providing synergistic effects on reducing levels of Aβ. The potential limitations to this study include that the behavior and rescue experiments were only performed in mice. I modified the experimental design as it was difficult to apply drugs that could have effects on the brain during the entire breeding period of ZLC and ZDF rats. However, my results showed that the expression levels of endolysosomal proteins were upregulated in both DM models. Based on the above findings, I suggest that the dysfunction of endocytosis and the auto-lysosomal pathway have detrimental effects on Aβ-producing endosomes in diabetes. Additionally, it is possible that early endosomal abnormalities are a common feature that facilitates AD pathology.

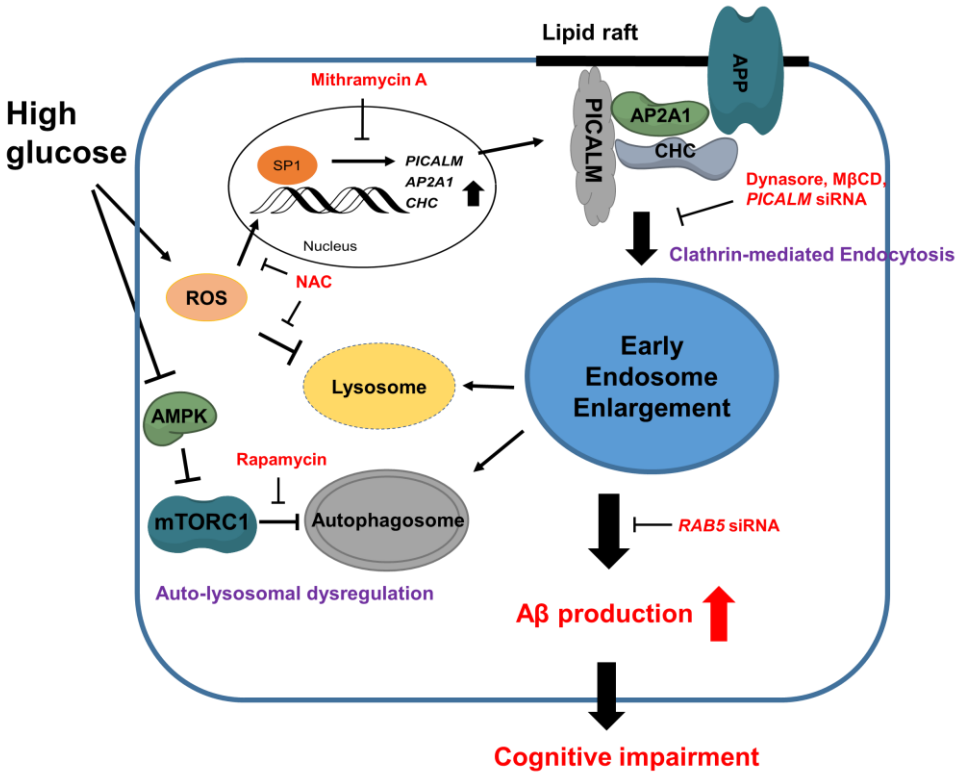

Figure 30. Diagram of the pathways underlying the up-regulation of A β production by abnormalities in early endosomes, under high glucose conditions.

High glucose increased PICALM, AP2A1, and CHC expression through ROS-stimulated Sp1 nuclear translocation. PICALM facilitates clathrin-mediated APP endocytosis at lipid rafts, which induces early endosomal enlargement. On the one hand, high glucose impairs endosomal clearance via AMPK/mTORC1- and ROS-mediated auto-lysosomal dysregulation. The consequences of early endosomal abnormalities are overproduction of Aβ and cognitive impairment.

CHAPTER Ⅱ

The effect of high glucose-mediated VPS26a downregulation on dysregulation of neuronal amyloid precursor protein processing and tau phosphorylation

Manuscript is published in *Br J Pharmacol*. 2022;179: 3934-3950

INTRODUCTION

The retromer, a protein complex involved in the retrograde transport of cargo from endosomes to the *trans*-Golgi network or recycling cargo from endosomes to the cell surface, has an important role in neuronal biology (Burd *et al.,* 2014). Impairment of endosomal sorting by retromer dysfunction causes synaptic disorders, neuroinflammation, and major pathological features of AD (Small *et al.*, 2015; Vagnozzi *et al.*, 2019). The retromer complex consists of a 'cargo recognition core (CRC)' composed of the vacuolar protein sorting-associated protein 35 (VPS35)/VPS26/VPS29 trimeric complex and sorting nexins (SNXs) (Burd *et al.*, Cullen 2014). A microarray profile revealed that VPS35 and VPS26 are down-regulated in the entorhinal cortex of AD patients (Small *et al.,* 2005). VPS35 is known to directly interact with β-secretase in mouse pyramidal neurons and early-onset AD-like phenotype can be induced by hemizygous deletion of VPS35 in the Tg2576 mouse model of AD (Wen *et al.,* 2011). Down-regulation of VPS35 in a mouse model of tauopathy exacerbated tau accumulation and cognitive impairment through regulation of cathepsin D (CTSD) availability (Vagnozzi *et al.,* 2021). VPS26a modulates APP trafficking and processing by binding the FANSHY motif of sortilin related receptor 1 (SORL1) (Cullen *et al.,* 2018). Both VPS35 and VPS26 are also reduced in the hippocampus of mouse models of type 2 diabetes (Morabito *et al.,* 2014). In addition, genome-wide

association studies have identified sortilin related VPS10 domain containing receptor 1 (SORCS1), a retromer-binding protein, as a major locus associated with both type 1 and type 2 diabetes pathogenesis (Paterson *et al.,* 2010; Clee *et al.,* 2006). Mice deficient in *Sorcs1* (Kebede *et al.,* 2014) and *Wiskott-Aldrich syndrome protein and SCAR homolog* (*Wash*) (Ding *et al.,* 2019), one of the other retromer-binding components, exhibited abnormal glycemic control. Retromers have been shown to be regulators in the pathogenesis of \DM, but no studies have investigated the role of retromer complex in DM-mediated AD pathogenesis, especially in APP processing and tau phosphorylation. Given that manipulation of retromer complex levels affects Aβ and p-Tau levels in human stem cell-derived neurons (Young *et al.,* 2018), retromer dysfunction in diabetes may provide mechanistic insights into AD pathogenesis.

In the present study, human induced-pluripotent stem cell-derived neuronal differentiated cells (iPSC-NDs) were used to investigate the effects of high glucose on the retromer complex and then to identify possible mechanisms related to APP processing and tau phosphorylation. SH-SY5Y neuroblastoma cells were used to study more detailed mechanisms. STZ-induced diabetic mice were used to elucidate whether the retromer contributes to the AD-like phenotype such as increased Aβ and p-Tau levels, synaptic deficits, astrocyte over-activation, and cognitive impairment. Together with both *in vitro*

and *in vivo* models, I investigated retromer-associated mechanisms and regulatory candidates of DM-mediated AD onset.

MATERIALS & METHODS

Animal studies

Male ICR mice (9 weeks of age) were acquired from OrientBio (Seongnam, Korea) and maintained in standard conditions with an appropriate humidity (less than 60%) and temperature (20-25℃) and a 12 h dark/12 h light cycle. They were given access to autoclaved chow and tap water on an ad libitum basis. Animal handling, care, and experimentation were performed in accordance with the regulations and ethical approval of the Institutional Animal Care and Use Committee of Seoul National University (Approval No.: SNU-201013-7-1). When designing animal experiments, it is critical to take sexes into account (Docherty *et al.,* 2019). However, male mice are practically used in previous diabetes researches (Rahman *et al.,* 2020; Ueda *et al.,* 2021), because the estrus cycle may affect the experimental conditions and results. Because the aim of my study is to investigate the effects of diabetes on the retromer and related dysregulation of mechanisms of APP processing and tau phosphorylation, male mice were used in the present study. Mice were randomly separated into equal-sized groups. Estimation of group size was undertaken in accordance with the rules

given by Seoul National University's Institutional Animal Care and Use Committee (SD: 6%, anticipated effect size: 15%, number of groups: 4; alpha: 0.05, power ($1-\beta$): 0.8). The number of animals employed was raised to account for the likelihood that not enough mice with the high glycaemic phenotype would be obtained. To examine the effect of high glucose on retromer dysfunction, STZ was injected into mice to create DM, as previously described (Furman 2015a). Mice were randomly assigned to receive STZ (75 mg · kg^{-1}) in sodium citrate buffer (0.1 M, pH 4.5, Vehicle, 200 μL) or vehicle intraperitoneally once daily for three consecutive days. Blood samples (50 μL) were taken via the tail vein without anaesthesia, and blood was drawn 3 times per animal (9, 18 weeks of age, and after STZ injection) before terminal sampling. Blood glucose level was determined using a glucose monitor (Roche, Germany), and body weight was determined prior to and after STZ injection. Mice with blood glucose levels above 300 mg dl were considered to be severely diabetic. After obtaining a sufficient number of diabetic mice, they were randomly separated into four groups (n = 5 per group): vehicle-injected mice, STZ-injected mice, R33-injected mice, and STZ with R33-injected mice. R33 injection was conducted as previously reported, with slight modifications (Li *et al.,* 2020). IP injection was used to deliver 100 μL of R33 (12.5 mg · kg^{-1}, dissolved in distilled water) and vehicle. For 8 weeks following DM induction, R33 was injected once daily. Body weight and blood glucose levels were measured at 9 and 18 weeks of age (Figure 31A). After

behavior testing, mice were anaesthetized by IP injection of alfaxalone (40 mg · kg^{-1}) with 10 mg · kg^{-1} xylazine and killed by exsanguination for further biochemical analysis. An overall schematic of experiments is shown in the Figure 31B.

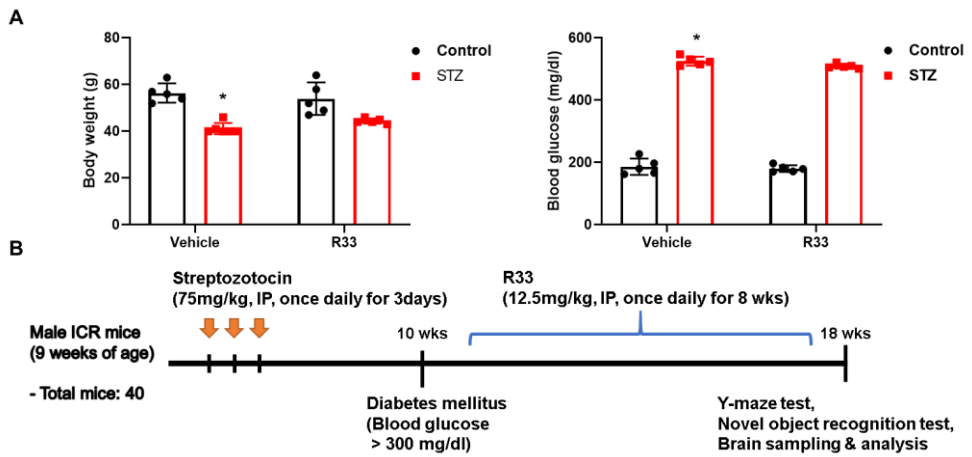

Figure 31. Body weight and blood glucose of experimental animals, and scheme of an *in vivo* experimental protocol using R33 treatment.

A Blood glucose and body weight were determined at 18 weeks of age. $n = 5$. $^{*}p < 0.05$ vs. vehicle. B The scheme of *in vivo.*

Y-maze spontaneous alternation test

The detailed method for Y-maze spontaneous alternation test is elucidated in Materials & Methods section of Chapter Ⅰ.

Novel object recognition (NOR) test

The novel object recognition test is a commonly used mouse behavior test for assessing object working memory and depends on the innate preference of mice for novelty. The mice were kept in an open field box for 5 min in the testing room for habituation. After 24 h, the mice were allowed to navigate freely for 10 min in the same open field with two similar objects during the first session. After 4 h, one of the two objects was replaced with a new one, then the mouse was allowed to explore freely for 10 min in the open field for a second session. The discrimination index which is the most commonly used value for assessing cognition was calculated as the time spent exploring a new object minus the time spent exploring a familiar object divided by the total exploration time. The novelty preference was calculated as the time spent exploring a novel object as a percentage of the total exploration time. An increase in the discrimination index indicated an improvement in cognitive memory (Lueptow 2017).

IHC

The detailed method for IHC is elucidated in Materials & Methods section of Chapter Ⅰ. Image analysis was performed with the Fiji software (RRID:SCR_002285) (Schindelin *et al.,* 2012). Measurement of signal intensities was conducted by applying the same threshold. IHC has been conducted the experimental detail provided conforms with BJP Guidelines (Alexander *et al.,* 2018).

iPSC-derived neuronal differentiation

To induce neuronal stem cells (NSCs), iPSCs were grown on plates covered with recombinant human vitronectin (Thermo Fisher, Waltham, USA, A14700) in the presence of neural induction media (A1647801, Thermo Fisher). Following NSC induction, the cells were re-cultured on dishes coated with poly-L-ornithine (Sigma, Massachusetts, USA, P3655) and laminin (Thermo Fisher, 23017). For more than 10 days, the NSCs were grown in neural differentiation media [Neurobasal medium (Thermo Fisher, 21103) supplemented with 2% B27 serum-free supplement (Thermo Fisher, 17504) and 1% GlutaMax-1 supplement (Thermo Fisher, 35050)]. Between 7 and 10 days after the initiation of differentiation, 0.5 mM dibutyryl-cAMP (Sigma, D0627) was given daily to the medium to enhance neural differentiation.

Cell cultivation

Undifferentiated SH-SY5Ys were grown at 37° C with 5% CO_2 in low glucose Dulbecco's modified Eagle's medium (DMEM) (Hyclone, Logan, USA, SH30021FS), 1% antibiotic-antimycotics, and 10% FBS(Liebsch *et al.,* 2019; Rodriguez *et al.,* 2020). The detailed method for cell cultivation is elucidated in Materials & Methods section of Chapter Ⅰ.

Plasmid DNA transfection

After reaching 60% confluence, the SH-SY5Ys were cultured for 24 h with a plasmid DNA mixture, low glucose DMEM, and lipofectamine 2000 (Thermo Fisher, 11,668,027). The cells were incubated in the serum-free medium with 1% antibiotics prior to experiments. pcDNA3.1-eGFP plasmid was used as a negative control. The cells were transfected before being exposed to high glucose.

Transfection with siRNA for gene silencing

The detailed method for transfection with siRNA for gene silencing is elucidated in Materials & Methods section of Chapter Ⅰ.

Immunofluorescence analysis

The detailed method for immunofluorescence analysis is elucidated in Materials & Methods section of Chapter Ⅰ. Immuno-stained cells were visualized by a super-resolution radial fluctuations (SRRF) imaging system (Andor Technology, Belfast, UK) (Gustafsson *et al.,* 2016) and a confocal microscope system (LSM 710, Carl Zeiss, Oberkochen, Germany). Fluorescent intensities quantification and measurement of the area of $Rab5^{+}$ endosomes were carried out with Fiji software. Analysis of co-localization was performed by measuring manders coefficients using Fiji's JACop plugin(Bolte *et al.,* 2006).

Marking and staining lysosomes

The detailed method for marking and staining lysosomes are elucidated in Materials & Methods section of Chapter Ⅰ. The signals of Lysotracker stained cells were visualized by a confocal microscope system (LSM 710, Carl Zeiss, Oberkochen, Germany).

qPCR

The detailed method for qPCR is elucidated in Materials & Methods section of Chapter Ⅰ. The cDNAs were amplified using a variety of mRNA primers (Table 4)

Table 4. The primer sequences used for real-time qPCR.

Gene	Forward primer	Reverse primer
VPS26B	TTCAAGCAGCAGGAAGTGGT	TTGTTGTCAGACAGCTGGCT
VPS29	TCTCGGGACACACACACAAA	ACCACTGTAGAAGCCTGGAT
SNX1	CGGAAACTGCATGCTGTTGT	AATGCCGTGTTGTCCTCAGA
SNX2	ATATTGTGCCACCAGCTCCA	TCAAGAGCTGCTCTCCGTTT
SNX3	AAGCGTTTTTGCGTCAGCTT	TGCTCCAGCCCTTGTTTTCT
SNX5	AGGCCCGGTTAAAGAGCAAA	TGCCACTCTCTTCCGTTTGA
SNX6	TGCTCTGCAGGTGGACATTT	TGCCGAACAACTGAAAACTCG
SNX27	AGCAGGCGAGAAGGAATTGA	ATTGTCCCAACGAGTCGTCA
DNMT1	TGAGGCCTTCACGTTCAACA	TCCAGGTTGCTGCCTTTGAT
DNMT3A	TGCCGGAACATTGAGGACAT	TGGCACATTCCTCCAACGAA
DNMT3B	ACGTCGCTTCTGAAGTGTGT	TCCGCCAATCACCAAGTCAA
TET1	ACGTGTTTCACTCAGCCTGT	TTCCGCTTGATTCGGGGAAT
TET2	TCCCCAGTGTTGAAACAGCA	ATGGTTGTGTTTGTGCTGCC
TET3	AGCTGTGGAACCCCATGA AA	TTCAGAGCCCCAAACAGCTT
ACTB	AACCGCGAGAAGATGACCCA GATCATGTTT	AGCAGCCGTGGCCATCTCTT GCTCGAAGTC

Western blot analysis & subcellular fractionation

The detailed method for western blot analysis & subcellular fractionation are elucidated in Materials & Methods section of Chapter Ⅰ.

Dot blot analysis

Dot blot analysis was carried out to detect DNA methylation levels in SH-SY5Ys. The genomic DNA (gDNA) was extracted by using

genomic DNA extraction kit (Bioneer, K-3032). As described previously (Jiang *et al.,* 2019), 100 ng of gDNA was denatured for 10 min at 95° C, then neutralized for 10 min on ice. gDNA was loaded on the N+ nylon membrane (Amersham, RPN203B). The membrane was dried and incubated for 2 h at 80° C. The membrane was blocked with 5% skim milk for 1 h and incubated overnight at 4° C with anti-5-mC antibody. The membrane was washed 3 times with TBST, then incubated with HRP-conjugated secondary antibody for 2 h at RT. DNA was detected by chemiluminescence detection kit (Advansta Inc., K-12045-D50). Quantification of the dot blot intensity was performed by the Image J software.

Methylation specific PCR (MSP)

The conversion of gDNA for methylation analysis was performed by bisulfite treatment using the EZ DNA methylation-lightning kit and following the manufacturer's instructions (Zymo Research, D5030). The methylation status of the *VPS26A* gene in the SH-SY5Ys was determined by MSP. I conducted MSP for the *VPS26A* promoter at two CpG sites (-118 and -346) which were designed by referring to the previous reports(Bell *et al.,* 2010; Nilsson *et al.,* 2014; Li *et al.,* 2002). Methylation status was assessed by relative methylation levels compared to unmethylated form. The primer sequences for each CpG

site of the *VPS26A* promoter are listed in the Table 5.

Table 5. The primer sequences used for methylation specific primer.

Gene	Forward primer	Reverse primer
Methylated *VPS26A* (CpG sites: -181)	GAGTTTGAGGTTTCGTTTTTAAGC	CAAACCCAAAAATAACCCGA
Unmethylated *VPS26A* (CpG sites: -181)	GAGTTTGAGGTTTTGTTTTTAAGTG	CCAAACCCAAAAATAACCCA
Methylated *VPS26A* (CpG sites: -346)	ATTTAGATTTAGAAGGAGGTGGAGC	TAAATCCTTAAATTACCGAAACGAA
Unmethylated *VPS26A* (CpG sites: -346)	TTTAGATTTAGAAGGAGGTGGAGTG	TAAATCCTTAAATTACCAAAACAAA

CTSD activation assay

CTSD activity was measured by using Cathepsin D activity fluorometric assay kit (abcam, K143-100). Assay was performed in compliance with manufacturer's protocol Briefly, harvested cells were lysed by proper lysis buffer on ice for 10 min and centrifuged for 5min at top speed. The equal amount of lysate was loaded into 96-well plate with reaction buffer and substrate, then incubated at 37° C for 2 h. Fluorescence intensities were read by fluorometer equipped with a 328-nm excitation/460-nm emission filter.

Measurement of Aβ in *in vitro* and *in vivo* samples

In *in vitro*, the cell culture was collected and centrifuged at 1,000 × g for 20 min. phosphatase inhibitors cocktail (100X) was added to the

supernatant to inhibit proteolysis. In *in vivo*, the equal amount of the hippocampus samples (100 μg) were prepared with lysis buffer and BCA assay. In compliance with the manufacturer's instructions, the optical density (OD) of Aβ (1- 42) in culture medium and tissue samples were obtained by using human Aβ (1- 42) ELISA kit (Thermo Fisher, KHB3544) and mouse & rat Aβ (1- 42) ELISA kit (Thermo Fisher, KMB3441), respectively. The absorbance at 450 nm were converted into the concentration and analyzed by using the standard curve.

Data and analysis

The manuscript complies with BJP's recommendation on experimental design and analysis(Curtis *et al.,* 2018). Through the use of randomization and blinded analysis, studies were meant to establish groups of equal size. Statistical analysis was performed on studies with a minimum group size of n = 5. The sample size n defined the number of biologically independent replicates utilized for statistical analysis. I tested for outliers beyond an outer boundary (Q3 + 3IQ or Q1 − 3IQ) in a box plot and found none. The Shapiro–Wilk test was used to determine the normality of all data, which was then analysed using parametric statistics. To compare the treatment and control group means, an unpaired Student's t−test with two−tailed was performed. To compare the differences among several groups, One−way ANOVA

or Two-way ANOVA were utilised. Post hoc tests were done only if ANOVA revealed a significant F and no significant variance inhomogeneity. Spearman's test was used to determine the sample's heteroscedasticity, and logarithmic or square root transformations were used if the variance did not match the homogeneity requirement. Quantitative data are presented as a mean and standard deviation (SD) and analysed using the Prism 8 software (Graphpad, USA, RRID:SCR_000306). A level of probability of $p < 0.05$ was taken as statistically significant.

Materials

The iPSCs and human neuroblastoma cell line SH-SY5Y were purchased from Kangstem Biotech (Seoul, Korea) and Korean Cell Line Bank (Seoul, Korea), respectively. Fetal bovine serum (FBS) and antibiotics were obtained by Hyclone (Logan, UT, USA) and Gibco (Grand Island, NY, USA) respectively. The antibodies of β-Actin (sc-47778), lamin A/C (sc-2068), VPS35 (sc-374372), VSP26a (sc-390304), VPS29 (sc-398874), NF-κB p65 (sc-8008), EEA1 (sc-365652), TGN38 (sc-166594), PP2A (sc-80665), GSK-3β (sc-9166), Phospho-GSK 3β Ser 9 (sc-9166), and CTSD (sc-13148) were acquired from Santa Cruz Biotechnology (Santa Cruz, CA, USA). The antibodies of VPS26a (MA5-31365), VPS26b (PA5-101953), CI-MPR (PA3-850), Tau 5 (AHB-0042), PSD95 (51-

6900), α-tubulin (T6074), and NeuN (MA5-33103) were purchased from Thermo Fisher (Waltham, MA, USA). respectively. The antibodies of Rab5 (NB120-13253), SORCS1 (NBP 1-86096), and WASHC1 (NBP 1-90464) were obtained from Novus Biologicals (Centennial, CO, USA). The antibodies of SORL1 (79322), 5-mC (D3S2Z), p35/25 (C64B10), and Phospho-Tau Thr181 (12885) were acquired from Cell Signaling Technology (Beverly, MA, USA). The antibodies of APP (ab32136), Phospho-Tau Ser396 (ab109390), DNMT1 (ab19905), DNMT3a (ab23565), DNMT3b (ab16049), CTSD (ab6313), GFAP (ab7260), synaptophysin (ab32127), and MAP2 (ab11267) were purchased from Abcam (Cambridge, England). VPS35 (GTX108058) antibody was purchased from Genetex (Irvine, CA, USA). Secondary antibodies for anti-mouse Alexa Fluor 647 (A-21235), anti-mouse Alexa Fluor 488 (A32723), anti-rabbit Alexa Fluor 555 (A32732), anti-mouse Alex Fluor 555 (A32727), and Lysotracker Red DND-99 (L7528) were obtained from Thermo Fisher (Waltham, MA, USA). NAC (A7250), D-glucose (G8769), L-glucose (G5500), Pepstatin A (P5318), Thioflavine S (T1892), DAPI (D9542), Bay 11-7082 (196870), normal goat serum (NGS; 566380), and STZ (S0130) were purchased from Sigma Chemical Company (St. Louis, MO, USA). TPT-172 (R33) (504211) was obtained from MedKoo Biosciences (Morrisville, NC, USA). pcDNA3.1(+)-VPS26A-eGFP and pcDNA3.1(+)-eGFP were purchased from Koma Biotech (Seoul, Korea). mRNA primers for *VPS26B, VPS29, SNX1, SNX2, SNX3,*

SNX5, SNX6, SNX27, DNMT1, DNMT3A, DNMT3B, TET1, TET2, TET3, ACTB, and primers for CpG site of *VPS26A* were purchased from Cosmo Genetech (Seoul, Korea). mRNA primers for *VPS35*, *VPS26A*, *SORCS1*, *SORT1*, *SORL1*, and siRNAs for *DNMT1* was acquired from Bioneer (Daejeon, Korea). Non-targeting (NT) siRNA was purchased from Dharmacon (Lafayette, CO, USA).

RESULTS

VPS26a is down-regulated in STZ-diabetic mice and neuronal cells exposed to high glucose

To elucidate the effect of diabetes on retromer assembly, I first measured hippocampal levels of VPS35, VPS26a, VPS26b, VPS29, SORCS1, SORL1, and WASH Complex Subunit 1 (WASHC1). Among these retromer components, only the protein levels of VPS26a were decreased in STZ-induced diabetic mice compared with those of vehicle-treated mice (Figure 32A). STZ-induced diabetic mice also had lower staining intensities of hippocampal VPS26a than those of vehicle-treated mice (Figure 32B). In *in vitro* experiments, iPSC-NDs exposed to high glucose showed only down-regulated VPS26a (Figure 33A). In SH-SY5Ys, high glucose also decreased mRNA expression and protein levels of VPS26a after 12 h (Figure 33B, C). Only D-glucose treatment, not L-glucose treatment, decreased VPS26a

protein levels in cells, which implies that osmotic effects were not involved in protein down-regulation (Figure 33D). As recruitment of retromer complexes to endosomes is essential for CRC-mediated cargo transport (Seaman 2012), I measured the recruitment of VPS35 binding cargo directly to early endosomes to investigate the effect of high glucose on retromer function. Compared with normal glucose treated cells, high glucose treatment decreased the degree of co-localization between Rab5, an early endosomal marker and VPS35 in iPSC-NDs (Figure 33E). These results suggest that high glucose down-regulates expression of VPS26a, which induces retromer dysfunction.

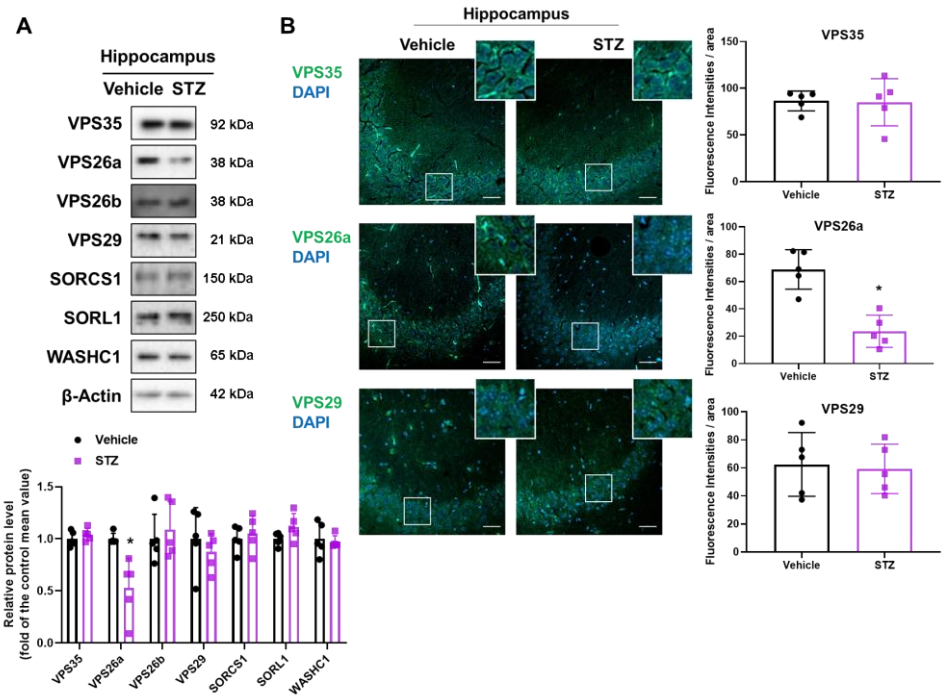

Figure 32. VPS26a is down-regulated in the hippocampus of STZ-diabetic mice.

A, B Samples were obtained from Vehicle-or STZ-treated mice hippocampus. **A** VPS35, VPS26a, VPS26b, VPS29, SORCS1, SORL1, WASHC1, and β-Actin were detected by western blot. **B** Tissue slides for IHC were immunostained with VPS35, VPS26a, and VPS29-specific antibodies and counterstained with DAPI. Scale bars, 20 μm. $n = 5$. $^{*}p < 0.05$, $^{**}p < 0.01$ vs. control.

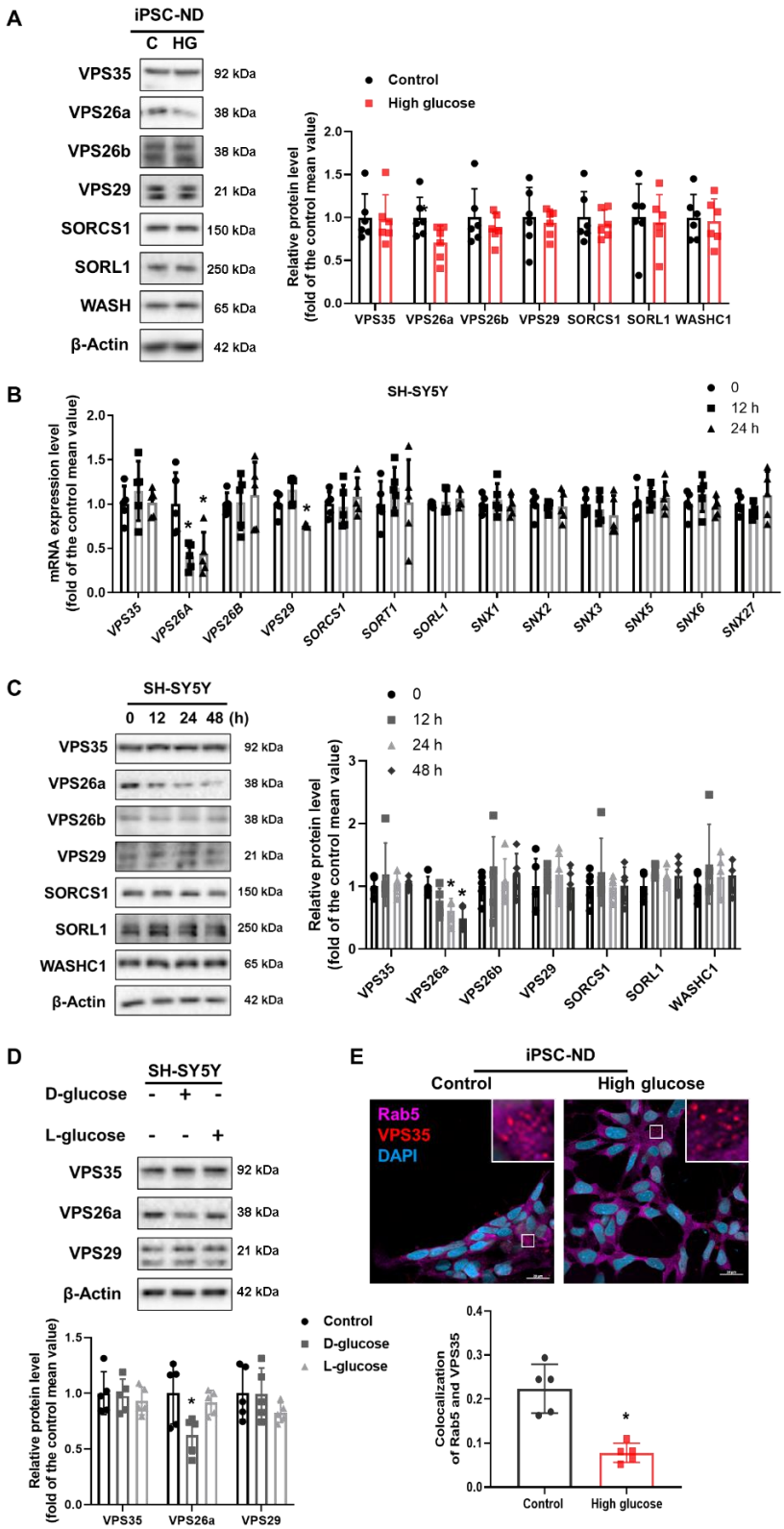
A
iPSC-ND
C HG
VPS35 92 kDa
VPS26a 38 kDa
VPS26b 38 kDa
VPS29 21 kDa
SORCS1 150 kDa
SORL1 250 kDa
WASH 65 kDa
β-Actin 42 kDa
Control
High glucose
Relative protein level (fold of the control mean value)
VPS35 VPS26a VPS26b VPS29 SORCS1 SORL1 WASHC1
B
SH-SY5Y
0
12 h
24 h
mRNA expression level (fold of the control mean value)
VPS35 VPS26A VPS26B VPS29 SORCS1 SORT1 SORL1 SNX1 SNX2 SNX3 SNX5 SNX6 SNX27
C
SH-SY5Y
0 12 24 48 (h)
VPS35 92 kDa
VPS26a 38 kDa
VPS26b 38 kDa
VPS29 21 kDa
SORCS1 150 kDa
SORL1 250 kDa
WASHC1 65 kDa
β-Actin 42 kDa
0
12 h
24 h
48 h
Relative protein level (fold of the control mean value)
VPS35 VPS26a VPS26b VPS29 SORCS1 SORL1 WASHC1
D
SH-SY5Y
D-glucose - + -
L-glucose - - +
VPS35 92 kDa
VPS26a 38 kDa
VPS29 21 kDa
β-Actin 42 kDa
Control
D-glucose
L-glucose
Relative protein level (fold of the control mean value)
VPS35 VPS26a VPS29
E
iPSC-ND
Control
High glucose
Rab5
VPS35
DAPI
Colocalization of Rab5 and VPS35
Control
High glucose

Figure 33. VPS26a is down-regulated in neuronal cell exposed to high glucose.

A, C iPSC-NDs or SH-SY5Ys were treated with D-glucose (25 mM) for 24 h. Then, VPS35, VPS26a, VPS26b, VPS29, SORCS1, SORL1, WASHC1, and β-Actin were detected by western blot. $n = 5$. **B** SH-SY5Ys were treated with high glucose (25 mM) in a time dependent manner. The mRNA expression levels of *VPS35*, *VPS26A*, *VPS26B*, *VPS29*, *SORCS1*, *SORT1*, *SORL1*, *SNX1*, *SNX2*, *SNX3*, *SNX5*, *SNX6,* and *SNX27* were analyzed. **D** The SH-SY5Ys were treated with D-glucose (25 mM) or L-glucose (25 mM) for 24 h. VPS35, VPS26a, VPS29, and β-Actin were detected. **E** iPSC-NDs were treated with high glucose (25 mM) for 24 h which were immunostained with Rab5 and VPS35-specific antibodies and counterstained with DAPI. Scale bars, 20 μm. $n = 5$. $^{*}p < 0.05$ vs. control.

High glucose down-regulates VPS26a through ROS/NF-κB/DNMT1-mediated promoter hypermethylation.

Given that diabetes-mediated genetic repression is mainly caused by epigenetic downregulation (Kato *et al.,* 2019), I focused on the expression changes of epigenetic regulators to investigate how high glucose down-regulates VPS26a. First, I examined the changes in the mRNA expression levels of DNA methyltransferases, enzymes that methylate DNA, including DNMT1, DNMT3A, DNMT3B, and ten-eleven translocation methylcytosine dioxygenases, enzymes that demethylate DNA, such as TET1, TET2, and TET3. Among them, only the mRNA expression of DNMT1 was increased by high glucose (Figure 34A). The protein levels of DNMT1 also increased in a time-dependent manner upon high glucose treatment (Figure 34B). STZ-induced diabetic mice had higher hippocampal DNMT1 levels compared with those of vehicle-treated mice (Figure 34C). As ROS are known to stimulate NF-κB (Morgan *et al.,* 2011), which may upregulate DNMT1 expression, I investigated whether high glucose-stimulated nuclear translocation of NF-κB could be blocked by NAC (a ROS scavenger) (Figure 34D). The mRNA expression (Figure 34E) and protein (Figure 34F) levels of DNMT1 increased by high glucose were also reduced by Bay 11-7082 (an NF-κB inhibitor). These results suggest that the ROS-stimulated NF-κB pathway upregulates DNMT1 expression in high glucose conditions. To elucidate the

relationship between high glucose-mediated-DNMT1 and VPS26a down-regulation, I first determined global DNA methylation status by measuring 5-mC staining intensities in cells exposed to high glucose. High glucose-mediated increase of 5-mC staining intensities was reduced by DNMT1 silencing (Figure 35A, B). I further measured the specific methylation status of the VPS26A promoter containing two CpG sites, at -118 and -346. As shown in Figure 35C, D cells transfected with NT siRNA in high glucose increased the levels of *VPS26A* promoter methylation at -118 and -346 compared with those of cells transfected with NT siRNA in normal glucose conditions. Interestingly, *DNMT1* silencing reduced high glucose-mediated hypermethylation of the *VPS26A* promoter. Furthermore, down-regulated mRNA (Figure 35E) and protein (Figure 35F) expression levels of VPS26a in high glucose were reversed by *DNMT1* silencing. These data indicate that upregulated DNMT1 by high glucose suppressed VPS26a expression through hypermethylation of the *VPS26A* promoter.

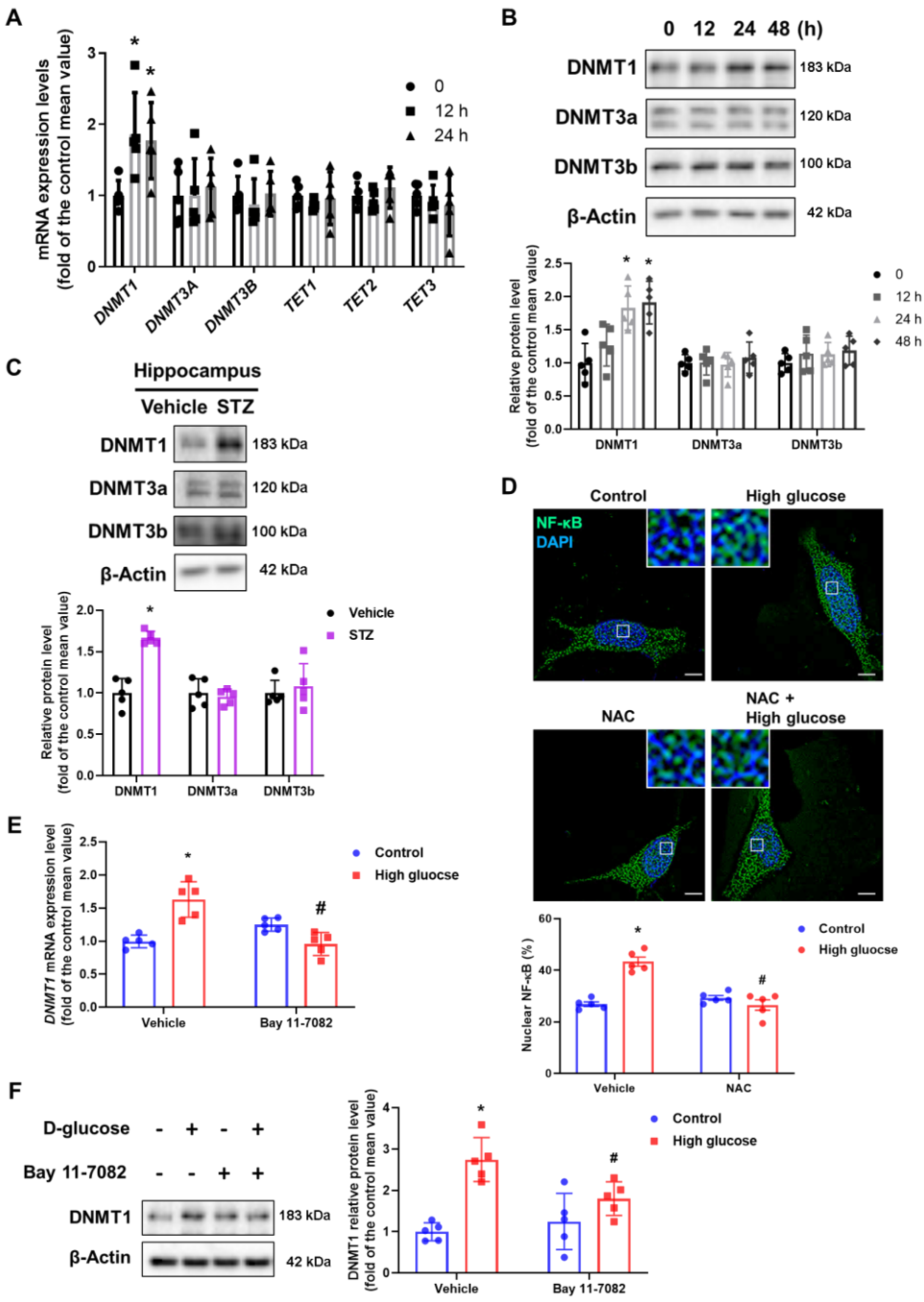
A
mRNA expression levels (fold of the control mean value)
0
12 h
24 h
DNMT1
DNMT3A
DNMT3B
TET1
TET2
TET3
B
0 12 24 48 (h)
DNMT1
DNMT3a
DNMT3b
β-Actin
183 kDa
120 kDa
100 kDa
42 kDa
Relative protein level (fold of the control mean value)
0
12 h
24 h
48 h
C
Hippocampus
Vehicle STZ
Vehicle
STZ
D
Control
High glucose
NF-κB
DAPI
NAC
NAC +
High glucose
Nuclear NF-κB (%)
E
DNMT1 mRNA expression level (fold of the control mean value)
Control
High gluocse
Vehicle
Bay 11-7082
F
D-glucose
Bay 11-7082
DNMT1 relative protein level (fold of the control mean value)

Figure 34. High glucose upregulates DNMT1 through ROS/NF-κB signaling pathway.

A, B SH-SY5Ys were treated with high glucose (25 mM) in a time dependent manner. A The mRNA expression levels of *DNMT1*, *DNMT3A*, *DNMT3B*, *TET1*, *TET2*, and *TET3* were analyzed. **B** DNMT1, DNMT3a, DNMT3b, and β-Actin were detected. **C** The hippocampal samples were obtained from vehicle-or STZ-treated mice. DNMT1, DNMT3a, DNMT3b, and β-Actin were detected by western blot. $n = 5$. **D** The cells were incubated with NAC (4 mM) for 30 min prior to high glucose treatment (25 mM) for 12 h. The cells were immunostained with NF-κB-specific antibody and counterstained with DAPI. Scale bars, 3 μm. $n = 6$. **E, F** The cells were treated with Bay 11-7082 (10 μM) for 30 min prior to high glucose treatment (25 mM) for 24 h. The mRNA expression and protein levels of DNMT1 were analyzed by qPCR and western blot, respectively. $n = 5$. $^{*}p < 0.05$ vs. control, $^{\#}p < 0.05$, vs. high glucose.

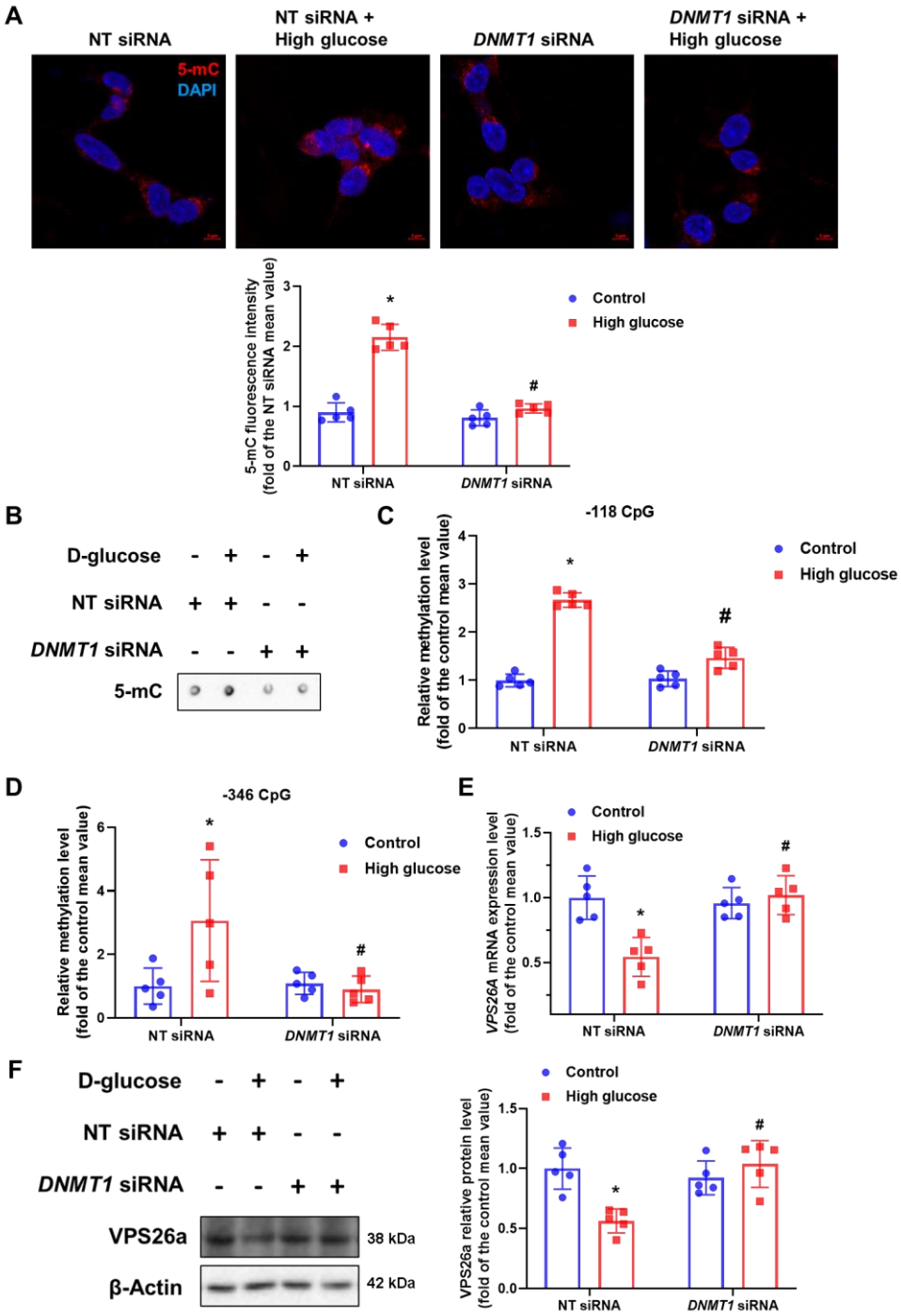
A
NT siRNA
NT siRNA +
High glucose
DNMT1 siRNA
DNMT1 siRNA +
High glucose
5-mC
DAPI
5-mC fluorescence intensity
(fold of the NT siRNA mean value)
Control
High glucose
NT siRNA
DNMT1 siRNA
B
D-glucose - + - +
NT siRNA + + - -
DNMT1 siRNA - - + +
5-mC
C
-118 CpG
Relative methylation level
(fold of the control mean value)
D
-346 CpG
E
VPS26A mRNA expression level
(fold of the control mean value)
F
VPS26a
β-Actin
38 kDa
42 kDa
VPS26a relative protein level
(fold of the control mean value)

Figure 35. DNMT1-mediated promoter hypermethylation down-regulates VPS26a under high glucose conditions.

A-F SH-SY5Ys were transfected with NT siRNA or *DNMT1* siRNA for 12 h prior to high glucose treatment (25 mM) for 24 h. **A** The cells were immunostained with 5-mC-specific antibody and counterstained with DAPI. Scale bars, 5 μm. **B** The expression levels of 5-mC in cellular gDNA were detected. Logarithmic transformation was performed. **C, D** The methylation status at the -118 and -346 CpG sites of the *VPS26A* gene of gDNA was determined by MSP analysis. The relative methylation level of *VPS26A* is shown, compared to the unmethylated form. **E, F** The mRNA and protein expression levels of VPS26a were analyzed by qPCR and western blot, respectively. $n = 5$. $^{*}p < 0.05$ vs. control, $^{\#}p < 0.05$ vs. high glucose.

High glucose-induced retromer dysfunction increases APP and p-Tau levels

To investigate the effects of retromer dysfunction on high glucose-mediated amyloidogenesis and tau phosphorylation, I used R33, a pharmacological chaperone, to stabilize and recover retromer function (Mecozzi *et al.,* 2014). Treatment of R33 recovered high glucose-mediated downregulation of VPS26a (Figure 36A). Recovered retromer by R33 treatment decreased the size of early endosomes (Morel *et al.,* 2013), the earliest pathological features of AD (Kwart *et al.,* 2019), in iPSC-NDs exposed to high glucose (Figure 36B). Given that high glucose modulates APP processing in abnormal early endosomes (Chae *et al.,* 2020), R33 could normalize the APP process. Increased APP, C99, and Aβ were recovered by R33 under high glucose conditions in iPSC-NDs (Figure 36C, D). As the degradation of phosphorylated tau was regulated by retromer-mediated CTSD maturation, the retromer might therefore be involved in tau phosphorylation in diabetes. I found that R33 treatment down-regulated tau phosphorylation at Ser396 and Thr181 in iPSC-NDs exposed to high glucose (Figure 36E). These findings suggest that retromer dysfunction is involved in APP processing and tau phosphorylation in high glucose conditions.

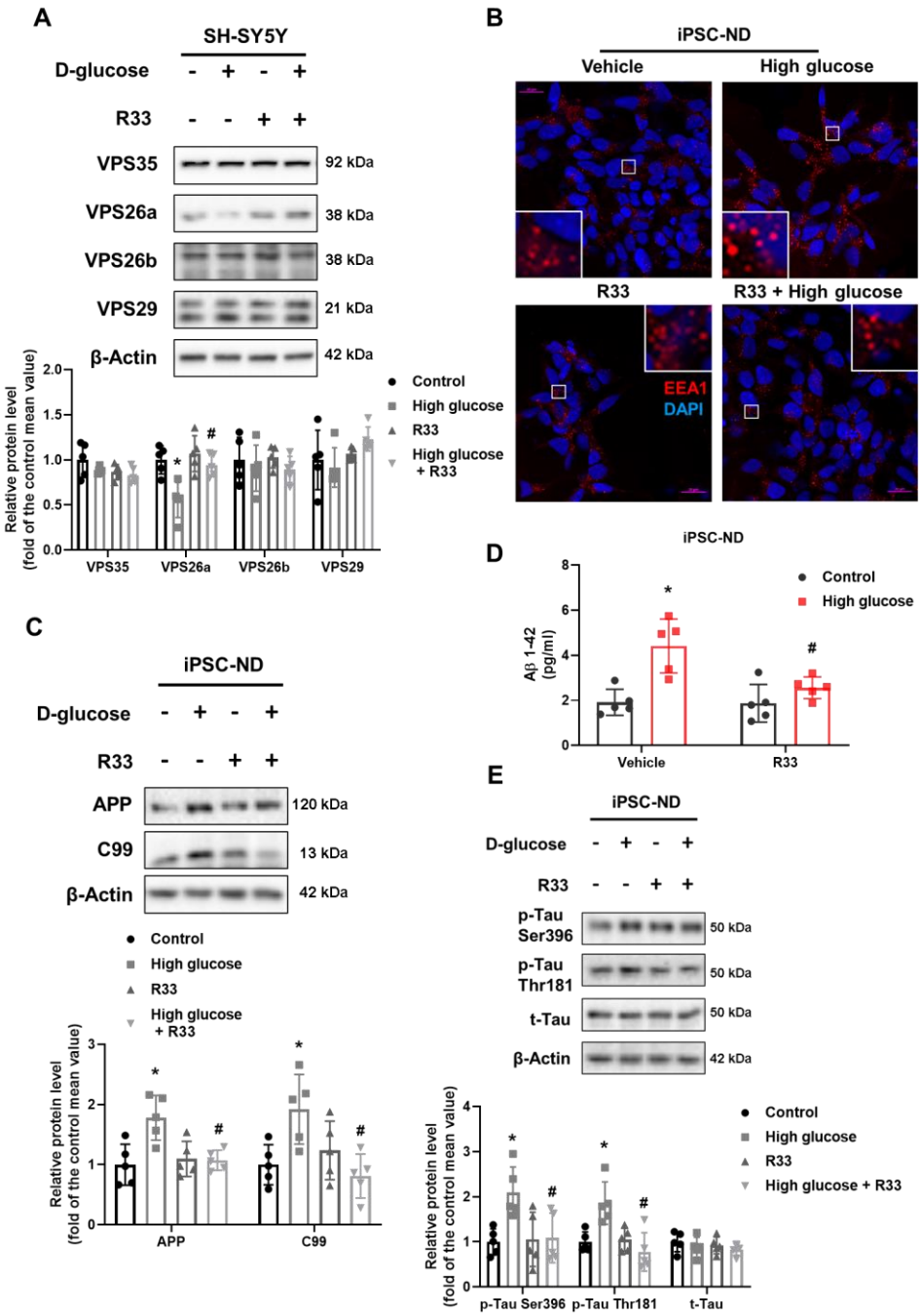

Figure 36. R33 blocks elevated Aβ and p-Tau levels by high glucose.

A–C, E The cells were treated with R33 (5 μM) for 30 min prior to high glucose treatment (25 mM) for 24 h. **A** VPS35, VPS26a, VPS26b, VPS29, and β–Actin were detected. **B** iPSC–NDs were immunostained with EEA1–specific antibody and counterstained with DAPI. Scale bars, 20 μm. **C** The protein expression levles of APP, C99, and β–Actin in were detected by western blot. $n = 5$. **D** The cells were treated with R33 (5 μM) for 30 min prior to high glucose treatement (25 mM) for 48 h. Aβ 1–42 from cell culture medium in iPSC–NDs were measured. **E** The protein expression levles of p–Tau Ser396, p–Tau Thr181, t–Tau, and β–Actin in iPSC–NDs were detected by western blot. $n = 5$. $^{*}p < 0.05$ vs. control, $^{\#}p < 0.05$ vs. high glucose.

High glucose-mediated downregulation of VPS26a increases retention of APP in the early endosomes

In order to elucidate how the retromer complex modulates APP processing, I measured the localization of APP to the early endosomes and *trans*-Golgi (Wen *et al.,* 2011). In iPSC-NDs, high glucose increased co-localization of APP and EEA1, an early endosomal marker, which was reversed by R33 (Figure 37A). The co-localization of APP and TGN38, a *trans*-Golgi marker, decreased in high glucose, and was recovered by R33 treatment (Figure 37B). To focus on the effect of VPS26a in high glucose, I overexpressed VPS26A by pcDNA3.1-VPS26A-eGFP transfection in SH-SY5Ys. The co-localization of APP and EEA1 increased in high glucose treated-cells with control pcDNA3.1-eGFP transfection was decreased by VPS26a overexpression (Figure 38A). The co-localization of APP and TGN38 in high glucose treated-cells with VPS26a overexpression was higher than that of high glucose treated-cells with control pcDNA3.1-eGFP transfection (Figure 38B). VPS26a overexpression down-regulated high glucose-mediated increases of APP, C99, and Aβ levels (Figure 38C, D). These results suggest that high glucose-mediated downregulation of VPS26a alters APP processing by impairing APP movement from the early endosome to the *trans*-Golgi.

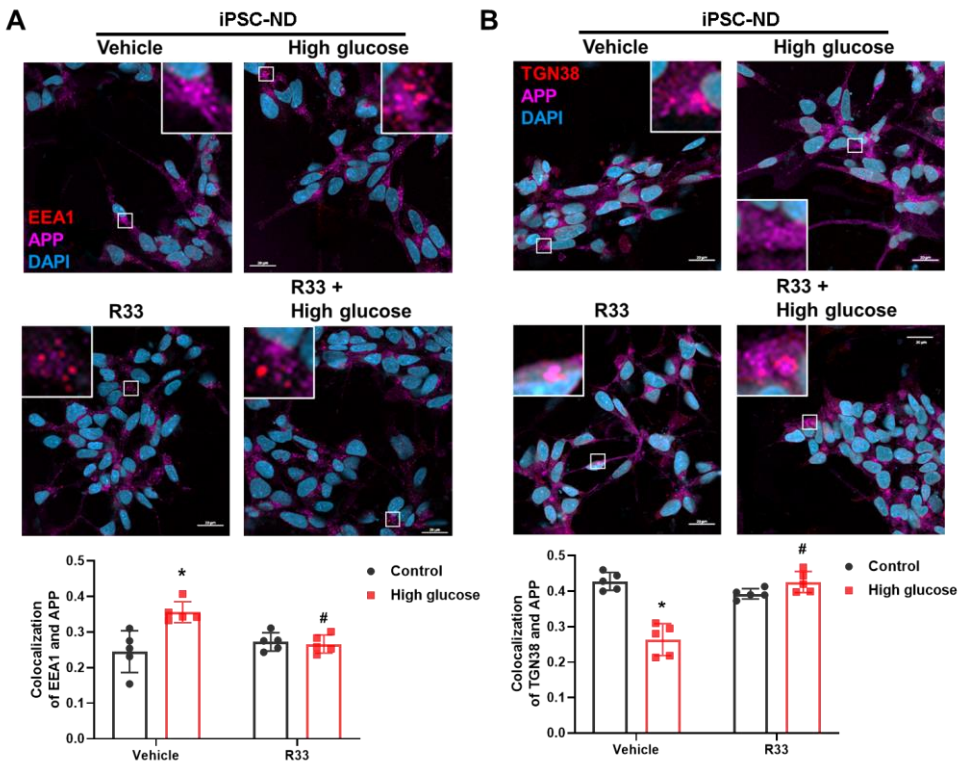

Figure 37. R33 reverses the retention of APP to the early endosomes by high glucose in iPSC-NDs.

A, B iPSC-NDs were treated with R33 (5 μM) for 30 min prior to high glucose treatement (25 mM) for 24 h. **A** The cells were immunostained with EEA1-and APP-specific antibodies and counterstained with DAPI. Scale bars, 20 μm. **B** The cells were visualized with TGN38- and APP-specific antibodies and counterstained with DAPI. Scale bars, 20 μm. $n = 5$. $^{*}p < 0.05$ vs. control, $^{\#}p < 0.05$ vs. high glucose.

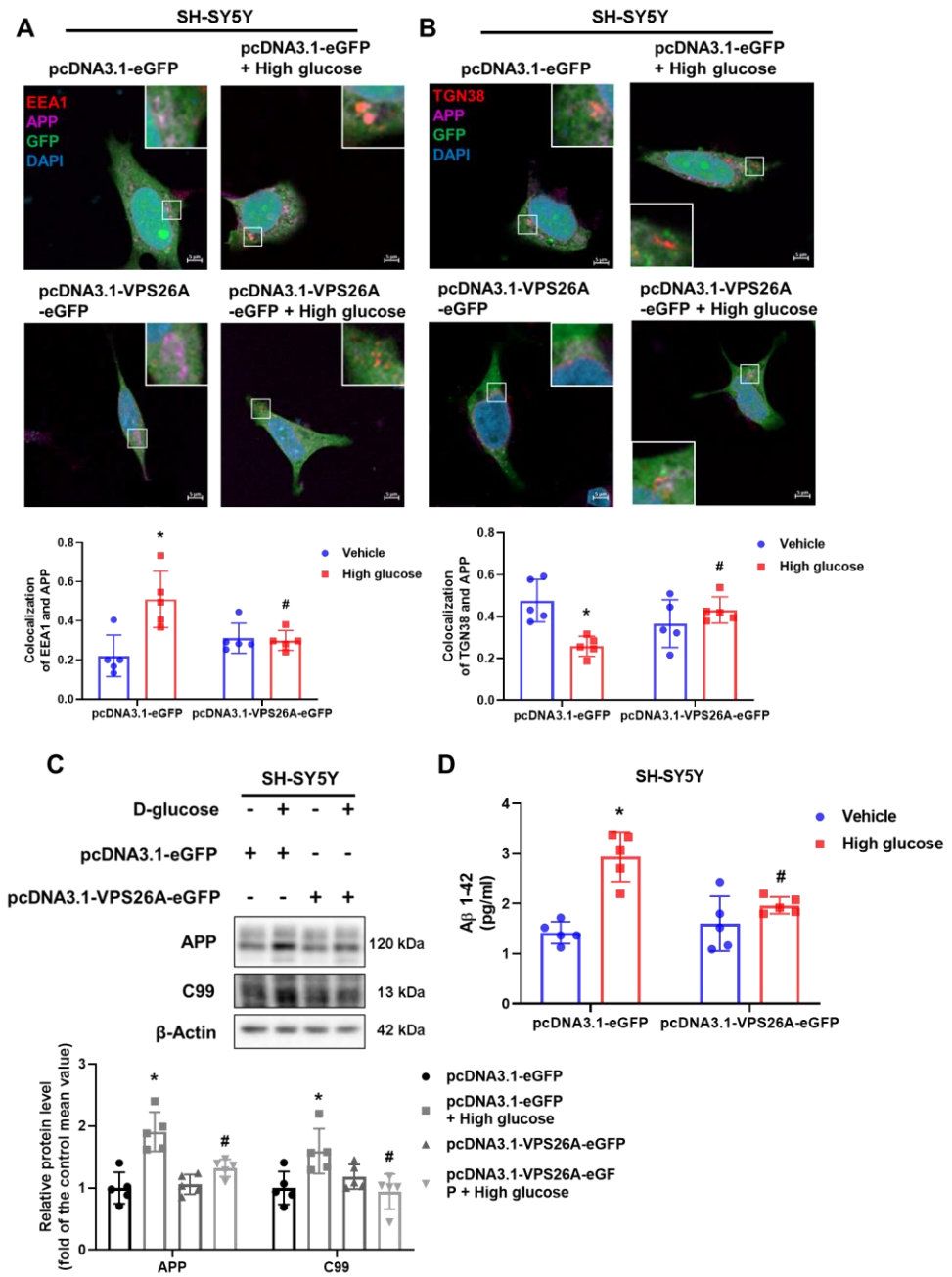

Figure 38. VSP26A overexpression reverses the retention of APP to the early endosomes by high glucose, which reduces Aβ.

A–C SH–SY5Ys were transfected with pcDNA3.1–eGFP or pcDNA3.1–VPS26A–eGFP plasmids for 24 h prior to high glucose treatment (25 mM) for 24 h. **A** The cells were immunostained with EEA1–and APP–specific antibodies and counterstained with DAPI. Scale bars, 5 μm. **B** The cells were visualized with TGN38–and APP–specific antibodies and counterstained with DAPI. Scale bars, 5 μm. **C** APP, C99, and β–Actin were detected by western blot. **D** SH–SY5Ys were transfected with pcDNA3.1–eGFP or pcDNA3.1–VPS26A–eGFP plasmids for 24 h prior to high glucose treatment (25 mM) for 48 h. Then, Aβ 1–42 from cell culture medium was measured. $n = 5$. $^{*}p < 0.05$ vs. control, $^{\#}p < 0.05$ vs. high glucose.

Downregulation of VPS26a inhibits degradation of p-Tau through increased retention of CI-MPR in early endosomes

Although phosphorylation of tau could be regulated by kinases p35/25-CDK5 and GSK3β or protein phosphatase 2 (PP2A), there were no significant changes in the levels of these proteins in high glucose conditions (Figure 39A). Given that maturation of CTSD was regulated by retromer-mediated cation-independent mannose-6-phosphate receptor (CI-MPR) recycling (Miura *et al.,* 2014) and VPS35 interacts with CI-MPR and transports it from the early endosome to the *trans*-Golgi (Cui *et al.,* 2019), I first measured the localization of CI-MPR to early endosomes and the *trans*-Golgi. In iPSC-NDs, high glucose increased co-localization of CI-MPR and EEA1, which was reversed by R33 pre-treatment (Figure 40A). The co-localization of CI-MPR and TGN38 decreased in high glucose-treated cells and was recovered in cells pretreated with R33 (Figure 40B). Furthermore, cells under high glucose conditions had lower co-localization of lysosomes and CTSD than cells within normal glucose conditions, which was recovered by R33 pre-treatment (Figure 40C). In SH-SY5Ys transfected with pcDNA3.1-eGFP or pcDNA3.1-VPS26a-eGFP, the co-localization of CI-MPR and EEA1 increased by high glucose was reduced by VPS26a overexpression (Figure 41A). Cells transfected with pcDNA3.1-VPS26a-eGFP at high glucose had higher co-localization of CI-MPR and TGN38 than cells with pcDNA3.1-eGFP transfection at high glucose (Figure 41B). The co-localization of

lysosomes and CTSD was decreased by high glucose with pcDNA3.1-eGFP, and was recovered by pcDNA3.1-VPS26a-eGFP transfection (Figure 41C). Although high glucose-mediated upregulation of pro-CTSD and downregulation of mature-CTSD were reversed by pcDNA3.1-VPS26a-eGFP transfection, there was no significant change in CI-MPR expression levels in all groups (Figure 42A). Moreover, CTSD activity decreased by high glucose was recovered by VPS26a overexpression (Figure 42B). The levels of tau phosphorylated at Ser396 and Thr181 increased by high glucose were reduced by VPS26a overexpression, which was blocked by pre-treatment with pepstatin A, a CTSD inhibitor (Figure 42C). These results suggest that VPS26a, down-regulated at high glucose, inhibits maturation of CTSD by blocking CI-MPR recycling between early endosomes and the *trans*-Golgi, leading to a defect in the degradation of phosphorylated tau.

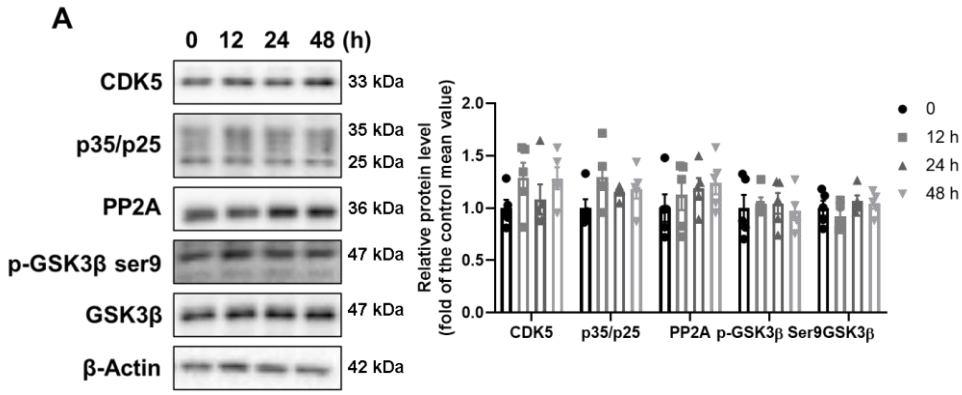

Figure 39. High glucose has no significant alteration on the expression levels of tau phosphorylation-related proteins.

A The SH-SY5Ys were treated with high glucose (25 mM) in a time dependent manner. CDK, p35/p25, p-GSK3β Ser9, GSK3β, and β-Actin were detected. n = 5.

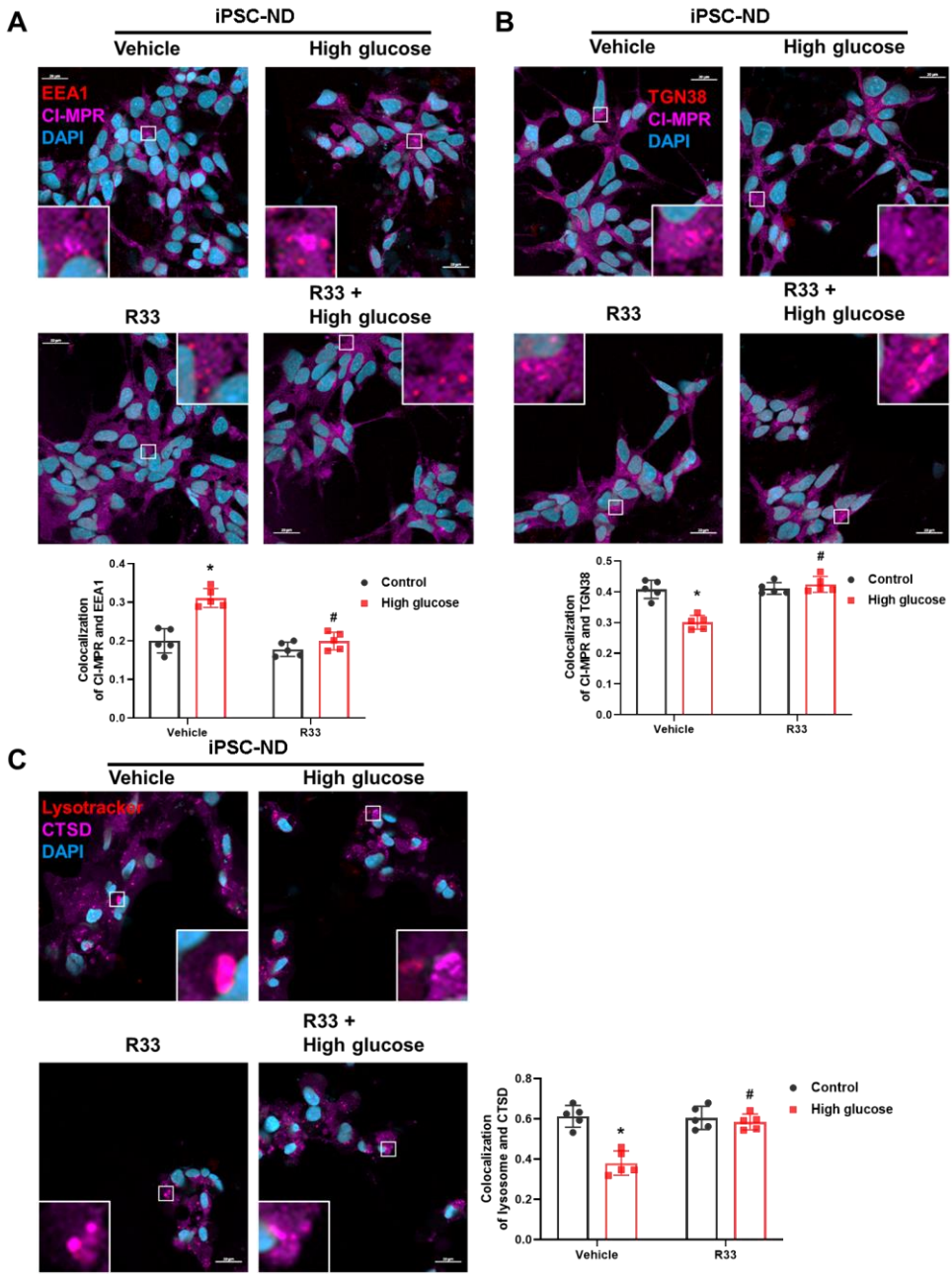
A
iPSC-ND
Vehicle
High glucose
EEA1
CI-MPR
DAPI
R33
R33 +
High glucose
Colocalization
of CI-MPR and EEA1
Control
High glucose
Vehicle
R33
B
iPSC-ND
Vehicle
High glucose
TGN38
CI-MPR
DAPI
R33
R33 +
High glucose
Colocalization
of CI-MPR and TGN38
Control
High glucose
Vehicle
R33
C
iPSC-ND
Vehicle
High glucose
Lysotracker
CTSD
DAPI
R33
R33 +
High glucose
Colocalization
of lysosome and CTSD
Control
High glucose
Vehicle
R33

Figure 40. R33 reverses the retention of CI-MPR to the early endosomes by high glucose in iPSC-NDs, which increases CTSD localization to the lysosomes.

A-C iPSC-NDs were treated with R33 (5 μM) for 30 min prior to high glucose treatement (25 mM) for 24 h. **A** The cells were visualized with EEA1-and CI-MPR-specific antibodies and counterstained with DAPI. Scale bars, 20 μm. **B** The cells were immunostained with TGN38-and CI-MPR-specific antibodies and counterstained with DAPI. Scale bars, 20 μm. **C** The cells were visualized with CTSD-specific antibody and stained with Lysotracker red and DAPI. Scale bars, 20 μm. $n = 5$. $^{*}p < 0.05$ vs. control, $^{\#}p < 0.05$ vs. high glucose.

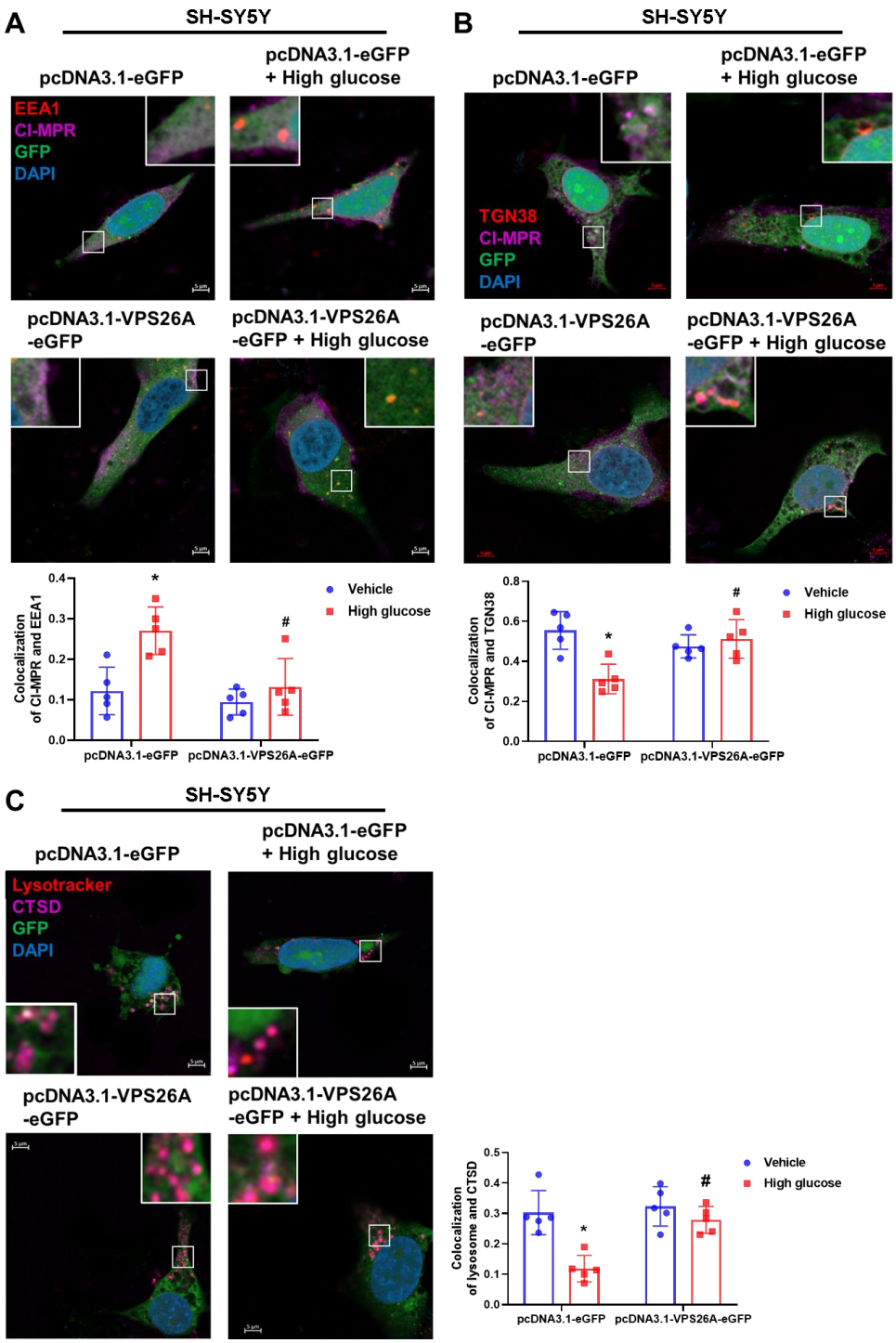
A
SH-SY5Y
pcDNA3.1-eGFP
pcDNA3.1-eGFP + High glucose
EEA1
CI-MPR
GFP
DAPI
pcDNA3.1-VPS26A -eGFP
pcDNA3.1-VPS26A -eGFP + High glucose
Colocalization of CI-MPR and EEA1
Vehicle
High glucose
pcDNA3.1-eGFP
pcDNA3.1-VPS26A-eGFP
B
SH-SY5Y
pcDNA3.1-eGFP
pcDNA3.1-eGFP + High glucose
TGN38
CI-MPR
GFP
DAPI
pcDNA3.1-VPS26A -eGFP
pcDNA3.1-VPS26A -eGFP + High glucose
Colocalization of CI-MPR and TGN38
Vehicle
High glucose
pcDNA3.1-eGFP
pcDNA3.1-VPS26A-eGFP
C
SH-SY5Y
pcDNA3.1-eGFP
pcDNA3.1-eGFP + High glucose
Lysotracker
CTSD
GFP
DAPI
pcDNA3.1-VPS26A -eGFP
pcDNA3.1-VPS26A -eGFP + High glucose
Colocalization of lysosome and CTSD
Vehicle
High glucose
pcDNA3.1-eGFP
pcDNA3.1-VPS26A-eGFP

Figure 41. VPS26A overexpression reverses the retention of CI-MPR to the early endosomes by high glucose, which increases CTSD localization to the lysosomes.

A-C SH-SY5Ys were transfected with pcDNA3.1-eGFP or pcDNA3.1-VPS26A-eGFP plasmids for 24 h prior to high glucose treatment (25 mM) for 24 h. **A** The cells were visualized with EEA1- and CI-MPR-specific antibodies and counterstained with DAPI. Scale bars, 5 μm. **B** The cells were immunostained with TGN38-and CI-MPR-specific antibodies and counterstained with DAPI. Scale bars, 5 μm. **C** The cells were visualized with CTSD-specific antibody and stained with Lysotracker red and DAPI. Scale bars, 5 μm. $n = 5$. $^{*}p < 0.05$ vs. control, $^{\#}p < 0.05$ vs. high glucose.

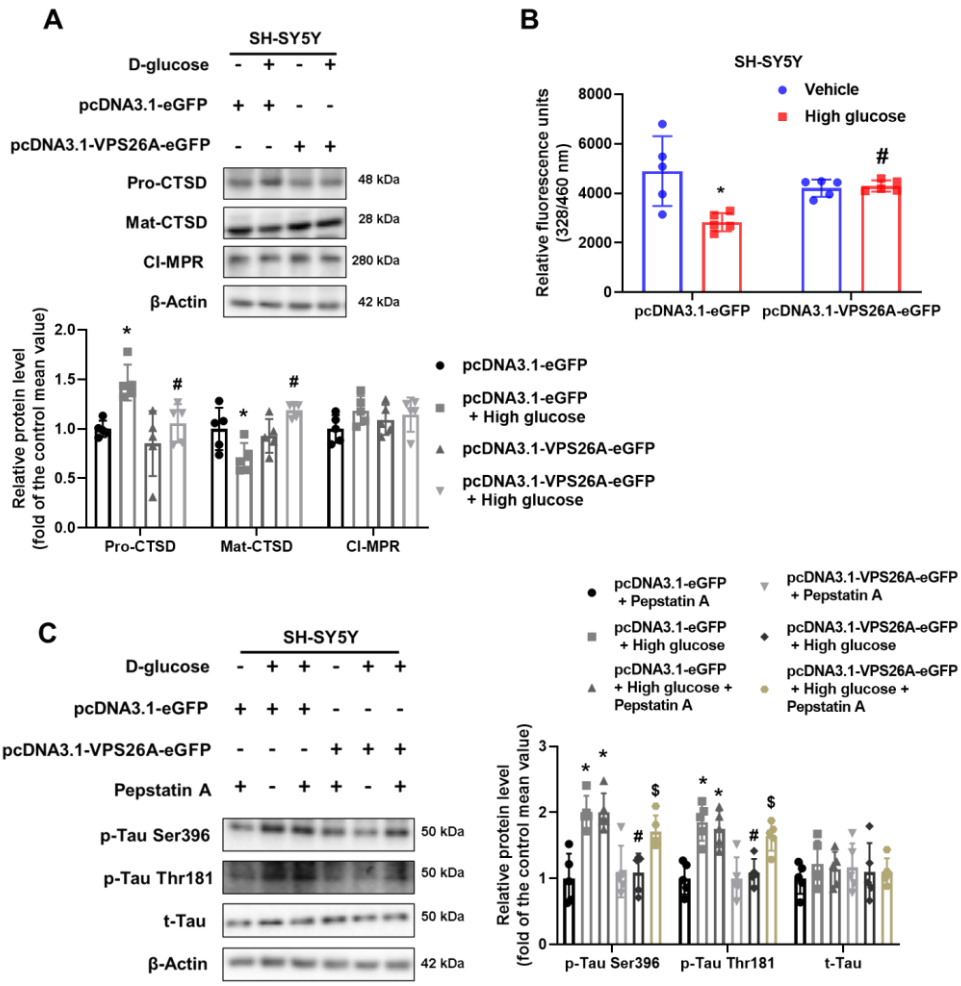

Figure 42. VPS26A overexpression recovers high glucose-inhibited CTSD activity, which induces p-Tau degradation.

A-C SH-SY5Ys were transfected with pcDNA3.1-eGFP or pcDNA3.1-VPS26A-eGFP plasmids for 24 h prior to high glucose treatment (25 mM) for 24 h. **A** Pro-CTSD, Mat-CTSD, CI-MPR, and β-Actin were detected by western blot. **B** The CTSD acitivty in the cell lysate were measured by CTSD activity fluorometric assay kit. **C** SH-SY5Ys were transfected with pcDNA3.1-eGFP or pcDNA3.1-VPS26A-eGFP plasmids for 24 h and then treated with pepstatin A (9 μM) for 30 min prior to high glucose treatment (25 mM) for 24 h. p-Tau Ser396, p-Tau Thr181, t-Tau, and β-Actin were detected by western blot. $n = 5$. $^{*}p < 0.05$ vs. control, $^{\#}p < 0.05$ vs. high glucose, $^{\$}p < 0.05$ vs. pcDNA3.1-VPS26a-eGFP with high glucose.

Retromer dysfunction induces the AD-like pathology in STZ-induced diabetic mice

Given that R33 treatment in 3×Tg AD mice increases the expression levels of retromer components and reduces Aβ and tau phosphorylation (Li *et al.,* 2020), I used R33 to alleviate diabetes-mediated retromer dysfunction and AD pathology. VPS26a levels were reduced in the hippocampus of STZ-diabetic mice, and recovered by R33 treatment (Figure 43A). The hippocampal Rab5 signal intensities of STZ mice were higher than those of both vehicle-injected and STZ withR33-injected mice (Figure 43B). Diabetic mice showed up-regulated levels of APP, C99, Aβ, phosphorylated tau, and pro-CTSD and down-regulated levels of mature-CTSD, all of which were restored by R33 treatment (Figure 43C, D). These results indicate that diabetes-associated AD phenotype is mediated by retromer dysfunction. Besides AD phenotype, I also investigated changes in synapse integrity and astrocyte over-activation. In STZ mice, levels of PSD95 (a post-synaptic marker) but not the levels of hippocampal synaptophysin (a pre-synaptic marker) were decreased, and GFAP (an astrocytic marker) levels were increased, all of which were reversed by R33 treatment (Figure 44A-D). The Y-maze results showed that both STZ-injected and STZ with R33-injected mice showed reduction of the total number of arm entries, but R33 increased the spontaneous alternation reduced by diabetes (Figure 45A). The NOR test results found that STZ-injected mice showed decreased

discrimination indices and novelty preference, which were recovered by R33 injection (Figure 45B). Results from the Y-maze and NOR indicate that R33 restored diabetes-impaired spatial and object working memory. These findings suggest that increased Aβ, p-Tau, synaptic deficits, astrocyte over-activation, and cognitive impairment in diabetic mice were induced by retromer dysfunction.

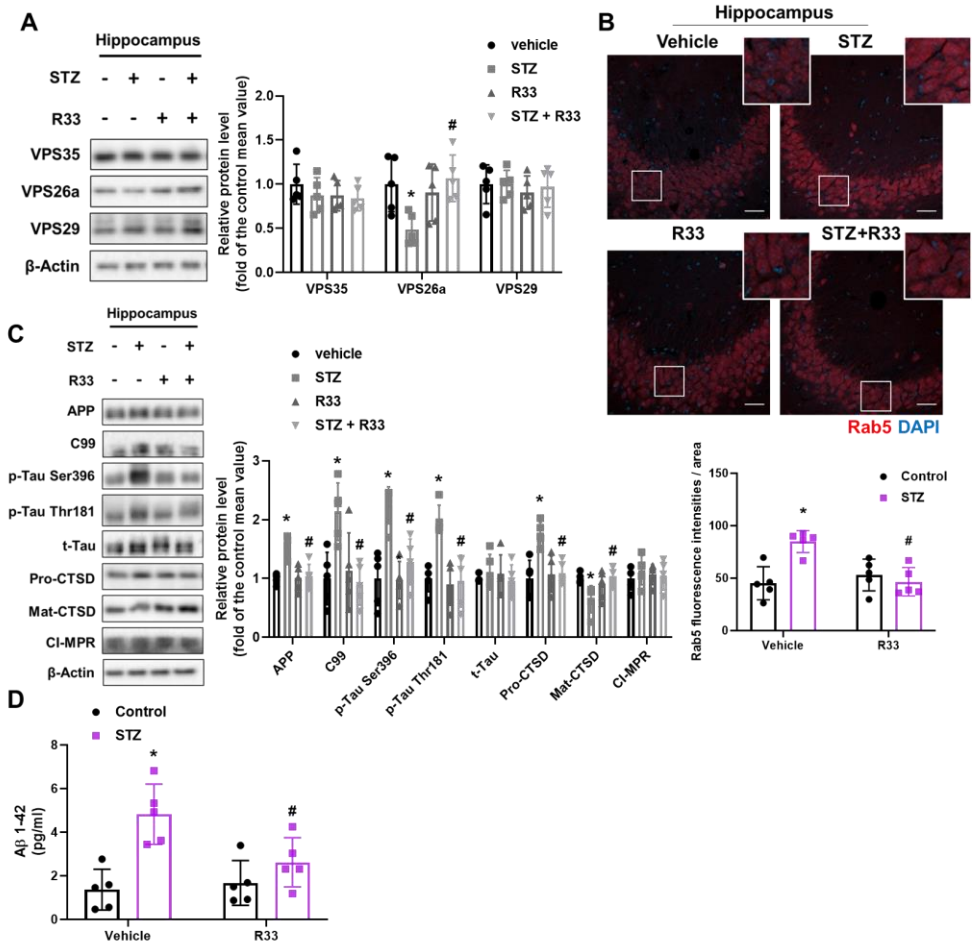

Figure 43. R33 reverses early endosomal enlargement, amyloidogenesis, and tau hyper-phosphorylation in diabetic mice.

A–D The experimental mice were divided into 4 groups: Vehicle, STZ, R33, and STZ with R33 as described detailed in Materials and methods. **A** The hippocampal VPS35, VPS26a, VPS29, and β-Actin were detected by western blot. **B** Hippocampal slides for IHC were immunostained with Rab5-specific antibodies and counterstained with DAPI, respectively. Scale bars, 20 μm. **C** The hippocampal APP, C99, p-Tau Ser396, p-Tau Thr181, t-Tau, Pro-CTSD, Mat-CTSD, CI-MPR, and β-Actin were detected by western blot. **D** Aβ 1-42 in the hippocampus were measured. $n = 5$. $^{*}p < 0.05$ vs. control, $^{\#}p < 0.05$ vs. STZ-treated mice.

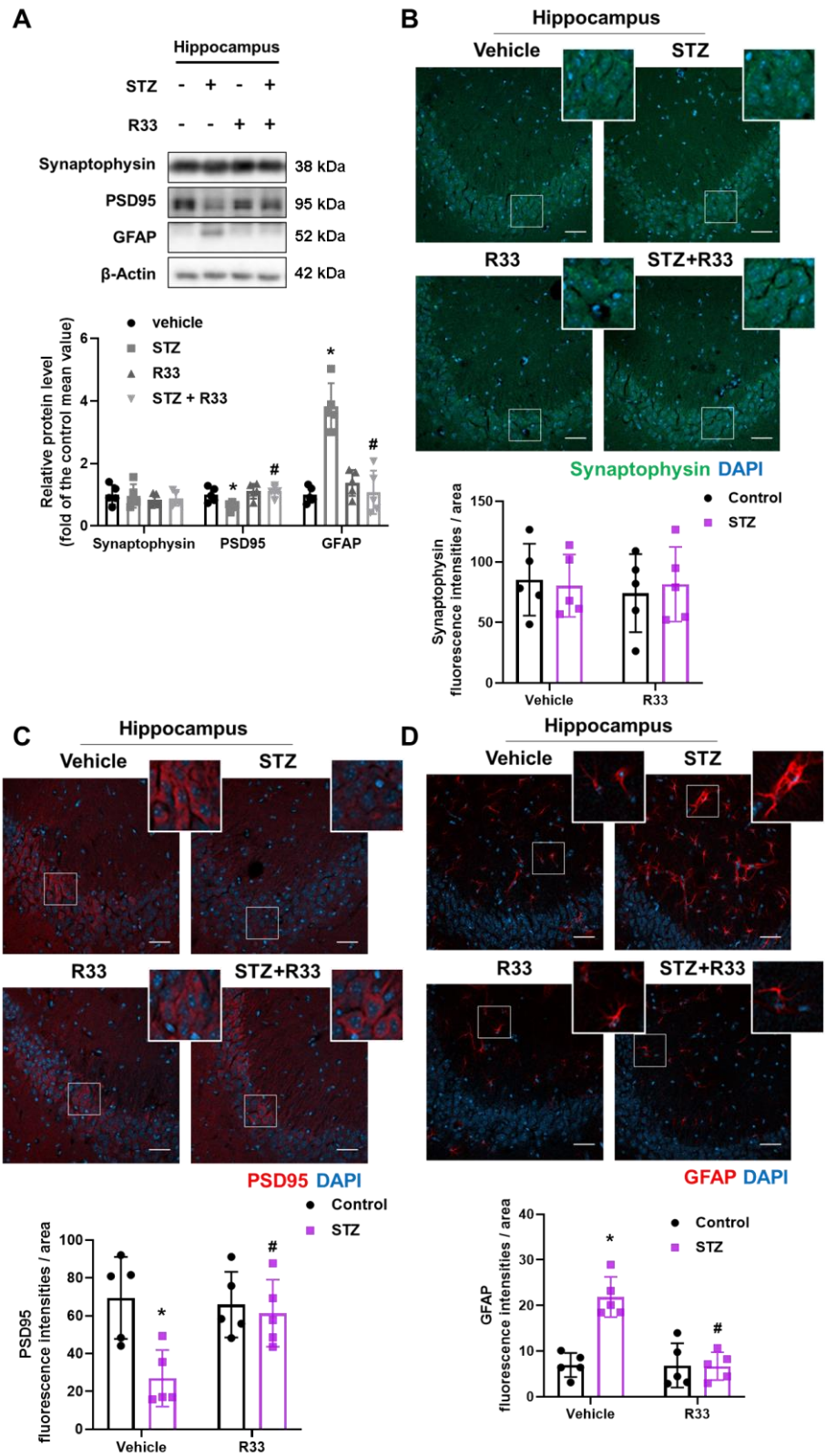
A
Hippocampus
STZ - + - +
R33 - - + +
Synaptophysin 38 kDa
PSD95 95 kDa
GFAP 52 kDa
β-Actin 42 kDa
vehicle
STZ
R33
STZ + R33
Relative protein level (fold of the control mean value)
Synaptophysin
PSD95
GFAP
B
Hippocampus
Vehicle
STZ
R33
STZ+R33
Synaptophysin DAPI
Control
STZ
Synaptophysin fluorescence intensities / area
Vehicle
R33
C
Hippocampus
Vehicle
STZ
R33
STZ+R33
PSD95 DAPI
Control
STZ
PSD95 fluorescence intensities / area
Vehicle
R33
D
Hippocampus
Vehicle
STZ
R33
STZ+R33
GFAP DAPI
Control
STZ
GFAP fluorescence intensities / area
Vehicle
R33

Figure 44. R33 reverses synaptic deficits and astrocyte over-activation in diabetic mice.

A-D The experimental mice were divided into 4 groups: Vehicle, STZ, R33, and STZ with R33 as described detailed in Materials and methods. **A** The hippocampal Synaptophysin, PSD95, GFAP, and β-Actin were detected by western blot. **B-D** Hippocampal slides for IHC were immunostained with Synaptophysin-, PSD95-, and GFAP-specific antibodies and counterstained with DAPI, respectively. Scale bars, 20 μm. $n = 5$. $^{*}p < 0.05$ vs. control, $^{\#}p < 0.05$ vs. STZ-treated mice.

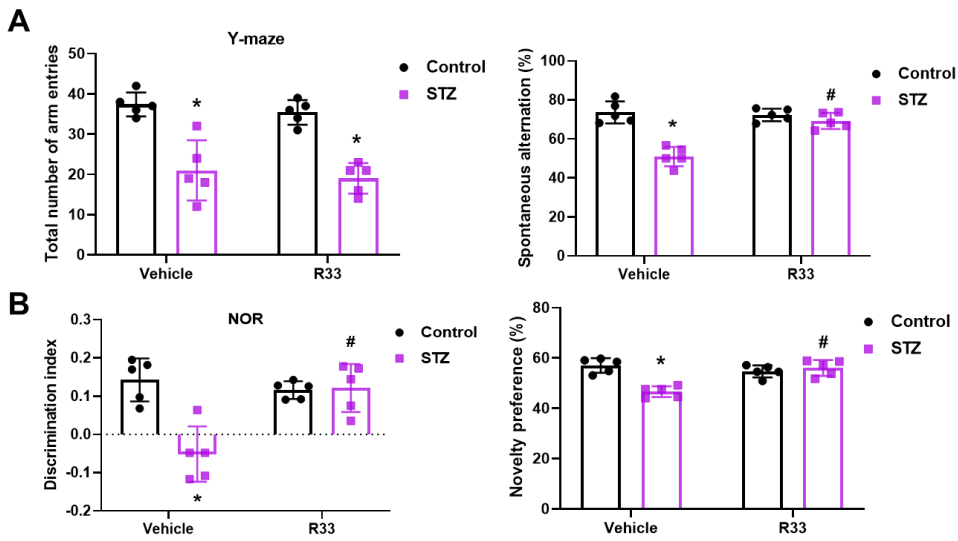

Figure 45. R33 ameliorates cognitive impairment in diabetic mice.

A, B The experimental mice were divided into 4 groups: Vehicle, STZ, R33, and STZ+R33 as described detailed in Materials and methods. The mice were subjected to Y-maze test and NOR test to evaluate spatial and object working memory function, respectively. $n = 5$. $^{*}p < 0.05$ vs. control, $^{\#}p < 0.05$ vs. STZ-treated mice.

DISCUSSION

The present study demonstrated that retromer dysfunction is a potential mechanism of DM-mediated AD pathogenesis. Indeed, *in vitro* data showed that high glucose-mediated downregulation of VPS26a induced abnormal APP processing and tau phosphorylation in neuronal cells. *In vivo* data showed that upregulation of Aβ, tau phosphorylation, synaptic deficits, astrocyte over-activation, and cognitive impairment were recovered by retromer enhancement in diabetic mice (Figure 46). Brain VPS35 and VPS26 levels down-regulated in AD patients (Small *et al.,* 2005) and SNX27, SNX1, SNX3, SORL1 and SXN6 were associated with amyloidognensis, which indicates that dysfunctional retromer complexes may contribute to AD onset (Huang *et al.,* 2016; Vardarajan *et al.,* 2012; Lambert *et al.,* 2013; Okada *et al.,* 2010). Although VPS35, VPS26, SORCS1, and WASHC1 have been associated with pathogenesis of DM, (Morabito *et al.,* 2014; Paterson *et al.,* 2010; Ding *et al.,* 2019) to my knowledge there is no study that investigates changes in expression levels of numerous retromer components in diabetes. Interestingly, my data showed that among retromer components, only the protein levels of VPS26a, but not VPS35, SORCS1, or WASHC1, were down-regulated in the hippocampus of STZ-induced diabetic mice and human neuronal cells exposed to high glucose. VPS35 deficiency led to reduced levels of both VPS26 and VPS29 (Vagnozzi *et al.,* 2021). However, I showed that high glucose-mediated VPS26a downregulation was not

accompanied by a decrease in VPS35 and VPS29, which may be due to difference in molecular stability. Moreover, I found that recruitment of VPS35 to early endosomes was reduced in high glucose conditions. Overall, these results indicate that VPS26a is a factor that causes high glucose-specific retromer dysfunction. Genome-wide DNA methylation analysis studies demonstrated that the *VPS26A* promoter is hypermethylated in both type 1 and 2 diabetes (Bell *et al.,* 2010; Nilsson *et al.,* 2014), but the consequences of hypermethylation and the mechanisms of cell-type specific hypermethylation are not known. DNMT1 in diabetic mice induces hypermethylation of wound healing-related genes, which leads to down-regulated expression of these proteins (Yan *et al.,* 2018). Destabilization of TET2 by diabetes-inhibited AMP-activated kinase dysregulates DNA methylation resulting in the loss of tumor suppressive function of TET2 (Wu *et al.,* 2018). However, my data showed that among DNA methylation-related genes, only DNMT1 was increased under diabetic conditions. The high glucose-stimulated Sp1/NF-κB p65 complex binds to the promoter region of *DNMT1* and up-regulates its expression, which leads to hypermethylation of podocyte slit diaphragm genes (Zhang *et al.,* 2017). In the present study, I also found that high glucose up-regulated DNMT1 expression via ROS-mediated NF-κB p65 stimulation. While numerous studies have revealed the function of retromer components in both AD and DM pathogenesis through gain or loss of function experiments (Vagnozzi *et al.,* 2021; Kebede *et al.,* 2014;

Li *et al.*, 2020), there are no studies on how the expression of retromer components is regulated. I found that DNMT1 induced hypermethylation of the *VPS26A* promoter containing two CpG sites (−118 and −346), which suggest that DNMT1−mediated epigenetic regulation reduced VPS26a expression in neuronal cells under diabetic conditions.

Retromer stabilizers, such as pharmacological chaperone R33, which increase the levels of protein expression in the CRC, thereby limit the pathogenic processing of APP in mouse hippocampal neurons (Mecozzi *et al.,* 2014). Moreover, using iPSC−derived neurons, it has been demonstrated that retromer stabilization has beneficial effects on the regulation of Aβ generation and tau phosphorylation in the human (Young *et al.,* 2018). My data found that R33 treatment recovered the VPS26a levels reduced by high glucose, which may result from retromer stabilization. Furthermore, high glucose−mediated early endosomal enlargement and increases of APP, Aβ, and tau phosphorylation were down−regulated by R33 treatment. These results suggest that the retromer is a potential modulator for both the alteration of APP processing and tau phosphorylation in neuronal cells exposed to high glucose. My data showed that high glucose increased the migration of APP to the early endosomes and decreased the migration to the *trans*−Golgi, which were restored by R33 treatment. Given that early endosomal abnormalities are associated with C99 accumulation, these results suggest that high glucose−mediated

retromer dysfunction induces pathogenic APP modulation in early endosomes. Previous studies have investigated the molecular mechanisms of retromer-mediated APP processing. VPS35 binds directly to APP in COS-7 cells (Vieira *et al.,* 2010) and its deficiency increased APP in the early endosomes in mouse hippocampal neurons (Bhalla *et al.,* 2012). Manipulation of the YAQM motif in the SORCS1 cytoplasmic tail increased APP retention in the early endosomes and decreased APP transport to the *trans*-Golgi in H4 neuroglioma cells (Lane *et al.,* 2013). Overexpression of SORL1, which interacts with APP, induced APP redistribution to the *trans*-Golgi in human neuroblastoma cells (Andersen *et al.,* 2005). SNX27 binds directly to the cytosolic tail of SORL1, which transports APP to the cell surface in mouse primary neurons (Huang *et al.,* 2016). However, through a gain-of-function experiment, my results show that VPS26a overexpression promoted the transport of APP from early endosomes to *trans*-Golgi, and reversed high glucose-mediated increases of APP, C99, and Aβ. Given that VPS26a acts as a cargo adapter with structural plasticity that supplies an additional binding surface for CRC-mediated cargo recognition through the closed-open conformational change upon SNX3 binding to the C-terminal region (Lucas *et al.,* 2016), the possible mechanism of the beneficial effect of the VPS26a overexpression is via the functional enhancement of the CRC. Although studies have mainly focused on the role of retromer on APP processing,

it is also essential to understand the relationship between retromer and tau phosphorylation.

As phosphorylated tau is broken-down by mature-CTSD in lysosomes (Vagnozzi *et al.,* 2021), a lack of CTSD proteolytic ability leads to an abnormal accumulation of phosphorylated tau. Previous study has shown that CI-MPR binds directly to CTSD and contributes to its maturation through retromer-mediated transport in HEK293 cells (Miura *et al.,* 2014). My data found that in iPSC-NDs, retromer enhancement by R33 treatment reversed high glucose-mediated increase of CI-MPR retention in early endosomes via transport to the *trans*-Golgi. In addition, R33 increased the co-localization of CTSD and lysosomes that was down-regulated by high glucose conditions. VPS35 knockout induced improper processing of CTSD and decreased its activity through impairment of CI-MPR transport from endosomes to the *trans*-Golgi in HeLa cells (Cui *et al.,* 2019). Although VPS35 regulates tau phosphorylation through modulation of active CTSD availability in neuronal cells (Vagnozzi *et al.,* 2021), there are no studies investigating the effects of VPS26a on CI-MPR trafficking and related CTSD maturation. My VPS26a overexpression results showed that high glucose-mediated improper CI-MPR and CTSD trafficking and reduced CTSD activity were dependent on VPS26a. Moreover, by using pepstatin A, I found that the effect of VPS26a on phosphorylated tau degradation was mediated by the proteolytic ability of active CTSD. On the other hand, Cdk5, p25, GSK3, and PP2A which possibly regulate

tau phosphorylation, are all activated in pancreatic β-cells exposed to high glucose (Ho *et al.,* 2020; Li *et al.,* 2020). However, my data showed that high glucose did not lead to significant changes in levels of Cdk5, p25, GSK3, or PP2A in neuronal cells. Differences in mechanism of action may be cell-type-specific and preferentially-related regulation. Overall, I suggest for the first time that VPS26a-mediated retromer dysfunction promotes pathogenic APP processing and tau phosphorylation via improper trafficking in high glucose conditions.

A gain-of-function experiment showed that *VPS35* gene delivery in the central nervous system of transgenic AD mice reduces the AD phenotype (Li *et al.*, 2020). R33 treatment for 9 months in AD mice restored CRC expression, reduced Aβ and tau phosphorylation levels, and improved learning, memory, and synaptic integrity (Li *et al.*, 2020). My *in vivo* data also showed that R33 increased VPS26a and reduced Aβ and tau phosphorylation levels in diabetic mice. I found that STZ-mediated reduction of PSD95, increase of GFAP, and impairment of both spatial and object working memory cognition were restored by R33 treatment. These results suggest that pharmacological restoration of retromer function ameliorates diabetes-mediated AD-like phenotype. Given that *Vps29* mutation induces mis-localization of the retromer to endosomes in soma, which inhibits synaptic transmission (Ye *et al.,* 2020) and the genetic deficiency of *SORCS2* impaired the N-methyl-D-aspartate receptor 2A subunit regulating synaptic

plasticity trafficking (Ma *et al.,* 2017), other retromer components may contribute to diabetes-mediated AD-like phenotype.

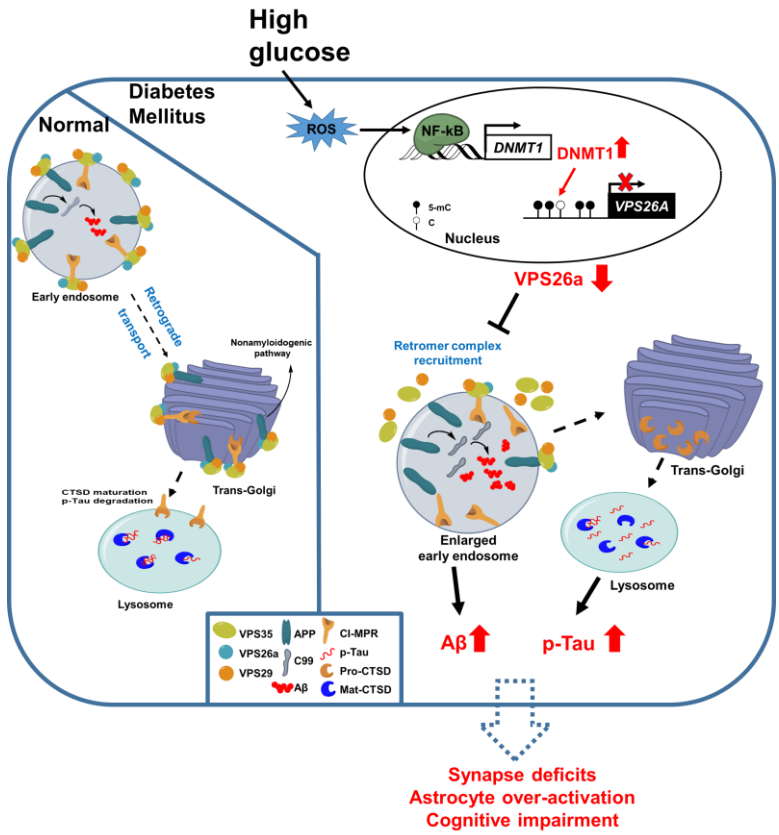

Figure 46. The schematic model for dysregulation of mechanisms of APP processing and tau hyperphosphorylation by high glucose-mediated downregulation of VPS26a.

High glucose increased DNMT1 expression through ROS-stimulated NF-κB nuclear translocation. DNMT1 induces hypermethylation of the *VPS26A* promoter regions resulting in VPS26a downregulation. Reduced VPS26a impaired retrograde-transport of APP and CI-MPR to the *trans*-Golgi, which increased APP and Aβ levels, and decreased CTSD activity, reducing p-Tau levels, respectively, which contributes to synapse deficits, astrocyte over-activation, and cognitive impairment.

CHAPTER Ⅲ

The protective effect of TRIM16-mediated lysophagy on high glucose-accumulated neuronal Aβ

INTRODUCTION

Although DM is considered as a risk factor for dementia, the relationship between diabetes and the development of AD has been controversial due to inconsistencies among human cohort studies, biochemical analyses, and animal studies (Arnold *et al.,* 2018; Lacy *et al.,* 2018). Nevertheless, as the recent trend of diabetes is decreasing the age of onset (Barbiellini *et al.,* 2021), which significantly increases the incidence of dementia, more sophisticated studies focusing on the early pathogenesis of the disease would help in identifying the possibility of diabetes-associated AD. In fact, lysosomal disorders inducing amyloid plaques and neurofibrillary tangles are observed before the onset of AD (Lambeth *et al.,* 2019; Lee *et al.,* 2022). In addition, previous studies have demonstrated that hyperglycemia up-regulates the expression of neuronal Aβ and phosphorylated-tau (p-Tau) through endolysosomal dysfunction (Chae *et al.,* 2022; Chae *et al.,* 2020), an early pathological feature of AD (Kwart *et al.,* 2019). Therefore, targeting lysosomes may help in elucidating the potential disease mechanism. To manage lysosomal dysfunction, lysosomal quality control is primarily performed through lysophagy (Yim *et al.*, 2020). Lysophagy, a selective macroautophagy that detects and removes damaged lysosomes, is activated through ubiquitination-inducing proteins such as tripartite motif containing 16 (TRIM16), f-box protein 27 (FBXO27), leucine-rich repeat and sterile alpha motif containing 1 (LRSAM1), ubiquitin-conjugating enzyme e2q family like

1 (UBE2QL1), and valosin-containing protein (VCP) (Papadopoulos *et al.*, 2017). Although genetic or chemical inhibition of lysophagy factors increases proteopathic seeding in neurons (Zhu *et al.,* 2022), the direct causal relationship between lysophagy and neurodegenerative diseases has not yet been elucidated. However, accumulating data suggest that high-efficiency lysophagy is essential for maintaining lysosomal function and protects against neurodegeneration (Papadopoulos *et al.*, 2017).

In chronic diabetic state, hyperglycemia induces LMP and inhibits lysosomal biogenesis, resulting in lysosomal dysfunction (Yang *et al.,* 2021). It has been shown that db/db diabetic mice exhibit hippocampal lysosomal dysfunction characterized by inhibition of the expression and activity of lysosomal hydrolases such as CTSD and hexosaminidase A (Sims-Robinson *et al.,* 2016). Lysosomal abnormalities are also induced through high mobility group box 1 (HMGB1)-mediated LMP in diabetic retinal pigment epithelial cells (Feng *et al.,* 2022). In diabetic renal tubular epithelial cells, SMAD3-mediated suppression of transcription factor EB (TFEB) activity was found to induce lysosomal depletion (Yang *et al.,* 2021). Although lysosomal dysfunction has been implicated in the pathogenesis of diabetes, no studies have examined how diabetes affects lysophagy and the subsequent effects on neuronal Aβ and p-Tau degradation. Considering that suppression of VCP function through autosomal-dominant genetic mutation increases tau aggregation in the human AD brain (Darwich *et al.,* 2020), investigating

impaired lysophagy in diabetes can provide mechanistic insights into AD pathology. In the present study, I have explored the effects and molecular mechanisms of action of high glucose on neuronal lysophagy and subsequent accumulation of Aβ and p-Tau and cognitive impairment using iPSC-NDs, mouse hippocampal neurons, and STZ-induced diabetic mice. This study elucidates the lysophagy-related mechanisms and potential regulatory candidates of DM-associated AD pathology.

MATERIALS & METHODS

Cell culture

The detailed method for differentiation of iPSC-NDs and cultivation of SH-SY5Ys are elucidated in Materials & Methods section of Chapter Ⅱ. Mouse hippocampal neurons from E18 embryos were cultured as described following a modified protocol (Fath *et al.,* 2009) and performed in compliance with the approval of the Institutional Animal Care and Use Committee of Seoul National University (SNU-201013-7-2). In brief, hippocampal neurons were cultured at low density on poly-D-lysine-coated coverslips with cortical rings of neurons and glias or high density on six-well plates coated with poly-D-lysine in neurobasal medium (Thermo Fisher, 21103) supplemented with 2% B27 supplement (Thermo Fisher, 17504) and 0.25% GlutaMax-1

(Thermo Fisher, 35050). The cells were exposed to 25 mM D-glucose to mimic diabetic conditions (Feng *et al.,* 2022; Chae *et al.,* 2022).

Plasmid DNA transfection

The tfGal3 plasmid, pcDNA3.1-Trim16-GFP, or pcDNA3.1-TRIM16-GFP were transfected into hippocampal neuron and SH-SY5Ys using lipofectamine 2000 (Thermo Fisher, 11668019). Neurons were transfected at DIV 4 for 2 h and replaced with fresh media (Lie *et al.,* 2022). SH-SY5Ys were transfected at 60% confluence for 12 h and replaced with fresh media. After transfection, cells were exposed to high glucose.

siRNA transfection

SH-SY5Ys were transfected with 25 nM of *FBXO27, LRSAM1,* or *VCP* siRNAs by using TurboFect™ (Thermo Fisher, R0531) for 12 h. The cells were transfected before being exposed to high glucose.

Immunofluorescence assay

The detailed method for immunofluorescence assay is elucidated in materials & methods of Chapter Ⅰ. Quantification of fluorescent intensities and measurements of lysotracker-and galectin-3-positive

signals were carried out with Fiji software (Schindelin *et al.,* 2012). JACop plugin was used to measure and analyze co-localization (Bolte *et al.,* 2006).

Chromatin immunoprecipitation (ChIP) assay

ChIP assay was performed using an EZ-ChIP Kit (Sigma, 17-371) according to the manufacturer's instructions. Briefly, chromatin-protein complexes were incubated with the RNA polymerase (RNA Pol; positive control) antibody, the normal IgG (negative control), and primary antibodies for overnight at 4 ° C. Immunoprecipitated-DNA was eluted and then amplified using PCR. The sequences of TRIM16 primer are as follows: forward primer, 5′ -GAGACACGTGGTCTTCAGCA-3′ and reverse primer, 5′ -GCTCGGCCACTCATTACTGT -3′ .

qPCR analysis

The detailed method for cDNA synthesis and quantitative PCR (qPCR) analysis are elucidated in materials & methods of Chapter Ⅰ. Using mRNA primers (Table 6), cDNAs were amplified.

Table 6. List of primers used for real-time qPCR.

Gene	Forward primer	Reverse primer
TRIM16	ACTCAAGTGTCTGCCGTTGT	CGGGTCAAACGTGATGTCAT
FBXO27	TCCGAAAGTGGATGGTGCAA	AATCCTGCCACTATCCAGCA
LRSAM1	AGCTGTAAGAACCGGCTCAT	TTGCTGCCACGACAGAATCT
VCP	CGTGAATCCATCGAGAGTGA	GGTCTGGGCAAACATCTCAT
UBE2QL1	ATGAAGGAGCTGCAGGACAT	TCGGTGTTGGTCTCCTTCAT

Western blot analysis

The detailed method for western blot analysis is elucidated in materials & methods of Chapter Ⅰ.

Lysosomes staining

Lysosomal staining was performed using LAMP1 primary antibody. LAMP1-psotive lysosomes were visualized with confocal microscopy equipment (LSM 710, Carl Zeiss). Intact lysosomes were stained with lysotracker (Thermo Fisher, L12492). Cells were incubated with 100 nM lysotracker at 37 ℃ for 30 min. Lysotracker signals were analyzed by flow cytometry or confocal microscopy equipment.

Lysosome rupture and elimination assay

Lysosomal rupture and elimination assay were performed using LLOMe treatment and tfGal3 plasmid transfection (Maejima *et al.,* 2013).

Briefly, after drug treatment, iPSC-NDs were treated with LLOMe (1 mM) for 1 h to disrupt the lysosomal membrane, rinsed the reagent, and incubated the cells for additional hours in the absence of LLOMe. The lysosomal clearance was evaluated by immunostaining with galectin-3 antibody. The SH-SY5Ys were transfected with tfGal3 plasmids followed by drug and LLOMe treatment and then observed by confocal microscope. When LMP takes place, tfGal3 enters the ruptured lysosomal lumen and quickly attaches to the inner membrane, displaying both GFP and RFP fluorescence and producing yellow signals. Because PFP is relatively stable in acidic environment, GFP fluorescence is quenched in the lumen of intact lysosome during lysophagy.

Measurements of intracellular pH and calcium

The pH-sensitive fluorescent probe BCECF-AM (Thermo Fisher, B1150] and Fluo-4, AM (Thermo Fisher, F14201) exhibiting fluorescence upon binding Ca^{2+} were used for measuring the intracellular pH and calcium, respectively. Measurements were performed according to the manufacturer's instructions. The cells were stained with 2 μM BCECF-AM at 37 ℃ for 30 min after drug treatment. After incubation with Fluo-4 at 37 ℃ for 1 h, cells were stabilized and exposed to drugs. BCECF-AM- and Fluo-4-stained cells were measured via flow cytometry.

Lactate dehydrogenase (LDH) release assay

The optimization of cell concentration was determined according to the protocol provided in the LDH release assay kit (DoGenBio, Seoul, Korea, DG-LDH500). After drug treatment, cells were centrifugated at 600 × g and then supernatants were incubated with the LDH assay mixture at RT for 30 min. The level of released LDH was determined by measuring the optical density at 450 nm with an Epoch 2 spectrophotometer (BioTek, Vermont, USA).

Annexin V/PI staining

Annexin V/PI staining was performed using Annexin V/FITC apoptosis detection kit according to the manufacturer's instruction (556547, BD Bioscience, NewJersy, USA). After drug treatment, equal amount of cell was resuspended in binding buffer with Annexin V-FITC and PI at RT for 30 min. Stained cells were detected with flow cytometry and analyzed with CytExpert 2.3 software. Annexin V positive cells represent early apoptosis and PI positive cells represent necrosis. Both positive cells represent late apoptosis.

CTSB and CTSD activities assay

CTSB and CTSD activities were measured using CTSB (Biovision, Massachusetts, USA, K140) and CTSD (Biovision, K143) activity

fluorometric assay kit. Assays were performed according to manufacturer's protocol. Cells were lysed on ice for 10 min and centrifuged at 16,000 × g for 5 min. After protein quantification with BCA assay, lysates were incubated with substrate and reaction buffer at 37 ℃ for 2 h. Fluorescent intensities of CTSB and CTSD were measured by fluorometer equipped with a 400−nm excitation/505−nm emission and 328−nm excitation/460−nm emission filter, respectively.

Measurements of Aβ level

The detailed method for measurements of Aβ level is elucidated in materials & methods of Chapter Ⅱ.

Animal study

Animal handling and experimentation were undertaken according to the ethical approval of the Institutional Animal Care and Use Committee of Seoul National University (IACUC, Approval No.: SNU− 220307−1). Group size estimation was performed in compliance with the instructions given by IACUC (effect size: 15%, standard deviation (SD): 6%, number of groups: 4; alpha: 0.05, power (1−β): 0.8). Male ICR mice were used to investigate the effects of diabetes on hippocampal lysophagy impairment and subsequent Aβ and p−Tau accumulations, and cognitive impairment. Mice (9 weeks of age) were housed under

standard conditions of temperature (20–25 ℃), humidity (less than 60%), and a 12 h dark/12 h light cycle and free to access autoclaved chow and tap water. STZ was injected into mice to induce diabetes, as previously described with slight modifications (Furman 2021). Mice were randomized to receive STZ (75 mg/kg in 0.1 M sodium citrate buffer, pH 4.5) or vehicle intraperitoneally once daily for three days after 6 h of fasting. 1 week after STZ injection, blood glucose level was measured using a glucose monitor (Roche, Germany) and when the blood glucose level was 300 mg/dL or higher, severe diabetes was determined (Furman 2021). Once there were enough diabetic mice, they were separated into 4 groups at random (n = 5 per group): vehicle, STZ, Curcumin C1, and STZ with Curcumin C1. Curcumin C1 (10 mg/kg in 1% sodium carbonyl methylcellulose [CMCNa; Sigma, C5678]) was orally administrated by gavage once daily for 8 weeks following diabetes induction, as previous reported with slight modifications (Song *et al.,* 2016). At 18 weeks of age, body weight and blood glucose levels were measured followed by behavioral tests. For additional biochemical analysis, mice were anaesthetized by IP injection of avertin solution (250 mg/kg, mixture containing 2−Methyl−2−butanol; Sigma, 152463 and 2,2,2,−Tribromoethanol; Sigma, T48402) and euthanized by exsanguination.

Y-maze test

The detailed method for Y-maze test is elucidated in materials & methods of Chapter Ⅰ.

Open field test

The open field test is used to assess anxiety in rodents because they navigate around the open field when they feel anxious. To reduce stress before the test, animals were acclimatized to the testing chamber for 2 h. Mice were put into the rectangular plastic boxes (H30 × L30 × W30 cm) and their activities were monitored for 10 min. The amount of time spent in the open field's center and periphery was examined using Smart 3.0 video tracking system.

NOR test

The detailed method for NOR test is elucidated in materials & methods of Chapter Ⅱ.

IHC analysis

The detailed method for IHC analysis is elucidated in materials & methods of Chapter Ⅱ.

Data & statistical analysis

The detailed method for data & statistical analysis test are elucidated in materials & methods of Chapter Ⅱ.

Materials

The iPSCs and SH-SY5Ys were acquired from Kangstem Biotech (Seoul, Korea) and Korean Cell Line Bank (Seoul, Korea), respectively. Antibiotics and FBS were purchased from Gibco and Hyclone (Grand Island, USA), respectively. The antibodies of p-AMPK (Thr172) (sc-33524), β-Actin (sc-47778), LAMP1 (sc-20011), CTSB (sc-365558), Galectin-3 (sc-23938), Ubiquitin (sc-8017), VCP (sc-57492), TRIM16 (sc-398851), and CTSD (sc-13148) were obtained from Santa Cruz Biotechnology (Santa Cruz, USA). Tau 5 (AHB-0042) antibody was acquired from Thermo Fisher. The antibodies of Rab7 (NB120-13253), P62 (NBP1-48320), Aβ (NBP2-13075), LAMP1 (AF4800), and LC3 (NB100-2220) were purchased from Novus Biologicals (Centennial, USA). p-Tau (Thr212) antibody was obtained from Signalway antibody (Maryland, USA). The antibodies of LAMP1 (9091), p-mTOR (Ser 2448) (2971S), mTOR (2983S), AMPK (2532S), and p-Tau Thr181 (12885) were acquired from Cell Signaling Technology (Beverly, USA). The antibodies of APP (ab32136) and MAP2 (ab32454) were obtained from Abcam (Cambridge, England). FBXO27 (14570-1-AP), LRSAM1 (24666-

1-AP), TFEB (13372-1-AP), ALIX (12422-1-AP), CHMP4B (13683-1-AP) and TFE3 (14480-1-AP) antibodies were purchased from Proteintech (Illinois, USA). Secondary antibodies for anti-rat Alexa Fluor488 (A11006), anti-rat Alexa647 (A78947), anti-rabbit Alexa Fluor 647 (A21244), anti-mouse Alexa Fluor 488 (A32723), anti-Sheep Alexa Fluor488 (A11015), anti-rabbit Alexa Fluor 555 (A32732), anti-mouse Alex Fluor 555 (A32727), and Lysotracker Red DND-99 (L7528) were obtained from Thermo Fisher (Waltham, USA). H-Leu-Leu-OMe · HBr (LLOMe; G2550) was purchased from Bachem (California, USA). Leupeptin (L2884), N-Acetyl Cysteine (NAC, A7250), Bafilomycin A1 (B1793), D-glucose (G8769), Rapamycin (37094), Normal goat serum (NGS, 566380), Pepstatin A (P5318), DAPI (D9542), and STZ (S0130) were acquired from Sigma Chemical Company. Curcumin C1 (M9451) was obtained from Abmole Bioscience (Texas, USA). ptf-Galectin3 was a gift from Tamotsu Yoshimori (Maejima *et al.,* 2013). pcDNA3.1(+)-TRIM16-eGFP, pcDNA3.1(+)-Trim16-eGFP and pcDNA3.1(+)-eGFP were purchased from Koma Biotech (Seoul, Korea). mRNA primers for *TRIM16, FBXO27, LRSAM1, VCP, UBE2QL1*, and ChIP primers for *TRIM16* promoter region were obtained from Cosmo Genetech (Seoul, Korea). siRNAs for *FBXO27, LRSAM1, VCP* were purchased from Bioneer (Daejeon, Korea). Non-targeting siRNA (NT siRNA) was provided from Dharmacon provided (Lafayette, CO, USA).

RESULTS

High glucose induces neuronal lysosomal dysfunction, Aβ accumulation, and cell death

To elucidate the effect of high glucose on neuronal lysosomal function using lysotracker that has a strong affinity for acidic organelles, I first examined intact lysosomes in iPSC-NDs. High glucose decreased the mean lysotracker intensities and the degree of colocalization between the lysotracker and LAMP1, a lysosomal marker protein (Figure 47A, B). The results of BCECF staining showing that cytosolic pH was decreased by high glucose treatment indirectly implied lysosomal damage (Figure 47C). Moreover, to explore the relationship between lysosomal dysfunction and Aβ and p-Tau degradation under high glucose conditions, I evaluated the subcellular localization of CTSB and CTSD, which respectively degrade Aβ and p-Tau (Mueller-Steiner *et al.,* 2006; Vagnozzi *et al.,* 2021). I observed that the degree of colocalization between CTSB or CTSD and LAMP1 was decreased in both iPSC-NDs and mouse hippocampal neurons under high glucose conditions (Figure 48A-D). Similar to a previous report (Lee *et al.,* 2022), I found that high-glucose-induced Aβ accumulation in lysosomes (Figure 49A, B). The iPSC-NDs also underwent cell death under high glucose conditions (Figure 49C, D). These results demonstrate that high glucose induces lysosomal dysfunction, which may be involved in intraneuronal Aβ accumulation and cell death.

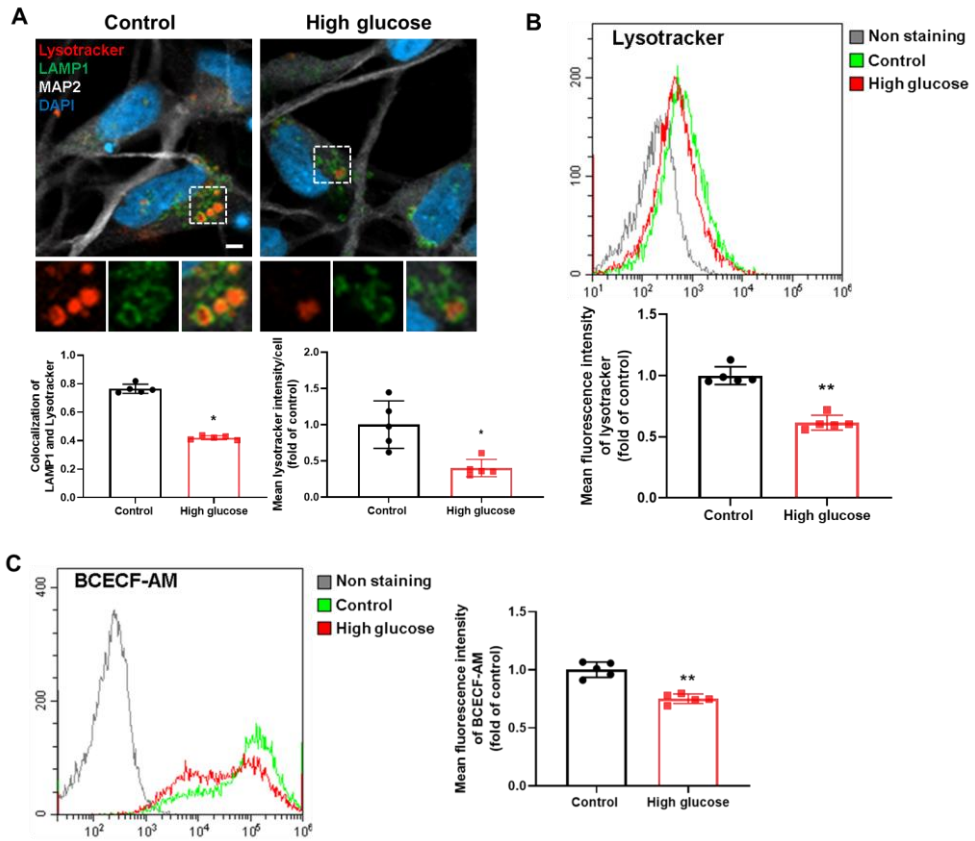

Figure 47. High glucose reduces intact lysosomes in iPSC-NDs.

A-C iPSC-NDs were exposed to high glucose for 24 h. **A** Immunofluorescence staining of LAMP1, MAP2, and lysotracker were visualized. DAPI was used to stain nuclei. **B** Mean fluorescence intensities of lysotracker were measured by flow cytometric analysis. **C** Mean fluorescence intensities of lysotracker of BCECF were measured by flow cytometric analysis. $n = 5$. $^{*}p < 0.05$, $^{**}p < 0.01$ vs. control.

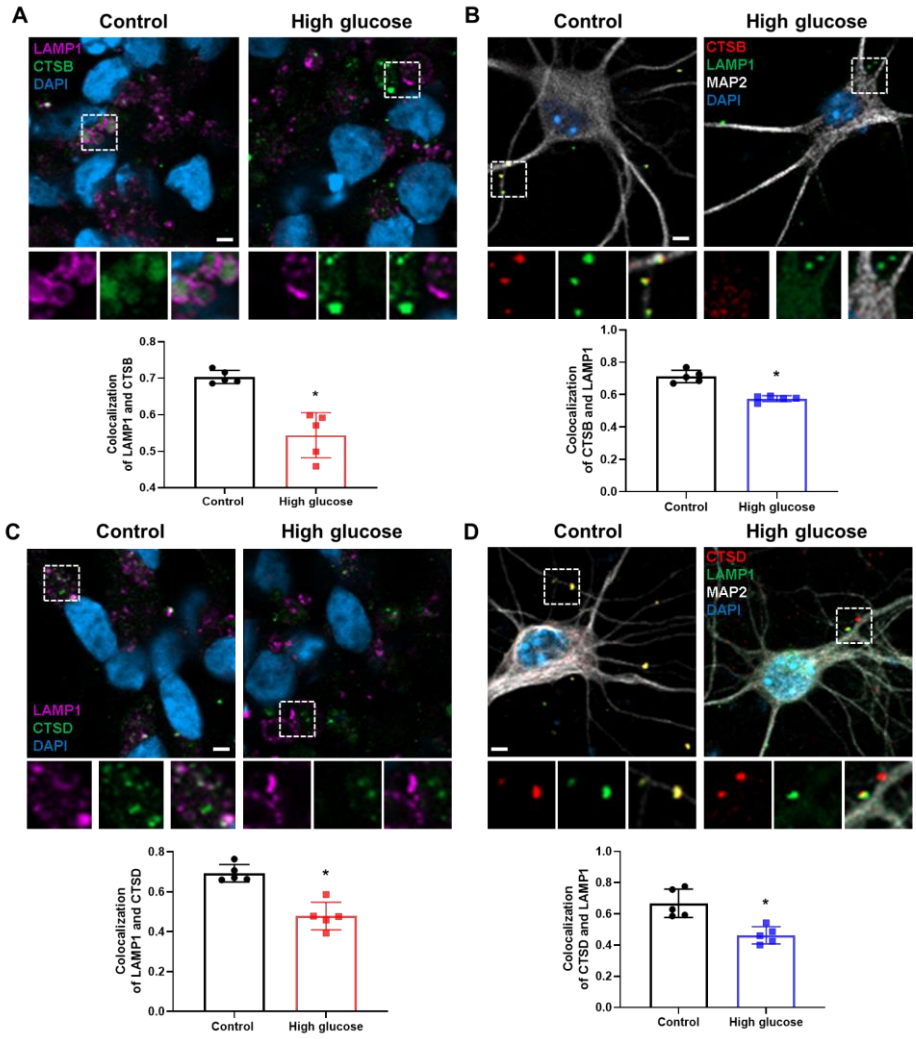

Figure 48. High glucose induces cytosolic release of CTSB and CTSD in both iPSC-NDs and hippocampal neurons.

A, C iPSC-NDs were exposed to high glucose for 24 h. **B, D** Hippocampal neurons were exposed to high glucose for 24 h at DIV 21. **A, B** Double immunofluorescence staining of LAMP1 and CTSB were analyzed in iPSC-NDs and hippocampal neurons. **C, D** iPSC-NDs and hippocampal neurons were immunostained with LAMP1 and CTSD. $n = 5$. $^{*}p < 0.05$ vs. control.

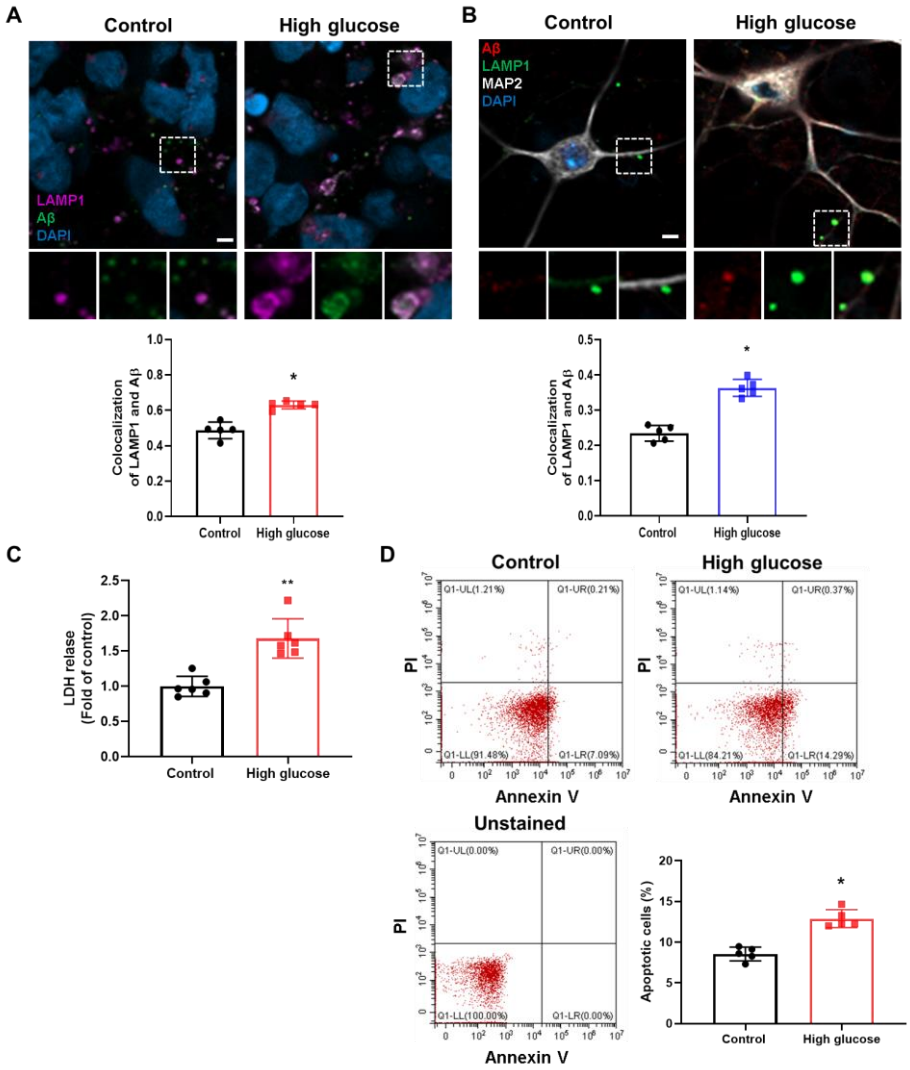

Figure 49. High glucose induces Aβ accumulation in lysosomes and neuronal apoptosis in iPSC-NDs.

A, B iPSC-NDs and hippocampal neurons at DIV 21 were exposed to high glucose for 48 h. Immunofluorescence staining of LAMP1 and Aβ were visualized. **C, D** iPSC-NDs were exposed to HG for 72 h. **C** LDH from cell supernatant were measured with LDH assay kit. **D** The percentage of apoptotic cells (Annexin V and PI positive) were measured by flow cytometric analysis. $n = 5$. Scale bars = 8 μm. $^{*}p < 0.05$, $^{**}p < 0.01$ vs. control.

High glucose suppresses neuronal lysophagy

Studies have reported that ROS overproduction, which is considered as the primary pathogenic mechanism of hyperglycemia-induced disorders, induces LMP (Shah *et al.,* 2016; Chae *et al.,* 2020); therefore, I confirmed whether ROS scavenging alleviates lysosomal dysfunction. Pretreatment with NAC reversed the high-glucose-induced decrease in the signal intensities of the lysotracker, indicating that lysosomal dysfunction was triggered by ROS-mediated LMP under high glucose conditions (Figure 50A). I next focused on the lysophagy machinery to explore how neurons cope with high-glucose-mediated lysosomal damage. In iPSC-NDs, high glucose treatment decreased the degree of colocalization between galectin-3, a marker for lysosomal damage (Miranda *et al.,* 2018), and microtubule-associated protein 1A/1B-light chain 3 (LC3) (Figure 51A). Moreover, high glucose inhibited the recruitments of p62 and ubiquitin to galectin-3 (Figure 51B). In lysosome elimination assay using LLOMe (Maejima *et al.,* 2013), a lysosomotropic reagent, after 3 h of LLOMe washout, the signal intensities of galectin-3 were extensively increased in both control and high-glucose-treated cells. However, 12 h after LLOMe washout, there were significant differences in galectin-3 signal intensities between the control and high-glucose-treated groups, where galectin-3 signal intensities in the control groups were similar to those measured immediately after LLOMe washout (Figure 52A). I conducted RFP and GFP tandem fluorescent-tagged LGALS3/Galetin-

3 (tfGal3) plasmid transfection (Maejima *et al.,* 2013) and lysotracker staining (Jia *et al.,* 2020) to further investigate lysophagy and confirmed that lysophagy was working under normal conditions (Figure 53A). Compared the data with high-glucose-treated groups, which showed that after 12 h of LLOMe washout, there were GFP signal reduction and more RFP-only positive puncta in the control groups, which were canceled by pretreatment with bafilomycin A1, a vacuolar-type ATPase inhibitor (Figure 53B). The signal intensities of the lysotracker were decreased 12 h after LLOMe washout under high glucose conditions, and pretreatment with pepstatin A + leupeptin, inhibitors of lysosomal hydrolases, also decreased lysotracker signal intensities in the control groups (Figure 54A). These findings suggest that high glucose treatment not only induces neuronal lysosomal membrane damage but also suppresses lysophagy activity.

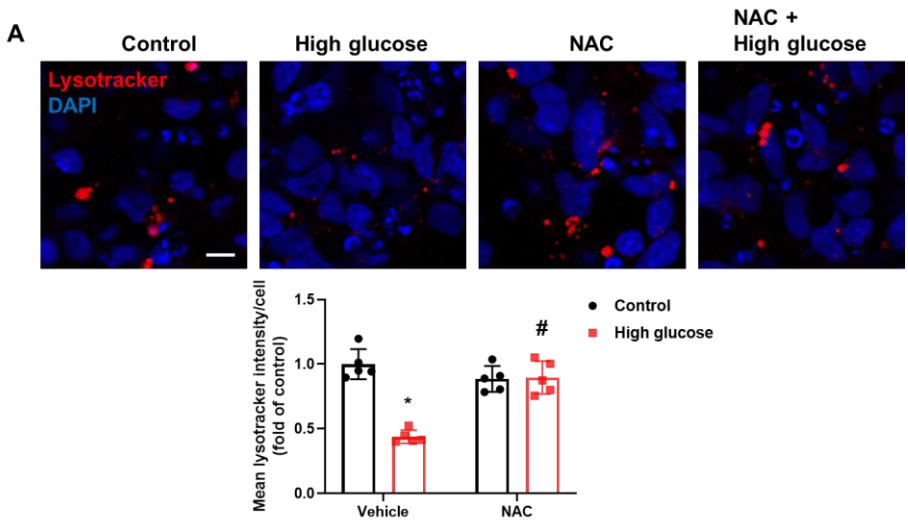

Figure 50. High glucose induces ROS –dependent lysosomal membrane permeabilization.

A iPSC-NDs were pretreated NAC (2 mM) for 30 min before high glucose exposure for 24 h. Lysotracker were visualized by confocal microscope. $n = 5$. Scale bars = 8 μm. $^{*}p < 0.05$ vs. control, $^{\#}p < 0.05$ vs. high glucose.

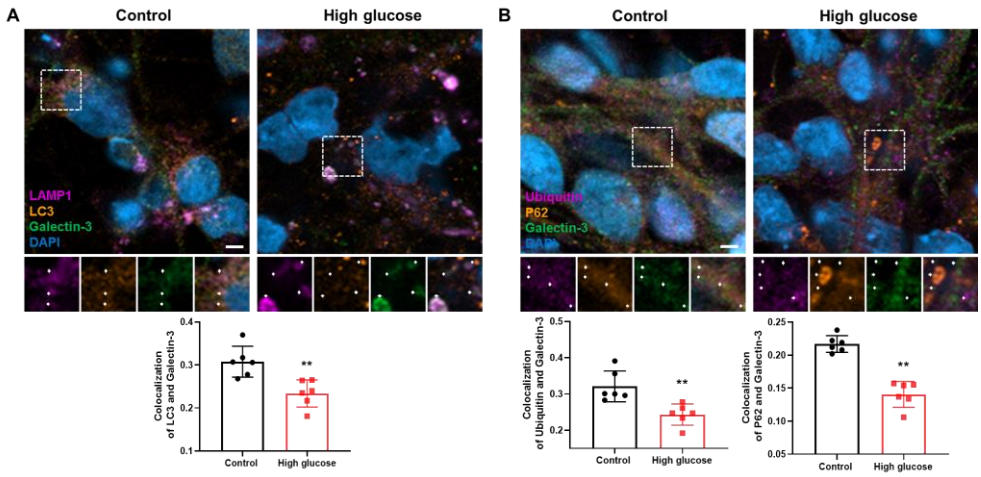

Figure 51. Recruitment of LC3, ubiquitin, and P62 to galectin-3 is blocked by high glucose.

A, B iPSC-NDs were exposed to high glucose for 24 h. **A** The cells were immunostained with LAMP1, LC3, and galectin-3, and counterstained with DAPI. **B** Representative immunofluorescence images showing ubiquitin, p62, galectin-3, and DAPI. $n = 6$. Scale bars = 8 μm. $^{**}p < 0.01$ vs. control.

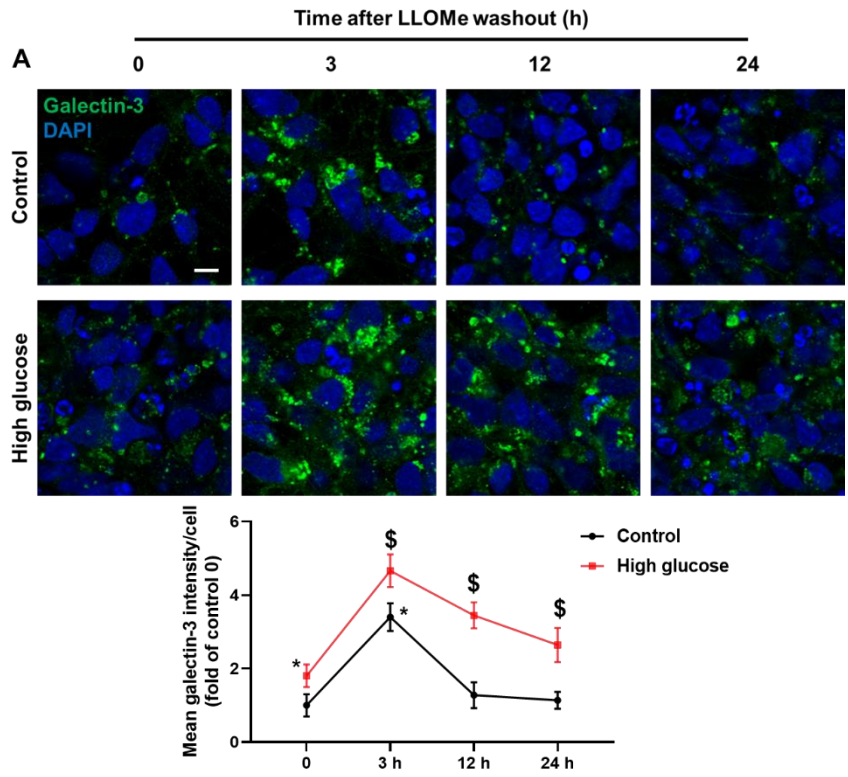

Figure 52. Removal of galectin-3 puncta after lysosomal injury is inhibited by high glucose.

A iPSC-NDs were exposed to high glucose for 24 h. iPSC-NDs were treated with LLOMe (1 mM) for 1 h after high glucose exposure and then washed away. The cells were further incubated for 0 or 3 or 12 or 24 h in the incubator. Immunofluorescence staining of Galectin-3 was visualized. $n = 5$. Scale bars = 8 μm. $^{*}p < 0.05$ vs. control at 0, $^{\$}p < 0.05$ vs. high glucose at 0.

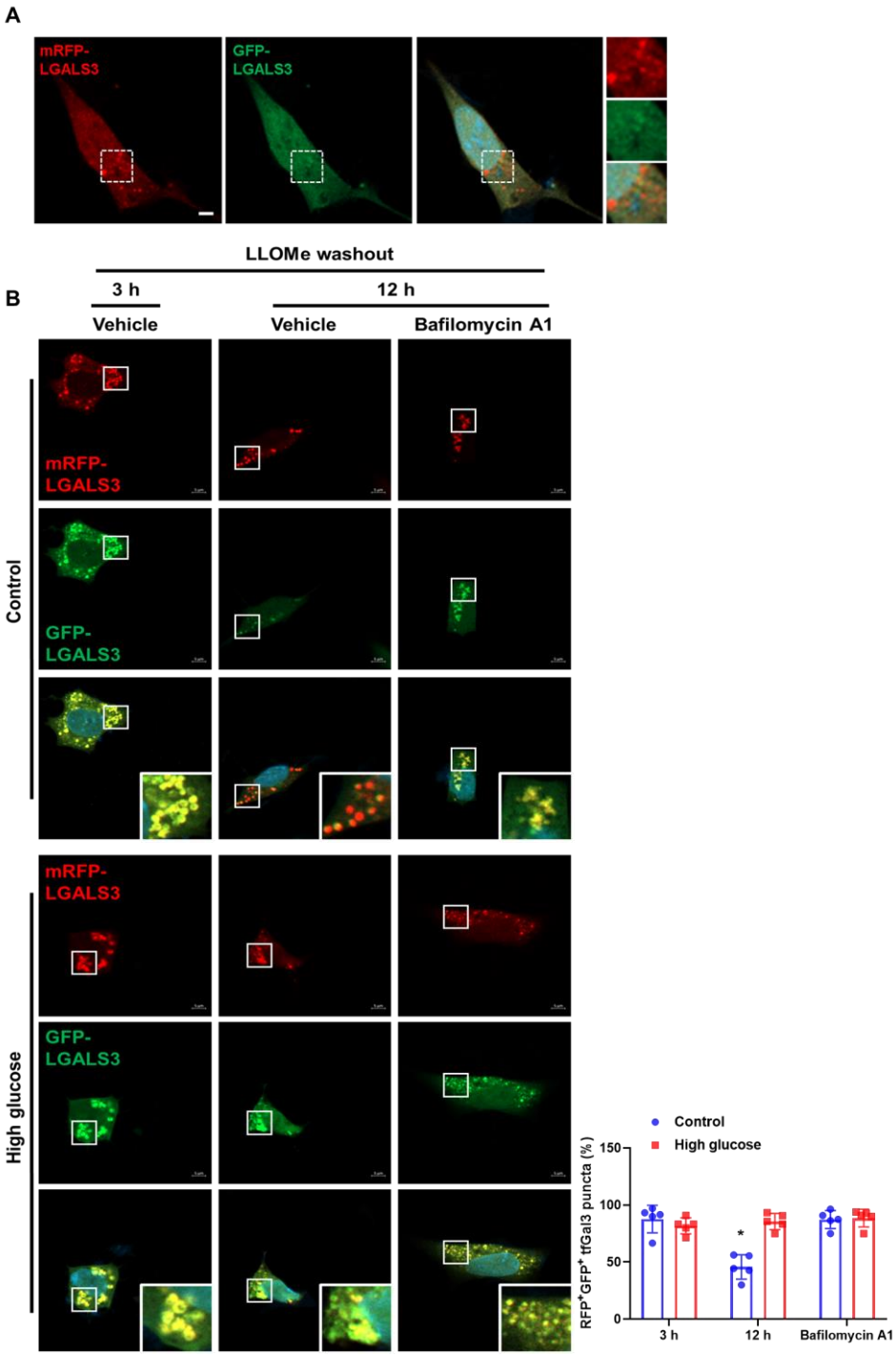

Figure 53. High glucose suppresses lysophagy.

A SH-SY5Ys were transfected with fluorescent-tagged LGALS3/Galetin-3 (tfGal3) plasmid. mRFP-LGALS3 and GFP-LGALS3 were visualized. B Cells were transfected with tfGal3 prior to high glucose exposure for 24 h followed by LLOMe (1 mM) washout assays for 3 or 12 h. Bafilomycin A1 (10 nM) was pretreated for 30 min before incubation for 12 h. mRFP-LGALS3 and GFP-LGALS3 were visualized. $n = 5$. Scale bars = 8 μm. $^{*}p < 0.05$ vs. control at 3 h.

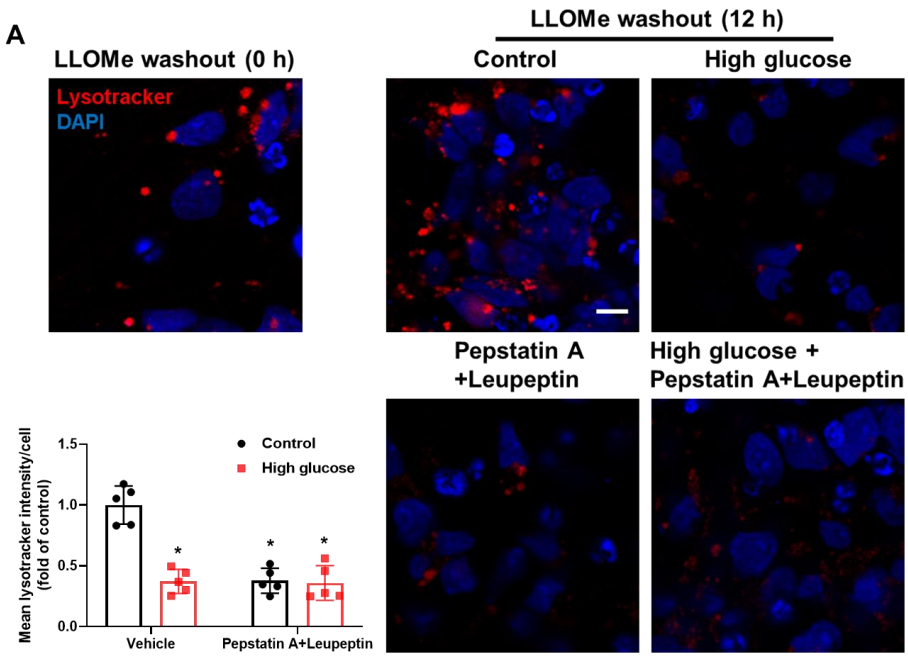

Figure 54. Recovery of intact lysosomes after lysosomal injury is depend on lysophagy.

A iPSC-NDs were exposed to high glucose for 24 h. The cells were exposed to HG for 24 h followed by LLOMe (1 mM) washout for 12 h. Lysotracker and DAPI were visualized. n = 5. Scale bars = 8 μm. $^{*}p$ < 0.05 vs. control.

High glucose-stimulated mTORC1 inhibits TFEB activity, resulting in TRIM16 downregulation.

Upon lysosomal damage, several ubiquitination-related enzymes such as TRIM16, FBXO27, UBE2QL1, LRSAM1, and VCP detect damaged lysosomal membranes, triggering lysophagy (Papadopoulos *et al.*, 2017). To examine how high glucose treatment dysregulates neuronal lysophagy, I measured the mRNA expression levels of lysophagy-related genes in iPSC-NDs, which showed that the mRNA expression of *TRIM16* was significantly down-regulated under high glucose conditions (Figure 55A). Furthermore, the protein level of TRIM16 was reduced in iPSC-NDs, mouse hippocampal neurons, STZ-induced diabetic hippocampus, and SH-SY5Ys (Figure 55B-D and Figure 56A, B). Because mTORC1 activation inhibits autophagy and lysosomal biogenesis, I hypothesized that mTORC1 down-regulates TRIM16 as an upstream signaling molecule under high glucose conditions. Considering that recruitment to the lysosomal membrane is required for mTORC1 activation in response to glucose (Liu *et al.*, 2020), I explored whether mTOR is transported to lysosomes in iPSC-NDs treated with high glucose. As shown in Figure 57A, the degree of colocalization between LAMP1 and mTOR was increased under high glucose conditions. Simultaneously, high glucose treatment decreased AMPK phosphorylation at Thr172 and increased mTOR phosphorylation at Ser2448 (Figure 57B). Activated mTORC1 at the lysosomal membrane inhibits lysosomal biogenesis through phosphorylation-mediated inactivation of TFEB and TFE3, master

regulators of lysosomes (Raben *et al.,* 2016). Other transcription factors that regulate lysosomal genes, such as MITC and TFEC, were excluded because they are rarely expressed in the brain (Uhlen *et al.,* 2015). However, as high glucose can stimulate calcium signaling (Shah *et al.*, 2016), which activates calcineurin, a calcium-dependent phosphatase, and inhibits GSK3β, resulting in activation of TFEB and TFE3 (Saftig *et al.,* 2016), I also examined whether high glucose treatment increases intracellular calcium levels. Considering that intracellular calcium levels were increased at 15 and 30 min after high glucose treatment (Figure 57C), I elucidated the effects of high glucose treatment on the nuclear translocation of TFEB and TFE3, for which I performed pretreatment with rapamycin, an mTOR inhibitor, and BAPTA-AM, a calcium chelator, before high glucose or vehicle treatment. Interestingly, high glucose treatment inhibited TFEB nuclear translocation, which was recovered by rapamycin pretreatment, and calcium chelation decreased TFEB nuclear translocation in the control group, but not in the high glucose conditions. (Figure 58A). This indicates that under high glucose conditions, mTORC1-mediated signaling is superior to calcium-mediated signaling for TFEB activation, suggesting that there is no effect of calcium influx on TFEB activation. However, the nuclear translocation of TFE3 remained unaffected by high glucose treatment and calcium chelation (Figure 58B). As TFEB and TFE3 can regulate the expression of targeted genes bearing the coordinated lysosomal expression and regulation motif (GTCACGTGAC) (Raben *et al.*, 2016), I speculated that there are

several motifs in the TRIM16 promoter region, 500 bp upstream of transcription starting site, to which TFEB and TFE3 can bind (Figure 59A). High glucose treatment suppressed the binding of TFEB to TRIM16 promoter (Figure 59B, C), but there were no significant changes in the binding of TFE3 to TRIM16 promoter (Figure 59D). I performed pretreatments with rapamycin and curcumin C1, an mTOR-independent TFEB activator (Song *et al.,* 2016), to determine whether there are other mTOR-mediated mechanisms for the regulation of TRIM16, except for TFEB inactivation. Results showed that rapamycin and curcumin C1 recovered the mRNA expression and protein levels of TRIM16 reduced by high glucose treatment (Figure 60A, B). These results indicate that mTOR-mediated TFEB inactivation directly down-regulates TRIM16 expression under high glucose conditions.

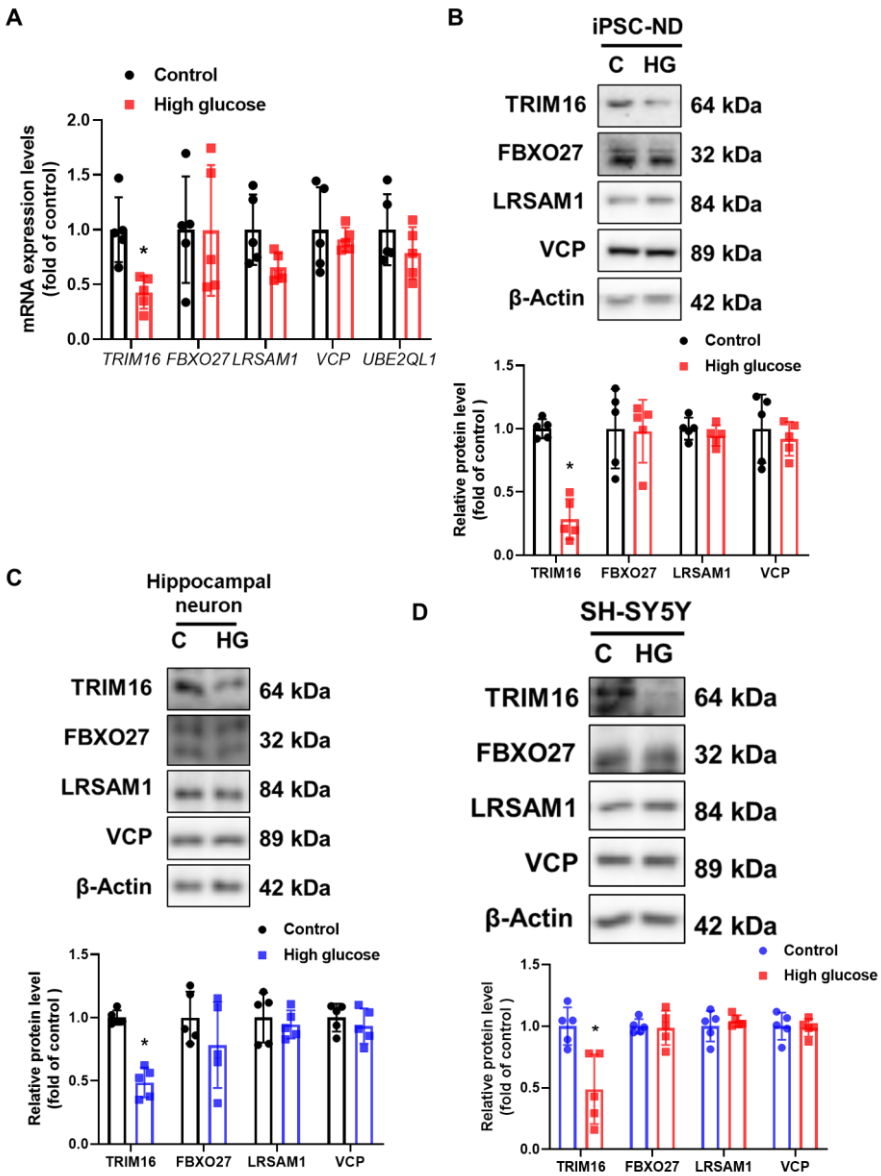

Figure 55. TRIM16 is down-regulated in iPSC-NDs, hippocampal neurons, and SH-SY5Ys exposed to high glucose.

A iPSC-NDs were exposed to high glucose for 24 h. The mRNA expression levels of *TRIM16*, *FBXO27*, *LRSAM1*, *VCP*, and *UBE2QL1* were investigated. **B–D** iPSC-NDs, hippocampal neurons at DIV 21, and SH-SY5Ys were exposed to high glucose for 24 h. The protein levels of TRIM16, FBXO27, LRSAM1, and VCP were detected by western blotting. $n = 5$. $^{*}p < 0.05$ vs. control.

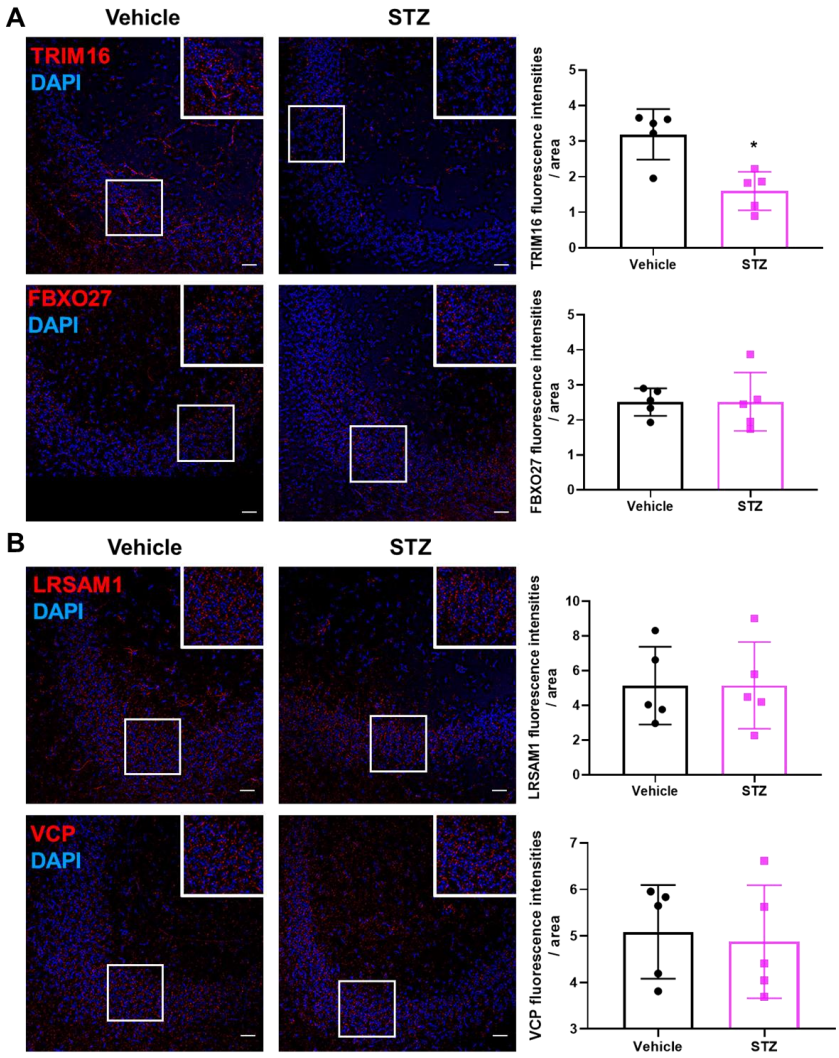

Figure 56. TRIM16 is down-regulated in the hippocampus of diabetic mice.

A, B Representative immunohistochemistry images of the hippocampus of vehicle-or STZ-injected mice showing TRIM16, FBXO27, LRSAM1, and VCP. $n = 5$. $^{*}p < 0.05$ vs. control.

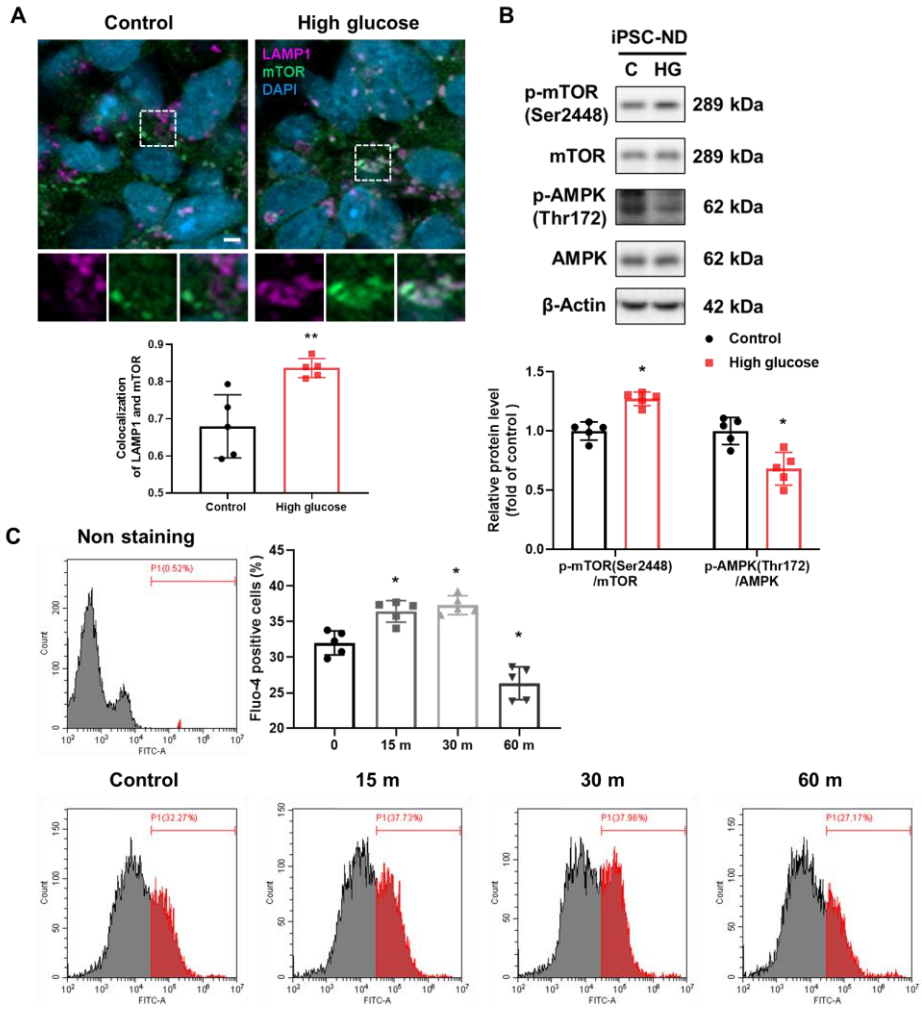

Figure 57. High glucose elevates intracellular calcium levels and activates mTORC1.

A, B iPSC-NDs were exposed to high glucose for 12 h. A LAMP1, mTOR, and DAPI were subjected to immunofluorescence analysis. **B** The protein levels of p-mTOR (Ser2448), mTOR, p-AMPK (Thr172), AMPK, and β-Actin were detected by western blotting. **C** iPSC-NDs were stained with Fluo-4-AM (4 mM) for 1 h and stabilized. The cells were exposed to high glucose for 0, 15, 30, or 60 min and analyzed by flow-cytometry. $n = 5$. Scale bars = 8 μm. $^{*}p < 0.05$, $^{**}p < 0.01$ vs. control.

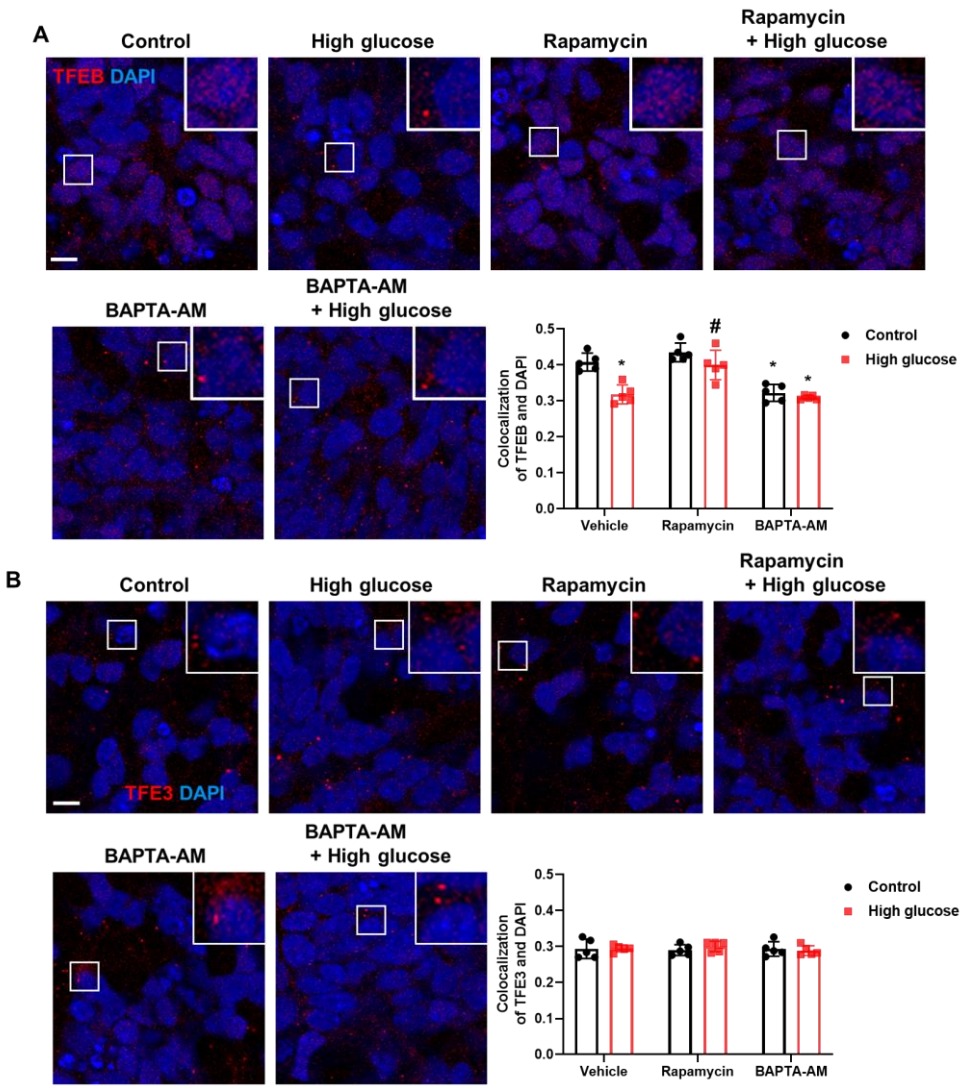

Figure 58. Nuclear translocation of TFEB, but not TFE3, is inhibited by high glucose-mediated mTORC1 activation, and calcium influx has no effect on TFEB nuclear translocation under high glucose conditions.

A, B iPSC-NDs were pretreated with rapamycin (200 nM) or BAPTA-AM (5 μM) for 30 min before high glucose exposure for 12 h. **A** TFEB was immunostained. **B** TFE3 was visualized. $n = 5$. Scale bars = 8 μm. $^{*}p < 0.05$ vs. control, $^{\#}p < 0.05$ vs. high glucose.

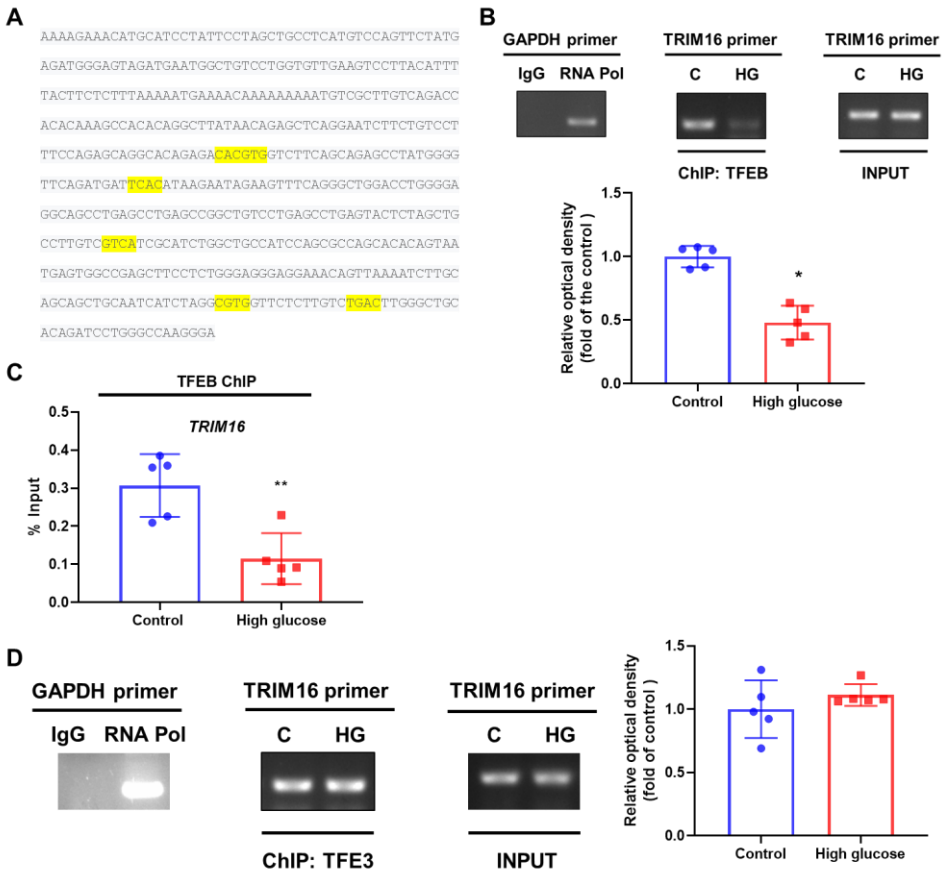

Figure 59. High glucose suppresses the binding of TFEB to TRIM16 promoter.

A 500 base pair upstream of the first codon of the TRIM16 was described and the putative TFEB and TFE3 binding sequences were emphasized with yellow labeling. **B, C** SH-SY5Ys were exposed to high glucose for 12 h. DNA was immunoprecipitated with IgG, RNA polymerase (RNAPol), and TFEB antibody. The samples of immunoprecipitation and input were amplified with primers of *GAPDH* and *TRIM16*. Data were analyzed by conventional PCR and qPCR, respectively. **D** SH-SY5Ys were exposed to high glucose for 12 h. DNA was immunoprecipitated with IgG, RNA polymerase (RNAPol), and TFE3 antibody. The samples of immunoprecipitation and input were amplified with primers of *GAPDH* and *TRIM16*. Data were analyzed by conventional PCR. $n = 5$. $^{*}p < 0.05$, $^{**}p < 0.01$ vs. control.

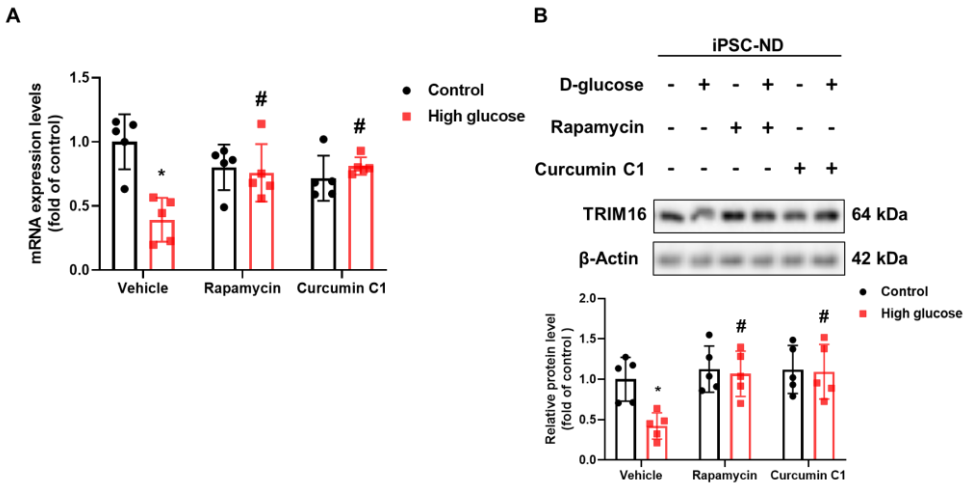

Figure 60. Pharmacological inhibition of mTORC1 and enhancement of TFEB recover high glucose-inhibited TRIM16 levels.

A, B iPSC-NDs were pretreated with rapamycin (200 nM) or curcumin C1 (1 μM) for 30 min before high glucose treatment for 24 h. The mRNA expression and protein levels of TRIM16 were analyzed by qPCR and western blotting, respectively. $n = 5$. $^{*}p < 0.05$, $^{**}p < 0.01$ vs. control; $^{\#}p < 0.05$ vs. high glucose.

Upregulation of TRIM16 recovers lysophagy and lysosomal biogenesis, which induces Aβ and p-Tau degradation.

Among lysophagy-related proteins, TRIM16 expression was decreased during recruitment to the lysosome, wherein the degree of colocalization between FBXO27 or LRSAM1 or VCP and LAMP1 was not significantly altered under high glucose conditions (Figure 61A-D). Because other lysophagy-related proteins other than TRIM16 were located to some extent with the lysosome in the control and high glucose conditions, I investigated whether these proteins did not actually affect lyosphagy. After 12 h of LLOMe washout, *FBXO27* silencing led to increased signal intensities of galectin-3, whereas *LRSAM1* and *VCP* silencing exerted no effects on galectin-3 signal intensities in SH-SY5Ys (Figure 62A). Moreover, *FBXO27* silencing reduced lysotracker signal intensities, whereas *LRSAM1* and *VCP* silencing exerted no effects (Figure 62B). Considering that the endosomal sorting complex required for transport (ESCRT) machinery promotes lysosomal repair (Skowyra *et al.,* 2018), I investigated whether ESCRT complexes were associated with high-glucose-mediated lysosomal quality control. I found that the degree of colocalization of charged multivesicular body protein 4b (CHMP4B) or CHMP4 interacting protein ALIX and LAMP1 was increased in high-glucose-treated iPSC-NDs (Figure 63A, B). These results indicate that although the FBXO27 and ESCRT machinery exerts effects on neuronal lysosomal quality control, TRIM16 downregulation may

impede lysophagy under high glucose conditions. Through pcDNA3.1-Trim16-GFP and pcDNA3.1-TRIM16-GFP transfection in hippocampal neurons and SH-SY5Ys, I observed that the inhibited neuronal lysophagy process was normalized by TRIM16 overexpression. The decreased colocalization between LC3 and galectin-3 induced by high glucose treatment were reversed by TRIM16 overexpression (Figure 64A, B). Moreover, the degree of colocalization between p62 or ubiquitin and galectin-3 in neurons treated with high glucose and transfected with pcDNA3.1-GFP was lower than that in cells treated with high glucose and transfected with pcDNA3.1-Trim16-GFP or pcDNA3.1-TRIM16-GFP (Figure 65A, B). After 12 h of LLOMe washout, the high glucose-inhibited reduction of galectin-3 signal intensities was recovered by TRIM16 overexpression (Figure 66A). Subsequently, the lysotracker signal intensities and number of lysotracker-positive cells that were decreased with high glucose treatment were reversed by TRIM16 overexpression (Figure 67A-C). These findings suggest that high-glucose-mediated TRIM16 downregulation impedes neuronal lysophagy. The quantities of intact lysosomes are maintained through the lysophagy-mediated removal of damaged lysosomes and lysosomal biogenesis-mediated replenishment (Yim *et al.*, 2020; Yang *et al.,* 2021). Also, defective clearance of damaged lysosomes inhibits lysosomal biogenesis (Maejima *et al.,* 2013). Hence, I investigated whether TRIM16-mediated lysophagy affects lysosomal biogenesis

and the function of lysosomal hydrolases. Rab7, a marker for late endosomes, −and LAMP1−positive indicates secondary lysosomes, whereas LAMP1 alone positive indicates primary lysosomes (Yang *et al.,* 2021). The number of Rab7− and LAMP1−positive vesicles was significantly increased under high glucose conditions; however, TRIM16 overexpression increased the number of LAMP1−alone−positive vesicles and decreased that of secondary lysosomes in hippocampal neurons and SH−SY5Ys (Figure 68A, B). Treatment with high glucose inhibited neuronal CTSD and CTSB activities, which were recovered by pcDNA3.1−TRIM16−GFP transfection (Figure 69A, B). Since the deficiency of autophagy is also a potential mechanism of Aβ accumulation caused by lysosomal dysfunction, I investigated whether TRIM16−mediated lysophagy affects autophagy. Indeed, the formation of autophagosome and autolysosome was inhibited under high glucose conditions and restored by TRIM16 overexpression (Figure 69C, D). The up−regulated expressions of C99, p−Tau thr181, p−Tau thr212, and Aβ were inhibited by TRIM16 overexpression (Figure 70A, B). The high−glucose−induced neuronal cell death was also protected by pcDNA3.1−TRIM16−GFP transfection (Figure 70C). These observations suggest that impairment of TRIM16−mediated lysophagy inhibits lysosomal biogenesis and inhibits Aβ and p−Tau degradation and neuronal cell death.

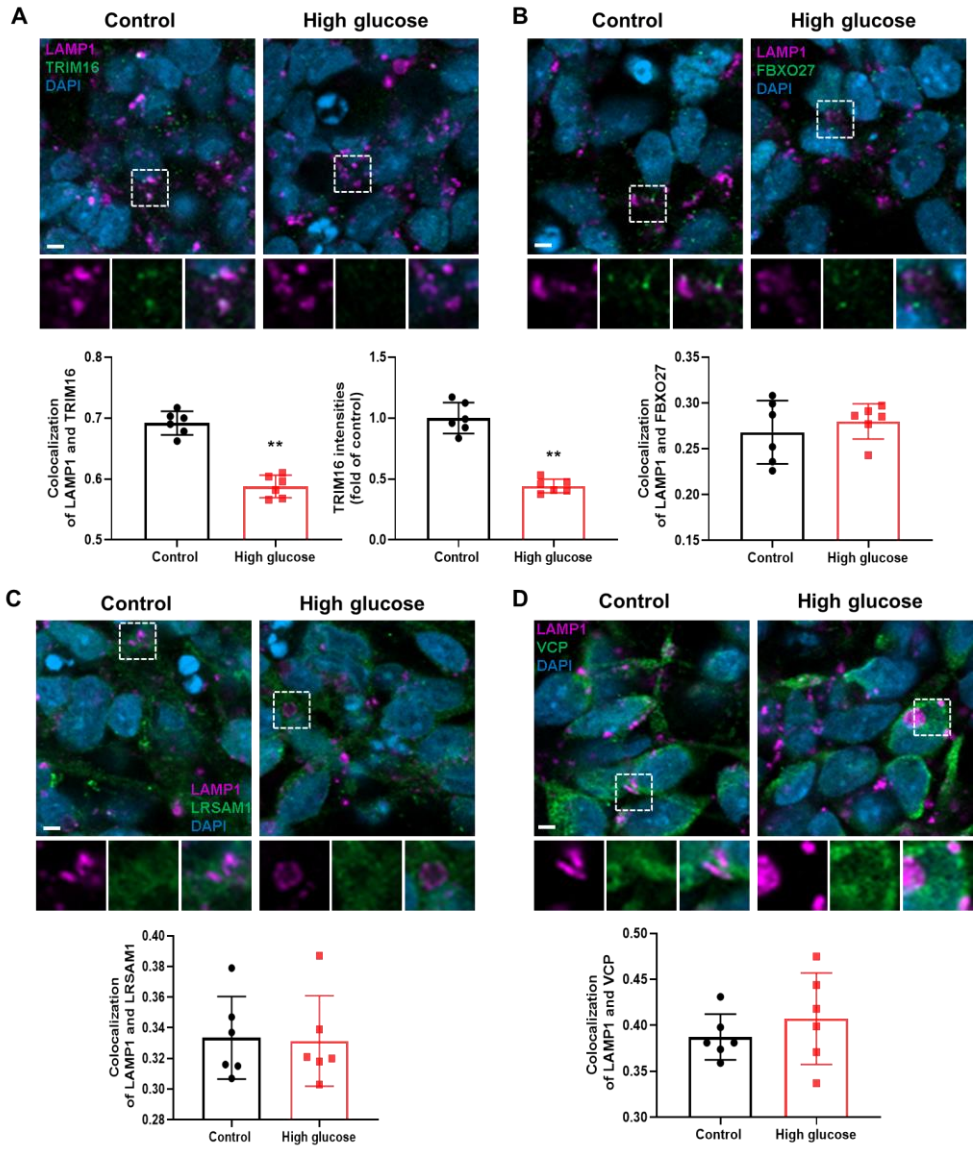

Figure 61. Recruitment of TRIM16, not FBXO27, LRSAM1, and VCP, to the lysosome is inhibited under high glucose conditions.

A–D iPSC–NDs were exposed to high glucose for 24 h. **A** Immunofluorescence images staining of LAMP1 and TRIM16 were visualized. **B** Immunofluorescence images showing LAMP1 and FBXO27. **C** The cells were immunostained with LAMP1 and LRSAM1. **D** iPSC–NDs were visualized with LAMP1–and VCP–specific antibodies. $n = 6$. Scale bars = 8 μm. $^{**}p < 0.01$ vs. control.

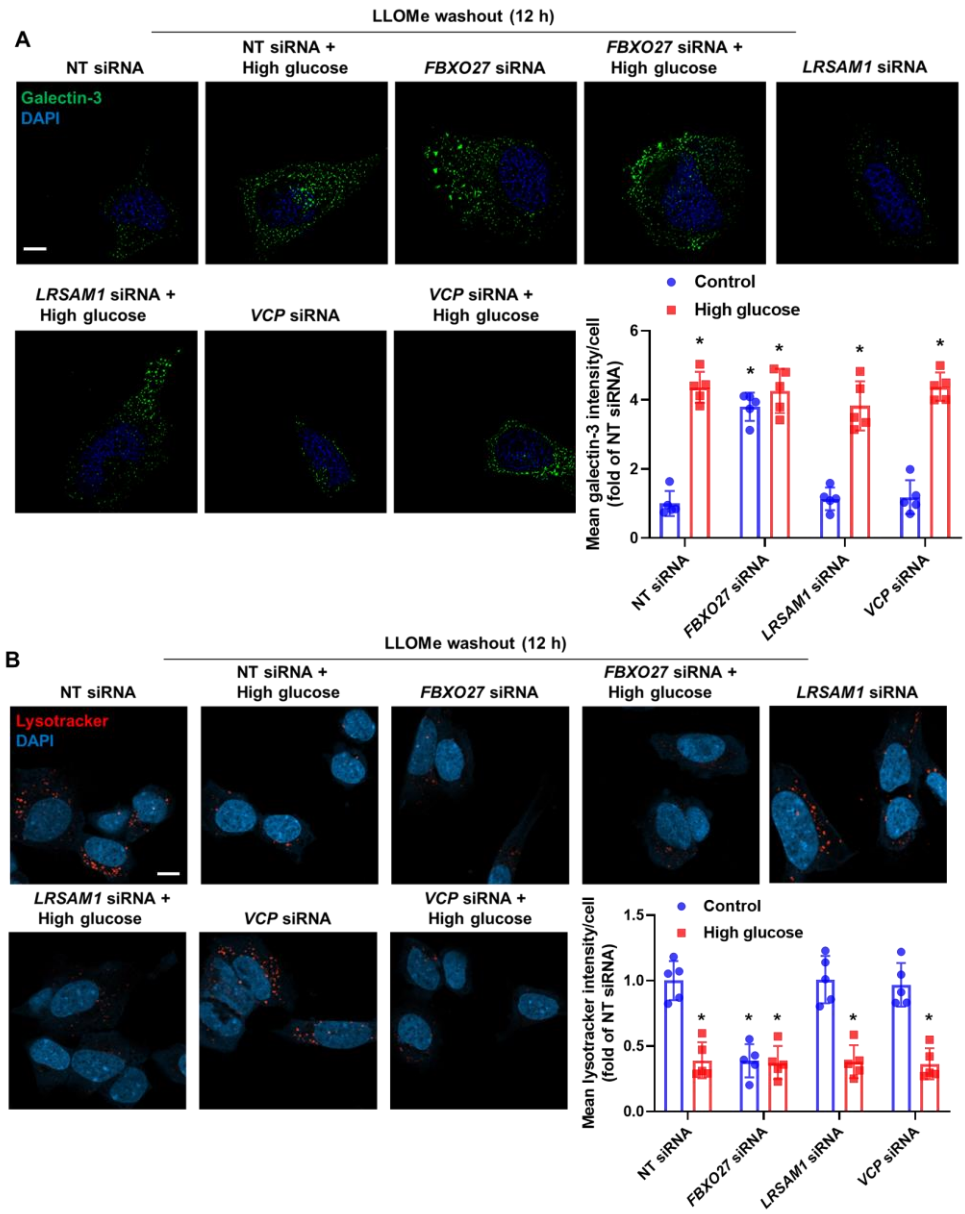

Figure 62. Silencing of *FBXO27*, not *LRSAM1* and *VCP*, inhibits lysophagy.

A, B SH-SY5Ys were transfected with NT, *FBXO27*, *LRSAM1*, or *VCP* siRNA for 12 h prior to high glucose exposure for 24 h. **A** The cells were treated with LLOMe (1 mM) for 1 h after HG treatment and further incubated for 12 h in the incubator. Damaged lysosomes were immunostained with galectin-3. **B** Representative images of lysotracker staining. $n = 5$. Scale bars = 8 μm. $^{*}p < 0.05$ vs. NT siRNA.

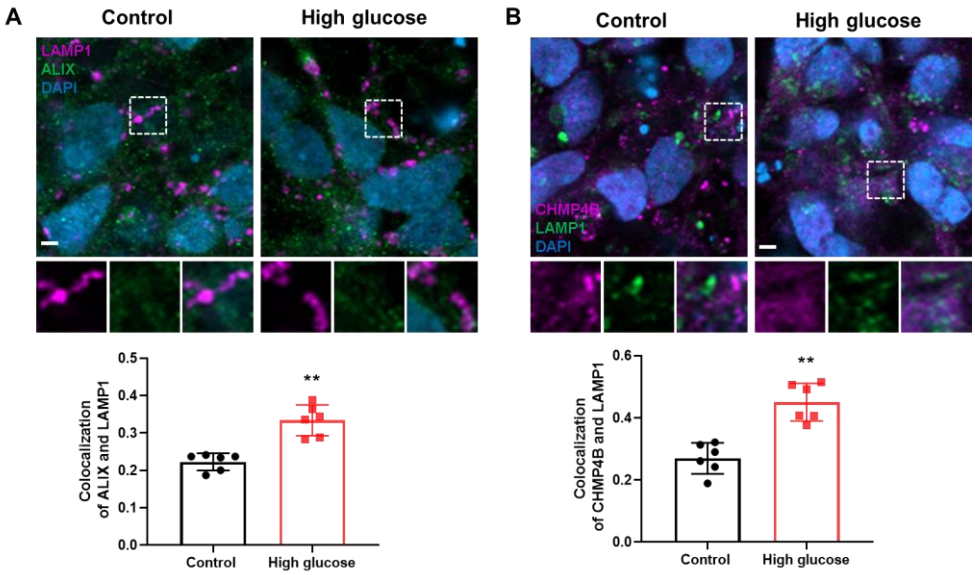

Figure 63. ALIX and CHMP4B recruitment to the lysosome is increased by high glucose.

A, B iPSC-NDs were exposed to high glucose for 24 h. **A** Representative image showing LAMP1 and ALIX. **B** CHMP4B and lAMP1 were immunostained. $n = 6$. Scale bars = 8 μm. $^{**}p < 0.01$ vs. control.

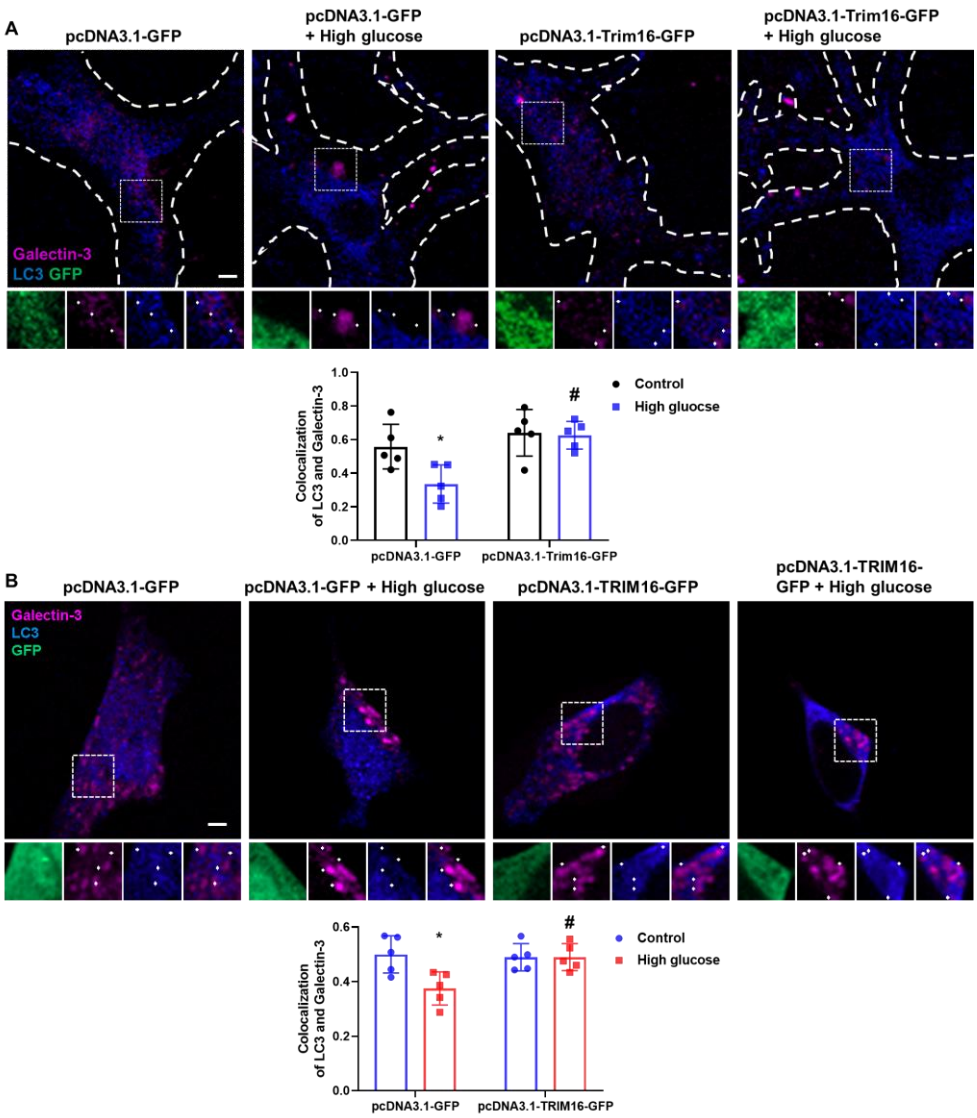

Figure 64. TRIM16 overexpression reverses the decreased colocalization between LC3 and galectin-3 induced by high glucose.

A Hippocampal neurons were transfected with pcDNA3.1−GFP or pcDNA3.1−Trim16−GFP at DIV 4 and exposed to high glucose for 24 h at DIV 21. **B** SH−SY5Ys were transfected with pcDNA3.1−GFP or pcDNA3.1−TRIM16−GFP before high glucose exposure for 24 h. **A, B** Representative immunofluorescence images showing LC3 and galectin−3. $n = 5$. Scale bars = 8 μm. $^{*}p < 0.05$ vs. control, $^{\#}p < 0.05$ vs. high glucose.

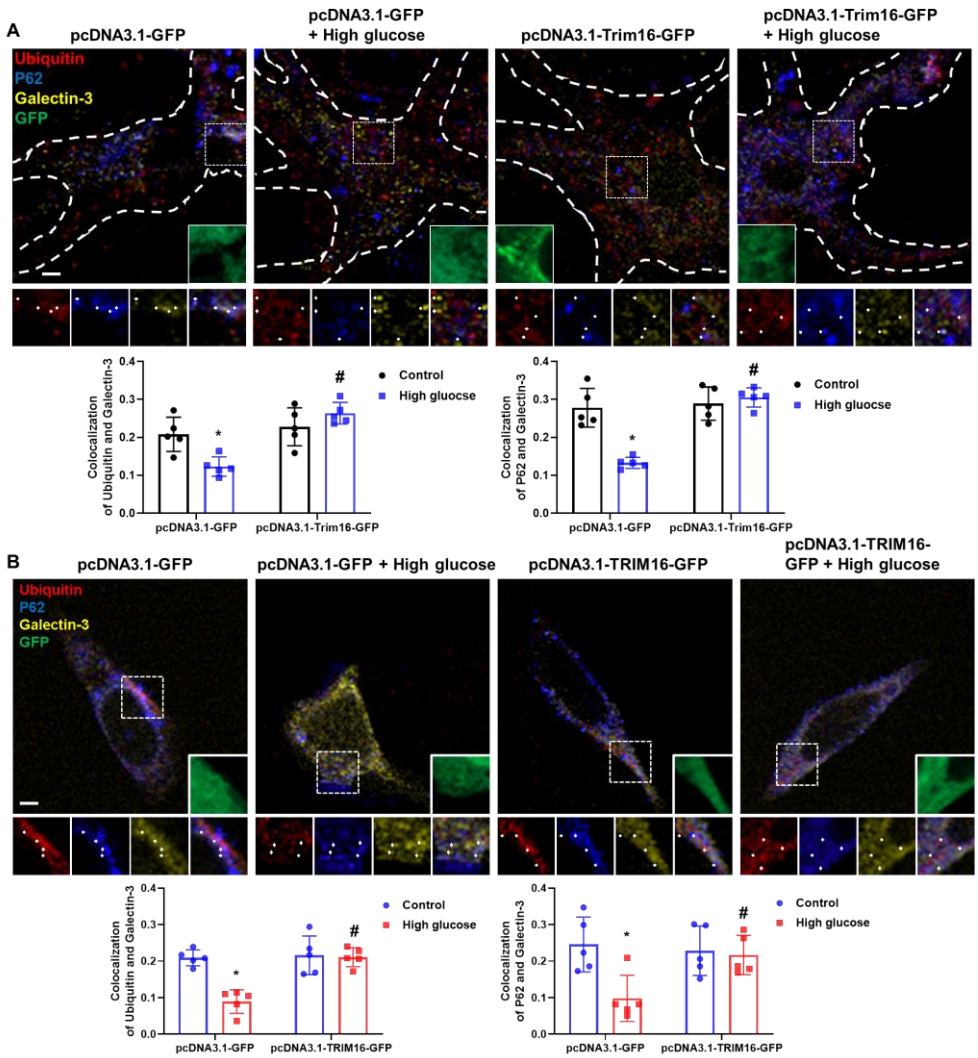

Figure 65. TRIM16 overexpression reverses the decreased colocalization between p62 or ubiquitin and galectin-3 induced by high glucose.

A Hippocampal neurons were transfected with pcDNA3.1−GFP or pcDNA3.1−Trim16−GFP at DIV 4 and exposed to high glucose for 24 h at DIV 21. **B** SH−SY5Ys were transfected with pcDNA3.1−GFP or pcDNA3.1−TRIM16−GFP before high glucose exposure for 24 h. **A, B** The cells were immunostained with ubiquitin, p62, and galectin−3. $n = 5$. Scale bars = 8 μm. $^{*}p < 0.05$ vs. control, $^{\#}p < 0.05$ vs. high glucose.

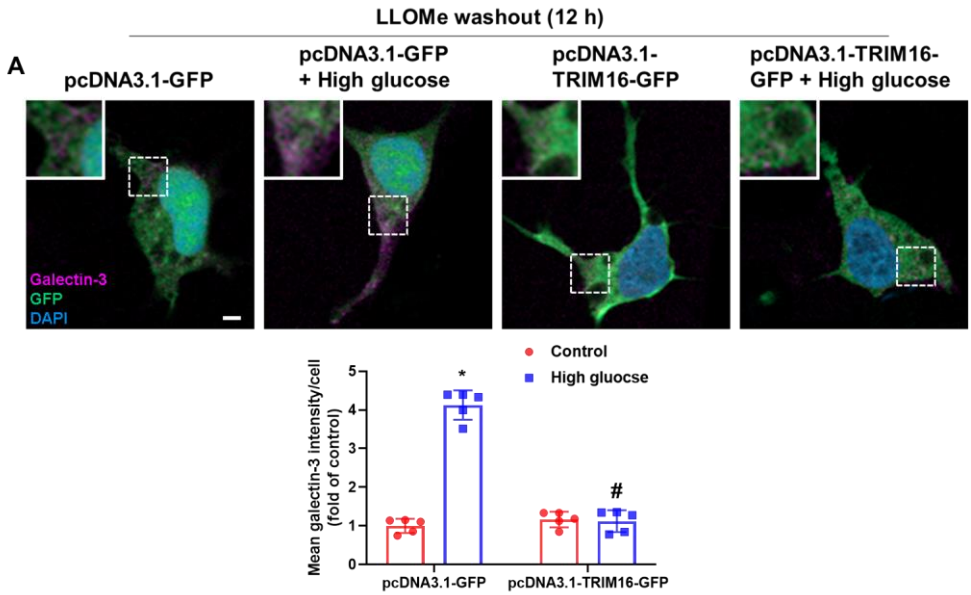

Figure 66. TRIM16 overexpression induces removal of galectin-3 signal intensities inhibited by high glucose after lysosomal injury.

A SH-SY5Ys were transfected with pcDNA3.1-GFP or pcDNA3.1-TRIM16-GFP before high glucose exposure for 24 h. LLOMe (1 mM) washout assay was performed for 12 h followed by immunostaining with galectin-3. n = 5. Scale bars = 8 μm. $^{*}p < 0.05$ vs. control, $^{\#}p$ <0.05 vs. high glucose.

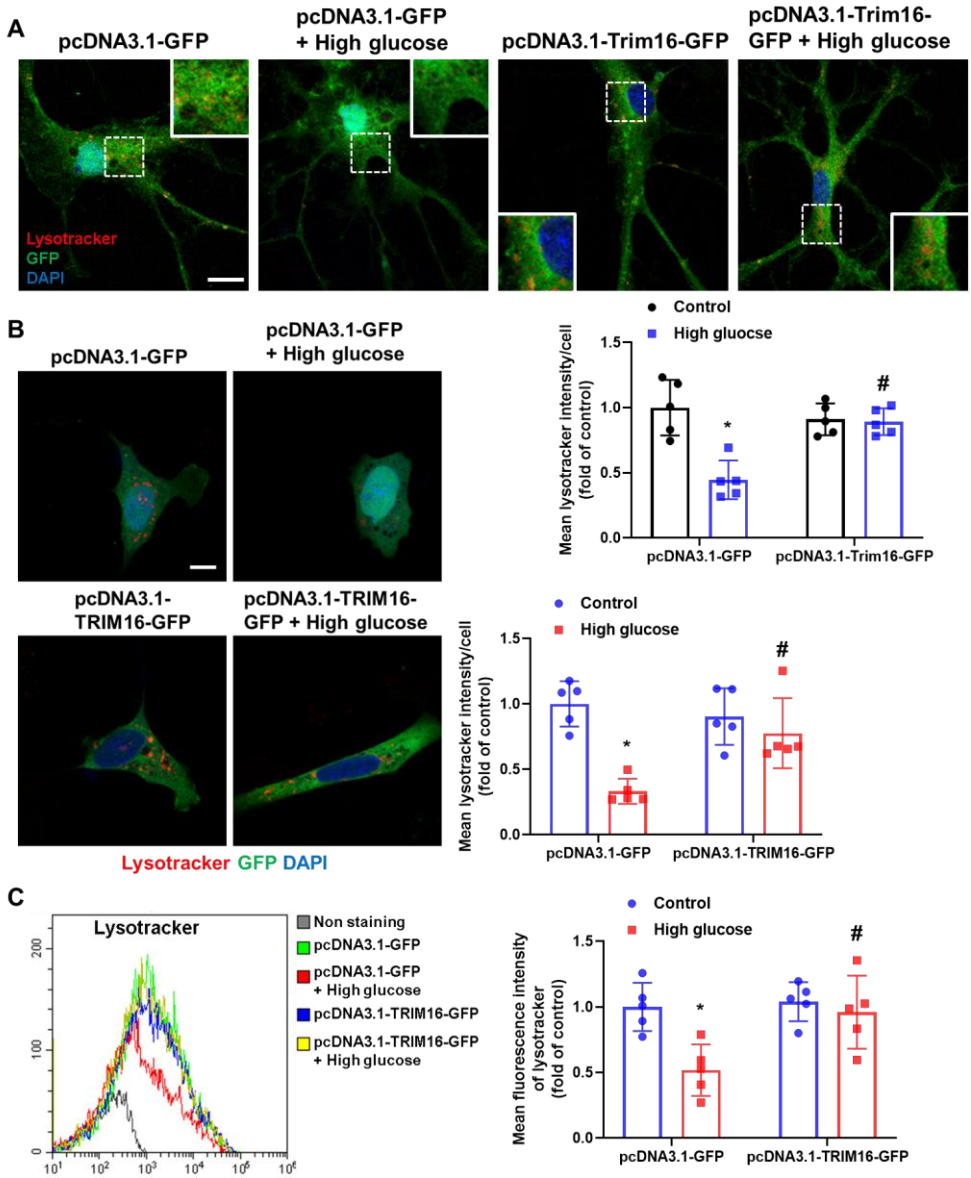

Figure 67. TRIM16 overexpression recovers lysotracker signal intensities inhibited by high glucose.

A Hippocampal neurons were transfected with pcDNA3.1−GFP or pcDNA3.1−Trim16−GFP at DIV 4 and exposed to high glucose for 24 h at DIV 21. B, C SH−SY5Ys were transfected with pcDNA3.1−GFP or pcDNA3.1−TRIM16−GFP before high glucose exposure for 24 h. **A, B** Lysotracker was visualized and DAPI was used to stain nuclei. **C** Mean fluorescence intensities of lysotracker were analyzed by flow cytometric analysis. $n = 5$. Scale bars = 8 μm. $^{*}p < 0.05$ vs. control, $^{\#}p < 0.05$ vs. high glucose.

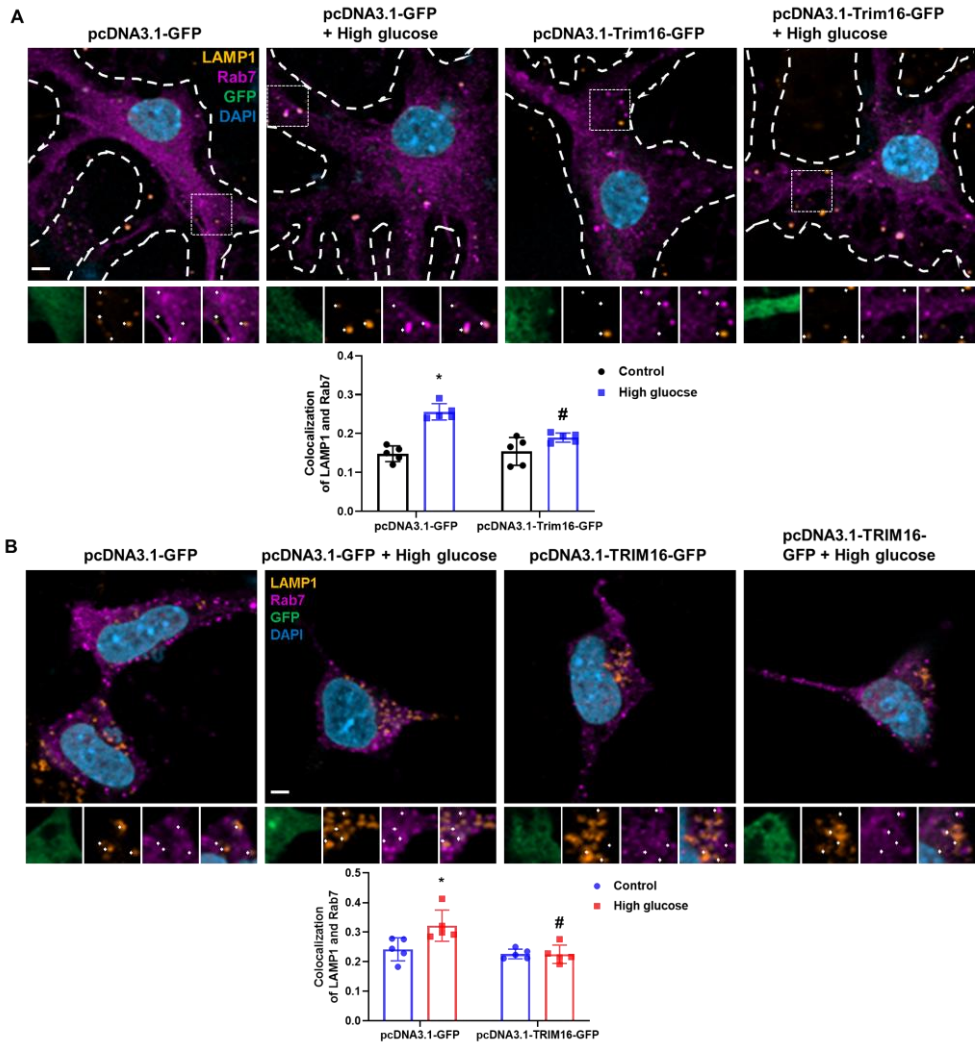

Figure 68. TRIM16 overexpression reverses the increased colocalization between Rab7 and LAMP1 induced by high glucose.

A Hippocampal neurons were transfected with pcDNA3.1−GFP or pcDNA3.1−Trim16−GFP at DIV 4 and exposed to high glucose for 24 h at DIV 21. **B** SH−SY5Ys were transfected with pcDNA3.1−GFP or pcDNA3.1−TRIM16−GFP prior to high glucose exposure. **A, B** Representative immunofluorescence images showing LAMP1 and Rab7. $n = 5$. Scale bars = 8 μm. $^{*}p < 0.05$ vs. control, $^{\#}p < 0.05$ vs. high glucose.

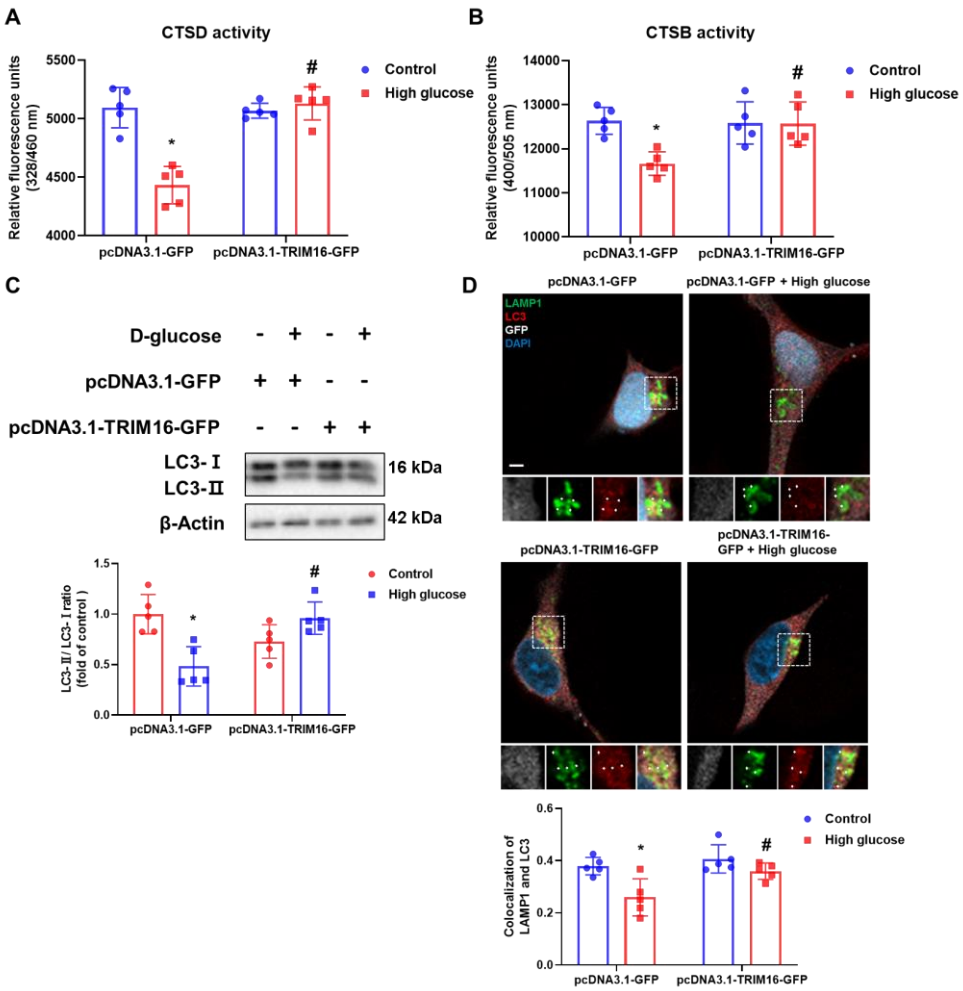

Figure 69. TRIM16 overexpression recovers activities of lysosomal hydrolases and autophagy inhibited by high glucose.

A–D SH-SY5Ys were transfected with pcDNA3.1-GFP or pcDNA3.1-TRIM16-GFP prior to high glucose exposure **A, B** The activities of CTSD and CTSB in the cell lysate were measured. **C** The protein levels of LC3 and β-Actin were detected **D** Representative immunofluorescence images showing LAMP1 and LC3. $n = 5$. Scale bars = 8 μm. $^{*}p < 0.05$ vs. control, $^{\#}p < 0.05$ vs. high glucose.

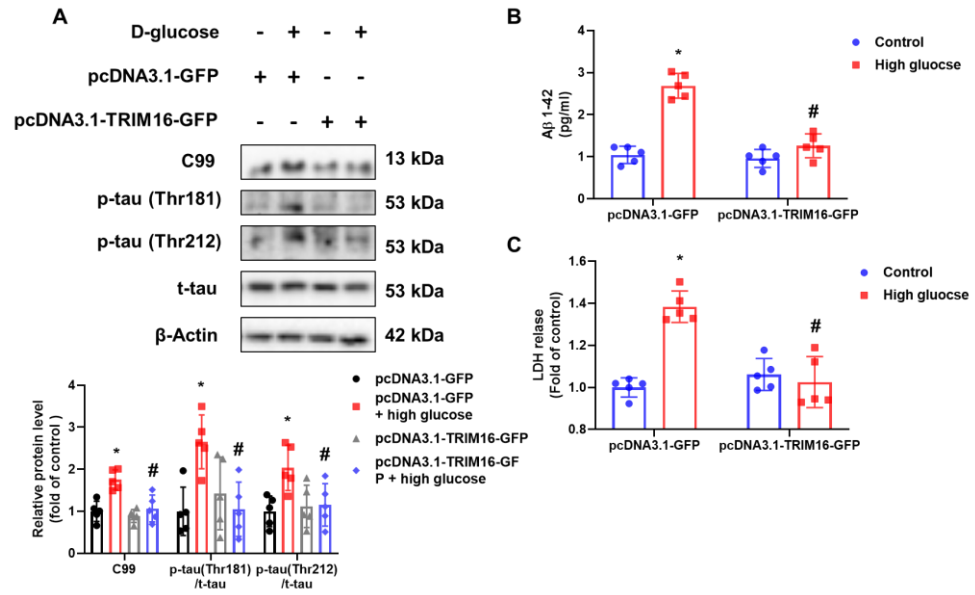

Figure 70. TRIM16 overexpression degrades high glucose-accumulated Aβ and p-Tau, and prevents cell death.

A-C SH-SY5Ys were transfected with pcDNA3.1-GFP or pcDNA3.1-TRIM16-GFP prior to high glucose exposure **A** The protein levels of C99, p-Tau (Thr181), p-Tau (Thr212), t-Tau, and β-Actin were detected by western blotting. **B** After exposure to high glucose for 48 h, Aβ 1-42 from cell culture medium were measured. **C** LDH from cell supernatant were measured after exposure to high glucose for 72 h. $n = 5$. $^{*}p < 0.05$ vs. control, $^{\#}p < 0.05$ vs. high glucose.

TFEB enhancement recovers TRIM16-mediated lysophagy, ameliorating cognitive impairment in STZ-induced diabetic mice

To explore whether TRIM16-mediated lysophagy is involved in the pathogenesis of diabetes-associated AD-like phenotype, I treated STZ-induced diabetic mice with the TFEB activator curcumin C1 (Song *et al.,* 2016) orally for 8 weeks (Figure 71A). I measured the body weight and blood glucose levels of mice at 8 and 18 weeks of age (Figure 71B, C). Results showed that TFEB nuclear translocation was inhibited in the hippocampus of STZ-induced diabetic mice, which was reversed by curcumin C1 (Figure 72A). Curcumin C1 increased the diabetes-reduced TRIM16 protein levels in the hippocampus (Figure 73A). The degree of colocalization between galectin-3 and LC3 in mice treated with STZ and curcumin C1 was higher than that in STZ-treated mice (Figure 73B). Curcumin C1 treatment also alleviated the cytosolic release of CTSB and CTSD in the hippocampus of STZ-treated mice (Figure 74A, B). Subsequently, curcumin C1 inhibited the upregulation of hippocampal C99, Aβ, and p-Tau expression in STZ-treated mice (Figure 75A, B). Results of the open field test showed that diabetic mice spent less time in the center compared with other mice groups (Figure 76A). Furthermore, results of the NOR test showed that STZ-treated mice had decreased discrimination index and novelty preference, which were alleviated by curcumin C1 treatment (Figure 76B). The results of Y-maze test revealed that curcumin C1 recovered the diabetes-reduced spontaneous alternation (Figure 76C). These

results suggest that Aβ and p-Tau accumulation, anxiety, and cognitive impairment in diabetic mice were caused by the impairment of TRIM16-mediated lysophagy.

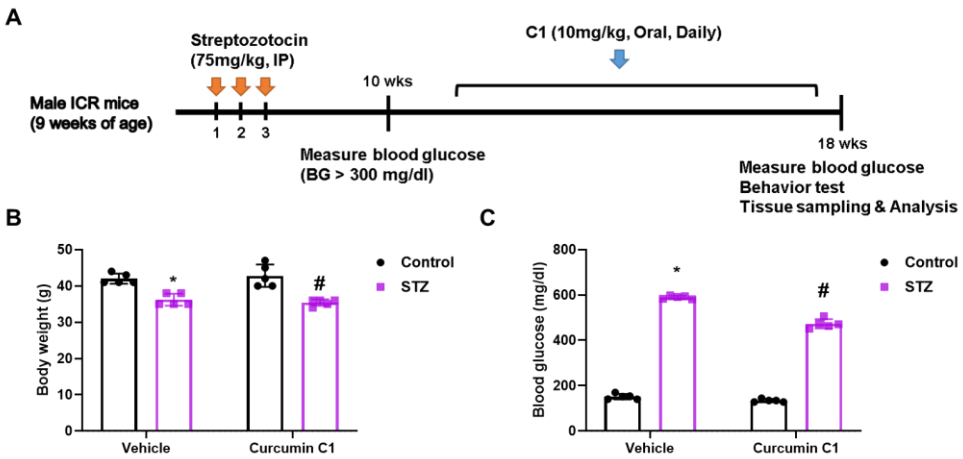

Figure 71. Scheme of an *in vivo* experimental protocol using curcumin C1 treatment, and body weight and blood glucose of experimental animals.

A The schematic *in vivo* flow chart. Mice (9 weeks of age) injected with vehicle or STZ were orally administrated vehicle or curcumin C1 (10 mg/kg) once daily for 8 weeks after diabetes induction, and then subjected to behavior tests and biochemical analysis. B, C Body weight and blood glucose levels were measured at 18 weeks of age, respectively. $n = 5$. $^{*}p < 0.05$ vs. vehicle-injected mice, $^{\#}p < 0.05$ vs. STZ-injected mice.

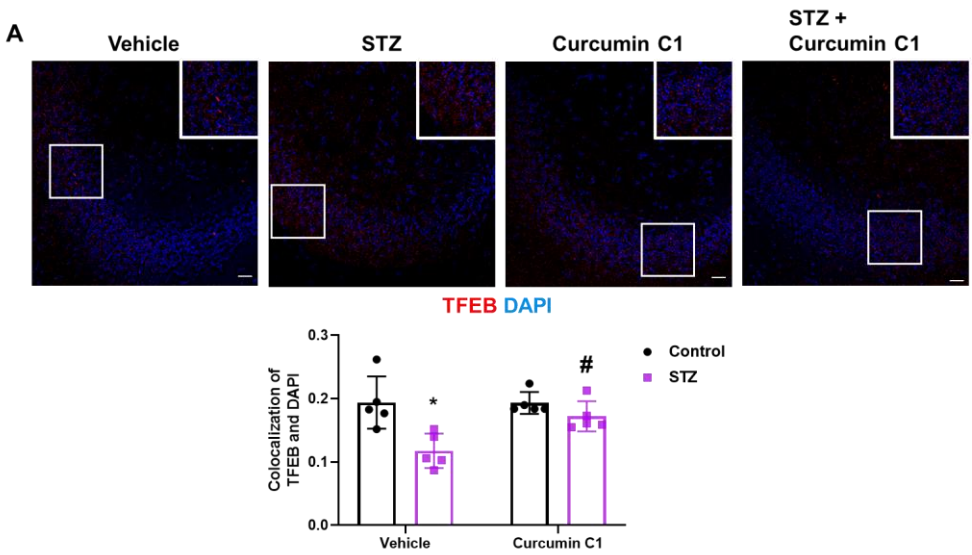

Figure 72. Curcumin C1 reverses TFEB nuclear translocation inhibited in the hippocampus of diabetic mice.

A Hippocampus were immunostained with TFEB and DAPI. $n = 5$. $^{*}p < 0.05$ vs. vehicle-injected mice, $^{\#}p < 0.05$ vs. STZ-injected mice.

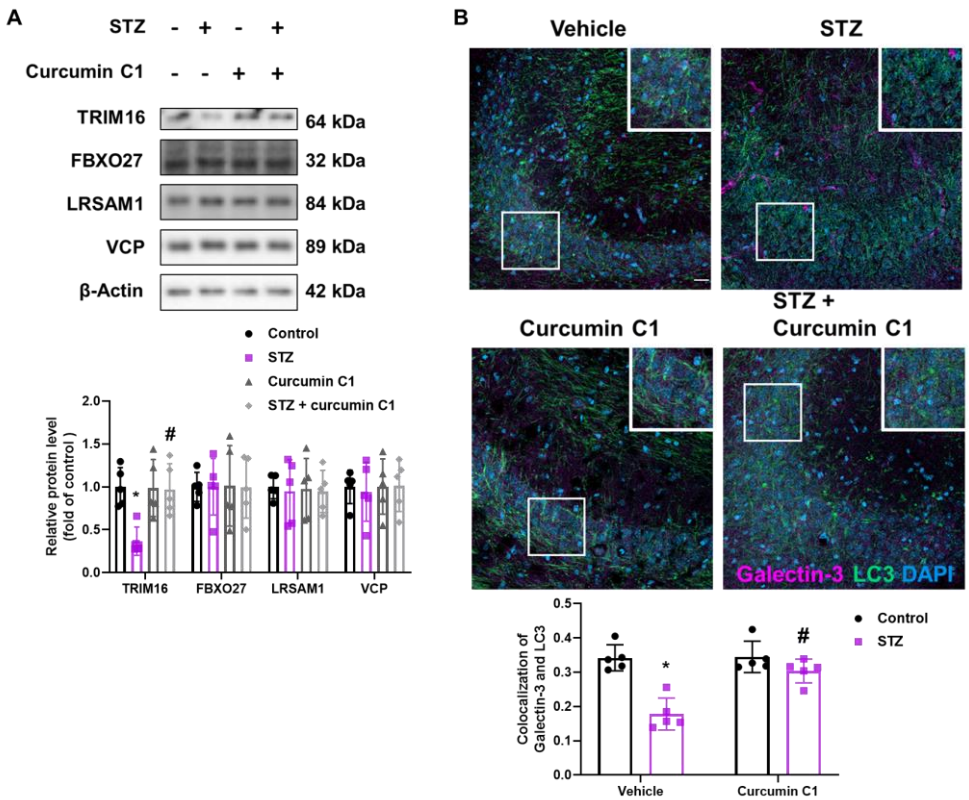

Figure 73. Curcumin C1 recovers lysophagy inhibited in the hippocampus of diabetic mice.

A, B Mice injected with vehicle or STZ were orally administrated vehicle or curcumin C1 (10 mg/kg) once daily for 8 weeks after diabetes induction. **A** Protein levels of the hippocampal TRIM16, FBXO27, LRSAM1, VCP, and β-Actin were determined by western blotting. **B** Representative immunohistochemistry images showing galectin-3 and LC3. $n = 5$. $^{*}p < 0.05$ vs. vehicle-injected mice, $^{\#}p < 0.05$ vs. STZ-injected mice.

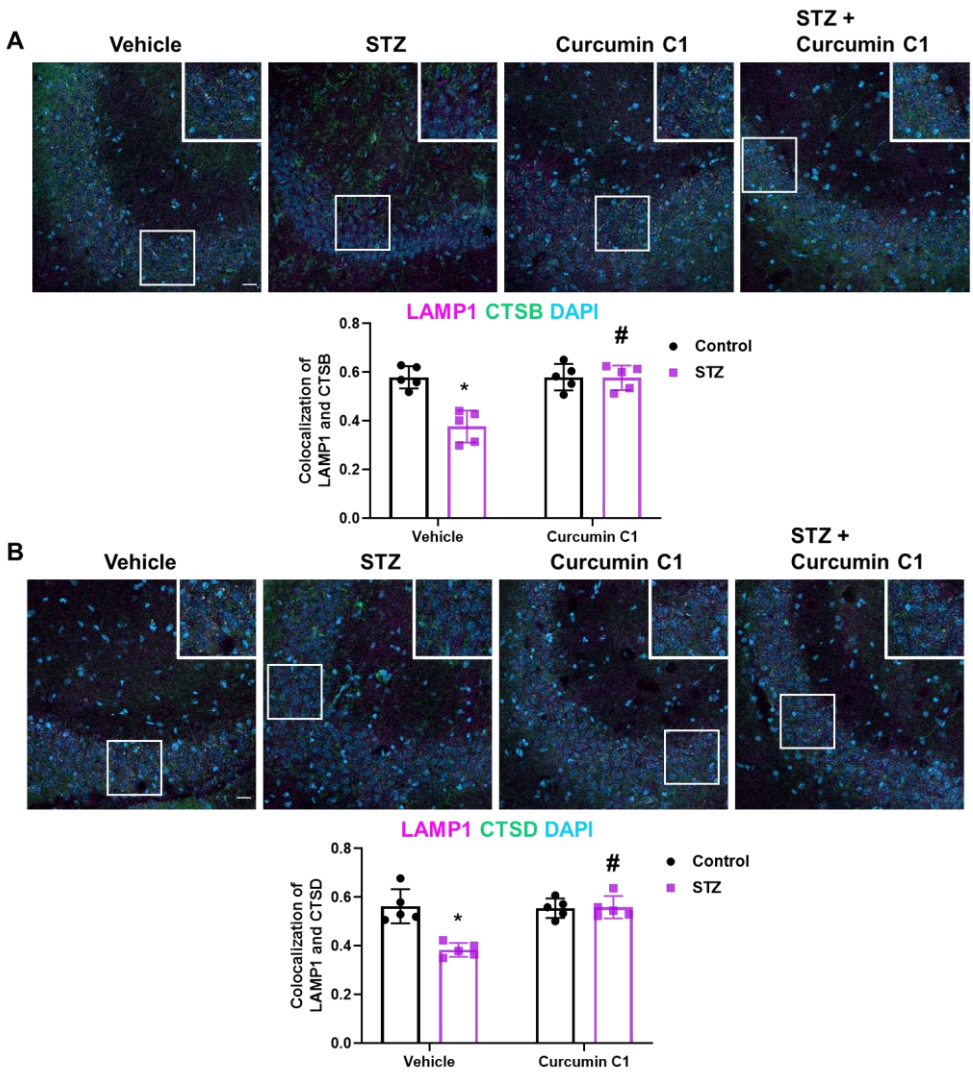

Figure 74. Curcumin C1 ameliorates cytosolic release of lysosomal hydrolases induced in the hippocampus of diabetic mice.

A, B Mice injected with vehicle or STZ were orally administrated vehicle or curcumin C1 (10 mg/kg) once daily for 8 weeks after diabetes induction. **A** The hippocampal slides were immunostained with LAMP1 and CTSB. **B** Immunofluorescence staining of LAMP1 and CTSD in the hippocampus. $n = 5$. $^{*}p < 0.05$ vs. vehicle−injected mice, $^{\#}p < 0.05$ vs. STZ−injected mice.

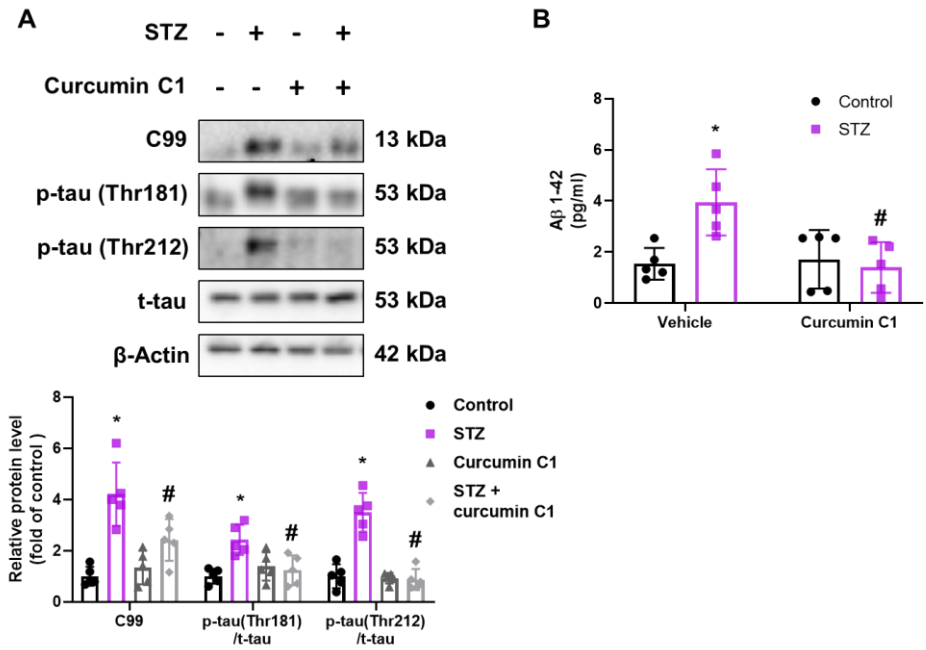

Figure 75. Curcumin C1 inhibits Aβ and p-Tau accumulation in the hippocampus of diabetic mice.

A, B Mice injected with vehicle or STZ were orally administrated vehicle or curcumin C1 (10 mg/kg) once daily for 8 weeks after diabetes induction. A Hippocampal C99, p-Tau (Thr181), p-Tau (Thr212), t-Tau, and β-Actin were subjected to western blotting. B Hippocampal Aβ 1-42 were measured. $n = 5$. $^{*}p < 0.05$ vs. vehicle-injected mice, $^{\#}p < 0.05$ vs. STZ-injected mice.

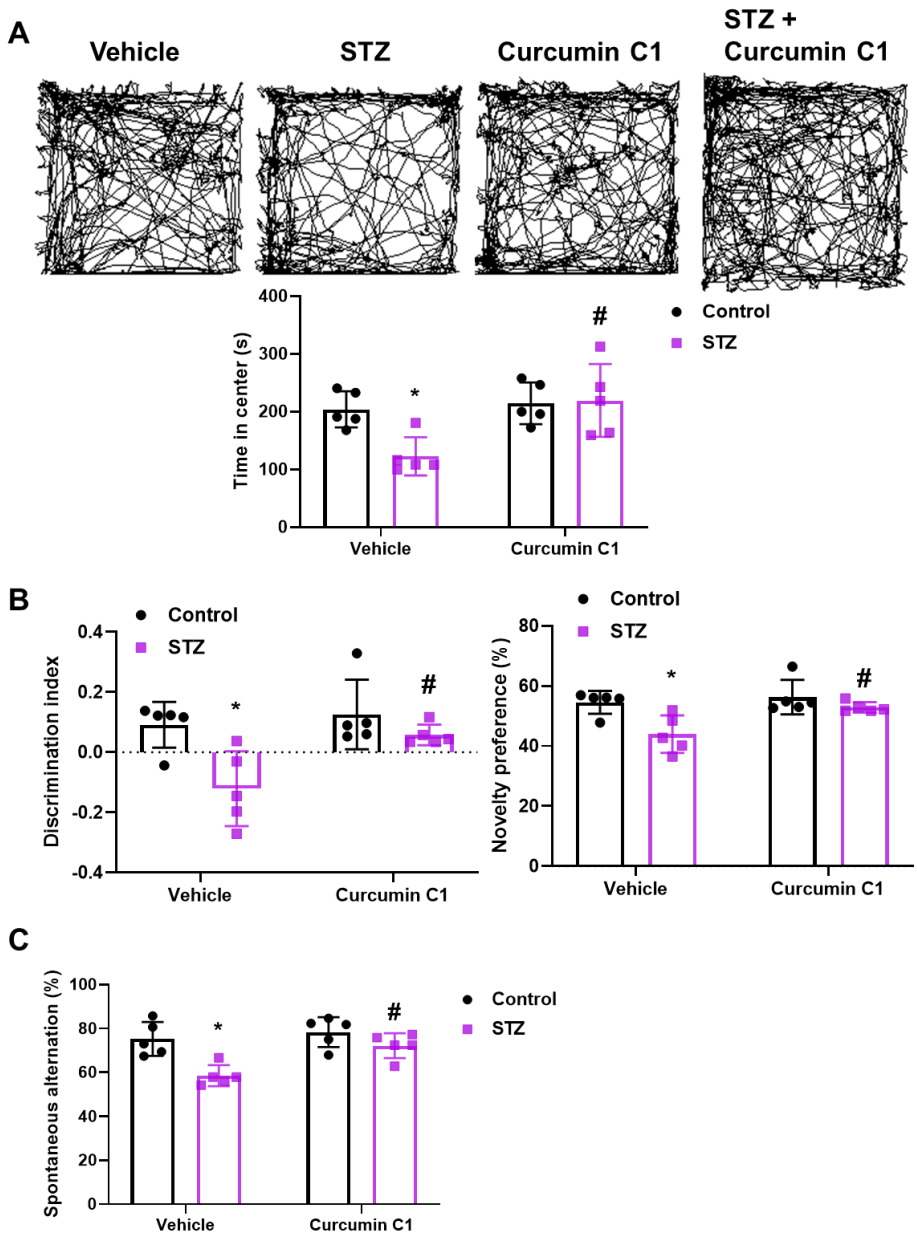

Figure 76. Curcumin C1 improves cognitive impairment induced in diabetic mice.

A–C Mice injected with vehicle or STZ were orally administrated vehicle or curcumin C1 (10 mg/kg) once daily for 8 weeks after diabetes induction. **A–C** The mice were subjected to open field test, NOR test, and Y–maze test, respectively. $n = 5$. $^{*}p < 0.05$ vs. vehicle–injected mice, $^{\#}p < 0.05$ vs. STZ–injected mice.

DISCUSSION

This study demonstrated that lysophagy dysfunction is a potential pathophysiological mechanism of DM-associated AD. In fact, *in vitro* findings showed that high glucose impaired TRIM16-mediated lysophagy, which impaired the degradation of Aβ and p-Tau. *In vivo* findings also showed that the accumulation of Aβ and p-Tau, resulting in cognitive impairment, was alleviated by TRIM16 recovery in diabetic mice (Figure 77). As mature neurons depend exceptionally on lysosomal systems to remove waste products such as protein aggregates and damaged organelles, lysosomal dysfunction is closely related to the pathogenesis of neurodegenerative diseases (Lawrence *et al.,* 2019). Patients with AD who have *PSEN1* mutations showed lysosomal dysfunction, and accumulation of Aβ/C99 in the enlarged lysosomes causes LMP, cathepsin release, and cell death (Lee *et al.,* 2022; Lee *et al.,* 2010). Moreover, glucolipotoxicity in human primary β-cells induced lysosomal dysfunction, resulting in islet failure (Zummo *et al.,* 2017). I observed that high glucose treatment reduced lysotracker signal intensities and cytosolic release of CTSD and CTSB in both iPSC-NDs and mouse hippocampal neurons. Considered that CTSD in the neocortical region of the human AD brain wass colocalized with p-Tau in neurons (Chai *et al.,* 2019) and lentivirus-mediated CTSB overexpression reduced amyloid deposits in hAPP mice (Mueller-Steiner *et al.,* 2006), my data indicated that high glucose treatment impaired Aβ and p-Tau degradation through lysosomal

dysfunction. Regarding the mechanism by which high glucose-induced lysosomal dysfunction, a previous study showed that high glucose-evoked ROS accumulation triggerd mechanistic damage to lysosomes, resulting in LMP in neuroblastoma cells (Chae *et al.,* 2020). Similarly, I observed that high glucose treatment resulted in ROS-mediated neuronal LMP. It has been reported that upon LMP, maintenance of lysosomal quality control through genetic and pharmacological restoration of lysosomes could recover damaged target cells and delay disease progression in both AD and DM (Cao *et al.,* 2021). Considering that *Atg5* deficiency in disease involving lysosomal damage inhibited lysophagy, which suppressed lysosomal restoration and exacerbated disease progression (Maejima *et al.,* 2013), lysophagy is essential for lysosomal restoration upon lysosomal damage. However, to the best of my knowledge, no study has investigated whether lysophagy occurs in neurons exposed to high glucose. Thus, I demonstrated for the first time that high glucose impaired neuronal lysophagy. These findings suggest that high glucose causes lysosomal dysfunction through LMP induction and lysophagy suppression, which inhibit the degradation of Aβ and p-Tau.

Lysosomes adapt their status in response to environmental cues to maintain cellular homeostasis through the regulation of lysosomal gene expression (Ballabio *et al.,* 2020). Under high glucose conditions, AMPK is dephosphorylated and mTORC1 is recruited to the lysosomal membrane by anchoring protein and activated, which inhibits catabolic

processes (Liu *et al.*, 2020). A previous study showed that the AMPK/mTORC1 signaling pathway was stimulated in high-glucose-treated neuronal cells and in the hippocampus of diabetic mice (Chae *et al.,* 2020). My data also demonstrated that mTORC1 was recruited to the lysosomes and activated in iPSC-NDs exposed to high glucose conditions. Although high glucose-induced ROS and lysosomal injury could inhibit AMPK/mTORC1 signaling (Jia *et al.,* 2020), lysosomal adaptation preceded and prevailed for modulation of mTORC1 activity in my experimental conditions. TFEB and TFE3 are members of the MiTF/TFE family that are considered as master regulators of lysosomal biogenesis and are implicated in the pathogenesis of both AD and DM (Bordi *et al.,* 2016; Yang *et al.,* 2021; Polito *et al.,* 2014). Regarding the regulation of TFEB/TFE3 activity, the mTORC1 and calcium mediated protein kinase C and calcineurin signaling pathways regulated their activity independently and inversely (Saftig *et al.*, 2016; Park *et al.,* 2022). Whether high glucose activates or inactivates TFEB/TFE3 remains controversial because high glucose could stimulate both signaling pathways under various conditions (Shah *et al.*, 2016). I observed that high glucose treatment inhibited the nuclear translocation of TFEB in an mTORC1-dependent manner, and calcium chelation also suppressed its translocation. This might be because high-glucose-mediated calcium signaling activated TFEB, but lysosomal adaptation-mediated mTORC1 signaling was predominant. Meanwhile, my data demonstrated that the nuclear translocation of

TFE3 was not altered in response to high glucose treatment, mTOR inhibition, and calcium chelation. In TFEB-depleted cells, TFE3 increased the number of lysosomes (Martina *et al.,* 2014). Furthermore, considering that nuclear TFE3 was present in all my experimental groups, TFE3 might be constitutively activated. However, although the altered activities of TFEB may regulate lysosomal biogenesis, whether it modulates lysophagy has not been elucidated, especially under high glucose conditions. I confirmed that TFEB was directly bound to the TRIM16 promoter, and TFEB activation recovered the high glucose-reduced mRNA expression and protein levels of TRIM16. These data indicate that lysophagy promotion is a novel mechanistic target of TFEB-mediated therapeutic strategy for neurogenerative disorders.

Lysophagy-related factors such as TRIM16, FBXO27, UBE2QL1, LRSAM1, and VCP detect damaged lysosomes and recruit ubiquitin and autophagic adaptors to degrade damaged lysosomes and maintain lysosomal function. Nevertheless, the role of lysophagy factors in the regulation of lysosome quality in the pathogenesis of neurodegenerative diseases has been investigated only recently (Zhu *et al.,* 2022), and the alterations and regulatory mechanisms of neuronal lysophagy in diabetic conditions have never been clarified. Among lysophagy-related factors, I observed that only TRIM16 expression was decreased in iPSC-NDs and mouse hippocampal neurons exposed to high glucose and in the hippocampus of diabetic mice, followed by decreased recruitment to lysosomes. Other

lysophagy-related factors that did not undergo significant changes in expression levels and recruitment to lysosomes may also affect the maintenance of basal lysosomal function (Liu *et al.,* 2020; Mishra *et al.,* 2019; Darwich *et al.,* 2020). However, present data revealed that only *FBXO27* silencing led to impaired clearance of galectin-3 upon lysosomal damage and reduction of lysotracker signal intensity, whereas knockdown of other lysophagy-related factors had no effects in neuronal cells. The variability in the knockdown effect may be attributed to differences in the degree of response of each factor to basal lysophagy. Furthermore, considering that LRSAM1 protected lymphoblasts against intracellular bacterial infection through lysosomal ubiquitination (Huett *et al.,* 2012), cell-type-specific differences may also contribute to it. In addition to lysophagy, the ESCRT machinery is recruited into the lysosome for repair upon acute lysosomal injury (Skowyra *et al.,* 2018); however, whether this affects the maintenance of lysosomal function in disease situations remains to be investigated. I first demonstrated that ALIX and CHMP4B were recruited to damaged lysosomes under high glucose conditions, but it was difficult to overcome LMP and lysophagy dysfunction. A recent study showed that TRIM16-mediated sensing of damaged lysosomes induced the unconventional seeding of intracellular wastes in human midbrain dopaminergic neurons (Burbidge *et al.,* 2022); however, gain-of-function studies focusing on lysophagy may provide an insight into the removal of wastes. Present data revealed that *TRIM16* overexpression

increased lysotracker signal intensities by promoting LC3, P62, and ubiquitin recruitment to damaged lysosomes. I also observed that lysosomal biogenesis, activities of CTSD and CTSB, and Aβ and p-Tau accumulation were reversed by TRIM16-mediated lysophagy activation. In addition to lysophagy, further studies are required because TRIM16-mediated protein ubiquitination is a crucial disease mechanism (Wang *et al.,* 2021; Liu *et al.,* 2022). However, considering that impairment of lysosomal maturation is a major mechanism of AD pathogenesis, maintenance of lysophagy and lysosomal biogenesis through TRIM16 regulation could provide synergistic effects in disease prevention.

A gain-of-function study demonstrated that TFEB delivery into the cerebral hemispheres of 5xFAD and rTg4510 AD transgenic mice ameliorated the AD phenotype (Polito *et al.,* 2014). Moreover, pharmacological enhancement of TFEB activity through curcumin C1 treatment for 3 months in AD mice restored lysosomal activity and reduced APP, C99, Aβ, and p-Tau levels followed by improvement of cognitive function (Song *et al.,* 2020). In addition to the inhibition of Aβ and p-Tau levels and improvement of cognitive function, my results demonstrated that curcumin C1 restored hippocampal TRIM16 protein levels, which elevated lysophagy and normalized lysosomal function. These findings indicate that TRIM16-mediated lysophagy suppresses diabetes-associated AD-like phenotype.

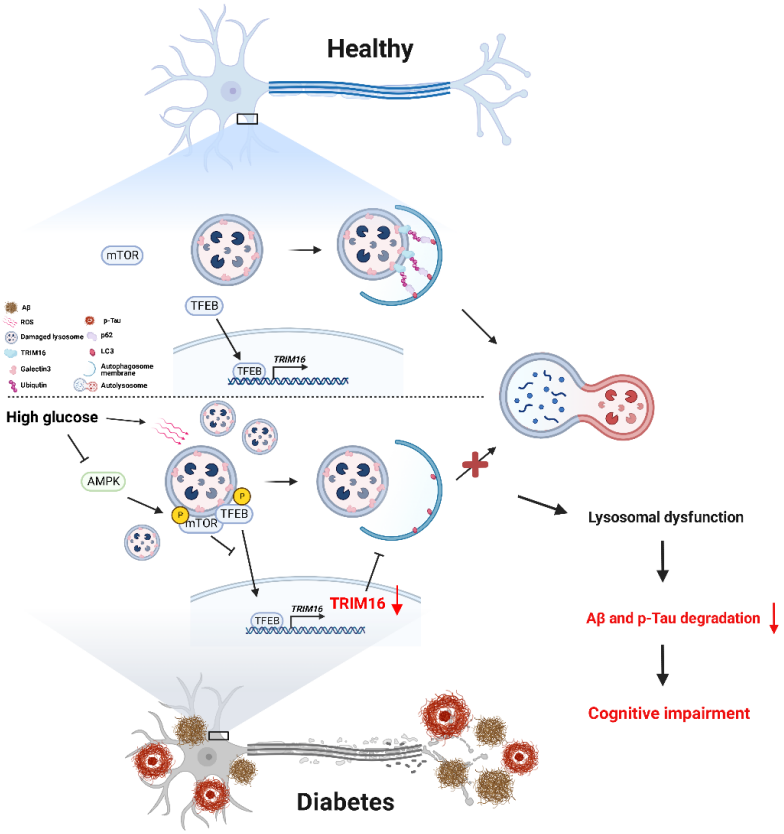

Figure 77. The schematic model for effects and molecular mechanism of action of high glucose on neuronal lysopahgy and subsequent accumulation of Aβ and p-Tau.

High glucose induces dysfunction of neuronal lysosomes through ROS-mediated LMP and lysophagy impairment. The expression of TRIM16 is down-regulated by mTORC1-inhibited TFEB activity under high glucose conditions, but its overexpression recovered lysophagy and lysosomal biogenesis, which in turn degrades Aβ and p-Tau and ameliorates cognitive impairment. Conclusively, lysophagy promotion through TRIM16 targeting is a promising strategy for the modulation of DM-associated AD.

GENERAL CONCLUSION

The current study has shown that high glucose causes endolysosomal dysfunction, leading to Aβ accumulation and cognitive impairment. According to previous studies, endolysosomal dysfunction in neurons is an early and prominent feature of AD, which causes accumulation of Aβ and p-Tau (Lee *et al.,* 2022; Small *et al.,* 2017). In addition, accumulated Aβ also causes endolysosomal abnormalities, exacerbating disease progression (Hung *et al.,* 2021). Other researches proposed that recovery of endolysosomal function reduces Aβ and tau phosphorylation levels, and improves synaptic integrity, learning, and memory (Li *et al.*, 2020; Cao *et al.,* 2021). My study also found that functional recovery of endolysosomes dysregulated by high glucose contributed to blocking Aβ and p-Tau accumulation and ameliorating cognitive impairment. Moreover, I demonstrated the molecular mechanism by which high glucose impaired endolysosomal function.

Indeed, my study proved that high glucose conditions upregulated Aβ production through early endosomal abnormalities induced by PICALM-mediated increases of APP endocytosis and ROS- and mTORC1-mediated impairment of the auto-lysosomal pathway. This investigation is the first to identify early endosomal dysregulation and their precise mechanisms in Aβ pathology in diabetes. These findings shed light into novel diabetes-related varieties of aberrant molecular

and cellular processes leading to AD. Thus, the present study provides compelling evidence that targeting PICALM and mTORC1 to prevent endosomal abnormalities is an attractive and promising strategies for managing DM-induced AD pathogenesis.

Next, my study revealed that amyloidogenic APP processing and tau hyperphosphorylation are inhibited by VPS26a, and down-regulated by ROS/NF-κB/DNMT1-mediated promoter hypermethylation in neuronal cells exposed to high glucose, which contributes to synaptic deficits, astrocyte over-activation, and cognitive impairment. Similarly, recent study showed that pharmacological enhancement of retromer function reduced Aβ and p-Tau levels in neurons (Curtis *et al.,* 2022). Taken together, by identifying a novel retromer-related mechanistic link between hyperglycaemia and AD pathogenesis, my results suggest that VPS26a is a promising candidate for the regulation of DM-related AD pathogenesis.

Moreover, I demonstrated that that impaired lysophagy due to mTORC1/TFEB-mediated TRIM16 downregulation inhibited Aβ and p-Tau degradation in neuronal cells exposed to high glucose conditions, resulting in cognitive impairment. These findings are the first to elucidate the defect of neuronal lysophagy and its regulatory mechanisms associated with Aβ and p-Tau pathology under high glucose conditions. Similar to my results, a recent study has shown that genetic inhibition of VCP, a lysophage-associated protein, increases tau aggregation in AD pathogenesis. Therefore, previous and present

study suggest that lysophagy promotion through TRIM16 targeting is a promising strategy for the modulation of DM-associated AD.

Although the relationship between DM and the development of AD has been controversial due to inconsistencies among human cohort studies and biochemical analyses, my data suggest that high glucose induces neuronal Aβ accumulation through endolysosomal dysfunction in the early stages of AD. In conclusion, present study demonstrated that endolysosomal dysfunction caused by PICALM-and mTORC1-mediated endosomal abnormalities, VPS26a-mediated retromer dysfunction, and TRIM16-mediated lysophagy impairment is a pathogenic link that elucidates the causal relationship between DM and AD (Figure 78).

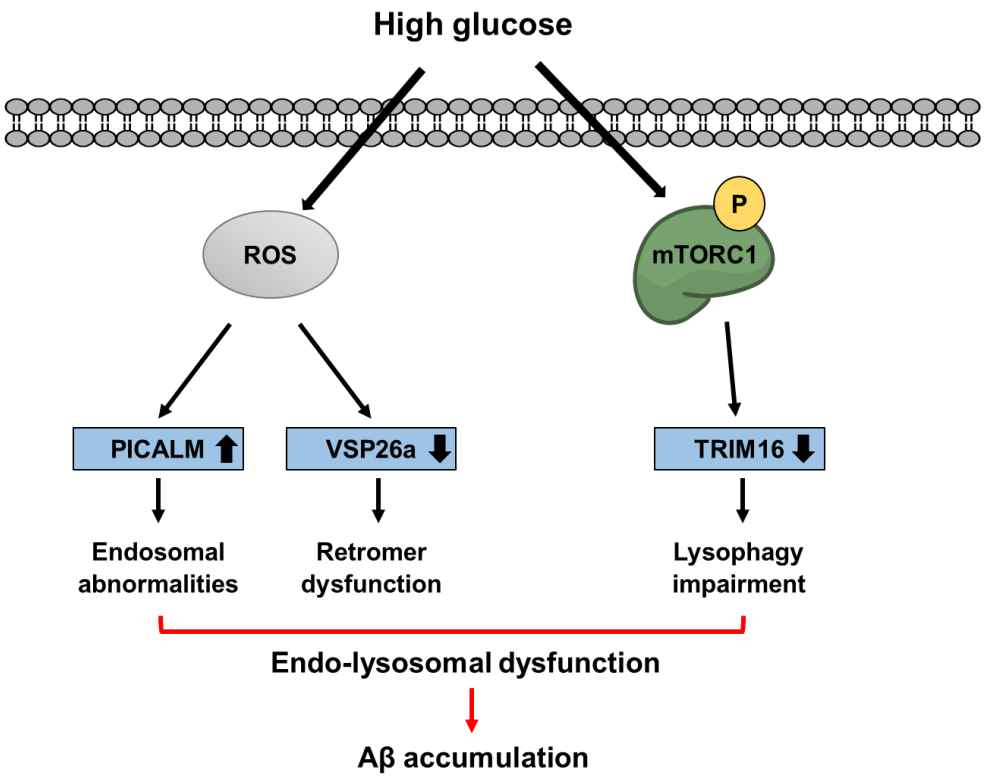

Figure 78. The schematic model summarizing the proposed pathway in high glucose-induced neuronal A β accumulation through endolysosomal dysfunction.

High glucose-evoked ROS induces PICALM-mediated endosomal abnormalities and VPS26a-mediated retromer dysfunction, and stimulated mTORC1 induces TRIM16-mediated lysophagy impairment, which leads to endolysosomal dysfunction. Subsequently, endolysosomal dysfunction causes neuronal A β accumulation.

REFERENCES

Abner, E. L., P. T. Nelson, R. J. Kryscio, F. A. Schmitt, D. W. Fardo, R. L. Woltjer, N. J. Cairns, L. Yu, H. H. Dodge, C. Xiong, K. Masaki, S. L. Tyas, D. A. Bennett, J. A. Schneider, and Z. Arvanitakis. (2016). Diabetes is associated with cerebrovascular but not Alzheimer's disease neuropathology. *Alzheimers Dement*. 12, 882-9.

Abuarab, N., T. S. Munsey, L. H. Jiang, J. Li, and A. Sivaprasadarao. (2017). High glucose-induced ROS activates TRPM2 to trigger lysosomal membrane permeabilization and Zn^{2+}-mediated mitochondrial fission. *Sci Signal*. 10, eaal4161.

Alexander, Steve P H, Richard E Roberts, Brad R S Broughton, Christopher G Sobey, Christopher H George, S Clare Stanford, Giuseppe Cirino, James R Docherty, Mark A Giembycz, Daniel Hoyer, Paul A Insel, Angelo A Izzo, Yong Ji, David J MacEwan, Jonathan Mangum, Sue Wonnacott, and Amrita Ahluwalia. (2018). Goals and practicalities of immunoblotting and immunohistochemistry: A guide for submission to the British Journal of Pharmacology. *Br J Pharmacol*. 175, 407-11.

Alsaqati, M., R. S. Thomas, and E. J. Kidd. (2018). Proteins involved in endocytosis are up-regulated by ageing in the normal human brain: implications for the development of Alzheimer's disease. *J Gerontol A Biol Sci Med Sci*. 73, 289-98.

Andersen, O. M., J. Reiche, V. Schmidt, M. Gotthardt, R. Spoelgen, J. Behlke, C. A. von Arnim, T. Breiderhoff, P. Jansen, X. Wu, K. R. Bales, R. Cappai, C. L. Masters, J. Gliemann, E. J. Mufson, B. T. Hyman, S. M. Paul, A.

Nykjaer, and T. E. Willnow. (2005). Neuronal sorting protein-related receptor sorLA/LR11 regulates processing of the amyloid precursor protein. *Proc Natl Acad Sci U S A*. 102, 13461-6.

Arnold, S. E., Z. Arvanitakis, S. L. Macauley-Rambach, A. M. Koenig, H. Y. Wang, R. S. Ahima, S. Craft, S. Gandy, C. Buettner, L. E. Stoeckel, D. M. Holtzman, and D. M. Nathan. (2018). Brain insulin resistance in type 2 diabetes and Alzheimer disease: concepts and conundrums. *Nat Rev Neurol*. 14, 168-81.

Bai, X. L., X. Y. Yang, J. Y. Li, Li Ye, X. Jia, Z. F. Xiong, Y. M. Wang, and S. Jin. (2017). Cavin-1 regulates caveolae-mediated LDL transcytosis: crosstalk in an AMPK/eNOS/ NF-κB/Sp1 loop. *Oncotarget*. 8, 103985-95.

Ballabio, A., and J. S. Bonifacino. (2020). Lysosomes as dynamic regulators of cell and organismal homeostasis. *Nat Rev Mol Cell Biol*. 21, 101-18.

Barbiellini Amidei, Claudio, Aurore Fayosse, Julien Dumurgier, Marcos D. Machado-Fragua, Adam G. Tabak, Thomas van Sloten, Mika Kivimäki, Aline Dugravot, Séverine Sabia, and Archana Singh-Manoux. (2021). Association between age at diabetes onset and subsequent risk of dementia. *JAMA*. 325, 1640-49.

Bartolome, A., M. Kimura-Koyanagi, S. Asahara, C. Guillen, H. Inoue, K. Teruyama, S. Shimizu, A. Kanno, A. Garcia-Aguilar, M. Koike, Y. Uchiyama, M. Benito, T. Noda, and Y. Kido. (2014). Pancreatic β-cell failure mediated by mTORC1 hyperactivity and autophagic impairment. *Diabetes*. 63, 2996-3008.

Bell, C. G., A. E. Teschendorff, V. K. Rakyan, A. P. Maxwell, S. Beck, and D. A. Savage. (2010). Genome-wide DNA methylation analysis for diabetic nephropathy in type 1 diabetes mellitus. *BMC Med Genomics*. 3, 1-11.

Bhalla, A., C. P. Vetanovetz, E. Morel, Z. Chamoun, G. Di Paolo, and S. A. Small. (2012). The location and trafficking routes of the neuronal retromer and its role in amyloid precursor protein transport. *Neurobiol Dis*. 47, 126-34.

Biessels, G. J., and F. Despa. (2018). Cognitive decline and dementia in diabetes mellitus: mechanisms and clinical implications. *Nat Rev Endocrinol*. 14, 591-604.

Boccardi, V., I. Murasecco, and P. Mecocci. (2019). Diabetes drugs in the fight against Alzheimer's disease. *Ageing Res Rev*. 54, 100936.

Bolte, S., and F. P. Cordelières. (2006). A guided tour into subcellular colocalization analysis in light microscopy. *J Microsc*. 224, 213-32.

Bordi, M., M. J. Berg, P. S. Mohan, C. M. Peterhoff, M. J. Alldred, S. Che, S. D. Ginsberg, and R. A. Nixon. (2016). Autophagy flux in CA1 neurons of Alzheimer hippocampus: Increased induction overburdens failing lysosomes to propel neuritic dystrophy. *Autophagy*. 12, 2467-83.

Burbidge, K., D. J. Rademacher, J. Mattick, S. Zack, A. Grillini, L. Bousset, O. Kwon, K. Kubicki, A. Simon, R. Melki, and E. M. Campbell. (2022). LGALS3 (galectin 3) mediates an unconventional secretion of SNCA/alpha-synuclein in response to lysosomal membrane damage by the autophagic-lysosomal pathway in human midbrain dopamine

neurons. *Autophagy*. 18, 1020-48.

Burd, C., and P. J. Cullen. (2014). Retromer: a master conductor of endosome sorting. *Cold Spring Harb Perspect Biol*. 6, a016774.

Cao, M., X. Luo, K. Wu, and X. He. (2021). Targeting lysosomes in human disease: from basic research to clinical applications. *Signal Transduct Target Ther*. 6, 379.

Cataldo, A. M., S. Petanceska, N. B. Terio, C. M. Peterhoff, R. Durham, M. Mercken, P. D. Mehta, J. Buxbaum, V. Haroutunian, and R. A. Nixon. (2004). Aβ localization in abnormal endosomes: association with earliest Aβ elevations in AD and Down syndrome. *Neurobiol Aging*. 25, 1263-72.

Chae, C. W., G. E. Choi, Y. H. Jung, J. R. Lim, J. H. Cho, J. H. Yoon, and H. J. Han. (2022). High glucose-mediated VPS26a down-regulation dysregulates neuronal amyloid precursor protein processing and tau phosphorylation. *Br J Pharmacol*. 179, 3934-50.

Chae, C. W., H. J. Lee, G. E. Choi, Y. H. Jung, J. S. Kim, J. R. Lim, S. Y. Kim, I. K. Hwang, J. K. Seong, and H. J. Han. (2020). High glucose-mediated PICALM and mTORC1 modulate processing of amyloid precursor protein via endosomal abnormalities. *Br J Pharmacol*. 177, 3828-47.

Chai, Y. L., J. R. Chong, J. Weng, D. Howlett, A. Halsey, J. H. Lee, J. Attems, D. Aarsland, P. T. Francis, C. P. Chen, and M. K. P. Lai. (2019). Lysosomal cathepsin D is up-regulated in Alzheimer's disease neocortex and may be a marker for neurofibrillary degeneration. *Brain Pathol*. 29, 63-74.

Cheng, H., K. S. Vetrivel, P. Gong, X. Meckler, A. Parent, and G. Thinakaran. (2007). Mechanisms of disease: new therapeutic strategies for Alzheimer's disease--targeting APP processing in lipid rafts. *Nat Clin Pract Neurol*. 3, 374-82.

Clee, S. M., B. S. Yandell, K. M. Schueler, M. E. Rabaglia, O. C. Richards, S. M. Raines, E. A. Kabara, D. M. Klass, E. T. Mui, D. S. Stapleton, M. P. Gray-Keller, M. B. Young, J. P. Stoehr, H. Lan, I. Boronenkov, P. W. Raess, M. T. Flowers, and A. D. Attie. (2006). Positional cloning of Sorcs1, a type 2 diabetes quantitative trait locus. *Nat Genet*. 38, 688-93.

Colacurcio, D. J., A. Pensalfini, Y. Jiang, and R. A. Nixon. (2018). Dysfunction of autophagy and endosomal-lysosomal pathways: Roles in pathogenesis of Down syndrome and Alzheimer's Disease. *Free Radic Biol Med*. 114, 40-51.

Cole, S. L., and R. Vassar. (2007). The Alzheimer's disease β-secretase enzyme, BACE1. *Mol Neurodegener*. 2, 1-25.

Crino, P. B. (2016). The mTOR signalling cascade: paving new roads to cure neurological disease. *Nat Rev Neurol*. 12, 379-92.

Cui, Y., J. M. Carosi, Z. Yang, N. Ariotti, M. C. Kerr, R. G. Parton, T. J. Sargeant, and R. D. Teasdale. (2019). Retromer has a selective function in cargo sorting via endosome transport carriers. *J Cell Biol*. 218, 615-31.

Cullen, P. J., and F. Steinberg. (2018). To degrade or not to degrade: mechanisms and significance of endocytic recycling. *Nat Rev Mol Cell Biol*. 19, 679-96.

Culmsee, C., J. Monnig, B. E. Kemp, and M. P. Mattson. (2001). AMP-activated protein kinase is highly expressed in neurons in the developing rat brain and promotes neuronal survival following glucose deprivation. *J Mol Neurosci*. 17, 45-58.

Curtis, M. E., T. Smith, B. E. Blass, and D. Praticò. (2022). Dysfunction of the retromer complex system contributes to amyloid and tau pathology in a stem cell model of Down syndrome. *Alzheimers Dement (N Y)*. 8, e12334.

Curtis, M. J., S. Alexander, G. Cirino, J. R. Docherty, C. H. George, M. A. Giembycz, D. Hoyer, P. A. Insel, A. A. Izzo, Y. Ji, D. J. MacEwan, C. G. Sobey, S. C. Stanford, M. M. Teixeira, S. Wonnacott, and A. Ahluwalia. (2018). Experimental design and analysis and their reporting II: updated and simplified guidance for authors and peer reviewers. *Br J Pharmacol*. 175, 987-93.

Darwich, N. F., J. M. Phan, B. Kim, E. Suh, J. D. Papatriantafyllou, L. Changolkar, A. T. Nguyen, C. M. O'Rourke, Z. He, S. Porta, G. S. Gibbons, K. C. Luk, S. G. Papageorgiou, M. Grossman, L. Massimo, D. J. Irwin, C. T. McMillan, I. M. Nasrallah, C. Toro, G. K. Aguirre, V. M. Van Deerlin, and E. B. Lee. (2020). Autosomal dominant VCP hypomorph mutation impairs disaggregation of PHF-tau. *Science*. 370, eaay8826.

Ding, L., L. Han, J. Dube, and D. D. Billadeau. (2019). WASH regulates glucose homeostasis by facilitating Glut2 receptor recycling in pancreatic β-Cells. *Diabetes*. 68, 377-86.

Docherty, James R, S Clare Stanford, Reynold A Panattieri, Steve PH

Alexander, Giuseppe Cirino, Christopher H George, Daniel Hoyer, Angelo A Izzo, Yong Ji, and Elliot Lilley. (2019). Sex: a change in our guidelines to authors to ensure that this is no longer an ignored experimental variable. *Br J Pharmacol*. 176, 4081-6.

Fath, T., Y. D. Ke, P. Gunning, J. Gotz, and L. M. Ittner. (2009). Primary support cultures of hippocampal and substantia nigra neurons. *Nat Protoc*. 4, 78-85.

Feng, L., L. Liang, S. Zhang, J. Yang, Y. Yue, and X. Zhang. (2022). HMGB1 downregulation in retinal pigment epithelial cells protects against diabetic retinopathy through the autophagy-lysosome pathway. *Autophagy*. 18, 320-39.

Fleming, Angeleen, Mathieu Bourdenx, Motoki Fujimaki, Cansu Karabiyik, Gregory J. Krause, Ana Lopez, Adrián Martín-Segura, Claudia Puri, Aurora Scrivo, John Skidmore, Sung Min Son, Eleanna Stamatakou, Lidia Wrobel, Ye Zhu, Ana Maria Cuervo, and David C. Rubinsztein. (2022). The different autophagy degradation pathways and neurodegeneration. *Neuron*. 110, 935-66.

Furman, B. L. (2015). Streptozotocin-induced diabetic models in mice and rats. *Curr Protoc Pharmacol*. 70, 5-47.

Furman, B. L. (2021). Streptozotocin-induced diabetic models in mice and rats. *Curr Protoc*. 1, e78.

Ginsberg, S. D., M. J. Alldred, S. E. Counts, A. M. Cataldo, R. L. Neve, Y. Jiang, J. Wuu, M. V. Chao, E. J. Mufson, R. A. Nixon, and S. Che. (2010). Microarray analysis of hippocampal CA1 neurons implicates early

endosomal dysfunction during Alzheimer's disease progression. *Biol Psychiatry*. 68, 885-93.

Ginsberg, S. D., E. J. Mufson, S. E. Counts, J. Wuu, M. J. Alldred, R. A. Nixon, and S. Che. (2010). Regional selectivity of rab5 and rab7 protein upregulation in mild cognitive impairment and Alzheimer's disease. *J Alzheimers Dis*. 22, 631-9.

Gonzalez, Claudio D., Myung-Shik Lee, Piero Marchetti, Massimo Pietropaolo, Roberto Towns, Maria I. Vaccaro, Hirotaka Watada, and John W. Wiley. (2014). The emerging role of autophagy in the pathophysiology of diabetes mellitus. *Autophagy*. 7, 2-11.

Grbovic, O. M., P. M. Mathews, Y. Jiang, S. D. Schmidt, R. Dinakar, N. B. Summers-Terio, B. P. Ceresa, R. A. Nixon, and A. M. Cataldo. (2003). Rab5-stimulated up-regulation of the endocytic pathway increases intracellular β-cleaved amyloid precursor protein carboxyl-terminal fragment levels and Aβ production. *J Biol Chem*. 278, 31261-8.

Guimas Almeida, C., F. Sadat Mirfakhar, C. Perdigao, and T. Burrinha. (2018). Impact of late-onset Alzheimer's genetic risk factors on β-amyloid endocytic production. *Cell Mol Life Sci*. 75, 2577-89.

Gustafsson, N., S. Culley, G. Ashdown, D. M. Owen, P. M. Pereira, and R. Henriques. (2016). Fast live-cell conventional fluorophore nanoscopy with ImageJ through super-resolution radial fluctuations. *Nat Commun*. 7, 12471.

Hampel, H., J. Hardy, K. Blennow, C. Chen, G. Perry, S. H. Kim, V. L. Villemagne, P. Aisen, M. Vendruscolo, T. Iwatsubo, C. L. Masters, M.

Cho, L. Lannfelt, J. L. Cummings, and A. Vergallo. (2021). The Amyloid-β Pathway in Alzheimer's Disease. *Mol Psychiatry*. 26, 5481-503.

Hansen, C., E. Angot, A. L. Bergstrom, J. A. Steiner, L. Pieri, G. Paul, T. F. Outeiro, R. Melki, P. Kallunki, K. Fog, J. Y. Li, and P. Brundin. (2011). α-synuclein propagates from mouse brain to grafted dopaminergic neurons and seeds aggregation in cultured human cells. *J Clin Invest*. 121, 715-25.

Haythorne, E., M. Rohm, M. van de Bunt, M. F. Brereton, A. I. Tarasov, T. S. Blacker, G. Sachse, M. Silva Dos Santos, R. Terron Exposito, S. Davis, O. Baba, R. Fischer, M. R. Duchen, P. Rorsman, J. I. MacRae, and F. M. Ashcroft. (2019). Diabetes causes marked inhibition of mitochondrial metabolism in pancreatic β-cells. *Nat Commun*. 10, 2474.

Ho, K. H., X. Yang, A. B. Osipovich, O. Cabrera, M. L. Hayashi, M. A. Magnuson, G. Gu, and I. Kaverina. (2020). Glucose regulates microtubule disassembly and the dose of insulin secretion via tau phosphorylation. *Diabetes*. 69, 1936-47.

Huang, T. Y., Y. Zhao, X. Li, X. Wang, I. C. Tseng, R. Thompson, S. Tu, T. E. Willnow, Y. W. Zhang, and H. Xu. (2016). SNX27 and SORLA interact to reduce amyloidogenic subcellular distribution and processing of amyloid precursor protein. *J Neurosci*. 36, 7996-8011.

Huett, A., R. J. Heath, J. Begun, S. O. Sassi, L. A. Baxt, J. M. Vyas, M. B. Goldberg, and R. J. Xavier. (2012). The LRR and RING domain protein LRSAM1 is an E3 ligase crucial for ubiquitin-dependent autophagy of

intracellular Salmonella Typhimurium. *Cell Host Microbe*. 12, 778-90.

Hung, C., E. Tuck, V. Stubbs, S. J. van der Lee, C. Aalfs, R. van Spaendonk, P. Scheltens, J. Hardy, H. Holstege, and F. J. Livesey. (2021). SORL1 deficiency in human excitatory neurons causes APP-dependent defects in the endolysosome-autophagy network. *Cell Rep*. 35, 109259.

Israel, Mason A., Shauna H. Yuan, Cedric Bardy, Sol M. Reyna, Yangling Mu, Cheryl Herrera, Michael P. Hefferan, Sebastiaan Van Gorp, Kristopher L. Nazor, Francesca S. Boscolo, Christian T. Carson, Louise C. Laurent, Martin Marsala, Fred H. Gage, Anne M. Remes, Edward H. Koo, and Lawrence S. B. Goldstein. (2012). Probing sporadic and familial Alzheimer's disease using induced pluripotent stem cells. *Nature*. 482, 216-20.

Jia, J., B. Bissa, L. Brecht, L. Allers, S. W. Choi, Y. Gu, M. Zbinden, M. R. Burge, G. Timmins, K. Hallows, C. Behrends, and V. Deretic. (2020). AMPK, a regulator of metabolism and autophagy, is activated by lysosomal damage via a novel galectin-directed ubiquitin signal transduction system. *Mol Cell*. 77, 951-69.

Jia, J., A. Claude-Taupin, Y. Gu, S. W. Choi, R. Peters, B. Bissa, M. H. Mudd, L. Allers, S. Pallikkuth, K. A. Lidke, M. Salemi, B. Phinney, M. Mari, F. Reggiori, and V. Deretic. (2020). Galectin-3 coordinates a cellular system for lysosomal repair and removal. *Dev Cell*. 52, 69-87.

Jiang, Dan, Min Sun, Linna You, Kai Lu, Lei Gao, Chunxiao Hu, Shiyong Wu, Guanglei Chang, Hongmei Tao, and Dongying Zhang. (2019). DNA

methylation and hydroxymethylation are associated with the degree of coronary atherosclerosis in elderly patients with coronary heart disease. *Life Sci*. 224, 241-48.

Kanatsu, K., Y. Hori, S. Takatori, T. Watanabe, T. Iwatsubo, and T. Tomita. (2016). Partial loss of CALM function reduces Aβ42 production and amyloid deposition in vivo. *Hum Mol Genet*. 25, 3988-97.

Kanatsu, K., Y. Morohashi, M. Suzuki, H. Kuroda, T. Watanabe, T. Tomita, and T. Iwatsubo. (2014). Decreased CALM expression reduces Aβ42 to total Abeta ratio through clathrin-mediated endocytosis of γ-secretase. *Nat Commun*. 5, 3386.

Kato, M., and R. Natarajan. (2019). Epigenetics and epigenomics in diabetic kidney disease and metabolic memory. *Nat Rev Nephrol*. 15, 327-45.

Kebede, M. A., A. T. Oler, T. Gregg, A. J. Balloon, A. Johnson, K. Mitok, M. Rabaglia, K. Schueler, D. Stapleton, C. Thorstenson, L. Wrighton, B. J. Floyd, O. Richards, S. Raines, K. Eliceiri, N. G. Seidah, C. Rhodes, M. P. Keller, J. L. Coon, A. Audhya, and A. D. Attie. (2014). SORCS1 is necessary for normal insulin secretory granule biogenesis in metabolically stressed beta cells. *J Clin Invest*. 124, 4240-56.

Kilkenny, Carol, William Browne, Innes C Cuthill, Michael Emerson, and Douglas G Altman. (2010). Animal research: reporting in vivo experiments: the ARRIVE guidelines. *Br J Pharmacol*. 160, 1577-9.

Kim, H. Y., D. K. Lee, B. R. Chung, H. V. Kim, and Y. Kim. (2016). Intracerebroventricular Injection of Aβ peptides in normal mice to acutely induce Alzheimer-like cognitive deficits. *J Vis Exp*. 109,

e53308.

Kim, S., Y. Sato, P. S. Mohan, C. Peterhoff, A. Pensalfini, A. Rigoglioso, Y. Jiang, and R. A. Nixon. (2016). Evidence that the rab5 effector APPL1 mediates APP-βCTF-induced dysfunction of endosomes in Down syndrome and Alzheimer's disease. *Mol Psychiatry*. 21, 707-16.

Kivipelto, M., F. Mangialasche, and T. Ngandu. (2018). Lifestyle interventions to prevent cognitive impairment, dementia and Alzheimer disease. *Nat Rev Neurol*. 14, 653-66.

Koekkoek, Paula S., L. Jaap Kappelle, Esther van den Berg, Guy E. H. M. Rutten, and Geert Jan Biessels. (2015). Cognitive function in patients with diabetes mellitus: guidance for daily care. *Lancet Neurol*. 14, 329-40.

Kong, F. J., L. L. Ma, J. J. Guo, L. H. Xu, Y. Li, and S. Qu. (2018). Endoplasmic reticulum stress/autophagy pathway is involved in diabetes-induced neuronal apoptosis and cognitive decline in mice. *Clin Sci (Lond)*. 132, 111-25.

Kwart, D., A. Gregg, C. Scheckel, E. A. Murphy, D. Paquet, M. Duffield, J. Fak, O. Olsen, R. B. Darnell, and M. Tessier-Lavigne. (2019). A large panel of isogenic APP and PSEN1 mutant human iPSC neurons reveals shared endosomal abnormalities mediated by APP βCTFs, not Aβ. *Neuron*. 104, 256-70.

Lacy, M. E., P. Gilsanz, A. J. Karter, C. P. Quesenberry, M. J. Pletcher, and R. A. Whitmer. (2018). Long-term glycemic control and dementia risk in type 1 Diabetes. *Diabetes Care*. 41, 2339-45.

Lambert, J. C., C. A. Ibrahim-Verbaas, D. Harold, A. C. Naj, R. Sims, C.

Bellenguez, A. L. DeStafano, J. C. Bis, G. W. Beecham, B. Grenier-Boley, G. Russo, T. A. Thorton-Wells, N. Jones, A. V. Smith, V. Chouraki, C. Thomas, M. A. Ikram, D. Zelenika, B. N. Vardarajan, Y. Kamatani, C. F. Lin, A. Gerrish, H. Schmidt, B. Kunkle, M. L. Dunstan, A. Ruiz, M. T. Bihoreau, S. H. Choi, C. Reitz, F. Pasquier, C. Cruchaga, D. Craig, N. Amin, C. Berr, O. L. Lopez, P. L. De Jager, V. Deramecourt, J. A. Johnston, D. Evans, S. Lovestone, L. Letenneur, F. J. Morón, D. C. Rubinsztein, G. Eiriksdottir, K. Sleegers, A. M. Goate, N. Fiévet, M. W. Huentelman, M. Gill, K. Brown, M. I. Kamboh, L. Keller, P. Barberger-Gateau, B. McGuiness, E. B. Larson, R. Green, A. J. Myers, C. Dufouil, S. Todd, D. Wallon, S. Love, E. Rogaeva, J. Gallacher, P. St George-Hyslop, J. Clarimon, A. Lleo, A. Bayer, D. W. Tsuang, L. Yu, M. Tsolaki, P. Bossù, G. Spalletta, P. Proitsi, J. Collinge, S. Sorbi, F. Sanchez-Garcia, N. C. Fox, J. Hardy, M. C. Deniz Naranjo, P. Bosco, R. Clarke, C. Brayne, D. Galimberti, M. Mancuso, F. Matthews, S. Moebus, P. Mecocci, M. Del Zompo, W. Maier, H. Hampel, A. Pilotto, M. Bullido, F. Panza, P. Caffarra, B. Nacmias, J. R. Gilbert, M. Mayhaus, L. Lannefelt, H. Hakonarson, S. Pichler, M. M. Carrasquillo, M. Ingelsson, D. Beekly, V. Alvarez, F. Zou, O. Valladares, S. G. Younkin, E. Coto, K. L. Hamilton-Nelson, W. Gu, C. Razquin, P. Pastor, I. Mateo, M. J. Owen, K. M. Faber, P. V. Jonsson, O. Combarros, M. C. O'Donovan, L. B. Cantwell, H. Soininen, D. Blacker, S. Mead, T. H. Mosley, Jr., D. A. Bennett, T. B. Harris, L. Fratiglioni, C. Holmes, R. F. de Bruijn, P. Passmore, T. J. Montine, K. Bettens, J. I. Rotter, A. Brice, K. Morgan,

T. M. Foroud, W. A. Kukull, D. Hannequin, J. F. Powell, M. A. Nalls, K. Ritchie, K. L. Lunetta, J. S. Kauwe, E. Boerwinkle, M. Riemenschneider, M. Boada, M. Hiltuenen, E. R. Martin, R. Schmidt, D. Rujescu, L. S. Wang, J. F. Dartigues, R. Mayeux, C. Tzourio, A. Hofman, M. M. Nöthen, C. Graff, B. M. Psaty, L. Jones, J. L. Haines, P. A. Holmans, M. Lathrop, M. A. Pericak-Vance, L. J. Launer, L. A. Farrer, C. M. van Duijn, C. Van Broeckhoven, V. Moskvina, S. Seshadri, J. Williams, G. D. Schellenberg, and P. Amouyel. (2013). Meta-analysis of 74,046 individuals identifies 11 new susceptibility loci for Alzheimer's disease. *Nat Genet*. 45, 1452-8.

Lambeth, T. R., D. L. Riggs, L. E. Talbert, J. Tang, E. Coburn, A. S. Kang, J. Noll, C. Augello, B. D. Ford, and R. R. Julian. (2019). Spontaneous isomerization of long-lived proteins provides a molecular mechanism for the lysosomal failure observed in Alzheimer's Disease. *ACS Cent Sci*. 5, 1387-95.

Lane, R. F., J. W. Steele, D. Cai, M. E. Ehrlich, A. D. Attie, and S. Gandy. (2013). Protein sorting motifs in the cytoplasmic tail of SorCS1 control generation of Alzheimer's amyloid-β peptide. *J Neurosci*. 33, 7099-107.

Law, F., J. H. Seo, Z. Wang, J. L. DeLeon, Y. Bolis, A. Brown, W. X. Zong, G. Du, and C. E. Rocheleau. (2017). The VPS34 PI3K negatively regulates RAB-5 during endosome maturation. *J Cell Sci*. 130, 2007-17.

Lawrence, R. E., and R. Zoncu. (2019). The lysosome as a cellular centre for signalling, metabolism and quality control. *Nat Cell Biol*. 21, 133-42.

Lee, H. J., J. M. Ryu, Y. H. Jung, S. J. Lee, J. Y. Kim, S. H. Lee, I. K. Hwang, J. K. Seong, and H. J. Han. (2016). High glucose up-regulates BACE1-mediated Aβ production through ROS-dependent HIF-1α and LXR α/ABCA1-regulated lipid raft reorganization in SK-N-MC cells. *Sci Rep*. 6, 36746.

Lee, J. H., M. K. McBrayer, D. M. Wolfe, L. J. Haslett, A. Kumar, Y. Sato, P. P. Lie, P. Mohan, E. E. Coffey, U. Kompella, C. H. Mitchell, E. Lloyd-Evans, and R. A. Nixon. (2015). Presenilin 1 maintains lysosomal Ca^{2+} homeostasis via TRPML1 by regulating vATPase-mediated lysosome acidification. *Cell Rep*. 12, 1430-44.

Lee, J. H., D. S. Yang, C. N. Goulbourne, E. Im, P. Stavrides, A. Pensalfini, H. Chan, C. Bouchet-Marquis, C. Bleiwas, M. J. Berg, C. Huo, J. Peddy, M. Pawlik, E. Levy, M. Rao, M. Staufenbiel, and R. A. Nixon. (2022). Faulty autolysosome acidification in Alzheimer's disease mouse models induces autophagic build-up of Aβ in neurons, yielding senile plaques. *Nat Neurosci*. 25, 688-701.

Lee, J. H., W. H. Yu, A. Kumar, S. Lee, P. S. Mohan, C. M. Peterhoff, D. M. Wolfe, M. Martinez-Vicente, A. C. Massey, G. Sovak, Y. Uchiyama, D. Westaway, A. M. Cuervo, and R. A. Nixon. (2010). Lysosomal proteolysis and autophagy require presenilin 1 and are disrupted by Alzheimer-related PS1 mutations. *Cell*. 141, 1146-58.

Li, J. G., J. Chiu, and D. Pratico. (2020). Full recovery of the Alzheimer's disease phenotype by gain of function of vacuolar protein sorting 35. *Mol Psychiatry*. 25, 2630-40.

Li, J. G., J. Chiu, M. Ramanjulu, B. E. Blass, and D. Pratico. (2020). A pharmacological chaperone improves memory by reducing Aβ and tau neuropathology in a mouse model with plaques and tangles. *Mol Neurodegener*. 15, 1-11.

Li, L. C., and R. Dahiya. (2002). MethPrimer: designing primers for methylation PCRs. *Bioinformatics*. 18, 1427-31.

Lie, Pearl PY, Lang Yoo, Chris N Goulbourne, Martin J Berg, Philip Stavrides, Chunfeng Huo, Ju-Hyun Lee, and Ralph A Nixon. (2022). Axonal transport of late endosomes and amphisomes is selectively modulated by local Ca^{2+} efflux and disrupted by PSEN1 loss of function. *Sci Adv*. 8, eabj5716.

Liebsch, Filip, Luka Kulic, Charlotte Teunissen, Adeola Shobo, Irem Ulku, Vivienne Engelschalt, Mark A. Hancock, Wiesje M. van der Flier, Peter Kunach, Pedro Rosa-Neto, Philip Scheltens, Judes Poirier, Paul Saftig, Randall J. Bateman, John Breitner, Christoph Hock, and Gerhard Multhaup. (2019). Aβ34 is a BACE1-derived degradation intermediate associated with amyloid clearance and Alzheimer's disease progression. *Nat Commun*. 10, 2240.

Lim, J. H., H. W. Kim, M. Y. Kim, T. W. Kim, E. N. Kim, Y. Kim, S. Chung, Y. S. Kim, B. S. Choi, Y. S. Kim, Y. S. Chang, H. W. Kim, and C. W. Park. (2018). Cinacalcet-mediated activation of the CaMKKβ-LKB1-AMPK pathway attenuates diabetic nephropathy in db/db mice by modulation of apoptosis and autophagy. *Cell Death Dis*. 9, 270.

Liu, E. A., M. L. Schultz, C. Mochida, C. Chung, H. L. Paulson, and A. P.

Lieberman. (2020). Fbxo2 mediates clearance of damaged lysosomes and modifies neurodegeneration in the Niemann-Pick C brain. *JCI Insight*. 5, e136676.

Liu, G. Y., and D. M. Sabatini. (2020). mTOR at the nexus of nutrition, growth, ageing and disease. *Nat Rev Mol Cell Biol*. 21, 183-203.

Liu, J., W. Li, K. Q. Deng, S. Tian, H. Liu, H. Shi, Q. Fang, Z. Liu, Z. Chen, T. Tian, S. Gan, F. Hu, M. Hu, X. Cheng, Y. X. Ji, P. Zhang, Z. G. She, X. J. Zhang, S. Chen, J. Cai, and H. Li. (2022). The E3 ligase TRIM16 is a key suppressor of pathological cardiac hypertrophy. *Circ Res*. 130, 1586-600.

Lucas, M., D. C. Gershlick, A. Vidaurrazaga, A. L. Rojas, J. S. Bonifacino, and A. Hierro. (2016). Structural mechanism for cargo recognition by the retromer complex. *Cell*. 167, 1623-35.

Lueptow, Lindsay M. (2017). Novel object recognition test for the investigation of learning and memory in mice. *JoVE*. 126, e55718.

Ma, Q., J. Yang, T. A. Milner, J. G. Vonsattel, M. E. Palko, L. Tessarollo, and B. L. Hempstead. (2017). SorCS2-mediated NR2A trafficking regulates motor deficits in Huntington's disease. *JCI Insight*. 2, e88995.

Maejima, I., A. Takahashi, H. Omori, T. Kimura, Y. Takabatake, T. Saitoh, A. Yamamoto, M. Hamasaki, T. Noda, Y. Isaka, and T. Yoshimori. (2013). Autophagy sequesters damaged lysosomes to control lysosomal biogenesis and kidney injury. *EMBO J*. 32, 2336-47.

Martina, J. A., H. I. Diab, L. Lishu, A. L. Jeong, S. Patange, N. Raben, and R. Puertollano. (2014). The nutrient-responsive transcription factor

TFE3 promotes autophagy, lysosomal biogenesis, and clearance of cellular debris. *Sci Signal*. 7, ra9.

Masters, C. L., R. Bateman, K. Blennow, C. C. Rowe, R. A. Sperling, and J. L. Cummings. (2015). Alzheimer's disease. *Nat Rev Dis Primers*. 1, 15056.

McFall, G. P., S. A. Wiebe, D. Vergote, K. J. Anstey, and R. A. Dixon. (2015). Alzheimer's genetic risk intensifies neurocognitive slowing associated with diabetes in non-demented older adults. *Alzheimers Dement (Amst)*. 1, 395-402.

McIntosh, E. C., D. A. Nation, and Initiative Alzheimer's Disease Neuroimaging. (2019). Importance of Treatment Status in Links Between Type 2 Diabetes and Alzheimer's Disease. *Diabetes Care*. 42, 972-79.

Mecozzi, V. J., D. E. Berman, S. Simoes, C. Vetanovetz, M. R. Awal, V. M. Patel, R. T. Schneider, G. A. Petsko, D. Ringe, and S. A. Small. (2014). Pharmacological chaperones stabilize retromer to limit APP processing. *Nat Chem Biol*. 10, 443-9.

Meng, L., X. Y. Li, L. Shen, and H. F. Ji. (2020). Type 2 diabetes mellitus drugs for Alzheimer's disease: current evidence and therapeutic opportunities. *Trends Mol Med*. 26, 597-614.

Miranda, A. M., Z. M. Lasiecka, Y. Xu, J. Neufeld, S. Shahriar, S. Simoes, R. B. Chan, T. G. Oliveira, S. A. Small, and G. Di Paolo. (2018). Neuronal lysosomal dysfunction releases exosomes harboring APP C-terminal fragments and unique lipid signatures. *Nat Commun*. 9, 291.

Mishra, R., A. Upadhyay, V. K. Prajapati, R. Dhiman, K. M. Poluri, N. R. Jana,

and A. Mishra. (2019). LRSAM1 E3 ubiquitin ligase: molecular neurobiological perspectives linked with brain diseases. *Cell Mol Life Sci*. 76, 2093-110.

Miura, E., T. Hasegawa, M. Konno, M. Suzuki, N. Sugeno, N. Fujikake, S. Geisler, M. Tabuchi, R. Oshima, A. Kikuchi, T. Baba, K. Wada, Y. Nagai, A. Takeda, and M. Aoki. (2014). VPS35 dysfunction impairs lysosomal degradation of alpha-synuclein and exacerbates neurotoxicity in a Drosophila model of Parkinson's disease. *Neurobiol Dis*. 71, 1-13.

Morabito, M. V., D. E. Berman, R. T. Schneider, Y. Zhang, R. L. Leibel, and S. A. Small. (2014). Hyperleucinemia causes hippocampal retromer deficiency linking diabetes to Alzheimer's disease. *Neurobiol Dis*. 65, 188-92.

Moreau, Kevin, Angeleen Fleming, Sara Imarisio, Ana Lopez Ramirez, Jacob L Mercer, Maria Jimenez-Sanchez, Carla F Bento, Claudia Puri, Eszter Zavodszky, and Farah Siddiqi. (2014). PICALM modulates autophagy activity and tau accumulation. *Nat Commun*. 5, 1-20.

Morel, E., Z. Chamoun, Z. M. Lasiecka, R. B. Chan, R. L. Williamson, C. Vetanovetz, C. Dall'Armi, S. Simoes, K. S. Point Du Jour, B. D. McCabe, S. A. Small, and G. Di Paolo. (2013). Phosphatidylinositol-3-phosphate regulates sorting and processing of amyloid precursor protein through the endosomal system. *Nat Commun*. 4, 2250.

Moreno-Gonzalez, I., G. Edwards Iii, N. Salvadores, M. Shahnawaz, R. Diaz-Espinoza, and C. Soto. (2017). Molecular interaction between type 2 diabetes and Alzheimer's disease through cross-seeding of protein

misfolding. *Mol Psychiatry*. 22, 1327-34.

Morgan, M. J., and Z. G. Liu. (2011). Crosstalk of reactive oxygen species and NF-κB signaling. *Cell Res*. 21, 103-15.

Moruno, F., E. Perez-Jimenez, and E. Knecht. (2012). Regulation of autophagy by glucose in Mammalian cells. *Cells*. 1, 372-95.

Moruno, Félix, Eva Pérez-Jiménez, and Erwin Knecht. (2012). Regulation of autophagy by glucose in mammalian cells. *Cells*. 1, 372-95.

Mueller-Steiner, S., Y. Zhou, H. Arai, E. D. Roberson, B. Sun, J. Chen, X. Wang, G. Yu, L. Esposito, L. Mucke, and L. Gan. (2006). Antiamyloidogenic and neuroprotective functions of cathepsin B: implications for Alzheimer's disease. *Neuron*. 51, 703-14.

Nilsson, E., P. A. Jansson, A. Perfilyev, P. Volkov, M. Pedersen, M. K. Svensson, P. Poulsen, R. Ribel-Madsen, N. L. Pedersen, P. Almgren, J. Fadista, T. Ronn, B. Klarlund Pedersen, C. Scheele, A. Vaag, and C. Ling. (2014). Altered DNA methylation and differential expression of genes influencing metabolism and inflammation in adipose tissue from subjects with type 2 diabetes. *Diabetes*. 63, 2962-76.

Nixon, R. A. (2017). Amyloid precursor protein and endosomal-lysosomal dysfunction in Alzheimer's disease: inseparable partners in a multifactorial disease. *Faseb J*. 31, 2729-43.

Ohara, T., Y. Doi, T. Ninomiya, Y. Hirakawa, J. Hata, T. Iwaki, S. Kanba, and Y. Kiyohara. (2011). Glucose tolerance status and risk of dementia in the community: the Hisayama study. *Neurology*. 77, 1126-34.

Okabayashi, S., N. Shimozawa, Y. Yasutomi, K. Yanagisawa, and N. Kimura.

(2015). Diabetes mellitus accelerates Aβ pathology in brain accompanied by enhanced GAβ generation in nonhuman primates. *PLoS One*. 10, e0117362.

Okada, H., W. Zhang, C. Peterhoff, J. C. Hwang, R. A. Nixon, S. H. Ryu, and T. W. Kim. (2010). Proteomic identification of sorting nexin 6 as a negative regulator of BACE1-mediated APP processing. *Faseb J.* 24, 2783-94.

Papadopoulos, C., B. Kravic, and H. Meyer. (2020). Repair or lysophagy: dealing with damaged lysosomes. *J Mol Biol.* 432, 231-39.

Papadopoulos, C., and H. Meyer. (2017). Detection and clearance of damaged lysosomes by the endolysosomal damage response and lysophagy. *Curr Biol.* 27, R1330-R41.

Park, Kihyoun, and Myung-Shik Lee. (2022). Essential role of lysosomal Ca^{2+}-mediated TFEB activation in mitophagy and functional adaptation of pancreatic β-cells to metabolic stress. *Autophagy*. 18, 3043-5.

Paterson, A. D., D. Waggott, A. P. Boright, S. M. Hosseini, E. Shen, M. P. Sylvestre, I. Wong, B. Bharaj, P. A. Cleary, J. M. Lachin, Magic, J. E. Below, D. Nicolae, N. J. Cox, A. J. Canty, L. Sun, S. B. Bull, Control Diabetes, Interventions Complications Trial/Epidemiology of Diabetes, and Group Complications Research. (2010). A genome-wide association study identifies a novel major locus for glycemic control in type 1 diabetes, as measured by both A1C and glucose. *Diabetes*. 59, 539-49.

Polito, V. A., H. Li, H. Martini-Stoica, B. Wang, L. Yang, Y. Xu, D. B.

Swartzlander, M. Palmieri, A. di Ronza, V. M. Lee, M. Sardiello, A. Ballabio, and H. Zheng. (2014). Selective clearance of aberrant tau proteins and rescue of neurotoxicity by transcription factor EB. *EMBO Mol Med*. 6, 1142-60.

Raben, N., and R. Puertollano. (2016). TFEB and TFE3: linking lysosomes to cellular adaptation to stress. *Annu Rev Cell Dev Biol*. 32, 255-78.

Rahman, Md Habibur, Anup Bhusal, Jae-Hong Kim, Mithilesh Kumar Jha, Gyun Jee Song, Younghoon Go, Il-Sung Jang, In-Kyu Lee, and Kyoungho Suk. (2020). Astrocytic pyruvate dehydrogenase kinase-2 is involved in hypothalamic inflammation in mouse models of diabetes. *Nat Commun*. 11, 5906.

Raja, Waseem K., Alison E. Mungenast, Yuan-Ta Lin, Tak Ko, Fatema Abdurrob, Jinsoo Seo, and Li-Huei Tsai. (2016). Self-organizing 3D human neural tissue derived from induced pluripotent stem cells recapitulate Alzheimer's disease phenotypes. *PLoS One*. 11, e0161969.

Rodriguez, Caitlin M., Shannon E. Wright, Michael G. Kearse, Jill M. Haenfler, Brittany N. Flores, Yu Liu, Marius F. Ifrim, Mary R. Glineburg, Amy Krans, Paymaan Jafar-Nejad, Michael A. Sutton, Gary J. Bassell, Jack M. Parent, Frank Rigo, Sami J. Barmada, and Peter K. Todd. (2020). A native function for RAN translation and CGG repeats in regulating fragile X protein synthesis. *Nat Neurosci*. 23, 386-97.

Saez-Atienzar, S., and E. Masliah. (2020). Cellular senescence and Alzheimer disease: the egg and the chicken scenario. *Nat Rev Neurosci*. 21, 433-

44.

Saftig, P., and A. Haas. (2016). Turn up the lysosome. *Nat Cell Biol*. 18, 1025-7.

Schindelin, J., I. Arganda-Carreras, E. Frise, V. Kaynig, M. Longair, T. Pietzsch, S. Preibisch, C. Rueden, S. Saalfeld, B. Schmid, J. Y. Tinevez, D. J. White, V. Hartenstein, K. Eliceiri, P. Tomancak, and A. Cardona. (2012). Fiji: an open-source platform for biological-image analysis. *Nat Methods*. 9, 676-82.

Seaman, M. N. (2012). The retromer complex - endosomal protein recycling and beyond. *J Cell Sci*. 125, 4693-702.

Serrano-Puebla, A., and P. Boya. (2016). Lysosomal membrane permeabilization in cell death: new evidence and implications for health and disease. *Ann N Y Acad Sci*. 1371, 30-44.

Sevigny, J., P. Chiao, T. Bussiere, P. H. Weinreb, L. Williams, M. Maier, R. Dunstan, S. Salloway, T. Chen, Y. Ling, J. O'Gorman, F. Qian, M. Arastu, M. Li, S. Chollate, M. S. Brennan, O. Quintero-Monzon, R. H. Scannevin, H. M. Arnold, T. Engber, K. Rhodes, J. Ferrero, Y. Hang, A. Mikulskis, J. Grimm, C. Hock, R. M. Nitsch, and A. Sandrock. (2016). The antibody aducanumab reduces Aβ plaques in Alzheimer's disease. *Nature*. 537, 50-6.

Shah, M. S., and M. Brownlee. (2016). Molecular and cellular mechanisms of cardiovascular disorders in diabetes. *Circ Res*. 118, 1808-29.

Sims-Robinson, C., A. Bakeman, A. Rosko, R. Glasser, and E. L. Feldman. (2016). The role of oxidized cholesterol in diabetes-induced

lysosomal dysfunction in the brain. *Mol Neurobiol*. 53, 2287-96.

Sims-Robinson, C., B. Kim, A. Rosko, and E. L. Feldman. (2010). How does diabetes accelerate Alzheimer disease pathology? *Nat Rev Neurol*. 6, 551-9.

Skowyra, M. L., P. H. Schlesinger, T. V. Naismith, and P. I. Hanson. (2018). Triggered recruitment of ESCRT machinery promotes endolysosomal repair. *Science*. 360, eaar5078.

Small, S. A., K. Kent, A. Pierce, C. Leung, M. S. Kang, H. Okada, L. Honig, J. P. Vonsattel, and T. W. Kim. (2005). Model-guided microarray implicates the retromer complex in Alzheimer's disease. *Ann Neurol*. 58, 909-19.

Small, S. A., and G. A. Petsko. (2015). Retromer in Alzheimer disease, Parkinson disease and other neurological disorders. *Nat Rev Neurosci*. 16, 126-32.

Small, S. A., S. Simoes-Spassov, R. Mayeux, and G. A. Petsko. (2017). Endosomal traffic jams represent a pathogenic hub and therapeutic target in Alzheimer's disease. *Trends Neurosci*. 40, 592-602.

Song, J. X., S. Malampati, Y. Zeng, S. S. K. Durairajan, C. B. Yang, B. C. Tong, A. Iyaswamy, W. B. Shang, S. G. Sreenivasmurthy, Z. Zhu, K. H. Cheung, J. H. Lu, C. Tang, N. Xu, and M. Li. (2020). A small molecule transcription factor EB activator ameliorates β-amyloid precursor protein and tau pathology in Alzheimer's disease models. *Aging Cell*. 19, e13069.

Song, J. X., Y. R. Sun, I. Peluso, Y. Zeng, X. Yu, J. H. Lu, Z. Xu, M. Z. Wang, L.

F. Liu, Y. Y. Huang, L. L. Chen, S. S. Durairajan, H. J. Zhang, B. Zhou, H. Q. Zhang, A. Lu, A. Ballabio, D. L. Medina, Z. Guo, and M. Li. (2016). A novel curcumin analog binds to and activates TFEB in vitro and in vivo independent of MTOR inhibition. *Autophagy*. 12, 1372-89.

Srinivasan, K., and P. Ramarao. (2007). Animal models in type 2 diabetes research: an overview. *Indian J Med Res*. 125, 451-72.

Steinberg, G. R., and B. E. Kemp. (2009). AMPK in Health and Disease. *Physiol Rev*. 89, 1025-78.

Su, X., I. J. Lodhi, A. R. Saltiel, and P. D. Stahl. (2006). Insulin-stimulated Interaction between insulin receptor substrate 1 and p85α and activation of protein kinase B/Akt require Rab5. *J Biol Chem*. 281, 27982-90.

Swanson, C. J., Y. Zhang, S. Dhadda, J. Wang, J. Kaplow, R. Y. K. Lai, L. Lannfelt, H. Bradley, M. Rabe, A. Koyama, L. Reyderman, D. A. Berry, S. Berry, R. Gordon, L. D. Kramer, and J. L. Cummings. (2021). A randomized, double-blind, phase 2b proof-of-concept clinical trial in early Alzheimer's disease with lecanemab, an anti-Aβ protofibril antibody. *Alzheimers Res Ther*. 13, 80.

Takahashi, A., Y. Takabatake, T. Kimura, I. Maejima, T. Namba, T. Yamamoto, J. Matsuda, S. Minami, J. Y. Kaimori, I. Matsui, T. Matsusaka, F. Niimura, T. Yoshimori, and Y. Isaka. (2017). Autophagy inhibits the accumulation of advanced glycation end products by promoting lysosomal biogenesis and function in the kidney proximal tubules. *Diabetes*. 66, 1359-72.

Teng, B., P. Schroder, J. Muller-Deile, H. Schenk, L. Staggs, I. Tossidou, I. Dikic, H. Haller, and M. Schiffer. (2016). CIN85 deficiency prevents nephrin endocytosis and proteinuria in diabetes. *Diabetes*. 65, 3667-79.

Tessneer, K. L., R. M. Jackson, B. A. Griesel, and A. L. Olson. (2014). Rab5 activity regulates GLUT4 sorting into insulin-responsive and non-insulin-responsive endosomal compartments: a potential mechanism for development of insulin resistance. *Endocrinology*. 155, 3315-28.

Thomas, R. S., A. Henson, A. Gerrish, L. Jones, J. Williams, and E. J. Kidd. (2016). Decreasing the expression of PICALM reduces endocytosis and the activity of β-secretase: implications for Alzheimer's disease. *BMC Neurosci*. 17, 50.

Tian, Yuan, Jerry C Chang, Emily Y Fan, Marc Flajolet, and Paul Greengard. (2013). Adaptor complex AP2/PICALM, through interaction with LC3, targets Alzheimer's APP-CTF for terminal degradation via autophagy. *Proc Nati Acad Sci U S A*. 110, 17071-76.

Ueda, Daiki, Naomi Yonemochi, Tomohiro Kamata, Masahiro Shibasaki, Junzo Kamei, John L Waddington, and Hiroko Ikeda. (2021). Increase in neuropeptide Y activity impairs social behaviour in association with glutamatergic dysregulation in diabetic mice. *Bri J Pharmacol*. 178, 726-40.

Uhlen, M., L. Fagerberg, B. M. Hallstrom, C. Lindskog, P. Oksvold, A. Mardinoglu, A. Sivertsson, C. Kampf, E. Sjostedt, A. Asplund, I. Olsson, K. Edlund, E. Lundberg, S. Navani, C. A. Szigyarto, J. Odeberg, D.

Djureinovic, J. O. Takanen, S. Hober, T. Alm, P. H. Edqvist, H. Berling, H. Tegel, J. Mulder, J. Rockberg, P. Nilsson, J. M. Schwenk, M. Hamsten, K. von Feilitzen, M. Forsberg, L. Persson, F. Johansson, M. Zwahlen, G. von Heijne, J. Nielsen, and F. Ponten. (2015). Proteomics. Tissue-based map of the human proteome. *Science*. 347, 1260419.

Usenovic, M., E. Tresse, J. R. Mazzulli, J. P. Taylor, and D. Krainc. (2012). Deficiency of ATP13A2 leads to lysosomal dysfunction, α-synuclein accumulation, and neurotoxicity. *J Neurosci*. 32, 4240-6.

Vacinova, G., D. Vejrazkova, P. Lukasova, O. Lischkova, K. Dvorakova, R. Rusina, I. Holmerova, H. Vankova, J. Vcelak, B. Bendlova, and M. Vankova. (2017). Associations of polymorphisms in the candidate genes for Alzheimer's disease BIN1, CLU, CR1 and PICALM with gestational diabetes and impaired glucose tolerance. *Mol Biol Rep*. 44, 227-31.

Vagnozzi, A. N., J. G. Li, J. Chiu, R. Razmpour, R. Warfield, S. H. Ramirez, and D. Pratico. (2021). VPS35 regulates tau phosphorylation and neuropathology in tauopathy. *Mol Psychiatry*. 26, 6992-7005.

Vagnozzi, A. N., and D. Pratico. (2019). Endosomal sorting and trafficking, the retromer complex and neurodegeneration. *Mol Psychiatry*. 24, 857-68.

Vardarajan, B. N., S. Y. Bruesegem, M. E. Harbour, R. Inzelberg, R. Friedland, P. St George-Hyslop, M. N. Seaman, and L. A. Farrer. (2012). Identification of Alzheimer disease-associated variants in genes that regulate retromer function. *Neurobiol Aging*. 33, 2231.e15-31.e30.

Vieira, S. I., S. Rebelo, H. Esselmann, J. Wiltfang, J. Lah, R. Lane, S. A. Small, S. Gandy, E. Silva E. F. da Cruz, and E. Silva O. A. da Cruz. (2010). Retrieval of the Alzheimer's amyloid precursor protein from the endosome to the TGN is S655 phosphorylation state-dependent and retromer-mediated. *Mol Neurodegener*. 5, 40.

von Kleist, L., W. Stahlschmidt, H. Bulut, K. Gromova, D. Puchkov, M. J. Robertson, K. A. MacGregor, N. Tomilin, A. Pechstein, N. Chau, M. Chircop, J. Sakoff, J. P. von Kries, W. Saenger, H. G. Krausslich, O. Shupliakov, P. J. Robinson, A. McCluskey, and V. Haucke. (2011). Role of the clathrin terminal domain in regulating coated pit dynamics revealed by small molecule inhibition. *Cell*. 146, 471-84.

Wang, K., and H. Liu. (2021). Early-onset subgroup of type 2 diabetes and risk of dementia, Alzheimer’ s disease and stroke: a cohort study. *JPAD*. 8, 442-7.

Wang, L., X. Zhang, Z. B. Lin, P. J. Yang, H. Xu, J. L. Duan, B. Ruan, P. Song, J. J. Liu, Z. S. Yue, Z. Q. Fang, H. Hu, Z. Liu, X. L. Huang, L. Yang, S. Tian, K. S. Tao, H. Han, and K. F. Dou. (2021). Tripartite motif 16 ameliorates nonalcoholic steatohepatitis by promoting the degradation of phospho-TAK1. *Cell Metab*. 33, 1372-88.

Wang, W., F. Duclot, B. R. Groveman, N. Carrier, H. Qiao, X. Q. Fang, H. Wang, W. Xin, X. H. Jiang, M. W. Salter, X. S. Ding, M. Kabbaj, and X. M. Yu. (2018). Hippocampal protein kinase D1 is necessary for DHPG-induced learning and memory impairments in rats. *PLoS One*. 13, e0195095.

Wang, X., Z. Feng, J. Li, L. Chen, and W. Tang. (2016). High glucose induces autophagy of MC3T3-E1 cells via ROS-AKT-mTOR axis. *Mol Cell Endocrinol*. 429, 62-72.

Wen, L., F. L. Tang, Y. Hong, S. W. Luo, C. L. Wang, W. He, C. Shen, J. U. Jung, F. Xiong, D. H. Lee, Q. G. Zhang, D. Brann, T. W. Kim, R. Yan, L. Mei, and W. C. Xiong. (2011). VPS35 haploinsufficiency increases Alzheimer's disease neuropathology. *J Cell Biol*. 195, 765-79.

Willette, A. A., S. C. Johnson, A. C. Birdsill, M. A. Sager, B. Christian, L. D. Baker, S. Craft, J. Oh, E. Statz, B. P. Hermann, E. M. Jonaitis, R. L. Koscik, A. La Rue, S. Asthana, and B. B. Bendlin. (2015). Insulin resistance predicts brain amyloid deposition in late middle-aged adults. *Alzheimers Dement*. 11, 504-10.

Wu, D., D. Hu, H. Chen, G. Shi, I. S. Fetahu, F. Wu, K. Rabidou, R. Fang, L. Tan, S. Xu, H. Liu, C. Argueta, L. Zhang, F. Mao, G. Yan, J. Chen, Z. Dong, R. Lv, Y. Xu, M. Wang, Y. Ye, S. Zhang, D. Duquette, S. Geng, C. Yin, C. G. Lian, G. F. Murphy, G. K. Adler, R. Garg, L. Lynch, P. Yang, Y. Li, F. Lan, J. Fan, Y. Shi, and Y. G. Shi. (2018). Glucose-regulated phosphorylation of TET2 by AMPK reveals a pathway linking diabetes to cancer. *Nature*. 559, 637-41.

Xia, Y., S. Prokop, and B. I. Giasson. (2021). "Don't Phos Over Tau": recent developments in clinical biomarkers and therapies targeting tau phosphorylation in Alzheimer's disease and other tauopathies. *Mol Neurodegener*. 16, 37.

Xiao, Q., S. C. Gil, P. Yan, Y. Wang, S. Han, E. Gonzales, R. Perez, J. R. Cirrito,

and J. M. Lee. (2012). Role of phosphatidylinositol clathrin assembly lymphoid-myeloid leukemia (PICALM) in intracellular amyloid precursor protein (APP) processing and amyloid plaque pathogenesis. *J Biol Chem*. 287, 21279-89.

Xu, W., L. Tan, and J. T. Yu. (2015). The role of PICALM in Alzheimer's disease. *Mol Neurobiol*. 52, 399-413.

Yan, J., G. Tie, S. Wang, A. Tutto, N. DeMarco, L. Khair, T. G. Fazzio, and L. M. Messina. (2018). Diabetes impairs wound healing by Dnmt1-dependent dysregulation of hematopoietic stem cells differentiation towards macrophages. *Nat Commun*. 9, 33.

Yang, C., X. C. Chen, Z. H. Li, H. L. Wu, K. P. Jing, X. R. Huang, L. Ye, B. Wei, H. Y. Lan, and H. F. Liu. (2021). SMAD3 promotes autophagy dysregulation by triggering lysosome depletion in tubular epithelial cells in diabetic nephropathy. *Autophagy*. 17, 2325-44.

Ye, H., S. A. Ojelade, D. Li-Kroeger, Z. Zuo, L. Wang, Y. Li, J. Y. Gu, U. Tepass, A. A. Rodal, H. J. Bellen, and J. M. Shulman. (2020). Retromer subunit, VPS29, regulates synaptic transmission and is required for endolysosomal function in the aging brain. *Elife*. 9, e51977.

Yim, W. W., and N. Mizushima. (2020). Lysosome biology in autophagy. *Cell Discov*. 6, 1-12.

Young, J. E., L. K. Fong, H. Frankowski, G. A. Petsko, S. A. Small, and L. S. B. Goldstein. (2018). Stabilizing the retromer complex in a human stem cell model of Alzheimer's disease reduces tau phosphorylation independently of amyloid precursor protein. *Stem Cell Reports*. 10,

1046-58.

Yu, W. H., A. M. Cuervo, A. Kumar, C. M. Peterhoff, S. D. Schmidt, J. H. Lee, P. S. Mohan, M. Mercken, M. R. Farmery, L. O. Tjernberg, Y. Jiang, K. Duff, Y. Uchiyama, J. Naslund, P. M. Mathews, A. M. Cataldo, and R. A. Nixon. (2005). Macroautophagy--a novel β-amyloid peptide-generating pathway activated in Alzheimer's disease. *J Cell Biol.* 171, 87-98.

Zhang, L., Q. Zhang, S. Liu, Y. Chen, R. Li, T. Lin, C. Yu, H. Zhang, Z. Huang, X. Zhao, X. Tan, Z. Li, Z. Ye, J. Ma, B. Zhang, W. Wang, W. Shi, and X. Liang. (2017). DNA methyltransferase 1 may be a therapy target for attenuating diabetic nephropathy and podocyte injury. *Kidney Int.* 92, 140-53.

Zhao, Z., A. P. Sagare, Q. Ma, M. R. Halliday, P. Kong, K. Kisler, E. A. Winkler, A. Ramanathan, T. Kanekiyo, G. Bu, N. C. Owens, S. V. Rege, G. Si, A. Ahuja, D. Zhu, C. A. Miller, J. A. Schneider, M. Maeda, T. Maeda, T. Sugawara, J. K. Ichida, and B. V. Zlokovic. (2015). Central role for PICALM in amyloid-β blood-brain barrier transcytosis and clearance. *Nat Neurosci.* 18, 978-87.

Zhou, J., J. Blundell, S. Ogawa, C. H. Kwon, W. Zhang, C. Sinton, C. M. Powell, and L. F. Parada. (2009). Pharmacological inhibition of mTORC1 suppresses anatomical, cellular, and behavioral abnormalities in neural-specific Pten knock-out mice. *J Neurosci.* 29, 1773-83.

Zhu, J., S. Pittman, D. Dhavale, R. French, J. N. Patterson, M. S. Kaleelurrrahuman, Y. Sun, J. Vaquer-Alicea, G. Maggiore, C. S.

Clemen, W. J. Buscher, J. Bieschke, P. Kotzbauer, Y. Ayala, M. I. Diamond, A. A. Davis, and C. Weihl. (2022). VCP suppresses proteopathic seeding in neurons. *Mol Neurodegener*. 17, 30.

Zummo, F. P., K. S. Cullen, M. Honkanen-Scott, J. A. M. Shaw, P. E. Lovat, and C. Arden. (2017). Glucagon-like peptide 1 protects pancreatic β-cells from death by increasing autophagic flux and restoring lysosomal function. *Diabetes*. 66, 1272-85.

국문초록

고농도 포도당에 의한 엔도리소좀 기능장애가 신경세포의 아밀로이드 베타 축적에 미치는 영향

서울대학교 대학원
수의학과 수의생명과학 전공
(수의생리학)
채 창 우

당뇨병은 알츠하이머병의 위험 인자로 간주되고 있지만, 당뇨병에 의한 아밀로이드 베타의 축적 조절에 대한 자세한 기전은 명확히 밝혀져 있지 않다. 엔도리소좀(Endolysosome) 기능장애는 두 질환 사이의 인과관계를 설명할 수 있는 병리학적 연관성을 가진다. 그러나, 고혈당에 의한 신경세포 내 엔도리소좀의 기능 조절에 대해서는 알려진 바가 적다. 따라서 이 연구의 목표는 고농도 포도당에 의한 1) 아밀로이드 전구체 단백질(APP)을 처리할 수 있는 엔도솜 및 관련 신호전달경로의 조절 기전, 2) 레트로머(Retromer)와 이와 관련된 아밀로이드 전구체 단백질의 처리 및 타우 단백질의 인산화 메커니즘의 조절 이상, 3) 리소좀 자가포식(Lysophagy)의 장애와 그로 인한 아밀로이드 베타 축적과 이와 관련된 기전을 규명하는 것이다. 연구결과는 다음과 같다:

1) 당뇨병에 이환된 랫드와 마우스의 해마에서 엔도솜 이상과 아밀로이드 베타 축적의 증가가 나타났다. 고농도 포도당은 지질 뗏목을 매개로 하는 아밀로이드 전구체 단백질의 세포내 이입의 증가로 인한 초기 엔도솜 확대를 통해 아밀로이드 베타의 생산을 증가시켰다. 고농도 포도당에 의해 유도된 활성산소종(Reactive oxygen species)은 Sp1 을 활성화시켰으며, 포스파티딜이노시톨 결합 클라트린 조립 단백질(Phosphatidylinositol-binding clathrin assembly protein), 클라트린 중쇄(Clathrin heavy chain), 어댑터 관련 단백질 복합체 2 알파 1(Adaptor-related protein complex 2 α1)을 상향 조절했다. 포스파티딜이노시톨 결합 클라트린 조립 단백질은 클라트린을 매개로 하는 아밀로이드 전구체 단백질의 세포내 이입을 촉진하여 초기 엔도솜을 확대시켰다. 한편, AMPK/mTORC1 에 의한 자가포식의 결함과 활성산소종 및 mTORC1 에 의한 리소좀의 기능장애는 고농도

포도당 조건에서의 초기 엔도솜 비대를 악화시켰다. 더욱이, 초기 엔도솜 확대의 억제는 당뇨병에 이환된 마우스에서 증가된 아밀로이드 베타의 생산과 인지 장애를 완화시켰다.

2) 당뇨병에 이환된 마우스의 해마와 고농도 포도당에 노출된 인간의 신경세포에서 액포 단백질 분류-관련 단백질 26a(Vacuolar protein sorting-associated protein 26a)가 감소했다. 고농도 포도당은 활성산소종/핵인자 카파비(NF-κB)/디옥시리보핵산 메틸트랜스퍼라제 1(DNA methyltransferase1)에 의한 촉진유전자의 과도한 메틸화를 통해 액포 단백질 분류-관련 단백질 26a 를 하향 조절했다. 액포 단백질 분류-관련 단백질 26a 의 회복은 아밀로이드 전구체 단백질과 양이온 독립적인 만노스-6-인산 수용체의 엔도솜 내 보존을 억제하고 트랜스-골지체로의 수송 촉진을 통해, 아밀로이드 베타의 수치를 감소시키고, 카텝신 D 의 활성을 향상시켜 인산화된 타우 단백질의 수치를 감소시켰다. 레트로머의 기능 회복은 당뇨병에 이환된 마우스의 시냅스 결손, 별아교세포의 과잉 활성 및 인지 장애를 완화시켰다.

3) 고농도 포도당은 활성산소종에 의해 매개된 리소좀 막 투과와 리소좀 자가포식 장애를 통해 신경세포의 리소좀 기능 이상을 유도했다. 리소좀 자가포식 관련 인자 중, TRIM16 의 발현은 mTORC1 에 의한 전사 인자 EB (TFEB)의 활성 억제를 통해 고농도 포도당에 노출된 신경세포와 당뇨병에 이환된 마우스의 해마에서 감소했다. TRIM16 의 과발현은 손상된 리소좀으로의 미세소관 관련 단백질 1A/1B-경쇄 3(LC3), p62, 유비퀴틴의 모집을 통해 리소좀 자가포식과 리소좀

생합성을 회복시켰으며, 이는 고농도 포도당에 의해 유도된 아밀로이드 베타와 인산화된 타우 단백질의 축적을 억제했다. 당뇨병에 이환된 마우스에서, TFEB 강화제는 해마에서의 리소좀 자가포식을 회복하여 인지장애를 완화시켰다.

결론적으로, 이 연구에서는 고농도 포도당이 1) 포스파티딜이노시톨 결합 클라트린 조립 단백질에 의한 아밀로이드 전구체 단백질의 세포내 이입 유도와 mTORC1 에 의한 엔도솜 제거 억제를 통해 초기 엔도솜 이상, 2) 핵인자 카파비(NF-κB)/디옥시리보핵산 메틸트랜스퍼라제 1(DNA methyltransferase1)에 의한 액포 단백질 분류-관련 단백질 26a 를 하향 조절을 통해 레트로머의 기능 이상, 3) mTORC1/전사 인자 EB 에 의한 TRIM16 의 하향 조절을 통해 신경세포의 리소좀 자가포식 장애를 유발함을 확인했으며, 이는 아밀로이드 베타의 축적을 유도함을 입증했다. 따라서, 엔도리소좀 기능 장애는 당뇨병과 관련된 알츠하이머병의 주요한 병리기전적 원인이며, 이를 조절하는 것은 알츠하이머병 예방 및 치료를 위한 전략이 될 수 있다.

주요어: 알츠하이머병, 자가포식, 당뇨병, 엔도솜, 리소좀, 소포 수송

학번: 2016-27822

감사의 글

2016년 9월, 대학원 입학 후 약 7년이라는 세월이 빠르게 흘러갔습니다. 박사학위 논문을 작성하기 위해서 제 나름대로 최선을 다했지만, 저의 학위과정이 결실을 맺을 수 있었던 것은 많은 분들의 도움, 격려, 배려가 있었기 때문이라고 생각합니다. 이 글을 감사하는 분들께 드리고자 합니다.

먼저, 수의과학자로서 지녀야 할 기본적인 마음가짐과 과학적인 사고방식을 지도해주시고, 지도 학생이 주체적인 연구자가 되기 위해 필요한 인내의 시간을 감내해 주신 한호재 교수님께 감사의 말씀을 드립니다. 학위과정 동안 격려와 활력을 불어넣어 주시고, 연구자로서 갖춰야할 방법론적인 지식을 섬세하게 지도해주신 이장헌 교수님께도 감사의 말씀을 드립니다. 또한, 실제 사회에서 독립적인 연구자로서 갖춰야할 능력과 역량에 대해 조언을 주신 이민영 교수님, 신입생 시절 마음을 다잡고 학위 과정을 지속해 나갈 수 있도록 진심 어린 조언을 주신 이세중 교수님, 실험방법 및 논문 작성에 큰 도움을 주시고 대학원 생활의 모범이셨던 이현직 교수님께도 감사의 말씀을 드립니다. 좋은 수업을 통해 지적인 깨달음과 자신감을 얻게 해 주신 허은미 교수님께도 늘 감사한 마음을 가지고 있습니다. 학위 과정 중 많이 의지가 됐던 김준성 형, 임재룡 형, 김서일, 선하고 믿음직한 윤나영, 박지용, 생리학 실험실의 맏형 정영현 선생님, 밝고 긍정적인 조지현, 한수종, 장한승에게도 고맙다는 말 전하고 싶습니다. 저를 바르게 키워 주시고 묵묵히 버팀목이 돼 주시는 부모님과, 항상 저를 지지해주는 든든한 가족인 누나와 매형께 감사하고 사랑한다는 말씀드리고 싶습니다. 언제나 저를 응원해주고 제 편이 돼 주는 수현이에게도 사랑하고 고맙다는 말 전하고 싶습니다. 이외에도 학위 과정 중에 도움을 주신 많은 분들께 진심으로 감사의 말씀을 드립니다.